2017

Determination of Polarization Transfer Coefficients and Hyperon Induced Polarization for Quasi–Free Hyperon Photoproduction off the Bound Neutron

Colin Gleason
University of South Carolina

Determination of Polarization Transfer Coefficients and Hyperon Induced Polarization for Quasi–Free Hyperon Photoproduction off the Bound Neutron

by

Colin Gleason

Bachelor of Science
Union College 2011

Submitted in Partial Fulfillment of the Requirements

for the Degree of Doctor of Philosophy in

Physics

College of Arts and Sciences

University of South Carolina

2017

Accepted by:

Yordanka Ilieva, Major Professor

Ralf Gothe, Committee Member

Matthias Schindler, Committee Member

Michael Vineyard, Committee Member

Cherly L. Addy, Vice Provost and Dean of the Graduate School

Dedication

To my family, friends, fiancé, and cat. What a long strange trip it's been.

Acknowledgments

First, I need to thank Yordanka Ilieva, who has been a fantastic advisor during my Ph.D. studies. When she took me on as a student, I had limited experience and knowledge when it came to medium energy nuclear physics. Her guidance, help, and most importantly patience has helped me learn so much about the field. Our many discussions have taught me not only so much about the field, but how to be a better researcher.

I would like to thank all the members of the Experimental Nuclear Physics Group who have helped me with my work along the way. Steffen Strauch's suggestions have provided key insight into my analysis and his scrutiny of my work on a near weekly basis has challenged me to look at my work in a new way. Nicholas Zachariou and Tongtong Cao have spent countless hours helping and discussing my work with me Much of this thesis is based off the many discussions we have had.

I would also like to thank everyone in the Experimental Nuclear Physics group at South Carolina and the members of the g13 run group for all the help along the way.

Last, and certainly not least, I need to thank my wonderful fiancé Ellen Bryan. Ellen and I met 6 months into my Ph.D. studies and she has been one of the few constants in my life throughout the process. She has been supportive, understanding, and patient. Thank you, Ellen. I can not express how much I love and appreciate you.

Work supported by NSF PHY–125782.

Abstract

The spectrum of the excited nucleon (N^*) states provides key information on the relevant degrees of freedom within the nucleon. The determination of the N^* spectrum requires an extensive set of high–quality experimental observables for a large number of nuclear reactions over a broad kinematic range. In particular, measurements of polarization observables of strangeness photoproduction are of high importance as many of the resonances that are predicted by quark models, but not observed in pion–nucleon channels, are expected to couple strongly to kaon–hyperon (KY) channels. While in the last decade a large body of polarization and cross–section data has been published for strangeness photoproduction off the proton, data off the neutron are very scarce. The goal of this dissertation is to determine the polarization observables C_x, C_z, and P in the reaction $\vec{\gamma}d \to K^0\vec{\Lambda}(p)$, where the deuteron is used as a neutron target. The data was collected in the experiment E06-103 with the CEBAF Large Acceptance Spectrometer (CLAS) at Thomas Jefferson National Accelerator Facility (JLab) using a circularly-polarized photon beam and an unpolarized LD_2 target. In this thesis I discuss the analysis technique and show results of C_x, C_z, and P for quasi–free photoproduction of $K^0\Lambda$ off the bound neutron for photon energies between 0.9–2.6 GeV and K^0 center–of–mass angles, $\cos\theta_{K^0}^{CM}$, between -1 and 1. This study is part of a larger program carried out at JLab to provide a nearly complete set of observables for strangeness photoproduction off the nucleon.

Table of Contents

Dedication iii

Acknowledgments iv

Abstract v

List of Tables ix

List of Figures xii

Chapter 1 Introduction 1

1.1 Standard Model 2

1.2 Quantum Chromodynamics 3

1.3 Baryon Spectroscopy 7

1.4 Hyperon Photoproduction 14

1.5 Summary and Structure 26

Chapter 2 Experiment 28

2.1 g13 Experiment 28

2.2 CEBAF 29

2.3 Hall B 30

Chapter 3 Event Selection 40

3.1 Particle Identification 40
3.2 Event Vertex 44
3.3 Photon Selection 45
3.4 Decay Vertex Reconstruction 48
3.5 Reconstruction of the K^0 and Λ 50
3.6 Missing Momentum 54

Chapter 4 Observable Extraction Method 56
4.1 Event Generator and Simulations 58
4.2 Axis Conventions 65
4.3 Maximum Likelihood Method 65
4.4 Background Subtraction 66

Chapter 5 Systematic Studies 78
5.1 Instrumental Asymmetry 79
5.2 Event–Selection Cuts 85
5.3 Combinatorial Background 108
5.4 Maximum Likelihood Extraction Method 109
5.5 Background Subtraction 122
5.6 Photon Polarization and Self–Analyzing Power of the Λ 127
5.7 Summary 128

Chapter 6 Results 131
6.1 Kinematic Binning 131

6.2 Photon Polarization 132

6.3 Unprimed Coordinate System 133

6.4 Primed Coordinate System 139

6.5 Comparison with $\gamma p \to K^+\Lambda$ 141

6.6 Observables as a Function of the Neutron Momentum 143

6.7 Discussion 146

Bibliography 149

List of Tables

Table 1.1 The status of the N^*s. A * means evidence for the state is poor, ** evidence is fair, *** evidence is very likely but more information is needed, and **** means the evidence is certain and the properties of the state have been explored. The table is adapted from the PDG [47]. 8

Table 1.2 The differential cross section and the 15 polarization observables for KY photoproduction. The left column shows the name of the observables, the middle column shows the expression for the observable in the transversity representation, and the right column lists the polarizations needed to extract the observable. Table adapted from [4]. 20

Table 4.1 Physics channels generated in the event generator and processed through the detector simulation. If desired, unstable final–state particles can be decayed in the generator. 58

Table 5.1 Pull distribution parameters (μ, σ) for different $\cos\theta^*_{\pi^-}$ bins. The means and widths do not significantly differ from 0 and 1, respectively. This means no instrumental asymmetry within specific $\cos\theta^*_{\pi^-}$ ranges is present in the data. 82

Table 5.2 Pull distribution parameters (μ, σ) for different ϕ bins. The means and widths do not significantly differ from 0 and 1, respectively. This means no instrumental asymmetry within specific ϕ ranges is present in the data. 83

Table 5.3 Pull Distribution parameters for p_X bins. The means and widths do not significantly differ from 0 and 1, respectively. This means no significant instrumental asymmetries are present within specific p_X ranges. 83

Table 5.4 Relative pull–distribution fit parameters for the different proton selection cuts. The means and widths of C_x, C_z, and P are consistent with 0 and 1, respectively. 87

Table 5.5 Relative pull–distribution calculated parameters for the proton selection. The means are all consistent with 0. The widths do not significantly differ from 1. 87

Table 5.6 Relative pull–distribution fit parameters for the π^+ selection. The means and widths of C_x, C_z, and P do not significantly differ from 0 and 1, respectively. 88

Table 5.7 Relative pull–distribution calculated parameters for the π^+ selection. The means of C_x, C_z, and P do not significantly differ from 0 and the widths are close to 1. 88

Table 5.8 Relative pull–distribution fit parameters for the π^- selection. The means and the widths of C_x, C_z, and P pulls do not significantly differ from 0 and 1, respectively. 88

Table 5.9 Relative pull distributions for C_x (left), C_z (middle), and P (right) from the π^- selection. The means do not significantly differ from 0 and the widths are close to 1. 89

Table 5.10 Relative pull-distribution fit parameters for the different $M(p\pi^-)$ regions. The means and widths of C_x and C_z are consistent with 0 and 1. The mean of P is more than 3 standard deviations from 0. 91

Table 5.11 Relative pull-distribution calculated parameters for the $M(p\pi^-)$ cut. The means of C_x and C_z are consistent with 0. The mean of P is significantly different than 0. 92

Table 5.12 Calculated weighted mean of the difference ΔObs for the $M(p\pi^-)$ cut. 93

Table 5.13 Calculated mean of the σ^2_{sys} for the $M(p\pi^-)$ cut. 95

Table 5.14 The mean ($\mu \pm \sigma_\mu$), number of standard deviations of the mean from 0 ($N\sigma_\mu$), width (width$\pm\sigma_{width}$), and number of standard deviations of the width from 1 ($N\sigma_{width}$) of the relative pull distribution fit parameters for the $M(\pi^+\pi^-)$ cut. From the fits, the mean and width do not significantly deviate from 0 and 1, respectively. 96

Table 5.15 Relative pull distribution calculated parameters for the $M(\pi^+\pi^-)$ cut. The means are all consistent with 0. The widths are all close to 1. 96

Table 5.16 Relative pull-distribution fit parameters for the fiducial cut. The means and widths for C_x and C_z are consistent with 0 and 1, respectively. The mean for P is $\approx 4\sigma$ from 0. 99

Table 5.17 Calculated relative pull-distribution parameters for the fiducial cut. 100

Table 5.18 Calculated weighted mean of the difference distribution, for the fiducial cut. Only the weighted mean for P is significantly different from 0. 101

Table 5.19 Calculated mean of the σ^2_{sys} for the fiducial cuts. The negative values for the calculated means of all observables suggest no significant systematic uncertainties can be attributed to the fiducial cuts. 102

Table 5.20 Relative pull–distribution fit parameters for the p_X cut. The means and widths do not significantly differ from 0 and 1, respectively. 105

Table 5.21 Relative pull–distribution calculated parameters for the p_X cut. The means for C_x and P are consistent with 0, while the mean of C_z is not. 105

Table 5.22 The calculated weighted mean of the difference distribution, ΔObs for the p_X cut. 106

Table 5.23 Calculated mean of the σ^2_{sys} for the p_X cut. The negative values for C_x, C_z, and P suggest there is no systematic uncertainty associated with the cut. 106

Table 5.24 Electron polarizations for each run in the g13a sample. A description of how the polarization was determined is given in [12]. . 128

Table 5.25 Summary of systematic uncertainties. The systematic error of P is 0.013 and all values of this observable need to be reduced by this amount. 129

Table 6.1 Average percentage of signal, polarized background, and unpolarized background for each E_γ bin. 132

Table 6.2 Fit parameters for each observable from Fig. 6.15. P is the only observable having a slope consistent with 0. C_x has a slope consistent within 2σ of 0 and C_z within 3σ of 0. 144

List of Figures

Figure 1.1 Elementary particles in the Standard Model that describes the fundamental interactions between elementary particles. Matter consists of three elementary, or fundamental, types of particles: quarks, leptons, and force carriers. This image was taken from Reference [2]. 2

Figure 1.2 The meson nonet. Particles with the same strangeness are arranged horizontally and particles with the same charge are arranged diagonally. This image is taken from Reference [1]. 6

Figure 1.3 The baryon octet. Particles with the same strangeness are arranged horizontally and particles with the same charge are arranged diagonally. Figure adapted from Reference [57]. 6

Figure 1.4 A simple schematic of the quark arrangement in constituent quark models. Each of the three quarks interacts equally with each other. 10

Figure 1.5 Predicted N^* decays into $N\gamma$ (white), $N\pi$(light grey), and $K\Lambda$(black). States seen in $N^* \rightarrow N\pi$ decays have an additional wider dark grey band. Weak or missing states have a wider light grey band. The Y–axis is the mass of the state in MeV and the X–axis lists the spin and parity, J^P, of the state. This image was taken with permission from Reference [15]. 11

Figure 1.6 A simple schematic of the quark arrangement in a baryon in diquark models. Excitations of the bound quark pair are suppressed, leading to fewer degrees of freedom than in CQMs, and therefore to less predicted N^*s. 12

Figure 1.7 Predicted N^* and Δ^* spectrum (black lines) for the diquark model of Reference [23] compared to the $***$ and $****$ states from the 2008 PDG[6]. This image was taken with permission from Reference [23]. 13

Figure 1.8 Predicted N^* (left) and Δ^* (right) spectrum from Lattice QCD calculations with the mass of the pion, $m_\pi = 396$ MeV. The X–axis lists the spin–parity, J^P, of the state (ex. $\frac{3}{2}^+$, $\frac{5}{2}^-$) and the Y–axis shows the mass of the state. The width of each different box is the uncertainty in the mass of the N^*. This image was adapted from Reference [21]. 14

Figure 1.9 A schematic of the coordinate systems used in the analysis of KY photoproduction. Two different coordinate systems are used: the unprimed and primed. The unprimed coordinate system has its z–axis aligned with the incoming photon momentum, $\hat{z} = \hat{p}_\gamma$. The y–axis, $\hat{y} = \hat{z} \times \hat{p}_K$. The x–axis, $\hat{x} = \hat{y} \times \hat{z}$. In the primed coordinate system, the z'–axis is along the kaon momentum $\hat{z} = \hat{p}_K$. The y'–axis is defined as $\hat{y'} = \hat{z'} \times \hat{p}_\gamma$. The x'–axis is thus $\hat{x'} = \hat{y'} \times \hat{z'}$. For both coordinate systems, the reaction occurs in the x–z (x'–z') plane. 15

Figure 1.10 The four helicity amplitudes in pseudoscalar meson photoproduction. The label "N" corresponds to the no–spin flip amplitude, "$S_{1(2)}$" corresponds to the single spin flip amplitudes, and "D" corresponds to the double spin flip amplitude. 19

Figure 1.11 Three mechanisms to photoproduce KY. A resonance, N^* is created in the s channel that then decays into the KY. In the t (u) channel, a K^* (Y^*) is exchanged. 21

Figure 1.12 Two example fits ((a) and (b)) of the cross section of $\gamma p \to K^+\Lambda$ from the Bonn–Gatchina group. The solid curves are the results of the fits, the dashed lines are P_{13} ($N(1900)\frac{3}{2}$, $N(1720)\frac{3}{2}$) contributions, the dotted lines are S_{11} ($N(15350\frac{1}{2}$, $N(1650)\frac{1}{2}$) contributions, and the dashed–dotted line is the t–channel contribution. This image was taken from Reference [8] 22

Figure 1.13 C_z as a function of the center–of–mass energy W for different $\cos\theta_K^{CM}$ bins. The open circles are the experimental values for the observable. The different colored curves represent predictions from different hadronic models. The image was taken from Reference [11]. 23

Figure 1.14 O_x as a function of the center–of–mass energy W for different $\cos\theta_K^{CM}$ bins. The black circles are the experimental values for the observable. The red curves are predictions from ANL–Osaka [31], green colored curves from the 2014 Bonn–Gatchina group[29], and the blue curves are ref–fits including the present data with and an additional $N^*\frac{3}{2}^+$ and $N^*\frac{5}{2}^+$ added. This image was taken from Reference [46] 24

Figure 1.15 The red and black data points on both histograms are the two sets of Jefferson Lab data. The left panel shows the data points with Kaon–MAID models with two different sets of input parameters [33]. The right panel shows the cross sections from $K^+\Lambda$ superimposed on top of the $K^0\Lambda$ data. Also drawn are two different PWA solutions from the Bonn–Gatchina group for the $K^0\Lambda$ (green lines) and the 2014 solution for the $K^+\Lambda$ data.This image was taken from [18]. 26

Figure 2.1 A schematic of CEBAF at the time the experiment took place. One can see the 0.6 GeV linacs, the recirculating arcs, and the three experimental halls (Hall A, Hall B, and Hall C) at the time of the experiment. This figure is taken from Reference [39] . 30

Figure 2.2 A schematic of the Hall–B beam line during the g13a experiment. From left to right, along the beam direction one can see the Møller polarimeter, the radiator and the tagging spectrometer, the subsystems of the CLAS detector, the photon profile monitor, and the total absorption counter. Not shown is the photon collimator placed between the tagger and the CLAS. Figure is from [39]. 30

Figure 2.3 A schematic of the photon tagger in Hall B. Electrons, incident from the left, that interacted with the radiator produced bremsstrahlung photons that continued in the original direction of the incident electron beam. The electrons were bent by a dipole magnet at different angles based on their energy. A two-plane hodoscope detected these electrons, which allowed for energy and time measurements. This figure is taken from Reference [53] 33

Figure 2.4 A schematic of the CLAS detector. Drift Chambers measure particles' trajectories and TOF Counters measure the time of flight. This image is taken from Reference [39]. 34

Figure 2.5 A cross section of the magnetic field vectors for the CLAS toroidal field in a plane perpendicular to the beam line. The locations of the coils are indicated by thick solid lines. One can see the field distortions in the areas close to the coils. This image is taken from Reference [39]. 35

Figure 2.6 A schematic of the start counter in CLAS. One can see the six identical sectors of four scintillators per sector. This image was taken from Reference [51]. 36

Figure 2.7 A schematic of CLAS detector as seen from the perspective of looking down the beam line. One can see how the CLAS is divided into six sectors by the main torus coils. The three regions of drift chambers are situated between these coils and track the trajectories of charged particles as they travel through the detector. The mini–torus is a magnet used in electro-production experiments. It was not used in g13, where the start counter was placed in its location. This image is taken from Reference [39]. 37

Figure 2.8 One sector of the time–of–flight system. Each sector of 56 paddles was positioned such that each paddle covers different polar angle. This image is taken from Reference [52]. 39

Figure 3.1 $\Delta\beta$ as a function of momentum for protons as measured by the CLAS, i.e. without any corrections applied. One clearly sees that true protons yield a distribution centered around $\Delta\beta$ of zero. The leaf–like structures that seem to originate from the proton distribution at low momenta and to follow a different trend at higher momenta are due to true protons that have incorrect timing. A lot of background events, such as pions and kaons are not seen in this figure. This is due to the fact that extra selection cuts, such as photon selection, K^0 selection, Λ selection, and missing mass cuts (all to be discussed) have been applied to the event sample in order to reduce the uncertainty of the proton PID cuts. The vertical black lines represent the different momentum bins used to determine the final PID cuts. . . 41

Figure 3.2 Projections and the Gaussian fit of the proton $\Delta\beta$ for the 10 momentum bins shown in Fig. 3.1. Even though extra cuts have been applied to the event sample to remove accidental background, some background events remain. Those contribute to the non–Gaussian tails of the projections. In order to determine the widths of those nearly–Gaussian distributions by fits to a Gaussian function in a consistent manner, the fit ranges were set to be [-0.025,0.025]. 42

Figure 3.3 Final $\Delta\beta$ cuts for the proton (red line). The red data points represent the $\pm 3\sigma$ points determined from the Gaussian fits in Fig. 3.2. These points were then fit with a 4^{th} order polynomial to determine the $\Delta\beta$ cut. 43

Figure 3.4 $\Delta\beta$ vs. p distribution for the π^+. The red data points represent the $\pm 3\sigma$ points determined from the Gaussian fits to the different momentum bins. These points were then fit with a 4^{th} order polynomial to determine the final $\Delta\beta$ cut (red line). The small structure at low momenta and positive delta beta is most likely due to true π^+s that decay before they reach the time–of–flight detector. The daughter muon moves along a path that is sufficiently close to the trajectory of the parent π^+ so that a single track is reconstructed. The momentum of the track however is different from the momentum of the parent π^+. 43

Figure 3.5 $\Delta\beta$ vs. p distribution for the π^-. The red data points represent the $\pm 3\sigma$ points determined from the Gaussian fits to the different momentum bins. These points were then fit with a 4^{th} order polynomial to determine the final $\Delta\beta$ cut (red line). The small structures at low momenta and positive delta beta are most likely due to true π^-s that decay before they reach the time–of–flight detector. The daughter muon moves along a path that is sufficiently close to the trajectory of the parent π^- so that a single track is reconstructed. The momentum of the track however is different from the momentum of the parent π^-. This effect is typically observed for out bending pions, i.e. π^- in g13a. 44

Figure 3.6 The z component of the production vertex. Events were kept if they originated within the target. 45

Figure 3.7 Number of photons detected per event in g13a. The photon selection uses time coincidence between the photon and the event in the CLAS to identify which among all photons initiated the event detected in the CLAS. 46

Figure 3.8 Coincidence time for all particles and the fastest particle in CLAS. The smaller peaks that are separated by 2 ns show the structure of different electron beam bunches. 47

Figure 3.9 Number of photons yielding a coincidence time within ± 1 ns per event. Events with 2 or more photons within the time-coincidence cut were removed from further analysis since there is no reliable mechanism to identify which amongst them was most likely the "good" photon. 48

Figure 3.10 The DOCA method used to reconstruct the decay vertices of the K^0 and Λ. The DOCA occurs along the line perpendicular to each track (solid black line). The reconstructed decay vertex, represented by the $\star$, is the bisector of the DOCA line. 50

Figure 3.11 $M(\pi^+\pi^-)$ as a function of $M(p\pi^-)$. The peak containing to $K^0\Lambda$ events sits on top of a broad background. The background is mostly due to $\gamma d \rightarrow p\pi^+\pi^-\pi^- X$ events uncorrelated with $K^0\Lambda$ production. 51

Figure 3.12 $M(\pi^+\pi^-)$ distribution after all previous cuts are applied. The peak was fit with a Gaussian and the vertical lines represent $\pm 4\sigma$ cuts used to select K^0 events. 52

Figure 3.13 $M(p\pi^-)$ distribution after all previous cuts, including K^0 selection, were applied. The peak was fit with a Gaussian and the solid vertical lines represent $\pm 4\sigma$ cuts used to select Λ events. . . 53

Figure 3.14 Distribution of $K^0\Lambda X$ events (where $X = p$) over the spectator momentum, $|\vec{p}_X|$. Events below 0.2 GeV/c form a sample dominated by the quasi–free reaction. 54

Figure 4.1 M_{K^0X} as a function of M_X. Visually, the main peak centered at $M_X = M_p$ and $M_{K^0X} = M_\Lambda$ contains the signal events. Higher mass channels in M_X and M_{K^0X} contain background channels such as $K^0\Sigma^0$, $K^0\Sigma^{*0}$, and $K^\star(892)\Lambda$ photoproduction. The arrows point to the general area of these different channels. 57

Figure 4.2 Fitting procedure and momentum correction example for the proton. The data were binned in different z–vertex, ϕ, and θ bins. For each bin, the Δp vs. $|\vec{p}|$ distribution was divided into 5 $|\vec{p}|$ bins. For each p bin, Δp was fit with a Gaussian. The means for the momentum bins were then fit with an exponential to determine the momentum corrections. 60

Figure 4.3 Momentum of the π^+ for the simulation scaled (red) to the data (blue) for 100–MeV wide E_γ bins. 61

Figure 4.4 Momentum of the π^- from the Λ for the simulation scaled (red) to the data (blue) for 100–MeV wide E_γ bins. 62

Figure 4.5 Momentum of the proton for the simulation scaled (red) to the data (blue) for 100–MeV wide E_γ bins. 63

Figure 4.6 Momentum of the π^- from the K^0 for the simulation scaled (red) to the data (blue) for 100–MeV wide E_γ bins. 63

Figure 4.7 $\cos\theta_{K^0}^{CM}$ for the $K^0\Lambda$ simulation scaled (red) to the data (blue) for 100–MeV wide E_γ bins. 64

Figure 4.8 The missing–mass, M_X, of $\gamma d \to K^0\Lambda(X)$ with the selection cuts described in Chapter 3 integrated over all kinematics. 67

Figure 4.9 A visualization of Eqs. 4.10, 4.11, 4.12, and 4.13 on M_X. In a given region of M_X, shown as the black lines at 0.9 and 0.98 GeV/c^2, the total observable is extracted. 69

Figure 4.10 An example fit and scaling of the non–resonant, unpolarized $\gamma d \to p\pi^+\pi^-\pi^-(p)$ simulated background to the data using Equation 4.23. A double Gaussian is used to describe the signal and a parameter from the fit, A_3, is used to scale the unpolarized background (magenta) to the data. 71

Figure 4.11 Example fits and scaling of the non–resonant, unpolarized simulation to the data for one E_γ bin. The red line is the total fit to the data and the magenta histogram is the $p\pi^+\pi^-\pi^-$ non–resonant background scaled using A_3 from Equation 4.23. 72

Figure 4.12 The χ^2/NDF and scale factor (A_3 in Eq. 4.23) for all the fits. The χ^2/NDF is used as a check on the goodness of fit, while A_3 provides the scale factor for the $p\pi^+\pi^-\pi^-$ non–resonant background. 73

Figure 4.13 Total fit using Equation 4.24 (red line) to the data (blue points) and scaling to M_X integrated over all kinematics. The magenta histogram is the scaled non–resonant background, the green histogram is the scaled $K^0\Sigma^0$ distribution, and the black distribution are the higher mass background channels. 75

Figure 4.14 Fits and scaling to M_X for $2.1 < E_\gamma < 2.2$ GeV. The red line is the total fit to the data, the red histogram is the scaled $p\pi^-\pi^+\pi^-$ distribution, the green histogram is the scaled $K^0\Sigma^0$ distribution, and the black and violet histograms are the scaled higher mass channels. The black lines are drawn to show the separation of the Regions. 76

Figure 4.15 The χ^2/NDF and scale factor (A_4 in Eq. 4.24) for all the fits. Generally speaking, the χ^2/NDF from these fits are larger than those seen in the $M(p\pi^-)$ fits. This is likely due to the fact that there are significantly more fit parameters in Equation 4.24 than there are in Equation 4.23. The small value for the scale factor suggests that there is enough statistics in the simulations to accurately scale the background. 77

Figure 5.1 (Top) The instrumental asymmetry as a function of run number for $p_X < 0.2$ GeV/c integrated over all kinematic variables. (Bottom) The pull distribution fit with a Gaussian. The results suggest that there is no time–dependent instrumental asymmetry in the g13a data set. 81

Figure 5.2 A as a function of ϕ (top row) for the pion (left) and proton (right) with their corresponding pull distributions (bottom row). The fits to the pull distributions show no significant biases or unaccounted for uncertainties in the data. 84

Figure 5.3 Relative pull distributions for C_x (left), C_z (middle), and P (right) from the proton selection. From the parameters, no significant systematic uncertainties are seen in C_x, C_z, or P. . . . 86

Figure 5.4 Relative pull distributions for C_x (left), C_z (middle), and P (right) from the π^+ selection. From the parameters, no significant systematic uncertainties are seen in C_x, C_z, or P. 87

Figure 5.5 Relative pull distributions for C_x (left), C_z (middle), and P (right) from the π^- selection. From the parameters, no significant biases or systematic uncertainties are seen in C_x, C_z, or P. 89

Figure 5.6 $M(p\pi^-)$ distribution with lines representing $\pm 4\sigma$ (black) and $\pm 0.7\sigma$ (red), where σ is determined from the fit in Fig. 3.13. To investigate the systematic uncertainties, a relative pull distribution between each region was fit with a Gaussian. 90

Figure 5.7 Relative pull distributions for the two different regions in $M(p\pi^-)$. From the parameters, no significant biases are seen for C_x or C_z. The mean for P is more than 3σ from 0, which suggests there may be some systematic uncertainty caused by the $M(p\pi^-)$ selection. 91

Figure 5.8 Differences between the observables for the two different regions in $M(p\pi^-)$. When fit with a Gaussian, the means of C_x and C_z are consistent with 0. The mean of P is significantly different than 0. 93

Figure 5.9 Distributions of σ^2_{sys} for the observables. The parameters of the fit suggest there are no significant systematic uncertainties. 94

Figure 5.10 $M(\pi^+\pi^-)$ distribution with lines representing $\pm 4\sigma$ (black) and $\pm 0.7\sigma$ (red), where σ is determined from the fit shown in Fig. 3.12. The systematic uncertainty related to the $M(\pi^+\pi^-)$ selection is studied through relative pull distributions and differences in observables between the two regions. 96

Figure 5.11 Relative pull distributions for C_x (left), C_z (middle), and P (right) from the $M(\pi^+\pi^-)$ selection. From the fit parameters, no significant biases are seen. 97

Figure 5.12 Distribution of ϕ as a function of θ for a π^- without (left) and with (right) fiducial cuts applied. The fiducial cuts reject particles that travel close to the sector edges. 98

Figure 5.13 Distribution of ϕ as a function of θ for the events removed by the fiducial cuts for the p (top left), π^+ (top right), and π^-s (bottom row). 99

Figure 5.14 Relative pull-distributions for C_x (left), C_z (middle), and P (right) from applying the fiducial cuts. From the parameters, no significant systematic uncertainties are seen in C_x or C_z. The mean of P is significantly different from 0, suggesting there may be some systematic uncertainty. 100

Figure 5.15 Differences between the observables when using "good" and "bad" samples. The means for C_x and C_z are consistent with 0, whereas the mean for P is $\approx 4\sigma_\mu$ from 0. 101

Figure 5.16 Distribution of σ^2_{sys} for C_x (left), C_z (middle), and P (right) . The means of the fits suggest there are no significant systematic uncertainties. 102

Figure 5.17 The correlation between "good" (estimated from events that pass the fiducial cuts) and "bad" (estimated from events where at least one particle fails the fiducial cut) observables. The parameters of the fits suggest there are no significant systematic biases for C_x and C_z. Since the Y-intercept for P is inconsistent with 0, while the slope is consistent with 1, the systematic bias in P is a bias with the form $\mu + \delta$. 103

Figure 5.18 Event distribution over the magnitude of spectator momentum, p_X. The red line divides p_X into two regions, Region 1 and Region 2. 104

Figure 5.19 Relative pull distributions for C_x (left), C_z (middle), and P (right) from the p_X selection. From the parameters, no significant systematic uncertainties are seen in C_x, C_z, or P. 105

Figure 5.20 Differences between the observables for the two different regions in p_X. When fit with a Gaussian, the means of the differences are consistent with 0. 106

Figure 5.21 Distribution of σ^2_{sys} for C_x (left), C_z (middle), and P (right) . The means of the fits suggest there are no significant systematic uncertainties. 107

Figure 5.22 Fits to M_X for different $\cos\theta^{CM}_{K^0}$ in the highest E_γ bin. There are multiple $\cos\theta^{CM}_{K^0}$ in this E_γ bin where the fits are not able to describe the data. 108

Figure 5.23 Generator flowchart for studying systematic effects originating from the maximum likelihood extraction method. 109

Figure 5.24 Pull distributions for $C_x = C_z = P = 0$ for 1,000 experiments, with 10,000 generated events in each experiment, fit with a Gaussian. The means and the widths of the pull distributions do not significantly differ from 0 and 1, respectively. 111

Figure 5.25 Observable differences for $C_x = C_z = P = 0$ for 1,000 experiments with 10,000 generated events fit with a Gaussian. 111

Figure 5.26 Pull distributions for $C_x = 0.2$, $C_z = 0.8$, and $P = 0.5$ for 1,000 experiments with 10,000 generated events fit with a Gaussian. The means and the widths of the distributions do not significantly differ from 0 and 1, respectively. 112

Figure 5.27 Observable differences for $C_x = 0.2$, $C_z = 0.8$, $P = 0.5$ for 1,000 experiments with 10,000 generated events fit with a Gaussian. 113

Figure 5.28 Pull distributions for random C_x, C_z, and P for 1,000 experiments with 10,000 generated events fit with a Gaussian. 114

Figure 5.29 Correlation plot for random C_x, C_z, and P for 1,000 experiments, with 10,000 generated events in each experiment, fit with a Gaussian. 115

Figure 5.30 Calculated acceptance from Equation 5.8 for each E_γ and $\cos\theta^{CM}_{K^0}$ bin. 116

Figure 5.31 Example of $A(\cos\theta_y, \cos\theta_z)$ for $1.5 < E_\gamma < 1.6$ GeV and 11 $\cos\theta^{CM}_{K^0}$ bins. We observe that the CLAS acceptance is non–uniform over the proton direction cosines. 117

Figure 5.32 Pull distributions for random C_x, C_z, and P for 1,000 experiments, with 500,000 generated events in each experiment, fit with a Gaussian. 118

Figure 5.33 Correlation plots for random C_x, C_z, and P for 1,000 experiments, with 500,000 generated events in each experiment, fit with a Gaussian. 118

Figure 5.34 Distributions of the difference between the extracted and the true values for random C_x, C_z, and P for 1,000 experiments, with 500,000 generated events in each experiment, fit with a Gaussian. C_x and C_z have means (μ) consistent with 0 and have no bias. P has $\mu = 0.026 \pm 0.001$ which shows that the extracted values of P are biased. 119

Figure 5.35 ΔObs as a function of the true observable for random C_x, C_z, and P for 1,000 experiments with 500,000 generated events fit with a Gaussian. The slope for each, C_x, C_z, and P is consistent with 0. This means any shift in ΔObs does not depend on the value of the observable. 120

Figure 5.36 Correlation plot for random C_x, C_z, and P for 1,000 experiments with 500,000 generated events in each experiment fit with a Gaussian. C_x and C_z have slopes and Y–intercepts consistent with 1 and 0, respectively. The constant for P is not consistent with 0, but is on the same order of magnitude as the calculated acceptance. 121

Figure 5.37 Normalized difference between the 0.97 and 0.99 GeV/c^2 selection cut for region 1. At low energies, there is a small difference between the number of events in region 1. At higher energies, there are $\approx 20\%$ more events in region 1 for the M_X separation of 0.99 GeV/c^2. 123

Figure 5.38 Difference in observables when changing the M_X range in the background subtraction method for region 1. The observables are fit with a Gaussian and the mean, μ, plus width, σ, added in quadrature, are reported as systematic uncertainties. 124

Figure 5.39 ΔC_z when changing the ratios in the background subtraction method for each kinematic bin. 125

Figure 5.40 Relative difference for C_x, C_z, and P for 25 and 50 M_X bins. All observables have relative differences of 10^{-3} or less and it can be concluded that decreasing the number of M_X bins from 50 to 25 does not cause any systematic error in the observables. The standard deviation of each distribution quantifies the systematic uncertainty of the corresponding observable. 126

Figure 5.41 Relative difference for C_x, C_z, and P for 75 M_X bins. All observables have relative differences of 10^{-3} or less and it can be concluded that increasing the number of M_X bins from 50 to 75 does not cause any systematic error in the observables. The standard deviation of each distribution quantifies the systematic uncertainty of the corresponding observable. 127

Figure 6.1 E_γ as a function of $\cos\theta_{K^0}^{CM}$ after selection cuts on $M(p\pi^-)$, $M(\pi^+\pi^-)$, and $p_X < 0.2$ GeV/c. The black lines represent the edges of the different kinematic bins. The background subtraction and observable extraction method were done for each kinematic bin. 131

Figure 6.2 The ratio of photon polarization to the electron polarization as a function of the ratio of photon energy to electron energy. The photon polarization was calculated using Eq. 5.10. The electron polarization was measured by the Møller polarimeter in Hall B. 133

Figure 6.3 C_x as a function of $\cos\theta_{K^0}^{CM}$ for the 16 different E_γ bins. The red and blue curves are the two Bonn–Gatchina soultions from the cross–sections projected (not fit) onto C_x. 134

Figure 6.4 C_z as a function of $\cos\theta_{K^0}^{CM}$ for the 16 different E_γ bins. The red and blue curves are the two Bonn–Gatchina soultions from the cross–sections projected (not fit) onto C_z. 134

Figure 6.5 P as a function of $\cos\theta_{K^0}^{CM}$ for the 16 different E_γ bins. The red and blue curves are the two Bonn–Gatchina soultions from the cross–sections projected (not fit) onto P. 135

Figure 6.6 $R = \sqrt{C_x^2 + C_z^2 + P^2}$ as a function of $\cos\theta_{K^0}^{CM}$ for the 16 different E_γ bins. The blue line is a constant fit to R for each E_γ bin. The width of the line is the uncertainty of the fit. 136

Figure 6.7 C_x as a function of $W = \sqrt{m_n^2 + 2m_n E_\gamma}$ for the 14 different $\cos\theta_{K^0}^{CM}$ bins. 137

Figure 6.8 C_z as a function of $W = \sqrt{m_n^2 + 2m_n E_\gamma}$ for the 14 different $\cos\theta_{K^0}^{CM}$ bins. 138

Figure 6.9 P as a function of $W = \sqrt{m_n^2 + 2m_n E_\gamma}$ for the 14 different $\cos\theta_{K^0}^{CM}$ bins. 138

Figure 6.10 C_x as a function of $\cos\theta_{K^0}^{CM}$ for the 16 different E_γ bins for the primed coordinate system. The dashed lines correspond to Kaon–MAID solutions [33] for the observable and the solid line are model predictions from A. Waluyo [55]. The red and blue lines correspond to predictions with and without an extra $N(1900)\frac{3}{2}^-$ state, respectively. 139

Figure 6.11 C_z as a function of $\cos\theta_{K^0}^{CM}$ for the 16 different E_γ bins for the primed coordinate system. The dashed lines correspond to Kaon–MAID models [33] for the observable and the solid line are model predictions from A. Waluyo [55]. The red and blue lines are predictions with and without an extra $N(1900)\frac{3}{2}^-$ state, respectively. 140

Figure 6.12 P as a function of $\cos\theta_{K^0}^{CM}$ for the 16 different E_γ bins for the primed coordinate system. The dashed lines are Kaon–MAID models [33] for the observable and the solid line are model predictions from A. Waluyo [55]. The red and blue lines are predictions with and without an extra $N(1900)\frac{3}{2}^-$ state, respectively. . 141

Figure 6.13 A comparison of C_x for $\gamma d \to K^0\Lambda(p)$ (black) and $\gamma p \to K^+\Lambda$ (blue). Each $\cos\theta^{CM}_{K^0}$ bin is drawn at the bin centroid as opposed to the bin average to match the free proton data. 142

Figure 6.14 A comparison of C_z for $\gamma d \to K^0\Lambda(p)$ (black) and $\gamma p \to K^+\Lambda$ (blue). Each $\cos\theta^{CM}_{K^0}$ bin is drawn at the bin centroid as opposed to the bin average to match the free proton data. 142

Figure 6.15 C_x (blue), C_z (red), and P (green), integrated over all E_γ and $\cos\theta^{CM}_{K^0}$, as a function of the neutron momentum. Each observable is fit with a first order polynomial. 144

Figure 6.16 C_x for 8 E_γ as a function of the neutron momentum integrated over all $\cos\theta^{CM}_{K^0}$. Each bin is fit with a line in the quasi–free region ($|p_n| < 0.2$ GeV/c). 145

Figure 6.17 C_z for 8 E_γ as a function of the neutron momentum integrated over all $\cos\theta^{CM}_{K^0}$. Each bin is fit with a first order polynomial in the quasi–free region ($|p_n| < 0.2$ GeV/c). The numbers in each panel denote the % difference between the average value of the observable within the quasi–free range of neutron momentum and the extrapolated value to a neutron momentum of zero. . . . 145

Figure 6.18 P for 8 E_γ as a function of the neutron momentum integrated over all $\cos\theta^{CM}_{K^0}$. Each bin is fit with a first order polynomial in the quasi–free region ($|p_n| < 0.2$ GeV/c). 146

Chapter 1

Introduction

Visible matter is made up of atoms, which consist of particles called protons, neutrons, and electrons. Protons and neutrons (known as nucleons) bind together to form the nucleus where nearly all the mass of the atom is concentrated. The nucleons are made up of even smaller particles, known as quarks and gluons. A simplistic picture of a nucleon consists of three quarks that interact to give a nucleon its physical properties. Along this line of thinking, summing the three quark masses (the gluons are massless) should lead to the mass of the nucleon. However, this summation only accounts for $\approx 2\%$ of the nucleon mass [47]. The rest of this mass emanates from the interactions between quarks and gluons.

One of the main goals of nuclear physics is to understand how the nucleons come into being and the fundamental interactions that lead to this. The Standard Model is a theory that aims to describe the interactions between all elementary particles, such as quarks, and the forces that mediate these interactions [27]. While there are still questions that remain in the Standard Model, theories like Quantum Electrodynamics (QED) and Quantum Chromodynamics (QCD) have done a fantastic job describing the interactions that occur between elementary particles. QED describes how light and matter interact with each other and served as a base for developing QCD. QCD is the theory that currently describes the interactions between quarks and gluons. It is able to describe how they interact at small distances, but not how they bind together to form the nucleons.

1.1 Standard Model

The Standard Model states that matter consist of three elementary, or fundamental, types of particles: quarks, leptons, and mediators [27]. It describes how these elementary particles interact with each other within three fundamental forces: the strong, weak, and electromagentic. The only fundamental force the Standard Model does not describe is the gravitational force.

Figure 1.1 lists the elementary particles in the Standard Model [2]. Matter is broken down into two subgroups: fermions and bosons. The fermions have half–

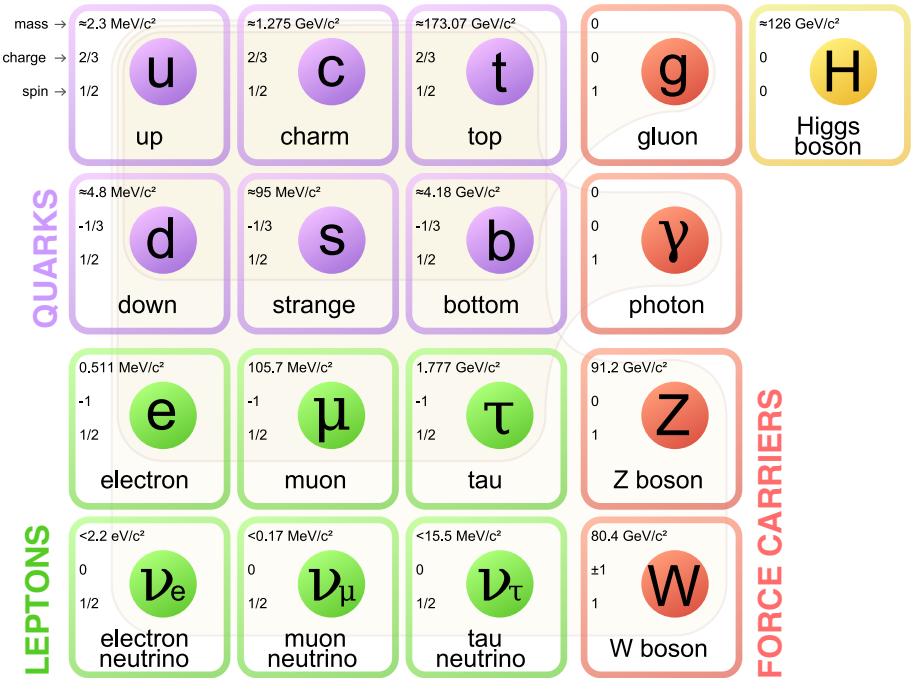

Figure 1.1: Elementary particles in the Standard Model that describes the fundamental interactions between elementary particles. Matter consists of three elementary, or fundamental, types of particles: quarks, leptons, and force carriers. This image was taken from Reference [2].

integer spin and consist of six quarks and six leptons. The quarks and leptons are split into three generations of matter based off the mass of the particles. The first and lightest generation contains the up quark, down quark, electron, and electron neutrino. Most visible matter is built from particles of this generation. The second

generation contains the charm quark, strange quark, muon, and muon neutrino. The third and heaviest generation contains the top quark, bottom quark, tau, and tau neutrino. The gauge bosons have integer spin and mediate the strong, weak, and electromagnetic forces.

The leptons are classified according to their charge, electron number, muon number, and tau number. There are also 6 antileptons whose internal quantum numbers have opposite sign, totaling 12 particles. Leptons can only interact via the electromagnetic, weak, and gravitational forces. Like the leptons, the quarks are classified according to their charge and flavor. Additionally, there are six antiquarks that have opposite charge and flavor. Quarks contain an additional property known as color charge. With 3 color charges (red, green, blue) and 12 particles, there are a total of 36 quarks.

The gauge bosons mediate 3 of the 4 fundamental forces. The gluon mediates the strong force, the photon the electromagnetic, and the W and Z bosons the weak. The massless gluon can only interact with themselves or quarks as they are the only particles that carry color charge. Photons, which are also massless, can only interact with particles that carry electromagnetic charge. The massive W and Z bosons mediate the weak interaction. Both leptons and quarks participate in the weak interaction

The Higgs Boson, predicted in 1964, was the last particle predicted by the Standard Model to be discovered [30]. A particle consistent with the Higgs Boson was discovered by the ATLAS and CMS Collaborations in 2012 [3, 16].

1.2 Quantum Chromodynamics

Quantum chromodynamics (QCD) is the theory of the strong interaction and it describes the interactions between quarks and gluons. As mentioned above, the three color charges in QCD are red (r), green (g), and blue (b). In addition to r, g, and

b, there are 3 anticolor charges: antired ($\bar{r}$), antigreen ($\bar{g}$), and antiblue ($\bar{b}$). Quarks carry a single color charge, while gluons carry both a color and anticolor charge. Color charge is analogous to the electric charge in Quantum Electrodynamics (QED). However, photons do not carry electromagnetic charge while gluons carry color charge.

The strength of the interaction in QCD is given by the strong coupling constant, α_S [27]. When α_S is much smaller than 1, the interaction is weak and perturbation theory can be used to solve QCD. When α_S is on the order of 1, then the interaction is strongly coupled and can not be solved using perturbation theory. For comparison, the coupling constant in QED, the fine structure constant, $\alpha = \frac{1}{137} << 1$, meaning perturbation theory can be used to solve QED. In QCD, α_S depends on the separation distance between the interacting particles [27]. At short interaction distances (high energies), α_S is small and approaches zero when the interaction distance approaches zero. This phenomenon is known as asymptotic freedom, discovered independently by Wilczeck and Gross [28] and Politzer[48]. At large interaction distances (low energies), α_S is on the order of 1, which leads to the phenomenon of color confinement. Color confinement prohibits an individual color–charged particle (quark or gluon) from being isolated as free particles. If one tries to separate one quark from another quark, it becomes more energetically favorable to create a new pair of quarks.

The fundamental degrees of freedom for QCD are the quarks and gluons. Since color confinement prevents quarks and gluons from being isolated, the fundamental degrees of freedom of QCD can not be directly studied. One way to study QCD in the confinement regime is to study the properties of hadrons, which are composite particles made up of quarks and gluons that are bound by the strong force. Inside of hadrons, like the proton and neutron, is what is referred to as a sea of quarks and gluons. The particles in the sea are constantly interacting with each other and with the valence quarks. Gluons spontaneously split into quark–antiquark pairs, which then instantly annihilate back to gluons. It is the interaction between valence quarks

and sea quarks that gives rise to the nucleon mass. A valence quark immersed in a cloud of sea quarks and gluons has a large mass, when compared to a bare quark, and is referred to as a constituent quark. Since confinement prevents the study of the fundamental degrees of freedom in QCD at large distances, the effective degrees of freedom, which are the constituent quarks and gluons, need to be studied.

1.2.1 Hadrons

Hadrons are divided into two subgroups: baryons and mesons. Baryons are particles that consist of three constituent quarks (qqq), while mesons are particles that are made up of a constituent quark–antiquark pair ($q\bar{q}$). In addition to being made up of a different number of constituent quarks, baryons have half–integer spin and are fermions while the mesons have integer spin and are bosons.

Prior to the discovery of the strange quark, SU(2) symmetry was successful in explaining the difference between the u and d quarks. Here, isospin is the symmetry that explains the difference between the observed properties of the discovered hadrons. As more hadrons were discovered, SU(2) symmetry could not explain the long lifetimes of some of these newer particle states [25]. This led to describing the hadrons with SU(3) symmetry, where 3 represents the three flavors of light quarks: u, d, and s.

Figure 1.2 shows the pseudoscalar meson nonet, introduced by Murray Gell–Mann in the Eightfold Way [25]. The Eightfold Way is a scheme used to order and classify hadrons according to their strangeness and charge. The mesons are ordered via properties determined from their constituent quarks. Only three quarks– (u, d, s) were included by Gell–Mann when he proposed the Eightfold Way. Figure 1.3 shows the corresponding baryon octet from the Eightfold Way. In Gell–Mann's SU(3) group, all three quarks have the same masses. However, it is known that the quarks do not have the same mass, which causes this symmetry to break and leads to the hadrons

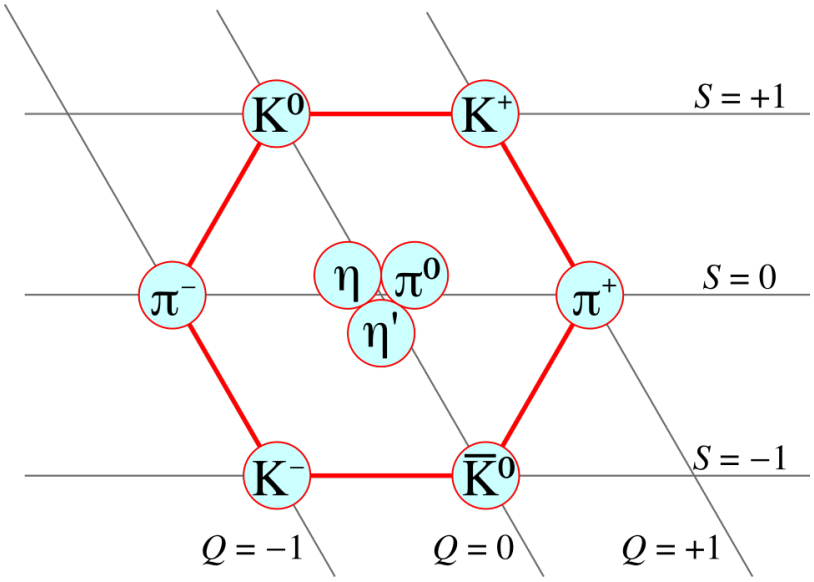

Figure 1.2: The meson nonet. Particles with the same strangeness are arranged horizontally and particles with the same charge are arranged diagonally. This image is taken from Reference [1].

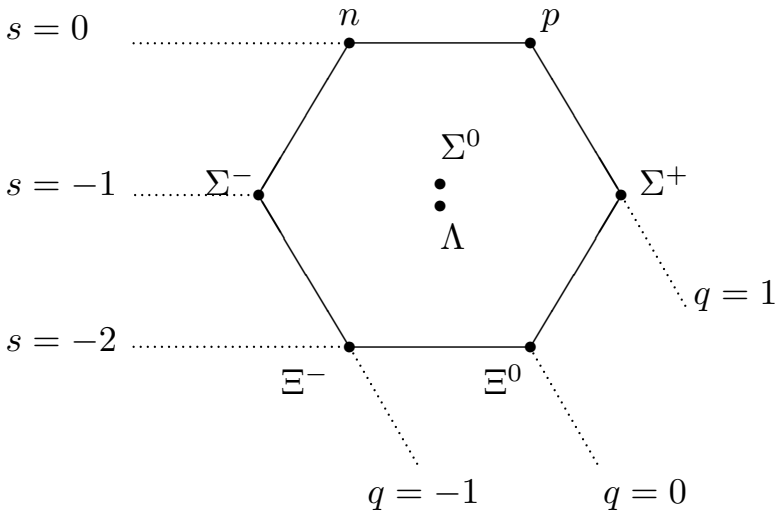

Figure 1.3: The baryon octet. Particles with the same strangeness are arranged horizontally and particles with the same charge are arranged diagonally. Figure adapted from Reference [57].

having different masses. In addition to organizing the already discovered particles, the Eightfold Way could predict new particles yet to be discovered.

1.3 Baryon Spectroscopy

One way to study the effective degrees of freedom of QCD is to measure the excited states of hadrons. In the early 1900's, atomic spectroscopy was used to measure excited states of the atom. In atomic spectroscopy, energy is absorbed by an atom, causing an electron to move to a higher energy state. Some time later, the atom will de–excite and typically emit a photon that corresponds to the energy between the initial and final states. By measuring these emitted photons, the atomic orbital structure was mapped out, leading to the modern understanding of the atom.

Hadron spectroscopy works in a similar manner. Adding energy to a hadron can cause the constituent quarks to reform and the hadron will enter an excited state, also called a resonance. Some time later, this excited state will decay by emitting some combination of hadrons and photons. Ultimately, the goal of baryon spectroscopy is to provide information about the effective degrees of freedom in the non–perturbative regime of QCD. The rest of this work will focus on baryon spectroscopy, specifically the excitation of nucleons.

The Particle Data Group (PDG) lists 15 established excited nucleon (N^*) states below 3000 MeV [47]. The PDG assigns a * to **** rating to excited states. * means evidence for the state is poor, ** evidence is fair, *** existence is very likely but more information is needed, and **** ratiing means that the existence is certain and the properties of the state have been explored. To move from *** to ****, the N^* needs to be seen across multiple decay modes. Table 1.1 lists the overall status of the N^*s and the rating for each decay channel. All states below 1800 MeV have an overall rating of *** or better and were predominately seen in either $N^* \to N\pi$ or $N^* \to N\gamma$. Above 1800 MeV, there are many states that only have a ** or * rating. It has been predicted that many of these higher–mass states have significant branching ratios into $K\Lambda$ or $K\Sigma$ channels, which recently have been the focus of analyses to be discussed in Section 1.4 [15].

Table 1.1: The status of the N^*s. A * means evidence for the state is poor, ** evidence is fair, *** evidence is very likely but more information is needed, and **** means the evidence is certain and the properties of the state have been explored. The table is adapted from the PDG [47].

Particle J^P	overall	$N\gamma$	$N\pi$	$N\eta$	$N\sigma$	$N\omega$	ΛK	ΣK	$N\rho$	$\Delta\pi$
$N1/2^+$	****									
$N(1440)1/2^+$	****	****	****	***	*	***				
$N(1520)3/2^-$	****	****	****	***	***	***				
$N(1535)1/2^-$	****	****	****	****	**	*				
$N(1650)1/2^-$	****	****	****	***	***	**	**	***		
$N(1675)5/2^-$	****	****	****	*	*	*	***			
$N(1680)5/2^+$	****	****	****	*	**	***	***			
$N(1700)3/2^-$	***	**	***	*	*	*	*	***		
$N(1710)1/2^+$	****	****	****	***	**	****	**	*	**	
$N(1720)3/2^+$	****	****	****	***	**	**	**	*		
$N(1860)5/2^+$	**		**	*	*					
$N(1875)3/2^-$	***	***	*	**	***	**	***			
$N(1880)1/2^+$	**	*	*		**		*			
$N(1895)1/2^-$	**	**	* **	**	*					
$N(1900)3/2^+$	***	***	**	**	**	***	**	*	**	
$N(1990)7/2^+$	**	**	**	*						
$N(2000)5/2^+$	**	**	*	**	**	*	**			
$N(2040)3/2^+$	*		*							
$N(2060)5/2^-$	**	**	**	*	**					
$N(2100)1/2^+$	*		*							
$N(2120)3/2^-$	**	**	**	*	*					
$N(2190)7/2^-$	****	***	****	*	**	*				
$N(2220)9/2^+$	****		****							
$N(2250)9/2^-$	****		****							
$N(2300)1/2^+$	**		**							
$N(2570)5/2^-$	**		**							
$N(2600)11/2^-$	***		***							
$N(2700)13/2^+$	**		**							

The cross section of a resonance produced by $a + b \to N^*$ has the shape of a Breit–Wigner distribution,

$$\sigma(s) = \sigma_{max} \frac{m_0^2 \Gamma^2}{(s - m_0^2)^2 + m_0^2 \Gamma^2}, \tag{1.1}$$

where $s = (\tilde{p}_a + \tilde{p}_b)^2$ is the center–of–mass energy squared, m_0 is the mass of the resonance, Γ is the width at half maximum of the resonance, and σ_{max} is the maximum

cross section that contains information about the spin of the incoming particles, a and b, as well as the angular momentum of the N^*. The lifetime of the resonance is inversely proportional to Γ. A short lifetime corresponds to a large width, whereas a long lifetime corresponds to a small width. Generally speaking, the typical lifetime of a nucleon or baryon resonance is 10^{-23}s, meaning the widths of the resonances are quite large (when compared to the excited states of a Hydrogen atom). This results in a spectrum of broad and overlapping resonances when looking at the energy dependence of the cross section of $a + b \rightarrow N^*$. Therefore, in depth analyses, both experimental and theoretical, need to be performed to extract the masses, spins, and parities of the N^*s. Experimentalists collect data and extract observables and cross sections by measuring the decay products of the N^*s. Theorists then use these observables to extract information about the states using partial wave analyses (PWA). PWAs break the cross section into a series of partial waves and relate each partial–wave to a corresponding angular momentum. Quark models and lattice QCD are also used by theorists to predict the resonant spectrum.

1.3.1 Constituent Quark Models

Different models have been developed in an attempt to understand the interactions of quarks and gluons inside of baryons. These models have different effective degrees of freedom, symmetries, and dynamics that lead to a different number of predicted excited states. Figure 1.4 shows the most general and simplest quark model, known as constituent quark models. These postulate a baryon consisting of three valence quarks. The baryon wave function, ψ, is given by,

$$\psi = \psi_{color}\psi_{spin}\psi_{space}\psi_{flavor}, \tag{1.2}$$

where ψ_{color} is the color component, ψ_{spin} is the spin component, ψ_{space} is the spatial component, and ψ_{flavor} is the flavor component [19]. Since baryons are fermions, ψ must be antisymmetric under the exchange of any two quarks. From confinement,

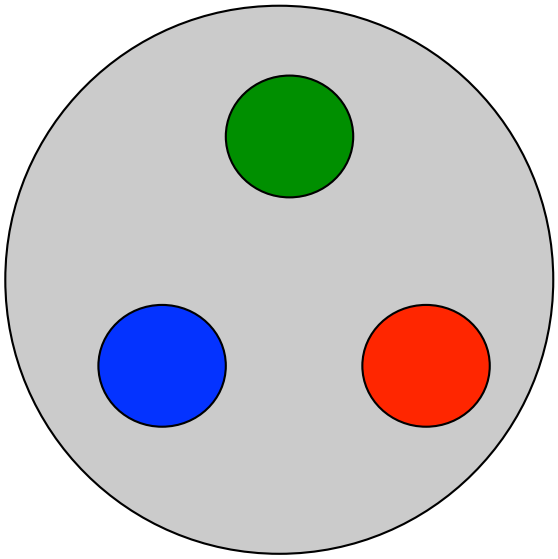

Figure 1.4: A simple schematic of the quark arrangement in constituent quark models. Each of the three quarks interacts equally with each other.

it is known that all hadrons must be in a colorless (a color singlet) antisymmetric state. Since ψ has to be antisymmetric and ψ_{color} is antisymmetric for all baryons, then $\psi_{spin}\psi_{space}\psi_{flavor}$ must be symmetric, as in the case of the Δ^{++}

The full spectrum of baryons can be obtained by solving the wave equation of three particles moving in a potential, $H\,|\psi\rangle = E\,|\psi\rangle$. The earliest constituent quark models (CQMs) treated the three quark interaction as an harmonic oscillator potential [22],

$$H = \sum_j \frac{p_j^2}{2M} + \frac{1}{2}M\omega^2 \sum_{i<j}(r_i - r_j)^2, \tag{1.3}$$

where p_j is the quark momentum and $r_i - r_j$ is the distance of separation between two non–identical quarks. More recent CQMs, like those of Capstick and Isgur treat the potential between quarks as arising from the exchange of gluons [14]. Depending on the model, the forms of these potentials can change. A review of the different quark models and their predictions for the spectrum of baryons can be found in Reference [13].

Generally speaking, CQMs predict more excited states than have been experimentally observed, known as the "missing" resonance problem. This could be due to

CQMs having the wrong degrees of freedom– that is more degrees of freedom than actually present inside of baryons. On the other hand, there may not be enough data available to observe these "missing" baryons. Up until the 2000's, data predominately consisted of measuring resonant decays into nucleon–pion final states. Capstick and Roberts suggested that several of these "missing" states were likely to be observed in channels decaying into strange particles, such as $K\Lambda$ [15].

Figure 1.5 shows the predicted excited nucleon spectrum for N^* decays into $N\gamma$ (white), $N\pi$(light grey), and $K\Lambda$(black) [15]. The Y–axis is the mass of the state

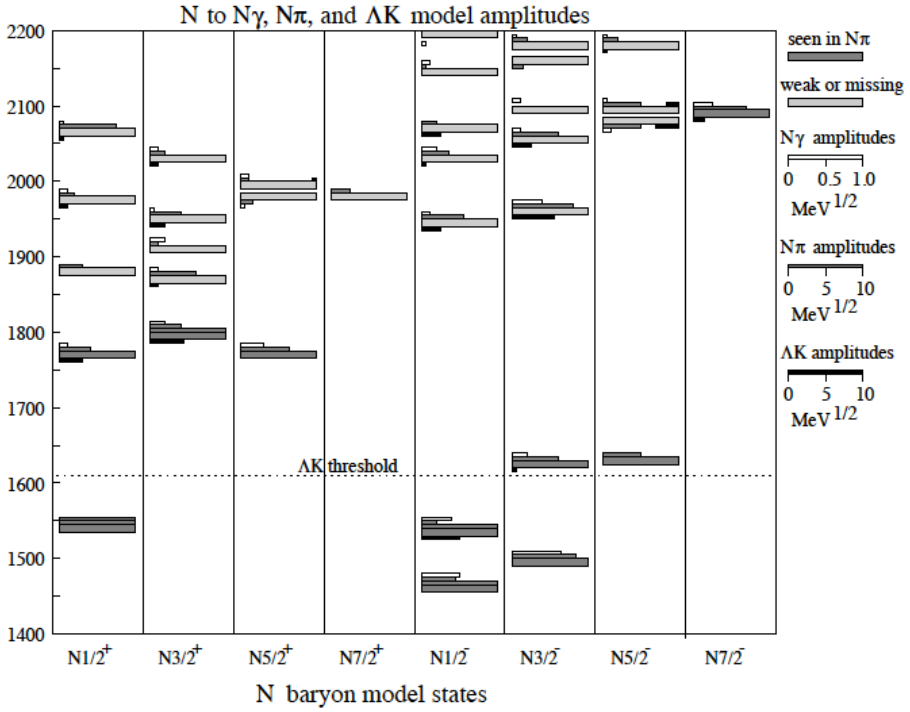

Figure 1.5: Predicted N^* decays into $N\gamma$ (white), $N\pi$(light grey), and $K\Lambda$(black). States seen in $N^* \to N\pi$ decays have an additional wider dark grey band. Weak or missing states have a wider light grey band. The Y–axis is the mass of the state in MeV and the X–axis lists the spin and parity, J^P, of the state. This image was taken with permission from Reference [15].

in MeV and the X–axis lists the spin and parity, J^P, of the state.ww States seen in $N^* \to N\pi$ decays have an additional wider dark grey band. Weak or missing states have a wider light grey band. Nearly all the states seen in $N^* \to N\pi$ occur at or

below 1800 MeV. At the time of this publication, the only state seen above 1800 MeV was the $N\frac{7}{2}^-$ state [15]. Many of these "missing" states, for example the state around 1950 MeV with $J^P = \frac{3}{2}^-$, are predicted to have significant branching ratios for $N^* \to K\Lambda$.

1.3.2 Diquark Models

Other popular models, known as diquark models, treat the nucleon as a quark–diquark pair. Figure 1.6 shows a simple schematic of the nucleon as modeled in a diquark model. In these models, the spatial excitations within the diquark are suppressed,

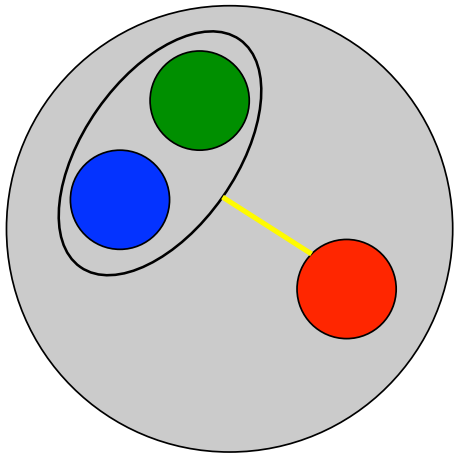

Figure 1.6: A simple schematic of the quark arrangement in a baryon in diquark models. Excitations of the bound quark pair are suppressed, leading to fewer degrees of freedom than in CQMs, and therefore to less predicted N^*s.

meaning they exist at energies much larger than the masses of the resonances to be studied [23]. Since diquark models have the spatial excitations within the diquark suppressed, they predict fewer excited states than in CQMs. A general overview of diquark models can be found in Reference [13].

Figure 1.7 shows the predicted N^* and Δ^* spectrum (black lines) for the diquark model of Reference [23] compared to the $***$ and $****$ states from the 2008 PDG[6]. In general, this diquark model predicts, with good accuracy, all the $***$ and $****$

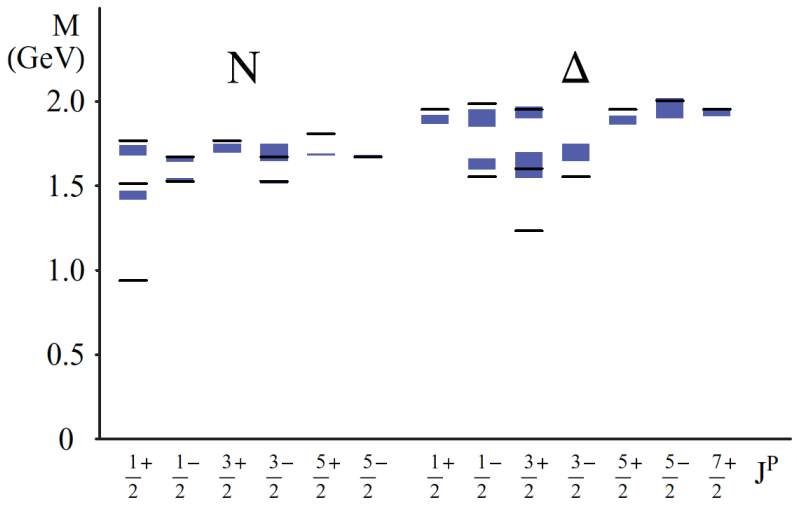

Figure 1.7: Predicted N^* and Δ^* spectrum (black lines) for the diquark model of Reference [23] compared to the $***$ and $****$ states from the 2008 PDG[6]. This image was taken with permission from Reference [23].

states of the 2008 Particle Data Group for masses below 2000 MeV. Additionally, this model does not predict any states yet to be observed.

1.3.3 Lattice QCD

Lattice QCD is a numerical tool used to solve QCD in the non–perturbative regime. In very broad terms, Lattice QCD uses a finite number of points in space–time with periodic boundary conditions to compute Green's functions in quantum field theories [24]. Physical results, like the prediction and calculation of the N^* spectrum, are then extrapolated to an infinite lattice size. Figure 1.8 shows the hadron spectrum as computed in the recent work of Edwards, Dudek, Richards, and Wallace [21]. Overall, this computation predicts a similar number of states as the CQMs and more than diquark models. However, these calculations predict masses that are much higher than experimental values. This is because the mass of the π (396 MeV in Fig. 1.8) in the calculations is much larger than its physical value. What is perhaps more interesting is the clustering, or "bands", in the N^* spectrum as predicted by Lattice QCD. Looking at the positive parity side of Fig. 1.8, one can see 3 distinct bands of

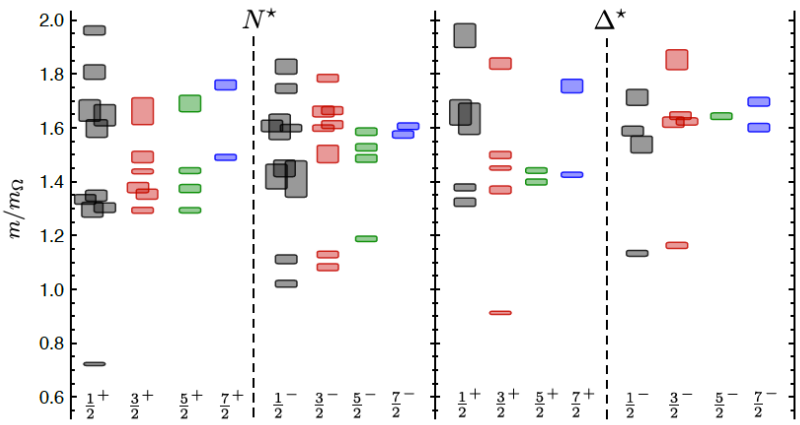

Figure 1.8: Predicted N^* (left) and Δ^* (right) spectrum from Lattice QCD calculations with the mass of the pion, $m_\pi = 396$ MeV. The X–axis lists the spin–parity, J^P, of the state (ex. $\frac{3}{2}^+$, $\frac{5}{2}^-$) and the Y–axis shows the mass of the state. The width of each different box is the uncertainty in the mass of the N^*. This image was adapted from Reference [21].

N^*s. The lowest "band" is the lone resonance at ≈ 0.7, the middle "band" can be seen in the states predicted between 1.2–1.5, and the highest "band" occurs at and above 1.6. The predictions, and specifically these "bands" seen in the higher mass state, share similar features with predictions from CQMs. Generally speaking, CQMs and Lattice QCD predict a similar number of excited states. The similar number and features of the predicted states suggest that the "missing" states exist, but have yet to be seen in the experimental data.

1.4 Hyperon Photoproduction

1.4.1 Polarization Observables

As discussed in Section 1.3, in–depth analyses, both experimental and theoretical, need to be performed to establish the N^* spectrum. This section describes the polarization observables used to extract information about the resonance spectrum. Due to the broad and overlapping nature of the N^* production cross section, cross sections alone are not sufficient to unambiguously determine N^* properties. Therefore, po-

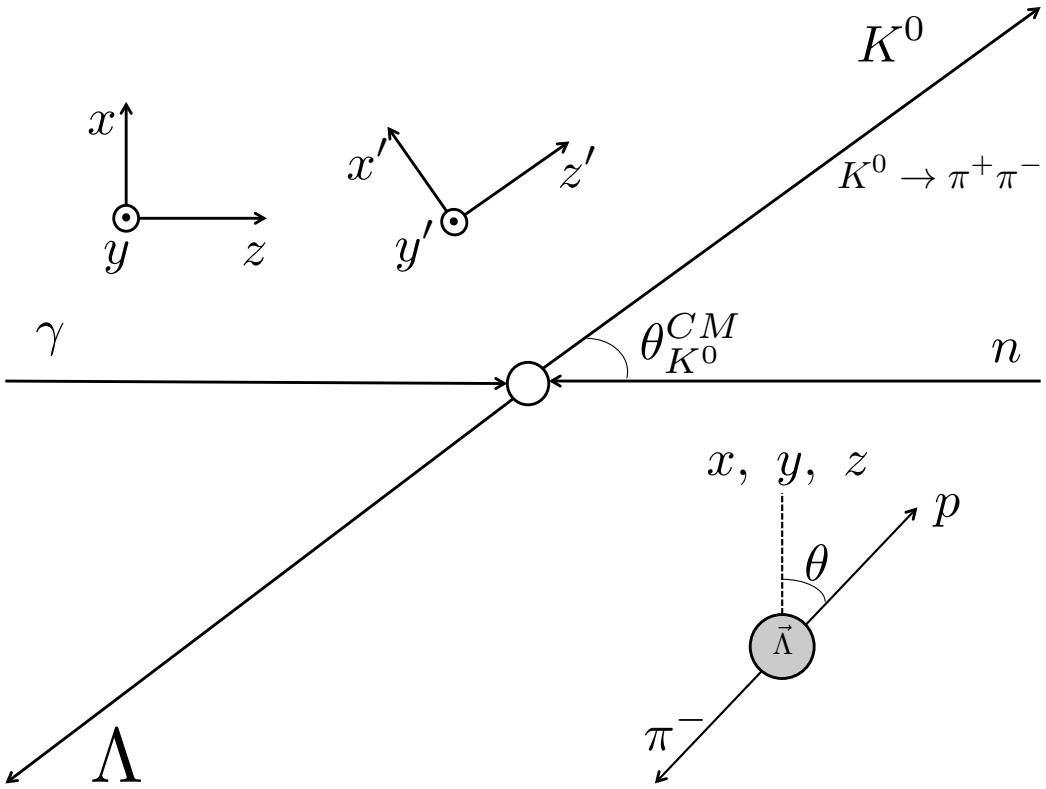

Figure 1.9: A schematic of the coordinate systems used in the analysis of KY photoproduction. Two different coordinate systems are used: the unprimed and primed. The unprimed coordinate system has its z–axis aligned with the incoming photon momentum, $\hat{z} = \hat{p}_\gamma$. The y–axis, $\hat{y} = \hat{z} \times \hat{p}_K$. The x–axis, $\hat{x} = \hat{y} \times \hat{z}$. In the primed coordinate system, the z'–axis is along the kaon momentum $\hat{z} = \hat{p}_K$. The y'–axis is defined as $\hat{y'} = \hat{z'} \times \hat{p}_\gamma$. The x'–axis is thus $\hat{x'} = \hat{y'} \times \hat{z'}$. For both coordinate systems, the reaction occurs in the x–z (x'–z') plane.

larization observables, which emerge from the scattering matrix, are extracted from experimental data to provide more information about the resonances. Since the work on this analysis focuses on the reaction $\gamma n \to K^0\Lambda$, the following discussion will focus on deriving the polarization observables associated with pseudoscalar meson photoproduction.

Figure 1.9 shows a schematic of a $K\Lambda$ photoproduction event and the coordinate systems used to calculate the observables. The choice of coordinate system defines the kinematics and resulting observables from the reaction. Two different coordinate systems are used: the unprimed and primed. The unprimed coordinate system has

its z–axis aligned with the incoming photon momentum in the center–of–mass frame, $\hat{z} = \hat{p}_\gamma^{CM}$. The y–axis, is given by $\hat{y} = \hat{z} \times \hat{p}_K^{CM}$. The x–axis, is given by $\hat{x} = \hat{y} \times \hat{z}$. The primed coordinate system has the z'–axis along the kaon momentum in the center–of–mass frame, $\hat{z'} = \hat{p}_K^{CM}$. The y'-axis is defined as $\hat{y'} = \hat{z'} \times \hat{p}_\gamma^{CM}$. The x'–axis is thus $\hat{x'} = \hat{y'} \times \hat{z'}$. For both coordinate systems, the reaction occurs in the x–z (x'–z') plane, and $\hat{y} = \hat{y'}$. The angle, θ_K^{CM}, is the polar angle of the kaon in the center–of–mass frame and, as will be shown below, the scattering amplitude depends on this variable (in addition to the photon energy). For a complete description of the various coordinate systems used in pseudoscalar meson photoproduction, see References [9] and [49].

There are a few different combinations of polarizations for the reaction $\gamma N \to KY$, where N is a nucleon and Y is a hyperon. The photon, spin–1/2 target nucleon, and spin–1/2 recoiling hyperon can each be in two possible spin states. This leads to a total of $2 \times 2 \times 2 = 8$ complex amplitudes of the scattering matrix ($\gamma,\ N,\ Y$ each have 2 spin states). However, parity and rotational invariance of the pseudoscalar meson reduces these amplitudes to 4. These four independent complex amplitudes can be defined using a Cartesian (F_i) [49], helicity, or transverse (b_i) representation [4, 9]. The following derivation of the polarization observables summarizes the derivation of Reference [4].

Matrix elements of the scattering matrix, $\mathcal{S}_{fi}$, can be written as,

$$\mathcal{S}_{fi} = \frac{1}{2\pi^2}\sqrt{\frac{M_N M_Y}{4E_Y E_K E_N E_\gamma}}\mathcal{M}_{fi} \times \delta(p_N + p_\gamma - p_K - p_Y), \tag{1.4}$$

where $\mathcal{M}_{fi}$ are the Lorentz invariant matrix elements, $p_N = (E_N, \vec{p_N})$, p_γ, p_Y, and p_K are the four–momenta of the target nucleon, photon, hyperon, and kaon, respectively. $\mathcal{M}_{fi}$ can be expressed through the four amplitudes, A_j, as:

$$\mathcal{M}_{fi} = \bar{u}(\vec{p}_Y, s_Y) \sum_{j=1}^{4} A_j \mathcal{M}_j u(\vec{p}_N, s_N). \tag{1.5}$$

The amplitudes A_j contain all the physics information about the reaction– they tell how much each N^* and decay channel contribute to the overall amplitude. The terms $\mathcal{M}_j$ are expressions containing the Dirac matrices ($\gamma^{0,1,2,3,5}$) and the four–momenta of the photon, target nucleon, and recoiling hyperon. $u(\vec{p}_N, s_N)$ and $\bar{u}(\vec{p}_Y, s_Y)$ represent the initial nucleon state and final hyperon state, respectively.

Alternatively, M_{fi} can be expressed in terms of two–component spinors, χ, and the Chew, Goldberg, Low, and Nambu (CGLN) amplitude, $\mathcal{F}$ [17]:

$$\mathcal{M}_{fi} = \sqrt{\frac{E_Y + M_Y}{2M_Y}} \sqrt{\frac{E_N + M_N}{2M_N}} \langle \chi(Y) | \mathcal{F} | \chi(N) \rangle \,. \tag{1.6}$$

The CGLN amplitude, $\mathcal{F}$, is a sum of four amplitudes, $\mathcal{F}_i$, that are built off the Pauli spin matrices, photon polarization, and the four–momenta of the incoming photon and outgoing kaon. These amplitudes are used as they can be subject to multipole analyses. They are defined as

$$\mathcal{F}_1 = \sum_{l=0} [P'_{l+1}(\cos\theta_K^{CM}) E_{l+} + P'_{l-1}(\cos\theta_K^{CM}) E_{l-} + l P'_{l+1}(\cos\theta_K^{CM}) M_{l+} + (l+1) P'_{l-1}(\cos\theta_K^{CM}) M_{l-}], \tag{1.7}$$

$$\mathcal{F}_2 = \sum_{l=0} [(l+1) P'_{l-1}(\cos\theta_K^{CM}) M_{l+} + l P'_{l-1}(\cos\theta_K^{CM}) M_{l-}], \tag{1.8}$$

$$\mathcal{F}_3 = \sum_{l=0} [P''_{l+1}(\cos\theta_K^{CM}) E_{l+} + P''_{l-1}(\cos\theta_K^{CM}) E_{l-} - P''_{l+1}(\cos\theta_K^{CM}) M_{l+} + P''_{l-1}(\cos\theta_K^{CM}) M_{l-}], \tag{1.9}$$

and

$$\mathcal{F}_4 = \sum_{l=0} [-P''_l(\cos\theta_K^{CM}) E_{l+} - P''_l(\cos\theta_K^{CM}) E_{l-} + P''_l(\cos\theta_K^{CM}) M_{l+} - P''_l(\cos\theta_K^{CM}) M_{l-}], \tag{1.10}$$

where l is the orbital angular momentum of the KY system, $P'_l(\cos\theta_K^{CM})$ and $P''_l(\cos\theta_K^{CM})$ are first and second derivatives of the Legendre Polynomials, θ_K^{CM} is the angle of the kaon in the center–of–mass frame, $E_{l\pm}$ are the electric multipoles, and $M_{l\pm}$ are the magnetic multipoles. $E_{l\pm}$ and $M_{l\pm}$ are energy dependent amplitudes that lead to final states with orbital angular momentum l and total angular momentum $l \pm \frac{1}{2}$.

To extract the polarization observables, it is more convenient to express the CGLN amplitudes in terms of transversity amplitudes, b_j, where

$$b_1 = \frac{i}{\sqrt{2}}(\mathcal{F}_1 - F_2 e^{-i\theta_K^{CM}})e^{i\theta_K/2}, \tag{1.11}$$

$$b_2 = \frac{i}{\sqrt{2}}(\mathcal{F}_1 - F_2 e^{i\theta_K^{CM}})e^{i-\theta_K/2}, \tag{1.12}$$

$$b_3 = -b_1 - \frac{\sin\theta_K^{CM}}{\sqrt{2}}(\mathcal{F}_3 + F_4 e^{-i\theta_K^{CM}})e^{i\theta_K/2}, \tag{1.13}$$

$$b_4 = -b_2 - \frac{\sin\theta_K^{CM}}{\sqrt{2}}(\mathcal{F}_3 + F_4 e^{i\theta_K^{CM}})e^{-i\theta_K^{CM}/2}, \tag{1.14}$$

with θ_K^{CM} being the angle between the photon and the kaon in the center–of–mass frame. Alternatively, the four transversity amplitudes can be defined as combinations of the helicity amplitudes, N, S_1, S_2, and D,

$$b_1 = \frac{1}{2}[(S_1 + S_2) + i(N - D)], \tag{1.15}$$

$$b_2 = \frac{1}{2}[(S_1 + S_2) - i(N - D)], \tag{1.16}$$

$$b_3 = \frac{1}{2}[(S_1 - S_2) - i(N + D)], \tag{1.17}$$

$$b_4 = \frac{1}{2}[(S_1 - S_2) + i(N + D)]. \tag{1.18}$$

Figure 1.10 depicts the spin–state transitions represented by the four helicity amplitudes for pseudoscalar meson photoproduction. The label "N" denotes a no–spin flip amplitude, "$S_{1(2)}$" denotes a single spin flip amplitude, and "D" denotes a double–spin flip amplitude. Helicity is a particle's spin–projection in the direction of its momentum.

Table 1.2 lists the differential cross section and the 15 polarization observables for KY photoproduction and their expressions in the transversity representation. P, T, and Σ are single–polarization observables as they only require one of the beam, target, or recoiling hyperon to be polarized. The rest are double–polarization observables as they require both the beam and target (beam–target), beam and recoiling baryon

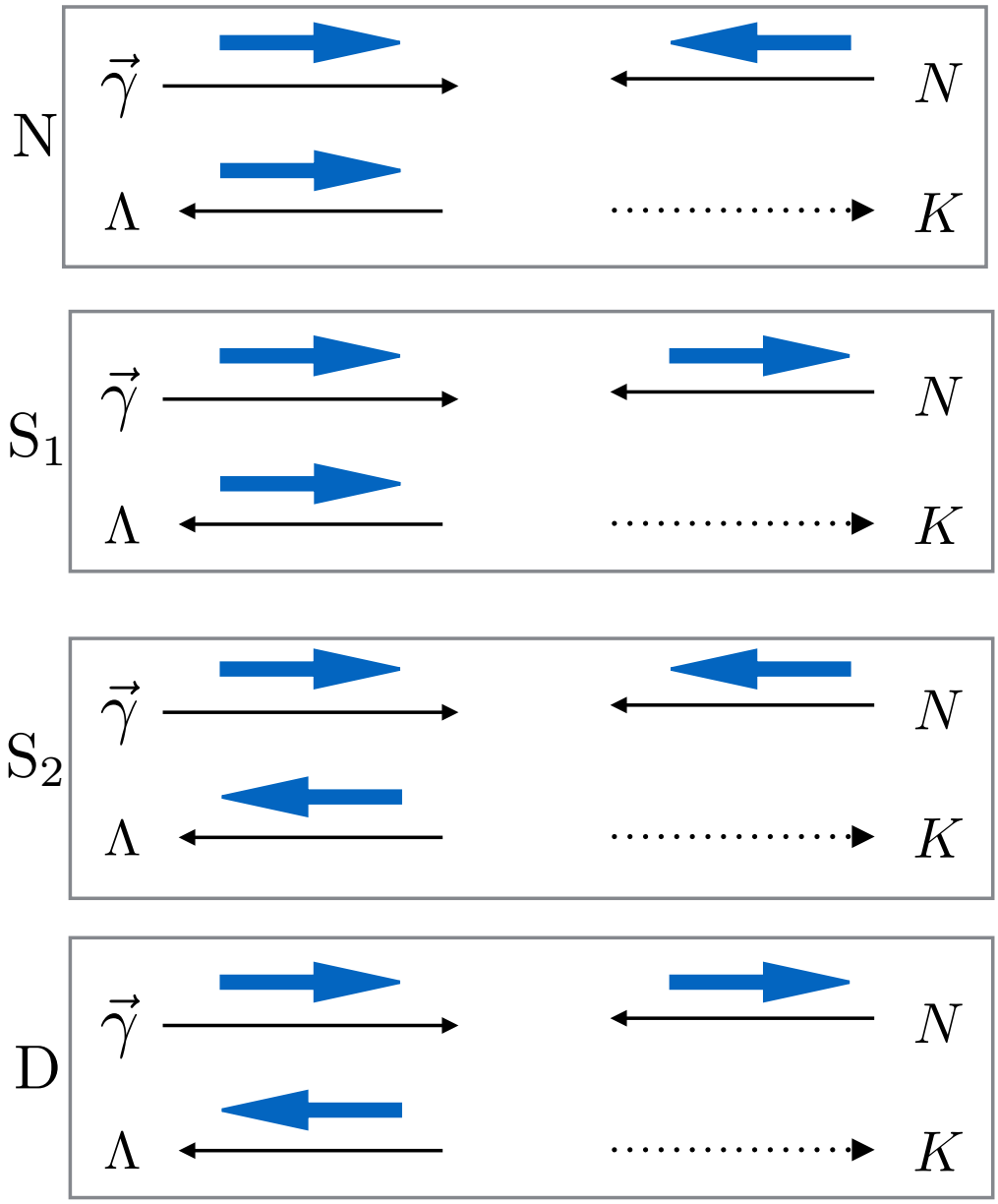

Figure 1.10: The four helicity amplitudes in pseudoscalar meson photoproduction. The label "N" corresponds to the no–spin flip amplitude, "$S_{1(2)}$" corresponds to the single spin flip amplitudes, and "D" corresponds to the double spin flip amplitude.

Table 1.2: The differential cross section and the 15 polarization observables for KY photoproduction. The left column shows the name of the observables, the middle column shows the expression for the observable in the transversity representation, and the right column lists the polarizations needed to extract the observable. Table adapted from [4].

Observable	Transversity Representation	Polarizations
Differential cross section, $\frac{d\sigma}{d\Omega}$	$\|b_1\|^2 + \|b_2\|^2 + \|b_3\|^2 + \|b_4\|^2$	–
Recoil polarization, P	$\|b_1\|^2 - \|b_2\|^2 + \|b_3\|^2 - \|b_4\|^2$	Recoiling Y
Photon beam asymmetry, Σ	$\|b_1\|^2 + \|b_2\|^2 - \|b_3\|^2 - \|b_4\|^2$	Linearly Polarized γ
Target Asymmetry, T	$\|b_1\|^2 - \|b_2\|^2 - \|b_3\|^2 + \|b_4\|^2$	Target
E	$2Re(b_1 b_3^* + b_2 b_4^*)$	Beam–Target
F	$2Im(b_1 b_3^* - b_2 b_4^*)$	Beam–Target
G	$2Im(b_1 b_3^* + b_2 b_4^*)$	Beam–Target
H	$-2Re(b_1 b_3^* + b_2 b_4^*)$	Beam–Target
C_x	$-2Im(b_1 b_4^* - b_2 b_3^*)$	Beam–Recoil
C_z	$2Re(b_1 b_4^* + b_2 b_3^*)$	Beam–Recoil
O_x	$-2Im(b_1 b_4^* - b_2 b_3^*)$	Beam–Recoil
O_z	$2Im(b_1 b_4^* + b_2 b_3^*)$	Beam–Recoil
T_x	$2Re(b_1 b_2^* - b_3 b_4^*)$	Target–Recoil
T_z	$2Im(b_1 b_2^* - b_3 b_4^*)$	Target–Recoil
L_x	$-2Im(b_1 b_2^* + b_3 b_4^*)$	Target–Recoil
L_z	$2Re(b_1 b_2^* - b_3 b_4^*)$	Target–Recoil

(beam–recoil), or target and recoiling baryon (target–recoil) to be polarized. These 16 observables are not independent of each other and several relations between the observables can be defined [49]. One such relation,

$$C_x^2 + C_z^2 + O_x^2 + O_z^2 = 1 - T^2 - P^2 - \Sigma^2, \tag{1.19}$$

relates the beam–recoil observables to the single–polarization observables. Relations like these impose conditions on the observables. To determine the full scattering amplitude up to a common phase, the differential cross section, $d\sigma/d\Omega$, and 7 different polarization observables must be experimentally determined. These may include the three single–polarization observables, P, T, and Σ, and four of the double–polarization observables. The four double–polarization observables can not come from the same category (i.e. the four cannot be all beam–recoil), and at least one observable must come from a different set (e.g. $C_x,\ C_z,\ L_x, F$). However, in practice,

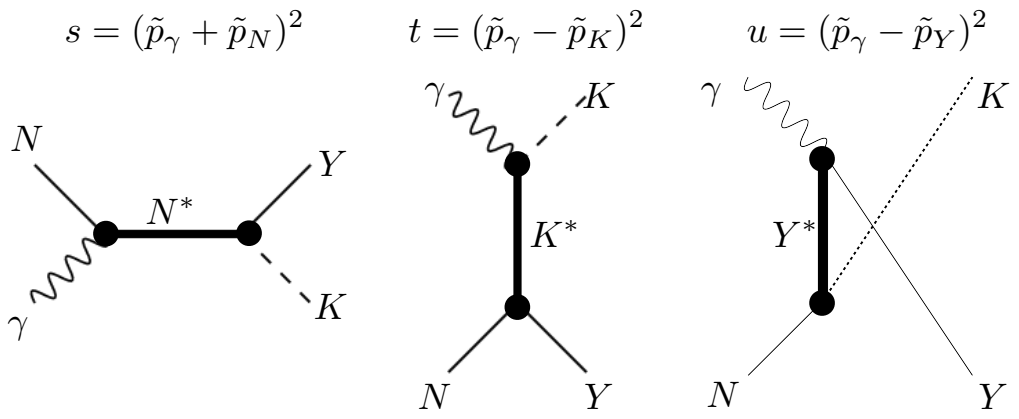

Figure 1.11: Three mechanisms to photoproduce KY. A resonance, N^* is created in the s channel that then decays into the KY. In the t (u) channel, a K^* (Y^*) is exchanged.

due to the statistical uncertainties of measuring the observables, more than 8 are needed to determine the amplitudes [49].

1.4.2 Fits To Experimental Data

Figure 1.11 shows three different photoproduction mechanisms for KY. Resonance production is typically associated with the s channel, while t and u channel production are background processes. The photon γ gets absorbed by the nucleon, N, which then enters some excited state, N^*. The N^* then decays into a KY. The t and u channels represent the exchange of a K^* and Y^*, respectively. Partial–wave analyses break the differential cross section into a series of partial waves that depend on the angular momentum of the KY system and are needed to extract the spins and masses of the N^*s by fits to experimental data. Additionally, PWAs are able to determine the KY production mechanisms and how much each mechanism contributes to the total cross section.

For KY photoproduction, particularly for $\gamma n \to K^0\Lambda$, there are two different PWAs commonly used to identify resonances: Kaon–MAID [33] and Bonn–Gatchina [8]. These models fit the experimental data (extracted cross sections and polarization

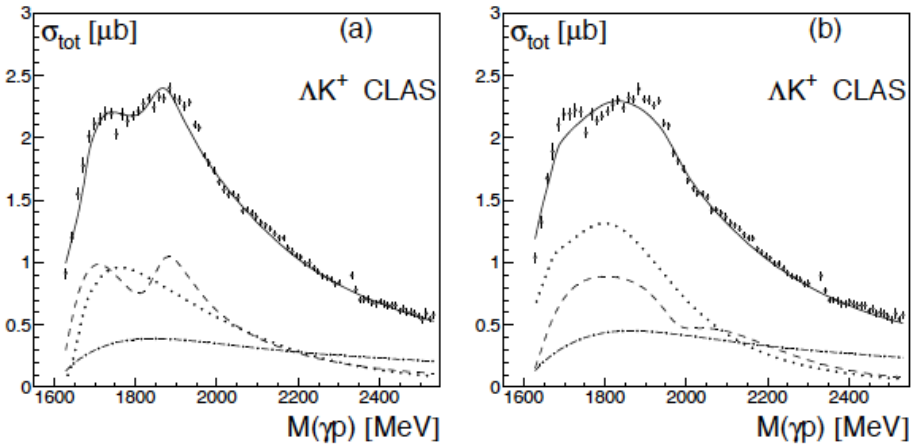

Figure 1.12: Two example fits ((a) and (b)) of the cross section of $\gamma p \to K^+\Lambda$ from the Bonn–Gatchina group. The solid curves are the results of the fits, the dashed lines are P_{13} ($N(1900)\frac{3}{2}$, $N(1720)\frac{3}{2}$) contributions, the dotted lines are S_{11} ($N(15350\frac{1}{2}$, $N(1650)\frac{1}{2}$) contributions, and the dashed–dotted line is the t–channel contribution. This image was taken from Reference [8]

observables) and try to determine the contributions from resonant and background (t, u channel) production. Figure 1.12 shows two example fits ((a) and (b)) of the cross section of $\gamma p \to K^+\Lambda$ from the Bonna–Gatchina group. For both (a) and (b), the solid curves are the results of the fits, the dashed lines are P_{13} ($N(1900)\frac{3}{2}$, $N(1720)\frac{3}{2}$) contributions, the dotted lines are S_{11} ($N(15350\frac{1}{2}$, $N(1650)\frac{1}{2}$) contributions, and the dashed–dotted line is the t–channel contribution. When performing these fits, the addition of the $N(1900)\frac{3}{2}$ resonance showed an overall improvement to the fits of the cross section and observables. The fits also determined the mass and width of this state.

1.4.3 K^+Y Photoproduction

The most widely studied channel in regards to KY photoproduction is the reaction $\gamma p \to K^+\Lambda$. Figure 1.13 shows existing data for C_z, which measures the polarization transfer from a circularly–polarized photon beam to the recoiling hyperon with respect to the z–axis, as a function of W, the center–of–mass energy, for different $\cos\theta_K^{CM}$ bins from R. Bradford and the CLAS collaboration [11]. The different col-

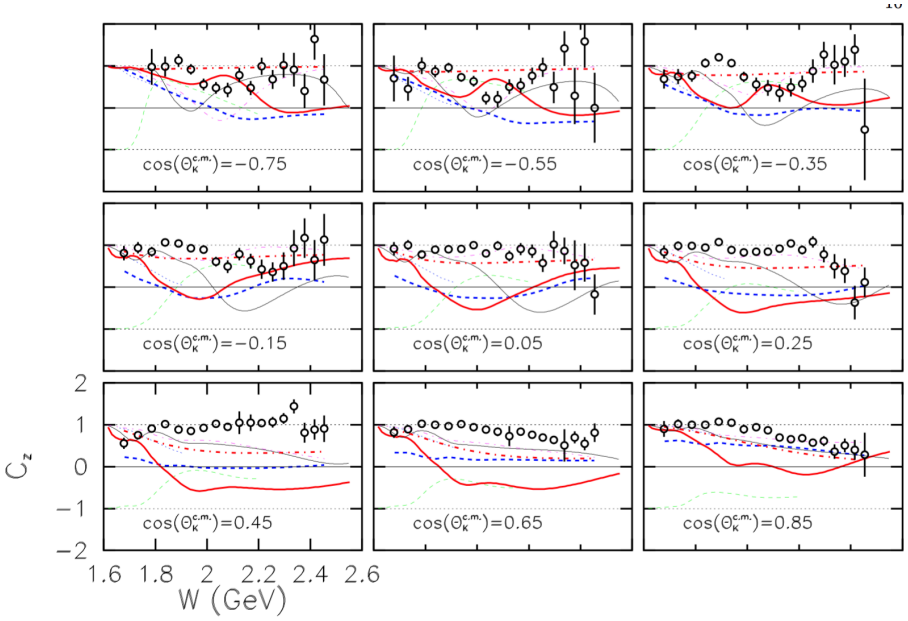

Figure 1.13: C_z as a function of the center–of–mass energy W for different $\cos\theta_K^{CM}$ bins. The open circles are the experimental values for the observable. The different colored curves represent predictions from different hadronic models. The image was taken from Reference [11].

ored curves represent predictions from different hadronic models. The observable C_x, which measures the polarization transfer from a circularly–polarized photon beam to the recoiling hyperon with respect to the x–axis, was published alongside C_z. Additionally, these observables were published for the reaction $\gamma p \to K^+\Sigma^0$. A few novel and unexpected conclusions were drawn from these observables at the time they were published. Firstly, it was unexpected that, for the Λ, C_z was close to unity across a wide range of kinematic bins. Physically, this means that the Λ is nearly fully polarized along the z–axis. Secondly, the total polarization, $R = \sqrt{C_x^2 + C_z + P^2}$, was found to be ≈ 1 throughout most kinematic bins. P, which is the induced or transverse polarization, was determined in a separate analysis [38].

Due to the large polarization transfer seen in the data, it was suggested that N^*s do not play a role in the polarization of the recoiling hyperon [50]. However,

the Bonn–Gatchina partial–wave–analysis group showed that the large polarization is in fact due to an intermediate N^* state [8]. The Bonn–Gatchina group refit the observables and found that all data sets can be described well by introducing an $N(1900)\frac{3}{2}^+$ state.

A more recent analysis on $\gamma p \to K^+ Y$, where $Y = \Lambda$ or Σ^0, was completed on data from linearly–polarized photons [31]. Figure 1.14 shows O_x as a function of the center–of–mass energy W for different $\cos\theta_K^{CM}$ bins. Three different theoretical

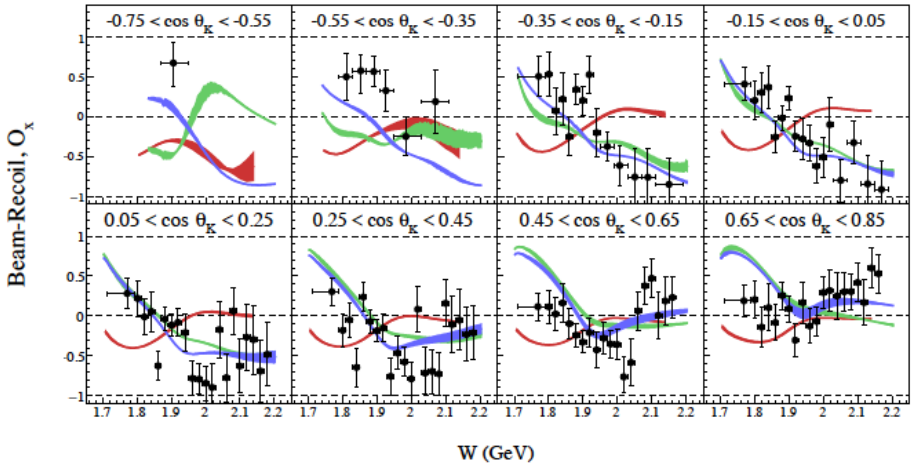

Figure 1.14: O_x as a function of the center–of–mass energy W for different $\cos\theta_K^{CM}$ bins. The black circles are the experimental values for the observable. The red curves are predictions from ANL–Osaka [31], green colored curves from the 2014 Bonn–Gatchina group[29], and the blue curves are ref–fits including the present data with and an additional $N^*\frac{3}{2}^+$ and $N^*\frac{5}{2}^+$ added. This image was taken from Reference [46]

calculations for the values of the observables are shown. The red curves are from calculations done by the ANL–Osaka group, the green colored curves are from the 2014 Bonn–Gatchina group, and the blue curves are refits including the present data with an $N^*\frac{3}{2}^+$ and $N^*\frac{5}{2}^+$ added [29, 31]. Generally speaking, the blue and green fits agree with the data at forward angles and over most W bins. These regions are areas that overlap with fits done to other data. In the areas where the data do not overlap, the fits are generally in poor agreement. The blue curves include two new N^* states and show a general improvement to the fits. Unfortunately, one is still unable to

determine the masses of the states or even support their existence.

The common theme from the study of $K^+\Lambda$ is that more data is needed in this and complimentary channels. As stated above, the two analyses have measured observables of the reaction $\gamma p \to K^+\Sigma^0$. Other analyses done by the CLAS collaboration have measured cross–sections and the recoil polarization, P, for the Σ^0 [20].

1.4.4 $K^0\Lambda$ Photoproduction

Studying the reaction $\gamma n \to K^0\Lambda$ is expected to provide new and complimentary information to the reaction $\gamma p \to K^+\Lambda$. Since the production of $K^0\Lambda$ occurs off the neutron, different states can be excited than in the reaction off the proton. As discussed in the previous section, the work on analyzing $K^+\Lambda$ led to the promotion of the $***\, N(1900)\frac{3}{2}^+$ to a $****$ state. Due to the different reaction dynamics, the reaction $\gamma n \to K^0\Lambda$ is sensitive to different states, such as the $***\, N(1875)\frac{3}{2}^-$ [47]. Studying $K^0\Lambda$ can also be used to provide additional constraints to N^*s that couple to all KY channels. In addition to these, it is interesting to see if the phenomenon of the fully polarized Λ is also seen in the $K^0\Lambda$ channel.

Measuring polarization observables and cross sections in the photoproduction of $K^0\Lambda$ has not been done as much as $K^+\Lambda$ as there are no free neutron targets. Therefore, the only way to study the photoproduction of $K^0\Lambda$ off the neutron is to use targets where the neutron is bound, like deuteron. For $K^0\Lambda$ photoproduction, the most extensive work has been on measuring the differential and total cross section of $K^0\Lambda$ photoproduction. The Research Center for Electron Photon Science, formerly known as the Laboratory for Nuclear Science, at Tohoku University in Japan first reported cross section measurements of neutral kaons with photon energies, E_γ, between 0.9 and 1.1 GeV using a liquid deuterium [54] and a ^{12}C target [56].

More recent experiments at Jefferson Lab have yielded cross section data in the range $0.9 < E_\gamma < 2.6$ GeV [18]. Figure 1.15 shows the cross section for the reaction

$\gamma d \to K^0\Lambda(p)$ from the recent Jefferson Lab results [18]. The red and black data

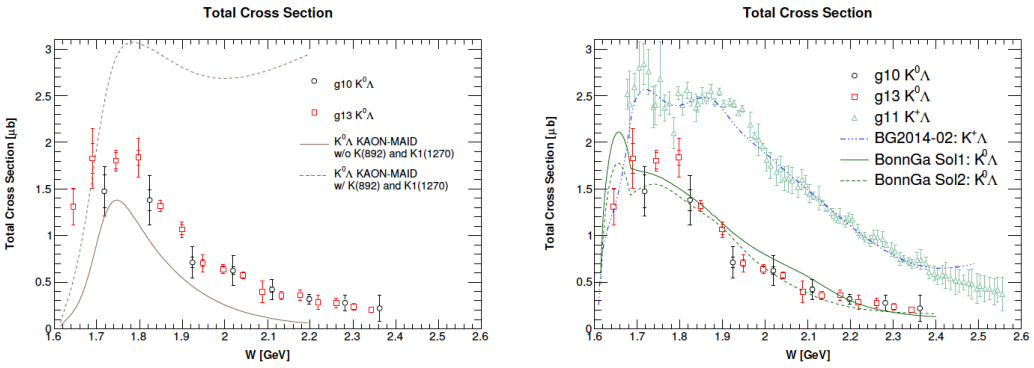

Figure 1.15: The red and black data points on both histograms are the two sets of Jefferson Lab data. The left panel shows the data points with Kaon–MAID models with two different sets of input parameters [33]. The right panel shows the cross sections from $K^+\Lambda$ superimposed on top of the $K^0\Lambda$ data. Also drawn are two different PWA solutions from the Bonn–Gatchina group for the $K^0\Lambda$ (green lines) and the 2014 solution for the $K^+\Lambda$ data.This image was taken from [18].

points on both histograms are the two sets of data. The left panel shows the data points together with Kaon–MAID curves with two different sets of input parameters [33]. The right panel shows the cross sections of $K^+\Lambda$ superimposed on top of the $K^0\Lambda$ data. Also drawn are two different PWA solutions from the Bonn–Gatchina for the $K^0\Lambda$ (green lines) and the 2014 solution for the $K^+\Lambda$ data. The channels for the $K^0\Lambda$ PWA contain input parameters from $\gamma d \to \pi^- p(p)$, $\pi^- p \to \gamma n$, $\gamma d \to \pi^0 n(p)$, $\gamma d \to \eta n(p)$, and $\gamma d \to K^+\Sigma^-(p)$. These preliminary solutions describe both the $K^+\Sigma^-$ and $K^0\Lambda$ data reasonably well. However, the $K^0\Lambda$ cross section data do not distinguish which Bonn–Gatchina solution describes the reaction better.

1.5 Summary and Structure

Since QCD can not be analytically solved at low energies, quark models have been developed in an attempt to describe the effective degrees of freedom of QCD. One way to test these models, and thus study the effective degrees of freedom, is to measure excited states of hadrons, known as hadron spectroscopy. By comparing

the experimentally measured spectrum of excited states to the states predicted by QCD–inspired quark models, information can be gained about the effective degrees of freedom. Recently, there has been work done to determine excited states that decay into KY as many predicted, but unobserved states, may be seen in this channel.

The work discussed in this thesis will present the first estimates for the polarization observables C_x, C_z, and P for $\vec{\gamma}d \rightarrow K^0\vec{\Lambda}(p)$. The experimental setup, analysis of data, and observable extraction method will be discussed in detail. The results will be shown alongside current theoretical calculations. In addition to this, the observables are also extracted as a function of the bound neutron momentum.

Chapter 2

Experiment

2.1 g13 Experiment

The data for this work was collected from October 2006 through June 2007 with the CLAS detector in Hall B of the Thomas Jefferson National Accelerator Facility (Jefferson Lab) as part of experiment E06-103 (g13) [43]. In general, the experiment involved a photon beam that was incident upon a liquid deuterium target. The photon beam was created by the beam of electrons generated by the Continuous Electron Beam Accelerator Facility (CEBAF) and the Hall–B photon-tagging system. The g13 experiment contains two different run groups: g13a, which used circularly–polarized photons, and g13b, which used linearly–polarized photons. Both run groups used the same 40–cm long LD_2 target. Data for this project were taken during the g13a run period.

The g13a run group contains events from three different run periods. The first run period occurred between October 30 and November 21, 2006 and had an e^- beam energy of 1.987 GeV. The second run period occurred between November 28 and December 22, 2006 and had an e^- beam energy of 2.649 GeV. The third run period occurred between March and Novermber 2007 and had an e^- beam energy of 1.987 GeV. All the g13a run periods had an electron beam polarization of 78%–85%. The CLAS torus magnet had a current of -1500 nA that was chosen to maximize the acceptance of low momentum π^- originating from hyperon decays [59]. Approximately 20 billion events were collected for the g13a run group.

The 40–cm–long unpolarized LD_2 target had a density of 6.5 g/cm^2. To increase the detector acceptance for forward scattered particles, the target was installed 20 cm upstream from the center of the detector.

g13a used a two–level trigger system to acquire events. The Level 1 trigger processed events from all photomultiplier tubes and had a 100–ns wide window. The Level 2 trigger only accepted events that passed Level 1 trigger and had tracks in the drift chambers. It also required charged tracks in at least two of the six sectors of the CLAS detector. g13a had event rates of up to 10 kHz with a total of 2×10^{10} triggers [42]. Combined with g13b, there is a total of 130 TB of raw data [42]. This chapter describes the main characteristics of the accelerator and the detector components that were used to collect the g13a data.

2.2 CEBAF

The Continuous Electron Beam Accelerator Facility, known as CEBAF, is an electron accelerator consisting of two parallel linear accelerators (linacs) connected with recirculating arcs, forming a racetrack shape. Figure 2.1 shows a schematic of CEBAF at the time the experiment took place [39]. CEBAF used superconducting radio frequency (rf) cavities to accelerate the electrons in the linacs. Magnets in the recirculation arcs were used to bend the beam and recirculate the electrons up to 5 times. Each pass through one of the linacs increased the beam energy by up to 0.6 GeV. This resulted in the electron beam having a maximum energy of 6 GeV. Furthermore, CEBAF could simultaneously supply electron beams of different energies to three different end stations: Hall A, Hall B, and Hall C. The electron beam was created with three entwined 0.499–GHz beams accelerated b 1.497–GHz rf cavities. Placing rf separators operating at 0.499 GHz at different recirculation paths made it possible to simultaneously supply the three halls with varying electron energies. A complete description of the CEBAF is given in Reference [39].

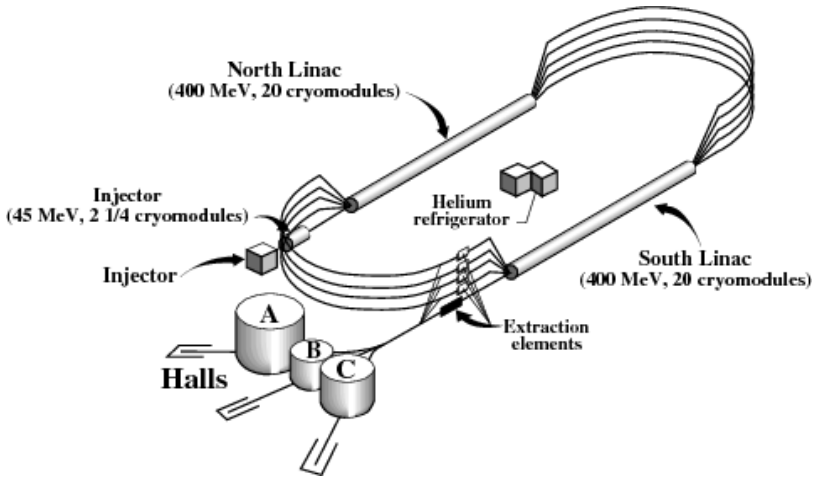

Figure 2.1: A schematic of CEBAF at the time the experiment took place. One can see the 0.6 GeV linacs, the recirculating arcs, and the three experimental halls (Hall A, Hall B, and Hall C) at the time of the experiment. This figure is taken from Reference [39]

2.3 Hall B

2.3.1 Beamline

Figure 2.2 shows a schematic diagram of the Hall-B detectors along the beam line at the time of the g13a experiment [39]. The electron beam from CEBAF was inci-

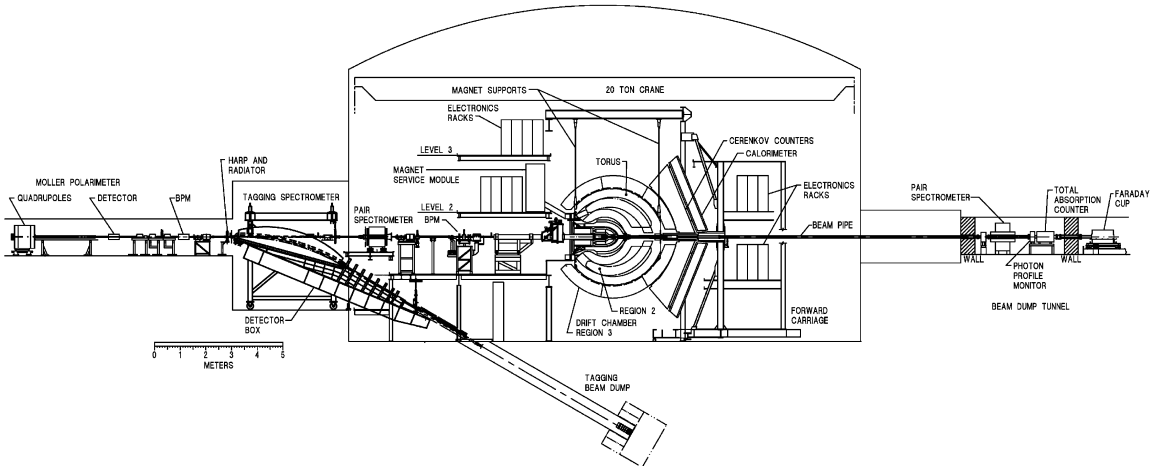

Figure 2.2: A schematic of the Hall–B beam line during the g13a experiment. From left to right, along the beam direction one can see the Møller polarimeter, the radiator and the tagging spectrometer, the subsystems of the CLAS detector, the photon profile monitor, and the total absorption counter. Not shown is the photon collimator placed between the tagger and the CLAS. Figure is from [39].

dent from the left and its polarization was measured using a Møller polarimeter [26]. The Møller measurements were done in dedicated runs, typically before and after any changes to the electron beam, such as energy change or tuning. Bremsstrahlung photons were produced from interactions of the electrons with the radiator. The photons would continue down the beam line towards the CEBAF Large Acceptance Spectrometer (CLAS). All electrons were directed out of the beam line toward the tagging beam dump using the tagging spectrometer (photon tagger). The main purpose of the tagger was to determine the energy and timing of the photons. The x– and y–positions of the electron beam were continuously monitored with the beam–position monitors (BPMs) located upstream of the tagger. Every time the electron beam had to be re–tuned (such as after energy change or a long shutdown), the electron–beam profile was measured with the harp located upstream of the radiator. The intensity of the electron beam, which was about 40 nA during g13a, was continuously monitored.

The circularly–polarized photons used in this experiment were produced using a longitudinally–polarized electron beam. In g13a, they were created using a thin gold radiator with a thickness of 10^{-4} radiation lengths located half a meter in front of the photon tagger [42]. The electron beam had polarizations up to 85%, and the bremsstrahlung photons, if produced at the endpoint of the bremsstrahlung spectrum, had 100% of the electron polarization. During g13b, linearly–polarized photons were produced via coherent bremsstrahlung in a thin diamond crystal radiator.

After the photons passed through the tagger magnet, they passed through a 6.4–mm collimator that restricted the width of the beam profile and allowed 90% transmission [42]. The choice of collimator depended on the polarization, or lack thereof, of the photon beam. For all polarizations, the photon beam size and position were monitored by the photon profile monitor consisting of scintillating fibers located further downstream from the CLAS.

2.3.2 Photon Tagger

The bremsstrahlung photon beam used in this experiment was produced using the photon tagger in Hall B. Shown in Fig. 2.3 is a schematic diagram of the tagger[53]. Electrons from CEBAF were incident upon a thin gold foil, called the radiator. An electron that interacted with the electromagnetic field of a nucleus in the foil were decelerated, emitting a bremsstrahlung photon. The bremsstrahlung photons continued along the direction of the electron beam, passing through the tagger magnet towards the target, while all electrons were bent by the tagger magnet. The electrons that did not radiate and, therefore, carried the energy of the primary beam, E_0, moved along the optical axis of the magnet and were stopped in the tagger beam dump. The electrons that did radiate carried a smaller energy, $E_e < E_0$, were incident upon a scintillator hodoscope located in the focal plane of the tagger magnet. The position of the scintillator that was hit by an electron combined with the known magnetic–field transport matrix of the magnet allowed to determine the electron energy E_e. The energy of the bremsstrahlung photon, E_γ, could then be determined using conservation of energy

$$E_\gamma = E_0 - E_e,$$

where E_0 is a value provided by the accelerator crew, based on the accelerator settings, and E_e is the energy measured in the tagger. E_0 was determined in the accelerator and E_e was measured by a hodoscope.

The scintillator hodoscope consisted of two detector planes: one for energy measurement (E–plane) and one for time measurement (T–plane). The E–plane contained 384 overlapping scintillators (E–counters). E–counters recorded the position of an electron hit and from this position, the momentum and energy of the decelerated electron was determined. The T–plane contained 61 scintillators (T–counters) that were located 20 cm behind the E–plane. The T–counters recorded the time of the electron hit relative to the trigger. This time was used to determine the time

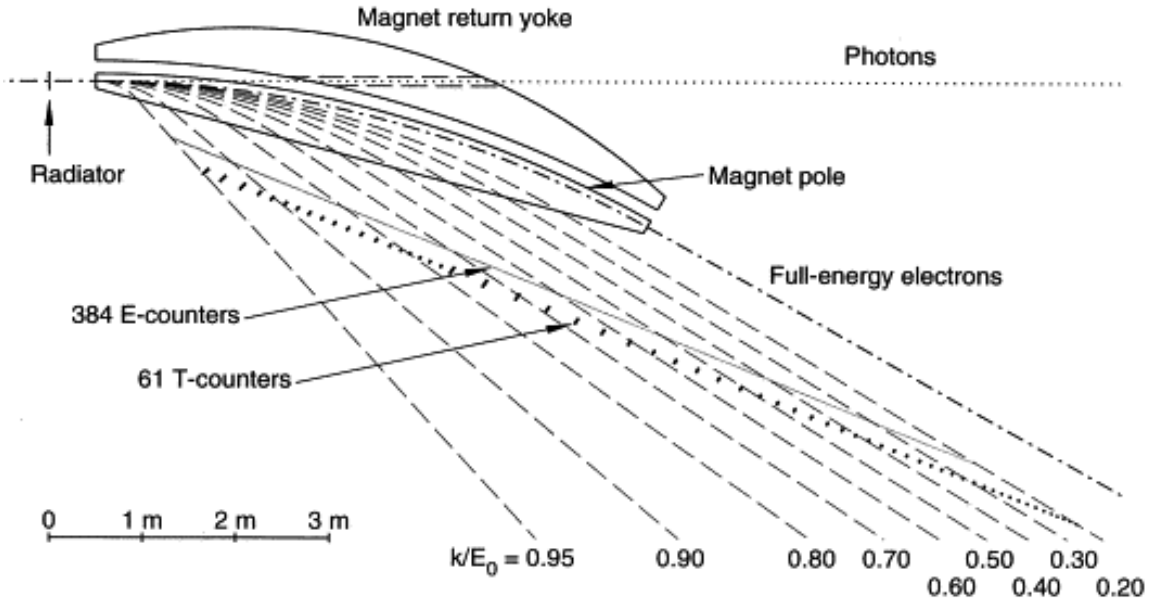

Figure 2.3: A schematic of the photon tagger in Hall B. Electrons, incident from the left, that interacted with the radiator produced bremsstrahlung photons that continued in the original direction of the incident electron beam. The electrons were bent by a dipole magnet at different angles based on their energy. A two-plane hodoscope detected these electrons, which allowed for energy and time measurements. This figure is taken from Reference [53]

of arrival of the corresponding photon at the production vertex of the target. The photon vertex time was critical for the identification of the photon that had produced the triggered event in CLAS. Mostly, the extra photons detected together with a triggered event were due to electrons from different electron-beam bunches. Since CEBAF delivered beam bunches in 2 ns pulses, the T–counters required a timing resolution of 300 ps or better. The final resolution of the T–counters was 110 ps [53]. The E–counters had a resolution of $0.001 \times E_0$.

2.3.3 CEBAF Large Acceptance Spectrometer (CLAS)

The CEBAF Large Acceptance Spectrometer (CLAS) was a large–acceptance detector used to detect multiple-charged-particle final states of nuclear reactions generated by electron or photon beams. Figure 2.4 shows a schematic of the CLAS. CLAS was separated into six independent spectrometers (sectors) by the superconducting coils,

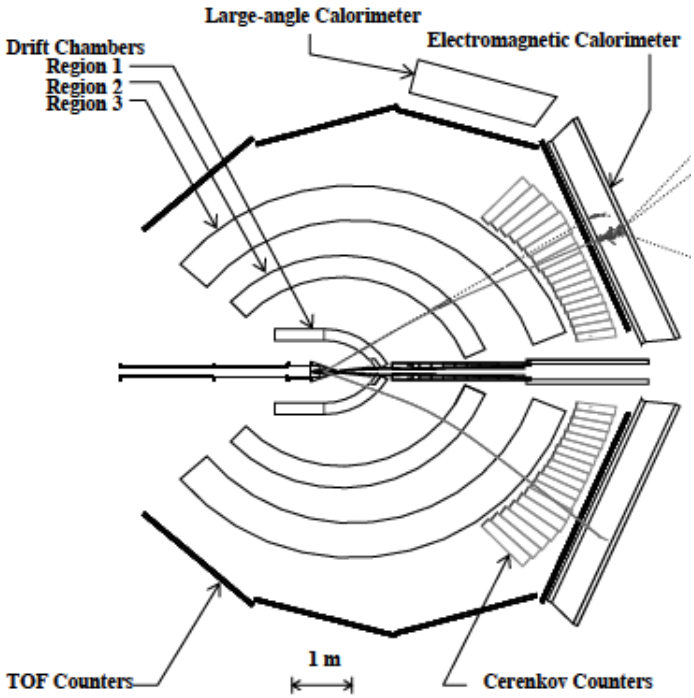

Figure 2.4: A schematic of the CLAS detector. Drift Chambers measure particles' trajectories and TOF Counters measure the time of flight. This image is taken from Reference [39].

which generated a toroidal magnetic field. The sectors were arranged symmetrically around the beam line. All sectors shared a common target and data acquisition system. The toroidal magnetic field, primarily in the azimuthal direction, was used to bend charged particles. In g13a, positively–charged particles were bent towards the beam line, whereas negatively–charged particles were bent away from the beam line. The detector was able to reconstruct charged particle trajectories using drift chambers and had and azimuthal–angle coverage of 360°, except for the areas of the magnetic coils and a polar angle coverage between 8° and 140° [39]. The Start Counter (ST) was used to provide the triggered–event start time. Time-of-flight (TOF) scintillators were used to measure the particles' time of flight. The electromagnetic calorimeter was used to detect neutrons and photons.

Torus Magnet

As mentioned above, the torus magnet consisted of six superconducting coils arranged radially around the beam line. Figure 2.5 shows a cross section of the six coils and the magnetic field they produce [39]. The coils are arranged in such a way that the main field component is along the azimuthal direction. However, close to coils there are significant deviations in the field. Thus, the toroidal field changes primarily the polar angle of a scattered particle, while the azimuthal angle remains unaffected. By design the magnetic field along the beam line and in the area of the target is zero. The g13 experiment ran at -1500 A, which is less than half the maximum current of the magnet.

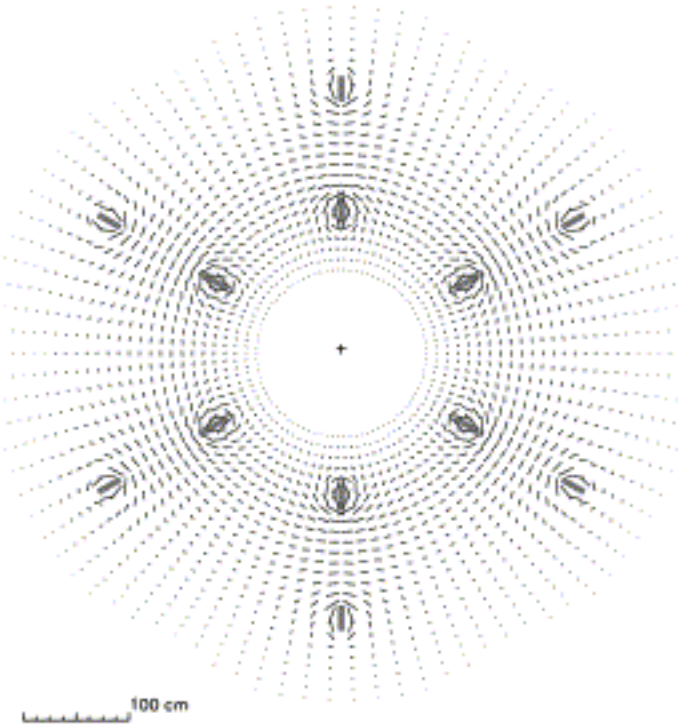

Figure 2.5: A cross section of the magnetic field vectors for the CLAS toroidal field in a plane perpendicular to the beam line. The locations of the coils are indicated by thick solid lines. One can see the field distortions in the areas close to the coils. This image is taken from Reference [39].

Start Counter

The start counter, shown in Fig. 2.6, surrounded the target and was used to determine the start time of an event [51]. The start time was used for time–of–flight calibration

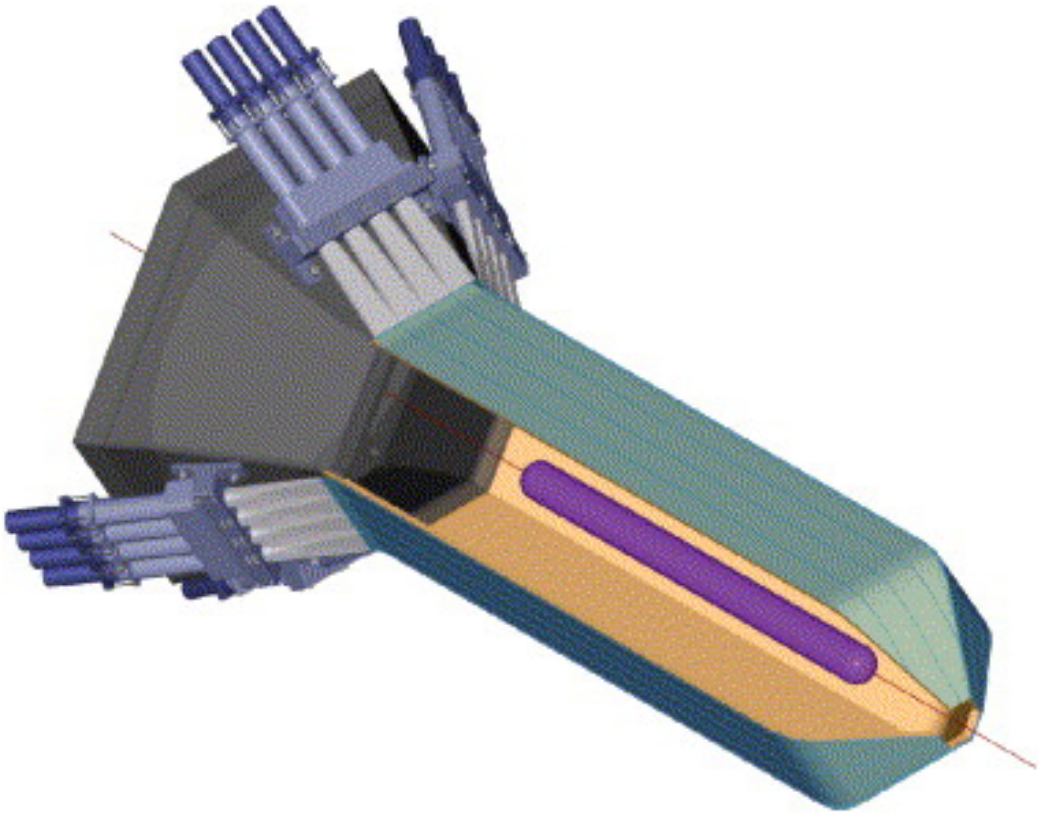

Figure 2.6: A schematic of the start counter in CLAS. One can see the six identical sectors of four scintillators per sector. This image was taken from Reference [51].

and for coincidence measurements between the particles detected in CLAS and the tagged photons. To correctly determine the start time, the beam bunch that caused the event needs to be identified. The start counter measured the time at which a particle passed through it, syncing the event with the tagged photons.

The start counter consisted of six identical sectors of four scintillators per sector, for a total of 24 scintillator paddles with a time resolution of 350 ps. It was designed to provide the same acceptance coverage as CLAS with a 40–cm long LH_2 target. Each paddle, seen as the different stripes, is a 29–mm wide continuous scintillator with a photomultiplier tube attached to the end.

Drift Chambers

The toroidal magnetic field in CLAS bends charged particles towards or away from the beam line. Three regions of drift chambers, Regions 1 (R1), 2 (R2), and 3 (R3), detected hits along the particles path. R1 surrounded the target and was in an area of low magnetic field. R2 was located between the main torus coils and experienced the largest magnetic field. R3 was located outside the magnetic coils. The particle's trajectory was reconstructed from these hits. The momentum of the particle was determined from the curvature of its trajectory and the magnetic–field map. For charged particles with momenta of 1 GeV/c, the design momentum resolution ($\delta p/p$) was $\leq 0.5\%$ and the angular resolution ($\delta\theta,\ \delta\phi$) (1 mrad, 4 mrad) [40].

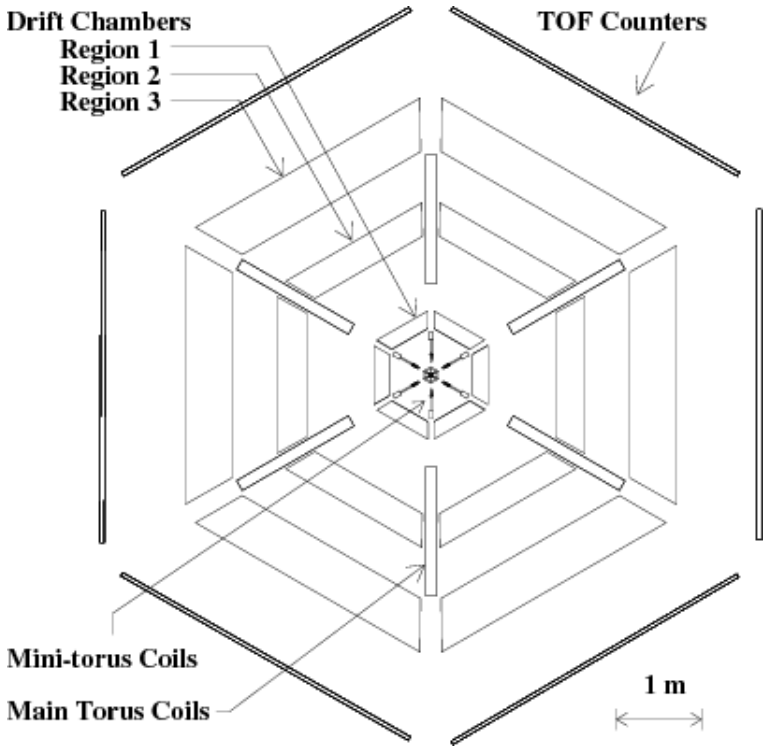

Figure 2.7: A schematic of CLAS detector as seen from the perspective of looking down the beam line. One can see how the CLAS is divided into six sectors by the main torus coils. The three regions of drift chambers are situated between these coils and track the trajectories of charged particles as they travel through the detector. The mini–torus is a magnet used in electro-production experiments. It was not used in g13, where the start counter was placed in its location. This image is taken from Reference [39].

Figure 2.7 shows the general setup of the drift chambers and the six sectors of CLAS. In total there are 18 separate drift chamber regions that are naturally divided by the main torus coils that generate the magnetic field. The 18 drift chamber regions consisted of $\approx$ 35,000 hexagonal drift cells. Inside each drift cell was a gold–plated tungsten sense wire of a diameter of 20 μm. Each drift cell was filled with a mixture of 90% argon and 10% CO_2 gas that provided the resolution and efficiency required for CLAS. When a charged particles passed through a drift cell, it ionized the gas and the resulting electrons drifted towards the sense wire yielding a signal that was amplified and processed further. A complete description of the drift chambers is given in [40].

Time–of–flight System

The time–of–flight (TOF) system for CLAS provided time information used for particle identification. To distinguish between pions and kaons with momenta up to 2 GeV/c, the system was required to achieve a timing resolution of σ=120–250 ps depending on the angle of the particles [52]. The TOF scintillators were placed between the drift chambers and the electromagnetic calorimeter. Figure 2.8 shows one sector of TOF scintillators.

Each sector consists of 56 scintillator paddles organized in four panels. Each paddle consisted of a scintillation bar and two light guides plus photomultipliers (PMT) (one on each end of the bar). The dimensions of the bars vary along the length of a TOF sector. For example, the most forward bars are 15-cm wide, while the large–angle bars are 22–cm wide. The timing resolution was also not constant within a TOF sector. Over both the most forward and backward bars, the TOF had a resolution of 163 ps [52].

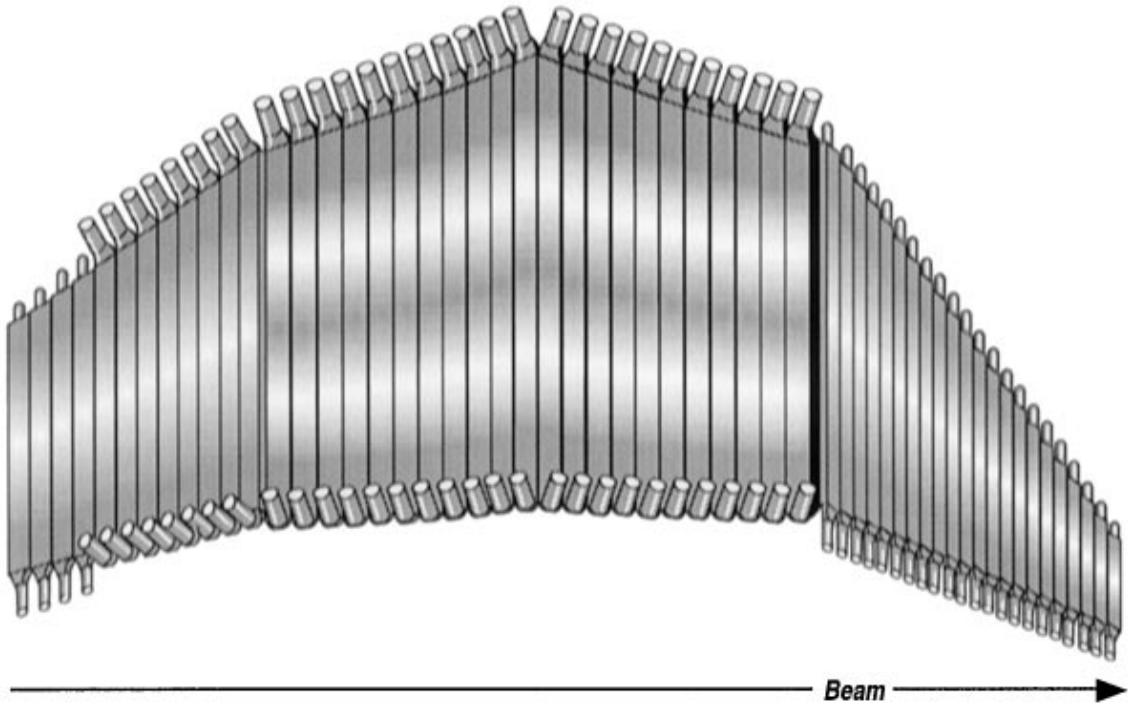

Figure 2.8: One sector of the time–of–flight system. Each sector of 56 paddles was positioned such that each paddle covers different polar angle. This image is taken from Reference [52].

Electromagnetic Calorimeter

Located outside the TOF system is the electromagnetic calorimeter, which is used to detect neutrons and photons. The electromagnetic calorimeter contains two detectors: a forward calorimeter that covers from 10° to 45° in six sectors and a large–angle calorimeter that extends from 45° to 75° in two sectors [5][7]. In addition to detecting neutrons and photons, the electromagnetic calorimeter was designed to detect electrons with an energy above 0.5 GeV/c. The electromagnetic calorimeters were not used in this analysis as the reaction of interest, $\gamma d \to K^0\Lambda(p) \to \pi^+\pi^- p\pi^-(p)$ contains only charged particles. Some background channels contain neutral particles, like $\Sigma^0 \to \Lambda\gamma$, but the missing–mass technique was used to identify these states.

Chapter 3

Event Selection

This chapter describes the process of selecting the $\gamma d \to K^0\Lambda(p)$ quasi–free events from the g13a data set. Since both, the K^0 and the Λ decay weakly, their lifetime is not long enough for them to be detected in the CLAS. Thus, the K^0 and the Λ are reconstructed by detecting their decay products. Specifically, the $K^0 \to \pi^+\pi^-$ and $\Lambda \to p\pi^-$ decays are used for reaction selection. The spectator proton in the final state of interest typically carries momentum that is below the momentum threshold of the CLAS for proton detection and is undetected in our analysis. Therefore, a triggered event in the full g13a data set was kept for further analysis only when it contained two positive and two negative tracks, with no limit on the number of neutral particles.

3.1 Particle Identification

The decay products of the K^0 and Λ are identified using information about the momentum and the time of flight of a given track. This is done by using the difference between the speed of the particle determined by the CLAS, $\beta_{measured}$, and the calculated speed under an assumption about the particle's mass, β_{calc}:

$$\Delta\beta = \beta_{measured} - \beta_{calc}, \tag{3.1}$$

where

$$\beta_{measured} = \frac{l}{ct}, \tag{3.2}$$

$$\beta_{calc} = \frac{p}{\sqrt{p^2 + m^2}}, \tag{3.3}$$

p is the measured momentum of the particle in the CLAS detector, m is the assumed mass i.e. the nominal mass of a particle of interest, l is the length of the particle's trajectory from the target to the TOF detector determined from its path through the drift chambers, and t is its time of flight. The time of flight, t, is the difference between the event start time at the vertex (relative to the trigger) and the time the particle hits the TOF detector. The event distribution over $\Delta\beta$ is expected to be centered at zero when the assumed mass is the true mass of the particle that had produced the track. The width of the $\Delta\beta$ distribution is determined by the finite resolutions of the quantities used to calculate it (p, l, t). Since the momentum resolution of the CLAS varies strongly with momentum, the width of the $\Delta\beta$ is momentum dependent.

Figure 3.1 shows $\Delta\beta$ for the proton as a function of its momentum. To identify

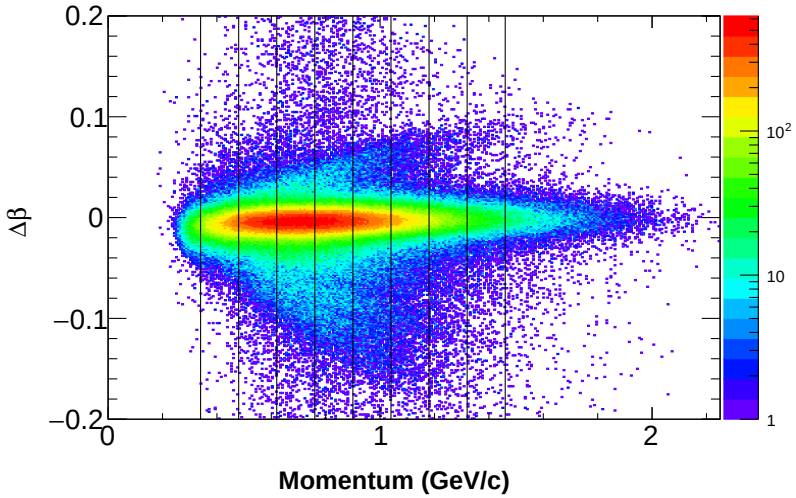

Figure 3.1: $\Delta\beta$ as a function of momentum for protons as measured by the CLAS, i.e. without any corrections applied. One clearly sees that true protons yield a distribution centered around $\Delta\beta$ of zero. The leaf–like structures that seem to originate from the proton distribution at low momenta and to follow a different trend at higher momenta are due to true protons that have incorrect timing. A lot of background events, such as pions and kaons are not seen in this figure. This is due to the fact that extra selection cuts, such as photon selection, K^0 selection, Λ selection, and missing mass cuts (all to be discussed) have been applied to the event sample in order to reduce the uncertainty of the proton PID cuts. The vertical black lines represent the different momentum bins used to determine the final PID cuts.

the protons, a momentum–dependent $\Delta\beta$ cut was determined by dividing Figure 3.1 into 10 momentum bins. For each bin in momentum, $\Delta\beta$ was projected and fit with a Gaussian. Figure 3.2 shows these projections and corresponding fit. Using the

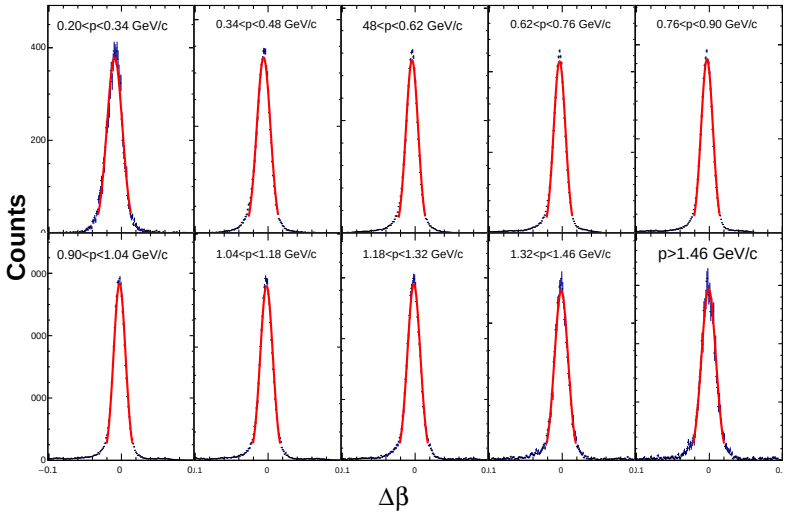

Figure 3.2: Projections and the Gaussian fit of the proton $\Delta\beta$ for the 10 momentum bins shown in Fig. 3.1. Even though extra cuts have been applied to the event sample to remove accidental background, some background events remain. Those contribute to the non–Gaussian tails of the projections. In order to determine the widths of those nearly–Gaussian distributions by fits to a Gaussian function in a consistent manner, the fit ranges were set to be [-0.025,0.025].

widths of the Gaussian fits, a $\pm 3\sigma$ range for each bin was determined. Figure 3.4 shows these $\pm 3\sigma$ points fit with 4^{th} order polynomials. The polynomials define the proton PID cut. Each track yielding a $\Delta\beta$ value falling within the interval defined by the cut are considered to be protons and are assigned the nominal proton mass in further kinematics calculations. The same procedure was applied to the rest of the tracks to determine the PID cuts for the π^+ and π^- Figures 3.4 and 3.5 show the fits for the π^+ and π^-, respectively.

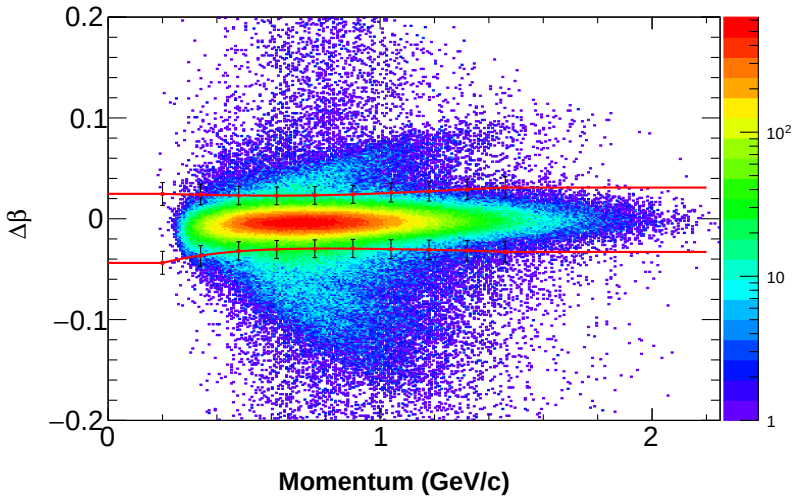

Figure 3.3: Final $\Delta\beta$ cuts for the proton (red line). The red data points represent the $\pm 3\sigma$ points determined from the Gaussian fits in Fig. 3.2. These points were then fit with a 4^{th} order polynomial to determine the $\Delta\beta$ cut.

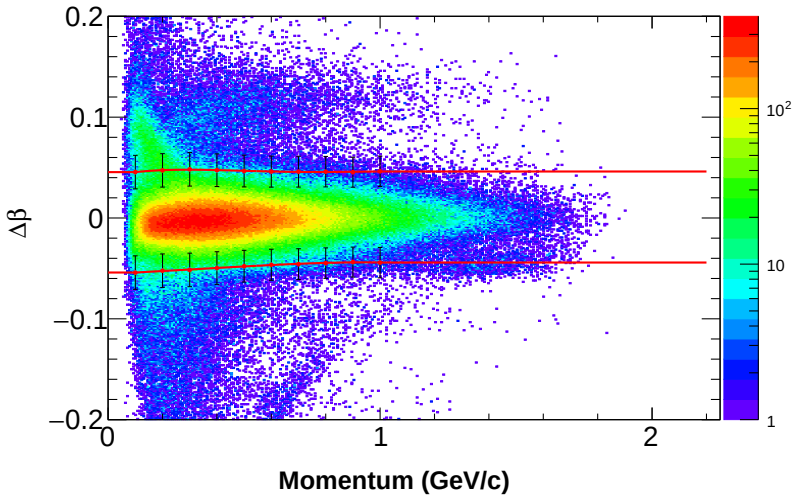

Figure 3.4: $\Delta\beta$ vs. p distribution for the π^+. The red data points represent the $\pm 3\sigma$ points determined from the Gaussian fits to the different momentum bins. These points were then fit with a 4^{th} order polynomial to determine the final $\Delta\beta$ cut (red line). The small structure at low momenta and positive delta beta is most likely due to true π^+s that decay before they reach the time–of–flight detector. The daughter muon moves along a path that is sufficiently close to the trajectory of the parent π^+ so that a single track is reconstructed. The momentum of the track however is different from the momentum of the parent π^+.

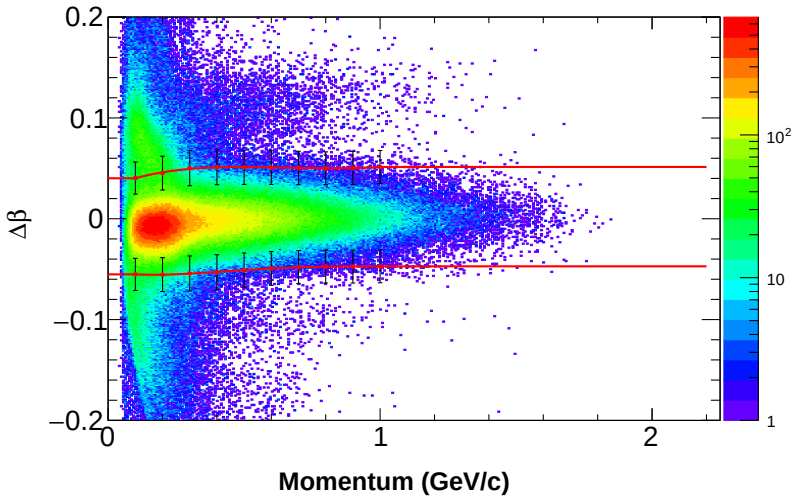

Figure 3.5: $\Delta\beta$ vs. p distribution for the π^-. The red data points represent the $\pm 3\sigma$ points determined from the Gaussian fits to the different momentum bins. These points were then fit with a 4^{th} order polynomial to determine the final $\Delta\beta$ cut (red line). The small structures at low momenta and positive delta beta are most likely due to true π^-s that decay before they reach the time–of–flight detector. The daughter muon moves along a path that is sufficiently close to the trajectory of the parent π^- so that a single track is reconstructed. The momentum of the track however is different from the momentum of the parent π^-. This effect is typically observed for out bending pions, i.e. π^- in g13a.

3.2 Event Vertex

After identifying the particles that produced the measured tracks, the reconstructed event vertex from CLAS was used to select events that originated within the target. The 40–cm–long LD_2 target for g13a was placed 20 cm upstream from the center of CLAS. Figure 3.6 shows the z component of the reaction vertex. The vertex was determined as the intersection of all four tracks in the event using a multi–track fitting routine [37]. Only events within $-40 < z < 0$ cm were kept as this range reflects the position and the length of the target. The z–vertex cut is shown be the vertical red lines in Fig. 3.6. This cut removes events that would be produced outside the target.

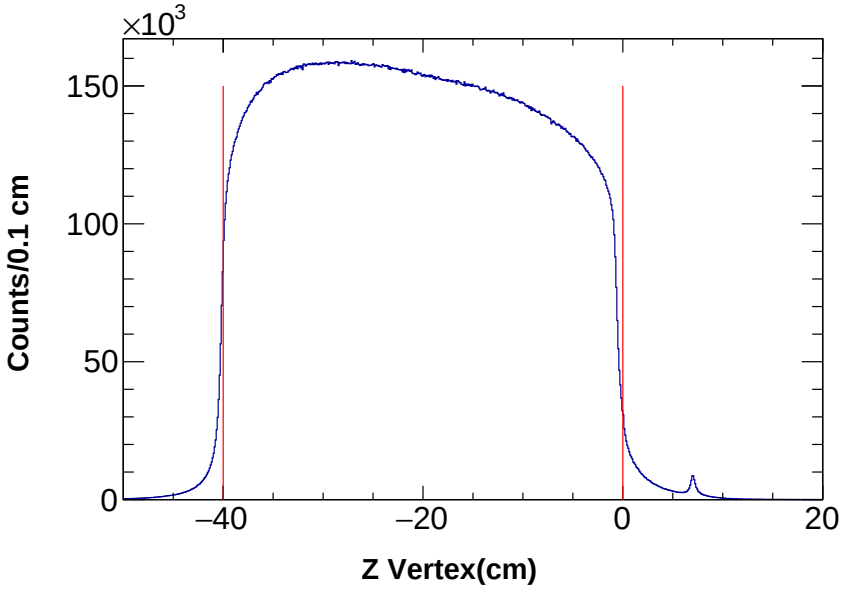

Figure 3.6: The z component of the production vertex. Events were kept if they originated within the target.

3.3 Photon Selection

The photon that initiated the reaction needs to be determined for further kinematic calculations. Figure 3.7 shows the number of photons detected in an event in g13a. The high intensity of the electron beam in g13a (current of 40 nA) caused there to be on average of 13–14 photons detected per event.

Determining which photon had initiated the reaction was done by comparing the time when the photon arrives at the vertex with the time when the event detected in the CLAS is created at the vertex. Since an event detected in the CLAS consists of four charged tracks, and none of them originates from the primary vertex, we take the vertex time of the fastest track in the event to be the event vertex time. The true photon that had initiated the event detected in CLAS should have a vertex time consistent with the event vertex time. The vertex time of the fastest track is determined as:

$$t_v = t_{SC} - \frac{d_{SC}}{\beta_{calc} c}, \tag{3.4}$$

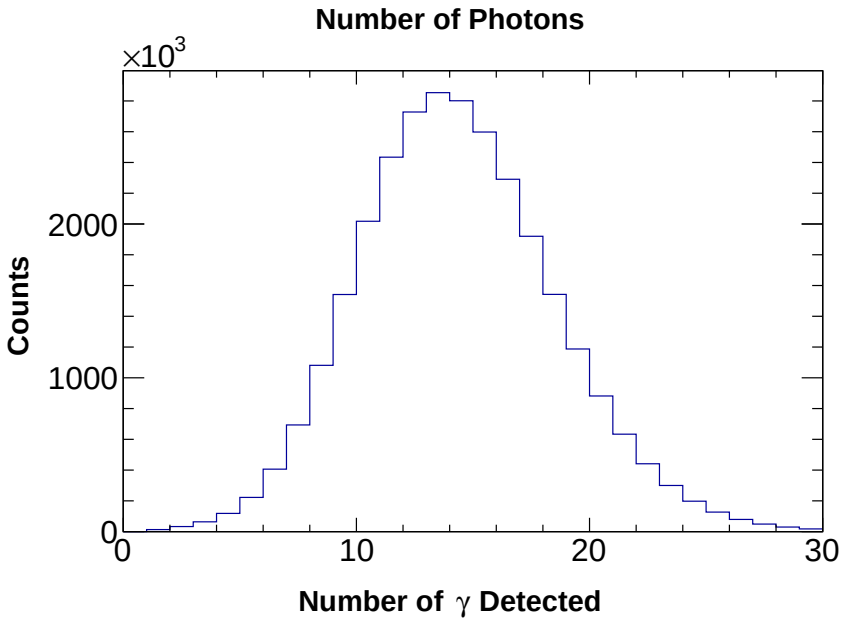

Figure 3.7: Number of photons detected per event in g13a. The photon selection uses time coincidence between the photon and the event in the CLAS to identify which among all photons initiated the event detected in the CLAS.

where t_{SC} is the time measured by the time-of-flight system in CLAS relative to the trigger, d_{SC} is the distance the fastest particle travels from the target to the TOF detector, and β_{calc} is the speed of the particle (in units of the speed of light) determined from Equation 3.2. The time the photon arrives at the vertex, t_γ, is obtained as

$$t_\gamma = t_{tagr} + \frac{z + 20}{c}, \tag{3.5}$$

where t_{tagr} is the time of arrival of the photon at the center of the CLAS, and z is the position of the event vertex from the MVRT BOS bank. The extra term of $\frac{z+20}{c}$ is needed because the target used in g13 was located 20 cm upstream from the center of the CLAS. The vertex time difference, Δt, i.e. the coincidence time, is calculated as:

$$\Delta t = t_v - t_\gamma. \tag{3.6}$$

The photon yielding the smallest Δt within the range of ± 1 ns is identified as the photon that initiated the reaction (referred to as the "good" photon). The cut

range of ±1 ns is chosen to be consistent with the 2.004–ns interval between adjacent beam bunches. The blue histogram on Figure 3.8 shows a typical coincidence time distribution. One can clearly see a large peak centered around zero. This peak contains photons and events in CLAS that originate from the same beam bunch. The smaller peaklets centered at ≈ ±2 ns and ≈ ±4 ns contain photons and CLAS events that originate from different beam bunches.

Since the K^0 and Λ decay before they traverse through CLAS, studies were done to determine if the fastest track should be used to determine Δt. Figure 3.8 shows Δt for the proton (black), π^+ (magenta), π^-s (green and red), and the fastest particle among them (blue). The fastest particle yields the largest number photons within ±1

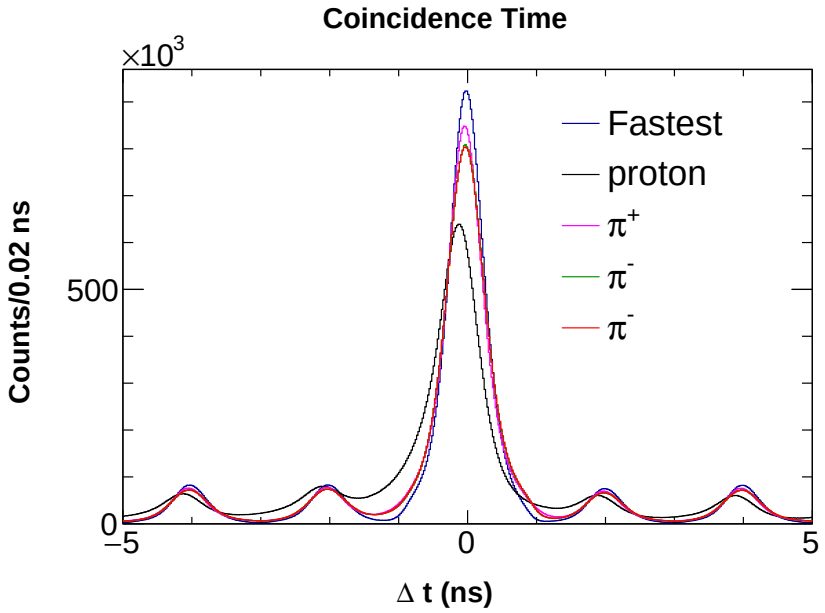

Figure 3.8: Coincidence time for all particles and the fastest particle in CLAS. The smaller peaks that are separated by 2 ns show the structure of different electron beam bunches.

ns and has the best resolution compared to all the particles. Therefore, the fastest particle yielding a coincidence time within $-1 < \Delta t < 1$ ns was used to select the photon that initiated the reaction.

Due to the large number of photons detected per event, there is a chance that

there are more than one photon yielding a coincidence time within ±1 ns for an event. Figure 3.9 shows the distribution of the number of good photons per event. Approximately 82.2% of events have 1 photon per event. An event was removed from

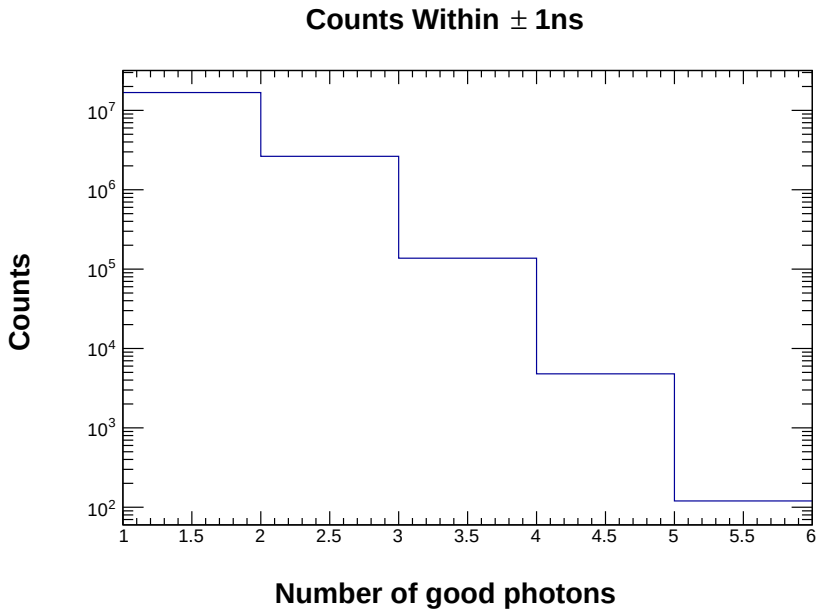

Figure 3.9: Number of photons yielding a coincidence time within ±1 ns per event. Events with 2 or more photons within the time-coincidence cut were removed from further analysis since there is no reliable mechanism to identify which amongst them was most likely the "good" photon.

further analysis if it had more than 1 good photon.

3.4 Decay Vertex Reconstruction

Corrections need to be applied to measured particle momenta in order to account for (a) energy loss in materials such as the target, target windows, beam line components, and start counter, and (b) for energy loss in the gas of the drift chambers and in air as a charged particle travels from the start counter to the TOF detector. These momentum corrections allow for a more accurate estimate of the particles' momenta at the production vertex.

The correction (a) is calculated for each track by using information about the particle mass, the vertex in the target where the particle originated, its measured

3-momentum vector, its path through all materials up to the start counter, and the properties of these materials [45]. The correction is then applied to the magnitude of the measured momentum. This correction is referred to as "e–loss" correction [45].

Even after the application of the e–loss correction, the momentum is still a subject of a bias due to the effects (b). To compensate for this bias, an extra correction, referred to as "momentum" correction, is applied to the e–loss-corrected momentum. The momentum for the proton and negatively–charged pions were determined from a kinematic fit to the reaction $\gamma d \rightarrow pp\pi^-$ [36]. The proton and the pions in our sample were corrected both with the e–loss and the momentum corrections. We have applied the proton momentum correction to the positively–charged pion momentum (the assumption that the momentum corrections for positively–charged pions are the same as for the protons is reasonable, as the largest energy loss occurs in the materials up to the start counter and this is properly corrected for each particle type by the e–loss correction). In addition to applying momentum and energy loss corrections, a correction was applied to the photon energy. This correction was applied due to the gravitational sag in the tagger scintillator paddles [34].

To apply the e–loss and momentum corrections to the p, π^+, and π^-s, the decay vertices of the K^0 and Λ need to be reconstructed. The Distance of Closest Approach (DOCA) method was used to reconstruct the decay vertices of the Λ and K^0. The decay vertex is defined as the position of common origin of two tracks that results from the smallest distance between these two tracks, such as a π^+ and π^-. This definition is based on the assumption that the vertex of a particle lies on the track of that particle. Figure 3.10 shows an illustration of how the decay vertex is reconstructed in this analysis. Since the drift chambers are located away from the target, in order to reconstruct the reaction or the decay vertex, the tracks in the drift chambers are extrapolated back to the area of the target by means of a linear extrapolation. Linear extrapolation is reasonable as the magnetic field between the target and R1 of the

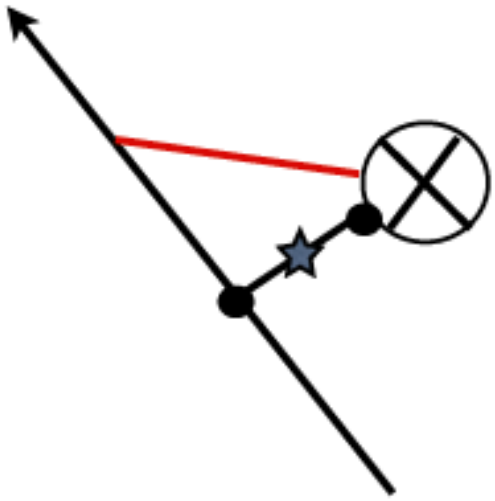

Figure 3.10: The DOCA method used to reconstruct the decay vertices of the K^0 and Λ. The DOCA occurs along the line perpendicular to each track (solid black line). The reconstructed decay vertex, represented by the $\star$, is the bisector of the DOCA line.

drift chamber is zero and the tracks of the charged particles in this area are straight lines. Due to the finite tracking resolution of CLAS the extrapolated tracks of two particles originating from the same vertex do not necessarily have an intersection point. The vertex is then determined to be a point on the line perpendicular to each track. In Figure 3.10, one particle is represented by the solid black arrow and is traveling in the plane of the paper. The other particle is traveling into the page and is represented by $\otimes$. The DOCA occurs along the line perpendicular to each track (solid black line). Any other line connecting the two trajectories, for example the red line in Fig. 3.10, will have a larger length than the DOCA. The reconstructed vertex, represented by the $\star$, is then the bisector of the DOCA line.

3.5 Reconstruction of the K^0 and Λ

The K^0 and Λ are reconstructed using the invariant mass of their decay products. Through four–momentum conservation, the invariant mass of the $\pi^+\pi^-$ system,

$M(\pi^+\pi^-)$, is expressed as

$$M(\pi^+\pi^-) = \sqrt{(\tilde{p}_{\pi^+} + \tilde{p}_{\pi^-})^2}. \tag{3.7}$$

Similarly, the invariant mass of the $p\pi^-$ system, $M(p\pi^-)$, is expressed as

$$M(p\pi^-) = \sqrt{(\tilde{p}_p + \tilde{p}_{\pi^-})^2}. \tag{3.8}$$

In Equations 3.7 and 3.8, $\tilde{p}_i$ represents the four–momentum of particle i, where $i = p,\ \pi^+$ or π^-. Figure 3.11 shows $M(\pi^+\pi^-)$ as a function of $M(p\pi^-)$. The events of

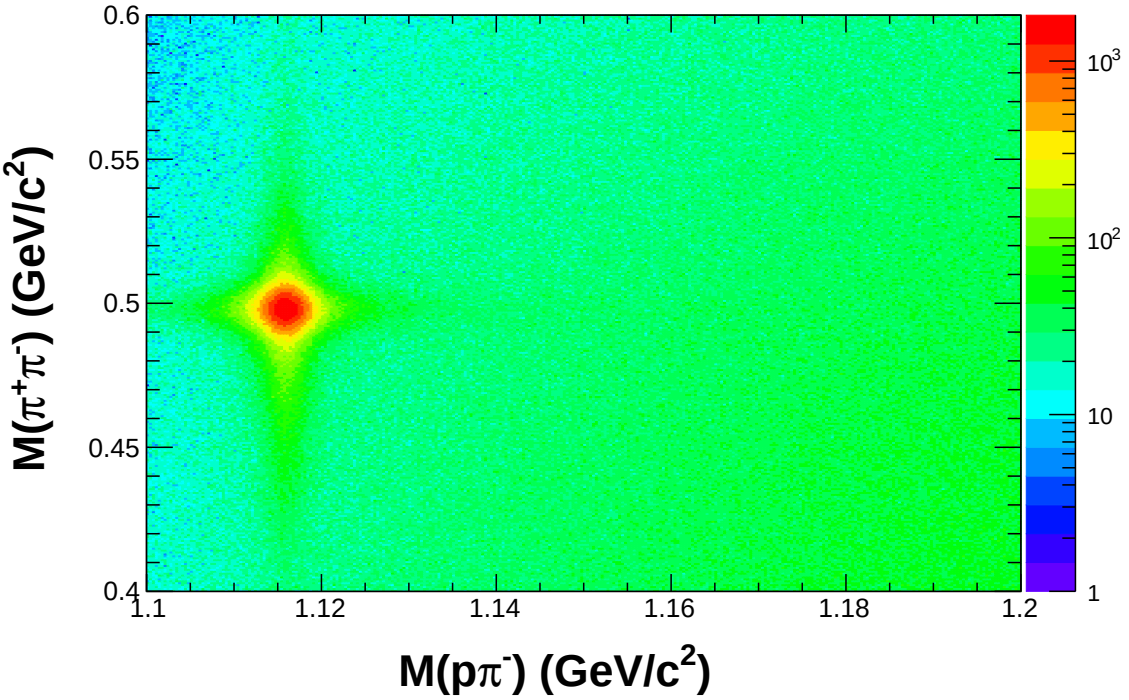

Figure 3.11: $M(\pi^+\pi^-)$ as a function of $M(p\pi^-)$. The peak containing to $K^0\Lambda$ events sits on top of a broad background. The background is mostly due to $\gamma d \to p\pi^+\pi^-\pi^- X$ events uncorrelated with $K^0\Lambda$ production.

interest form a peak centered around $M(\pi^+\pi^-) = M_{K^0}$ and $M(p\pi^-) = M_\Lambda$. These events sit on top of a broad background that comes from events uncorrelated to $K^0\Lambda$ photoproduction.

To select events containing a K^0, events within $1.10 < M(p\pi^-) < 1.13$ GeV/c^2 were projected onto $M(\pi^+\pi^-)$. The cut on $M(p\pi^-)$ selects Λ events and is important

to reduce the background in the $M(\pi^+\pi^-)$ distribution. Reduced background leads to a large signal–to–background ratio, a better understanding of the shape of the K^0 peak, and therefore, a more precise determination of the cuts selecting K^0 events. Figure 3.12 shows the event distribution over $M(\pi^+\pi^-)$ fitted with a Gaussian. Events

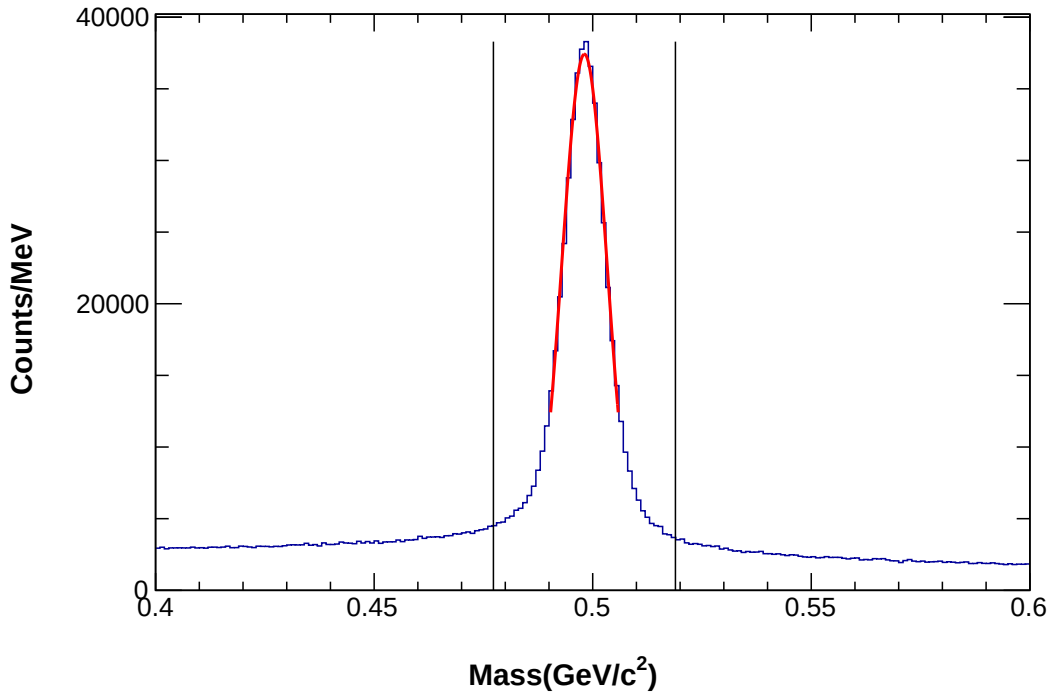

Figure 3.12: $M(\pi^+\pi^-)$ distribution after all previous cuts are applied. The peak was fit with a Gaussian and the vertical lines represent $\pm 4\sigma$ cuts used to select K^0 events.

within $\pm 4\sigma$ of the mean of the Gaussian were selected as this allows nearly all good K^0 events to be kept as the $M(\pi^+\pi^-)$ peak has tails that are best described by a double Gaussian. The $\pm 4\sigma$ cut allows for most of the events in the peak to be kept. The mean of the Gaussian is 0.49806 ± 0.00001 GeV/c^2, resulting in a 0.1% difference from the nominal mass of the K^0. This small difference is one control quantity that provides evidence that the e–loss and the momentum corrections are reasonable.

To select the Λ, events within $M(\pi^+\pi^-) = M_{K^0} \pm 4\sigma$ were projected onto $M(p\pi^-)$. Figure 3.13 shows the distribution of these events fitted with a Gaussian. As in the

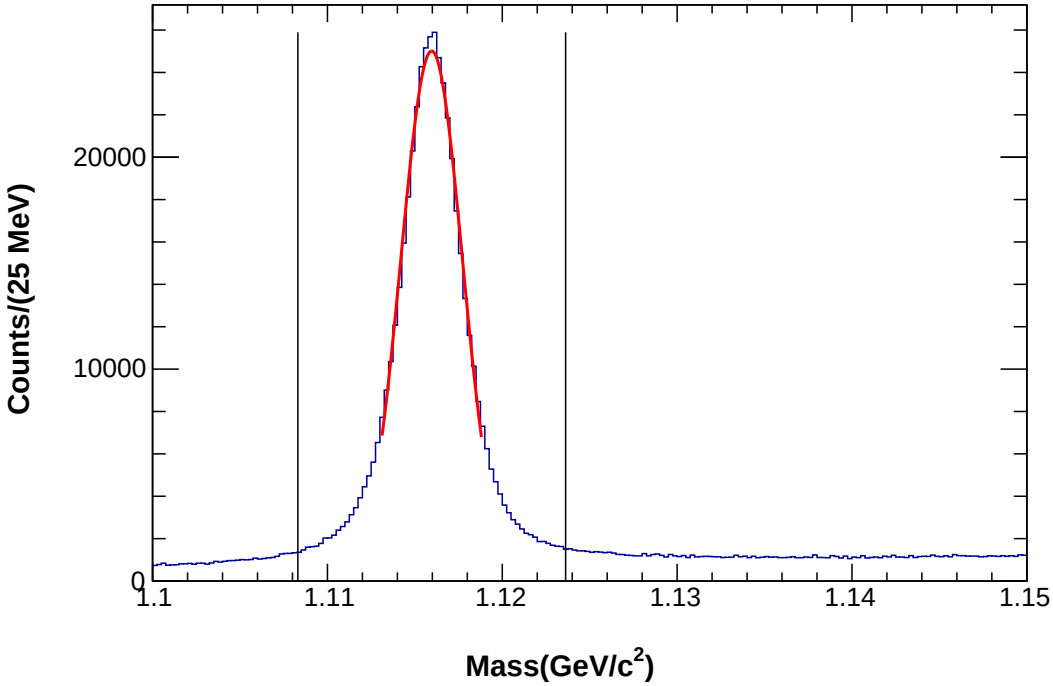

Figure 3.13: $M(p\pi^-)$ distribution after all previous cuts, including K^0 selection, were applied. The peak was fit with a Gaussian and the solid vertical lines represent $\pm 4\sigma$ cuts used to select Λ events.

selection of the K^0, a cut of $\pm 4\sigma$ was used to select the Λ. The mean of the Gaussian fit is 1.11595 ± 0.00006 GeV/c^2, resulting in a 0.02% difference from the nominal mass of the Λ.

In the above $K^0\Lambda$ selection, no estimation was made of the background under the invariant mass peaks. The amount of this background will be quantified at the next steps of the analysis. We note here, that one component of the background in the invariant mass spectra is a combinatorial background that arises from having two π^-s in the final state. The two pions are indistinguishable and one does not know a priori which π^- came from the Λ and which from the K^0 decay. There is even a small chance that both π^-s, when paired with the proton, yield a good Λ, and when paired with the π^+, yield a good K^0. This makes it impossible to distinguish which π^- belongs to the kaon and which one belongs to the lambda. More comprehensive

studies of the combinatorial background will be discussed in Chapter 4.4 to obtain a precise estimation.

3.6 Missing Momentum

The quasi–free reaction is identified using the momentum of the spectator proton. Since bound–nucleon momenta are small, the scattered proton in a quasi–free production is expected to carry its Fermi momentum. Thus, the momentum distribution of spectator protons produced in the reaction of interest should be consistent with the Fermi momentum distribution of a nucleon bound in the deuteron. Since the spectator proton is not detected, i.e. is "missing", its four–vector is referred to as "missing" momentum, denoted as p_X. By applying four-momentum conservation, p_X

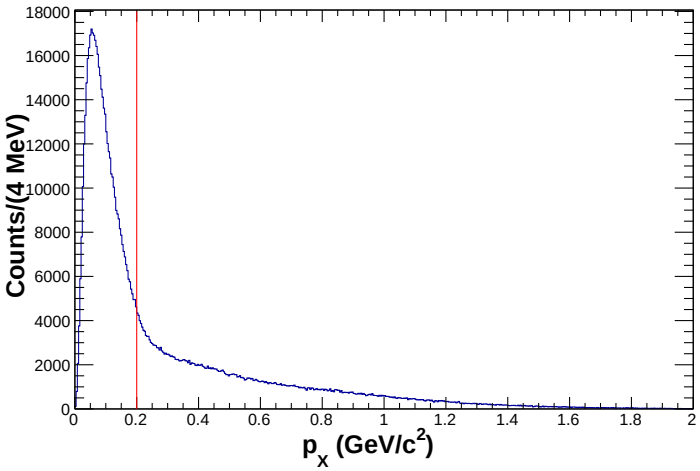

Figure 3.14: Distribution of $K^0\Lambda X$ events (where $X = p$) over the spectator momentum, $|\vec{p}_X|$. Events below 0.2 GeV/c form a sample dominated by the quasi–free reaction.

can be expressed as

$$\tilde{p}_X = \tilde{p}_\gamma + \tilde{p}_d - \tilde{p}_p - \tilde{p}_{\pi^+} - \tilde{p}_{\pi^-} - \tilde{p}_{\pi^-} = (E_X, \vec{p}_X) \tag{3.9}$$

where, in units of $c = 1$, $\tilde{p}_\gamma = (E_\gamma, 0, 0, E_\gamma)$ is the four–momentum of the photon, $\tilde{p}_d = (m_d, \vec{0})$ is the four–momentum of the deuteron, $\tilde{p}_p = (m_p, \vec{p}_p)$ is the four–momentum of

the proton, $\tilde{p}_{\pi^+} = (m_{\pi^+}, \vec{p}_{\pi^+})$ is the four–momentum of the π^+, and $\tilde{p}_{\pi^-} = (m_{\pi^-}, \vec{p}_{\pi^-})$ is the four–momentum of a π^-. Figure 3.14 shows the $|\vec{p}_X|$ spectrum. The quasi–free reaction was identified by selecting events with $|\vec{p}_X| < 0.2$ GeV/c. This cut eliminates most of the $K^0\Lambda p$ events produced by a more complex scattering, where the quasi–free mechanism was followed by final–state interactions, such as Λ or K^0 re–scattering off the proton and is further studied in Chapter 5.

Chapter 4

Observable Extraction Method

This section details the process of extracting the background–free polarization observables. In order to do this, the background channels and their contributions to the observables must be identified. This requires an accurate model of these channels. Lastly, a method to extract background free observables is needed.

The simplest way to identify the background channels is to investigate missing–mass distributions, where missing mass denotes the invariant mass of a state X that is produced in nuclear reaction. For the reaction of interest, $\gamma d \rightarrow K^0\Lambda(p)$, two different missing masses can be defined:

$$M_X = \sqrt{(\tilde{p}_\gamma + \tilde{p}_d - \tilde{p}_\Lambda - \tilde{p}_{K^0})^2} \tag{4.1}$$

and

$$M_{K^0X} = \sqrt{(\tilde{p}_\gamma + \tilde{p}_n - \tilde{p}_{K^0})^2}. \tag{4.2}$$

For an event produced in the reaction of interest (referred to as a "signal" event), $M_X = M_p$ (the spectator proton) and $M_{K^0X} = M_\Lambda$.

Figure 4.1 shows M_{K^0X} as a function of M_X. There are 3 main features of this distribution. The first one occurs at $M_X = M_p$ and $M_{K^0X} = M_\Lambda$. These events correspond to the signal events and are the events of interest. The second feature occurs when $0.98 < M_X < 1.08$ GeV/c^2 and $M_{K^0X} \approx 1.2$ GeV/c^2. These events correspond to Σ^0 production in the reaction $\gamma d \rightarrow K^0\Sigma^0$, where $\Sigma^0 \rightarrow \Lambda\gamma$. For these events $X = p\gamma$. The Σ^0 decays into a $\Lambda\gamma$ 100% of the time [47]. The final feature seen in the distribution occurs at $M_X > 1.08$ GeV/c^2. This part of the distribution

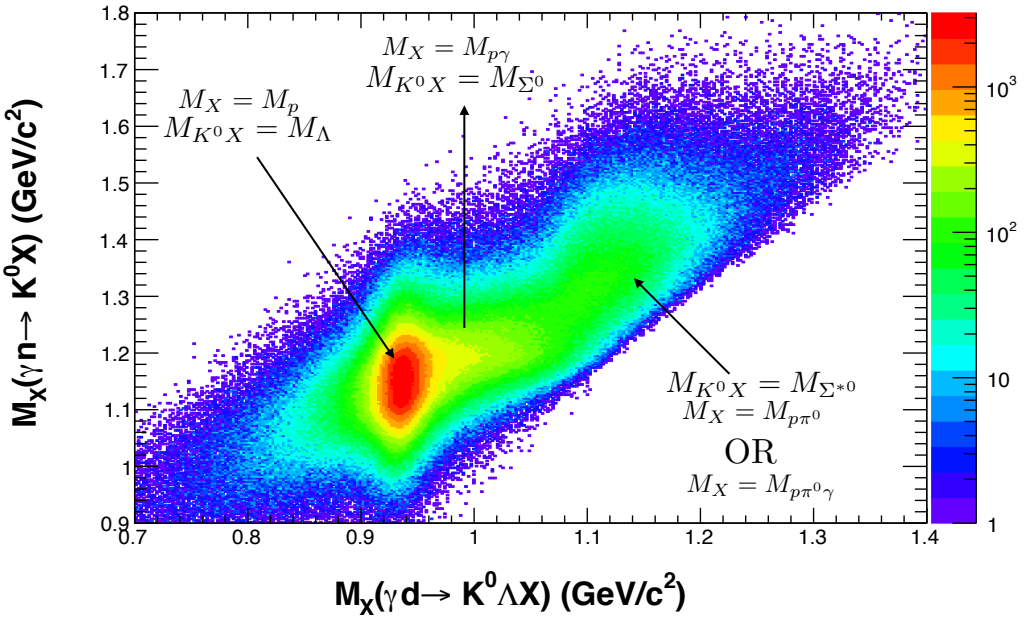

Figure 4.1: M_{K^0X} as a function of M_X. Visually, the main peak centered at $M_X = M_p$ and $M_{K^0X} = M_\Lambda$ contains the signal events. Higher mass channels in M_X and M_{K^0X} contain background channels such as $K^0\Sigma^0$, $K^0\Sigma^{*0}$, and $K^\star(892)\Lambda$ photoproduction. The arrows point to the general area of these different channels.

can contain many higher mass channels, such as $\Sigma^{\star 0}$ and $K^\star(892)$ production. These events predominately have an extra π^0 or $\gamma\pi^0$ missing in addition to the proton.

Since the calculation of M_{K^0X} assumes that the target neutron was at rest, while in reality the neutron carried its Fermi momentum, the event distribution over M_{K^0X} is broadened (Fermi smearing) such that one cannot distinguish $K^0\Lambda(p)$ from $K^0\Sigma^0(p)$ events. Thus, while the M_{K^0X} distribution is very useful to understand the sources of background in our sample, we use the event distribution over M_X to subtract the background and to extract background–free estimates of the polarization observables. In order to understand the shape of the background distributions in the M_X spectrum and be able to quantify how much each of these backgrounds contribute to the area of the proton peak, we used a customized event generator and a detector simulation.

4.1 Event Generator and Simulations

4.1.1 Introduction

In this work we have developed a realistic event generator and performed detector simulations to study the background channels. This generator was built off the framework developed by Tongtong Cao for his Ph.D. thesis to study $\gamma d \to K^+\Lambda(n)$[12]. Table 4.1 lists the channels we implemented in the event generator to study $\gamma d \to K^0\Lambda(p)$. The 5 channels in the generator are the photoproduction of $K^0\Lambda$, $p\pi^+\pi^-\pi^-$, $K^0\Sigma^0$, $K^0\Sigma^{\star 0}$, and $K^\star(892)\Lambda$. For each channel, the unstable particles in the final state can be decayed either in the generator or in the detector simulation.

Table 4.1: Physics channels generated in the event generator and processed through the detector simulation. If desired, unstable final–state particles can be decayed in the generator.

Channel	Process	Decay 1	Decay 2
1	$\gamma n \to K^0\Lambda$	$K^0 \to \pi^+\pi^-$, $\Lambda \to p\pi^-$	
2	$\gamma n \to \pi^+\pi^- p\pi^-$		
3	$\gamma n \to K^0\Sigma^0$	$K^0 \to \pi^+\pi^-$, $\Sigma^0 \to \Lambda\gamma$	$\Lambda \to p\pi^-$
4	$\gamma n \to K^0\Sigma^{\star 0}$	$K^0 \to \pi^+\pi^-$, $\Sigma^{\star 0} \to \Lambda\pi^0$	$\Lambda \to p\pi^-$
5	$\gamma n \to K^\star(892)\Lambda$	$K^\star(892) \to K^0\pi^0$, $\Lambda \to p\pi^-$	$K^0 \to \pi^+\pi^-$

Generally speaking, there are six steps in the generator and simulation process:

1. Generate the photon energy and Fermi momentum of the neutron.
2. Identify the physics channel to generate (via a random number, such that all physics channels are generated an equal number of times).
3. Generate phase–space distributed final–state particles for the identified physics channel.
4. If desired, modify the phase–space distribution by a cross–section and reject or accept the event accordingly.

5. Process the final–state particles through GSIM (Geant3 simulation of CLAS) [58].

6. Analyze the simulated data using the same procedures as in the analysis of real data.

First, an accept–reject method is used to generate the Fermi momentum of the spectator proton, $\vec{p}_f$, using the Paris potential [32]. Next, a uniform photon energy, E_γ, distribution is generated. The energy range of the E_γ was chosen to match the energy range of the g13a experiment, which was 0.9–2.6 GeV. Then, the four–momentum of the target neutron was set to be the difference between the four–momentum of the deuteron, $(m_d, \vec{0})$, and the proton, $(E_p, \vec{p}_f)$. In this scheme, the spectator proton is on its mass shell, while the target neutron is off its mass shell. After generating the random number that identifies which channel to generate, phase–space distributions were generated for the final–state particles of the process. After this step, a cross–section can be used to weight the phase–space distributions. The cross–section used to weight the distributions can be input from a table determined from, for example, Kaon–MAID or an analytic function [35]. After the final–state particle kinematics have been generated, the particles are then processed through GSIM.

Due to the fact that the GSIM environment is not exactly the same as the CLAS environment, the momentum corrections applied to the real data can not be used on the simulated data. Therefore, custom momentum corrections were calculated and applied to the simulated data. The momentum corrections were obtained by making use of simulated data on the reaction $\gamma d \to K^0\Lambda(p) \to p\pi^+\pi^-\pi^-(p)$. Here, the K^0 and Λ are forced to decay in the generator, allowing for the true momenta of the decay products to be kept throughout the analysis.

The momentum correction is a function of z–vertex position (z), polar and az-

imuthal scattering angles (θ, ϕ), and 3–momentum magnitude ($|\vec{p}|$). To perform the corrections, the data were divided into 6 z bins, 6 θ bins, and 6 ϕ bins. The momentum correction for each (z, ϕ, θ) bin was determined by fitting the difference between the generated (true) momentum, p_{true}, and the reconstructed momentum after particle processing through GSIM and applying the e–loss correction, p_{GSIM}. This difference, $\Delta p = p_{true} - p_{GSIM}$, was then divided into 5 $|\vec{p}|$ bins and fit with a Gaussian. The means of these Gaussian functions were then fit with an exponential to determine the final momentum corrections.

Figure 4.2 shows an example of calculating the proton momentum correction for one (z, ϕ, θ) bin. The Δp vs. p distribution (bottom right) was divided into 5 mo-

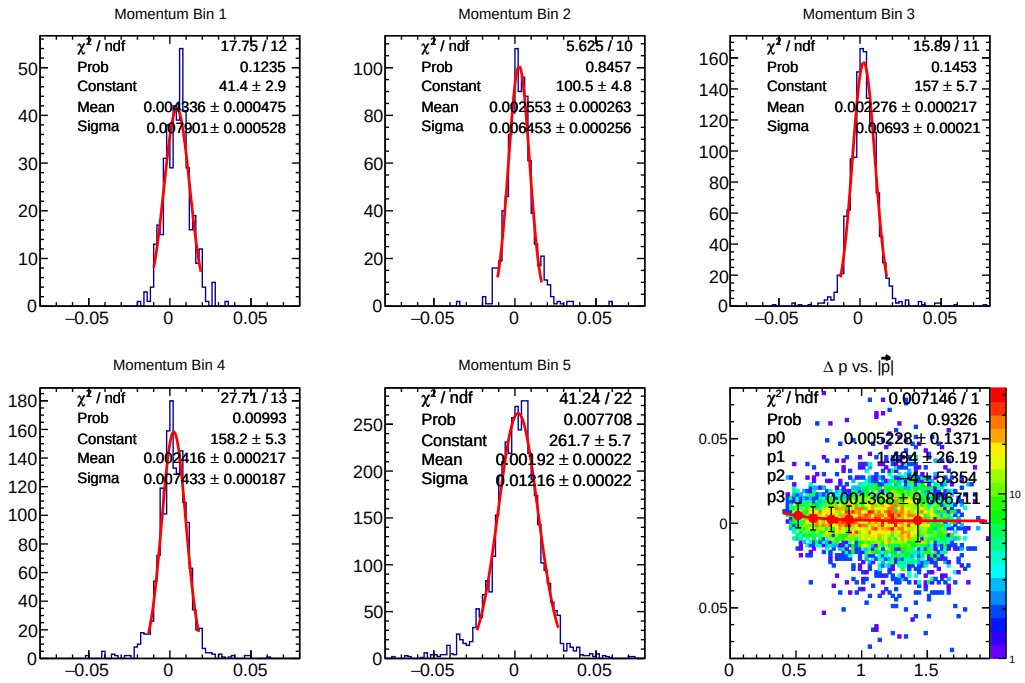

Figure 4.2: Fitting procedure and momentum correction example for the proton. The data were binned in different z–vertex, ϕ, and θ bins. For each bin, the Δp vs. $|\vec{p}|$ distribution was divided into 5 $|\vec{p}|$ bins. For each p bin, Δp was fit with a Gaussian. The means for the momentum bins were then fit with an exponential to determine the momentum corrections.

mentum bins. Each $(z, \phi, \theta, |\vec{p}|)$ bin's Δp was fit with a Gaussian (top row, bottom left and middle). The mean's for each Gaussian were fit with an exponential to de-

termine the correction function. The bottom right histogram, which shows the Δp vs $|\vec{p}|$ distribution for this kinematic bin, shows the mean and standard deviations of the Gaussians with the corresponding exponential fit.

4.1.2 Comparison to Data

Since simulated data will be used for background subtraction, it is important that the resolution and the acceptance of the simulated CLAS data matches well those of the real CLAS. To check this, we compare simulated with the real particle distributions. Figures 4.3–4.6 show the corrected momentum distributions of the simulated (red) and real (blue) for the π^+ and π^- from the K^0 decay, and proton and π^- from the Λ decay, respectively. All these distributions have the particles identified, $M(p\pi^-)$ and

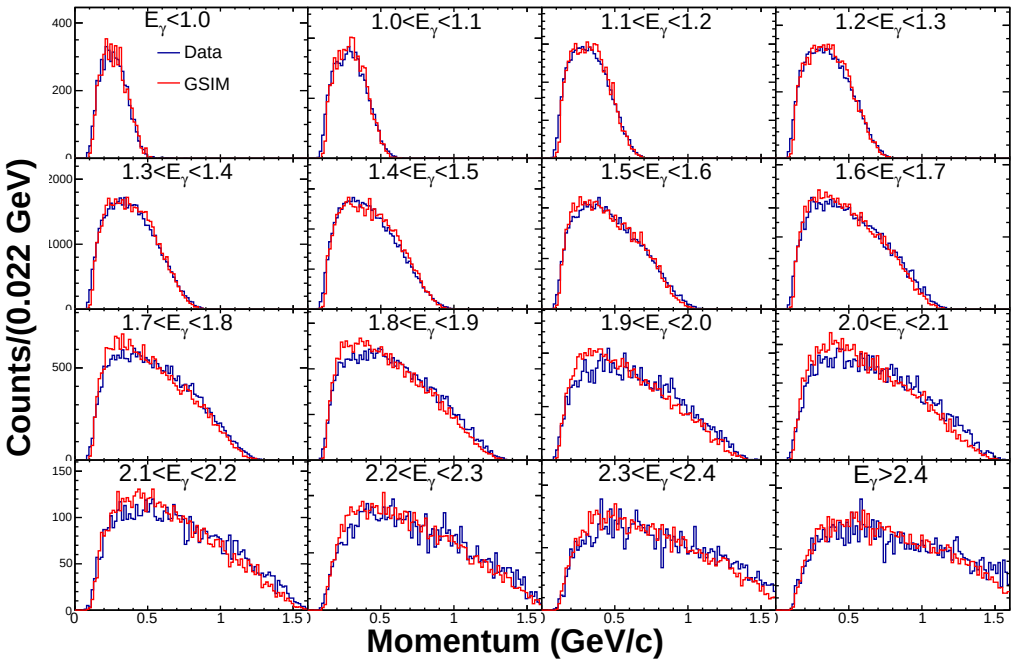

Figure 4.3: Momentum of the π^+ for the simulation scaled (red) to the data (blue) for 100–MeV wide E_γ bins.

$M(\pi^+\pi^-)$ selected, and the momentum of the spectator proton less than 0.2 GeV/c. These figures contain events generated from $K^0\Lambda$ weighted with cross–sections from g13, phase space distributions of $K^0\Sigma^0$ production, and phase–space distributions for

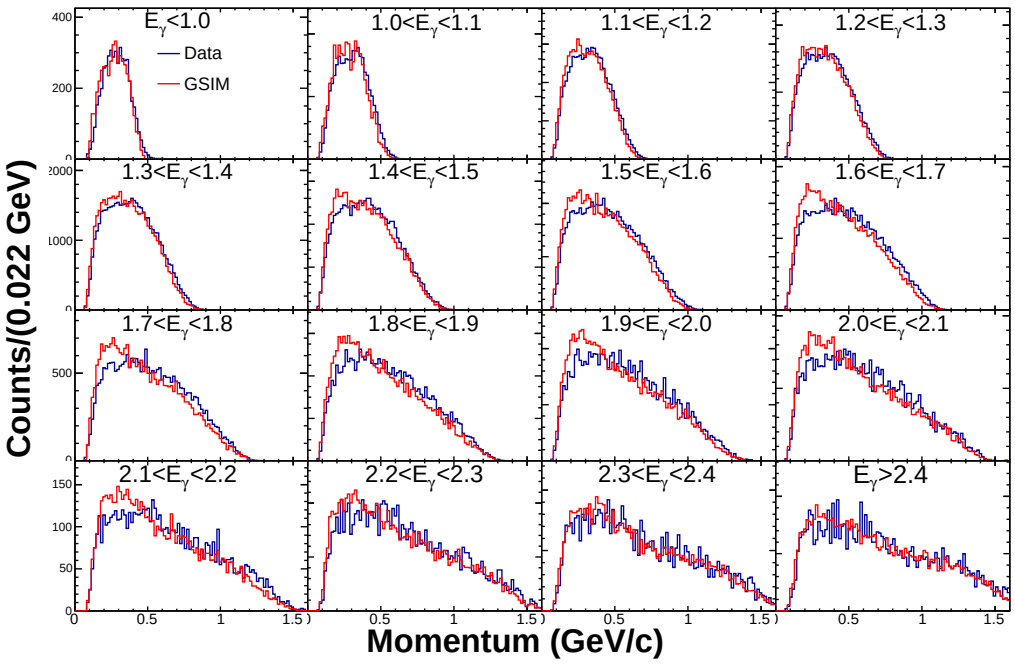

Figure 4.4: Momentum of the π^- from the Λ for the simulation scaled (red) to the data (blue) for 100–MeV wide E_γ bins.

the non–resonant $p\pi^+\pi^-\pi^-$ background. For each E_γ bin, the simulated distribution was scaled to the data by normalizing to the total number of events in the real–data distribution.

All the scaled simulated distributions reproduce the data very well. There are small discrepancies throughout Figures4.3–4.6, but nothing significant. For example, Figure 4.4 has some excess scaled simulation events below 0.5 GeV/c. This leads to a slight excess of data events from $\approx 0.5-1$ GeV/c. Even though these discrepancies occur, the distributions have similar maxima and go to zero at the same point. The observed matching of the shape of the momentum distributions at low momenta is especially relevant, since this shape strongly depends on the detector resolution. The matching at higher momenta suggests that either the $K^0\Lambda$ sample is the dominant contributor and/or that the $K^0\Sigma^0$ and $p\pi^+\pi^-\pi^-$ processes are well described by phase–space distributions.

Figure 4.7 shows $\cos\theta^{CM}_{K^0}$ for the $K^0\Lambda$ channel weighted with the g13 cross–

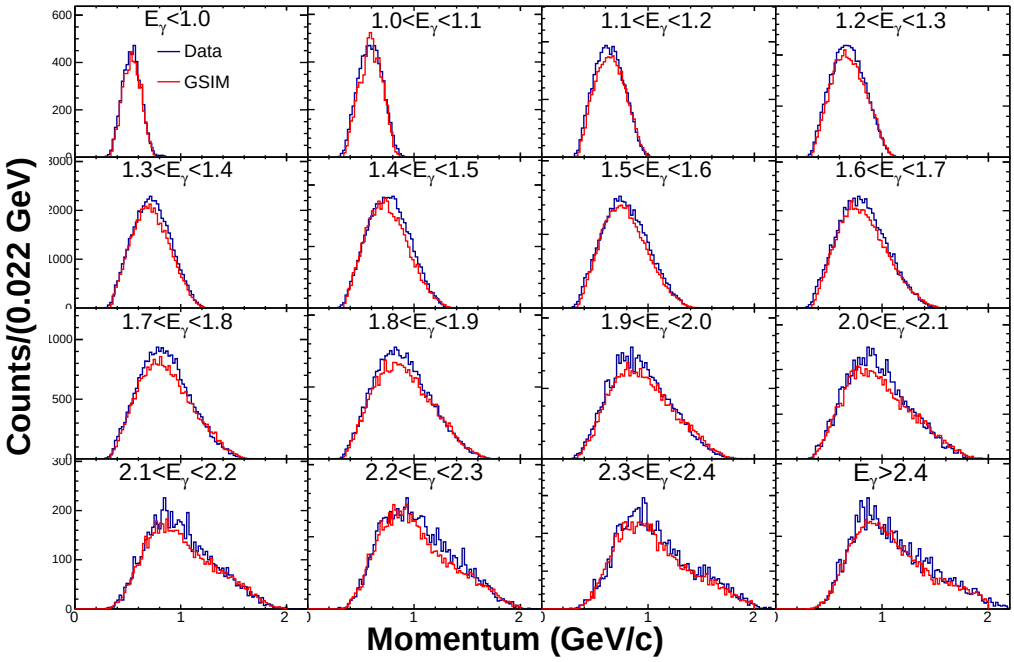

Figure 4.5: Momentum of the proton for the simulation scaled (red) to the data (blue) for 100–MeV wide E_γ bins.

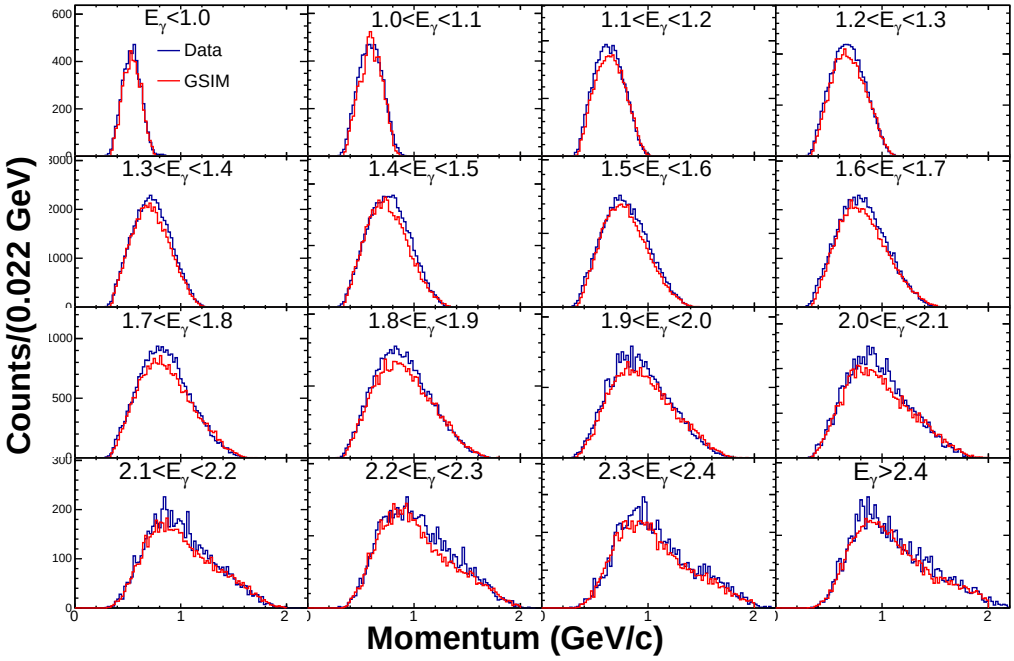

Figure 4.6: Momentum of the π^- from the K^0 for the simulation scaled (red) to the data (blue) for 100–MeV wide E_γ bins.

sections. For each E_γ bin the simulated distribution was scaled by normalizing the

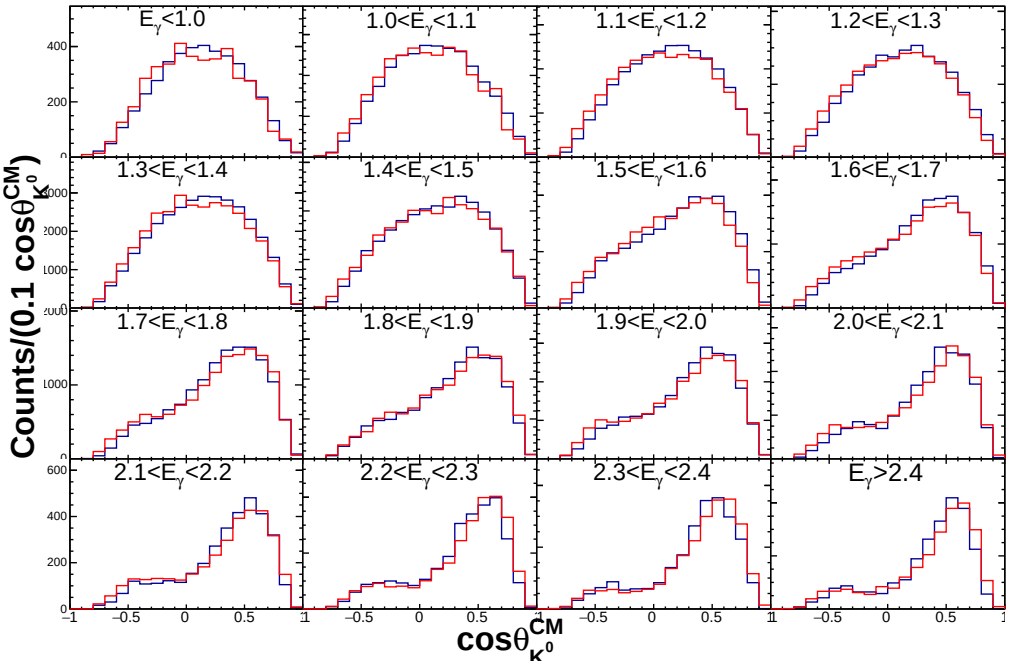

Figure 4.7: $\cos\theta_{K^0}^{CM}$ for the $K^0\Lambda$ simulation scaled (red) to the data (blue) for 100–MeV wide E_γ bins.

the total number of events in the real–data sample for that bin. Like the momentum distributions, these angular distributions accurately reproduce what is seen in the data. The distributions in Figure 4.7 also highlight the success of weighting the generator with cross–sections. Unfortunately, the only reliable cross–sections available for the channels studied in the generator were for the $K^0\Lambda$. All other channels were generated using phase–space distributions. These will be discussed in Section 4.4. The good results of the investigation of the quality with which the simulated data match real data gives us confidence that the shapes of the simulated background distributions over M_X would reproduce the real background reasonably well.

4.2 Axis Conventions

The coordinate systems used to extract the observables are defined in Section 1.4.1. Recall that the "primed" coordinate system is defined with the z'–axis along the K^0 momentum in the center–of–mass frame and the "unprimed" coordinate system is defined with the z–axis along the photon momentum in the center–of–mass frame. All momenta were boosted in the $K^0\Lambda$ center–of–mass frame, where the speed of the center–of–mass frame in lab system, $\vec{\beta}_B$, is defined as,

$$\vec{\beta}_B = \frac{1}{E_\Lambda + E_{K^0}}(\vec{p}_\Lambda + \vec{p}_{K^0}), \tag{4.3}$$

where $\vec{p}_{K^0}$, $\vec{p}_\Lambda$, E_{K^0}, and E_Λ are the momenta and energies of the K^0 and Λ, respectively. For the unprimed coordinate system, the y–axis is $\hat{z} \times \vec{p}^{CM}_{K^0}$. The x–axis is then perpendicular to both the y and z axes. For the primed coordinate system, the y'–axis is defined at $\hat{z'} \times \vec{p}^{CM}_{K^0}$.

The quantities of interest in Figure 1.9 are the decay angles of the proton with respect to the x, y, or z–axis, $\theta_{x,y,z}$. The polarization observables are extracted using helicity asymmetries in $\cos\theta_{x,y,z}$.

4.3 Maximum Likelihood Method

The observables C_x, C_z, and P were simultaneously extracted using a maximum likelihood estimator. The likelihood function, $L(x, y, z)$ is expressed as,

$$L_i^{\pm}(x, y, z) = 1 \pm x\cos\theta_{x,i} \pm z\cos\theta_{z,i} + y\cos\theta_{y,i}, \tag{4.4}$$

where $\theta_{x,y,z}$ is the decay angle of the proton in the Λ rest frame with respect to the x, y, or z–axis and $+$ or $-$ denotes the helicity of the photon beam. The best solution for the parameters $x,\ y, and\ z$ is the set that maximizes the log of the likelihood function:

$$log\ L = \sum_{i=1}^{N^+} log(L_i^+) + \sum_{i=1}^{N^-} log(L_i^-). \tag{4.5}$$

The observables are then obtained from the parameters x, y, and z as

$$C_x = \frac{x}{\alpha P_{circ}},\ C_z = \frac{z}{\alpha P_{circ}},\ P = \frac{y}{\alpha}, \tag{4.6}$$

where P_{circ} is the degree of circular polarization and α is the self–analyzing power of the Λ. Ideally, a normalized likelihood function would be used to extract the observables. This normalized likelihood function would have a normalization constant that would be observable independent and take care of normalizing the function and acceptance effects. The effect of using an unnormalized likelihood function to extract P, C_x, and C_z will be studied in Section 5.4.

4.4 Background Subtraction

After the event selection cuts described in Chapter 3, background still remains in the selected sample due to $p\pi^+\pi^-\pi^-$, $K^0\Sigma^0 \rightarrow K^0\Lambda\gamma$, and higher–mass channel events that pass the selection criteria. Figure 4.8 shows the missing–mass, M_X, of $\gamma d \rightarrow K^0\Lambda(p)$ integrated over all kinematics. Three different regions are emphasized by the arrows. The "signal" region corresponds to events where $X = p$, where p is the spectator proton. Two different background regions are also emphasized: $K^0\Sigma^0$ production where $X = p\gamma$ and higher–mass states ($K^{*0}(892)$, Σ^{*0}) where $X = p\pi^0$. This distribution, along with the simulations discussed in Section 4.1, are used to subtract the background.

The background subtraction method used here is based off the 2016 analysis note by N. Zachariou for studying final–state interactions on $\vec{\gamma}d \rightarrow K^+\vec{\Lambda}(n)$ [41]. The general idea of this method is to extract a total observable ($C_x^T,\ C_z^T,\ P^T$) using the maximum likelihood method that includes all signal ($X = p$) and background ($X = p\gamma,\ p\pi^0$) events. The total observables are then *corrected* using background–to–total ratios to get a signal observable ($C_x^S,\ C_z^S,\ P^S$). This is done by dividing M_X into two regions: a signal dominated region situated around $X = p$ and a background

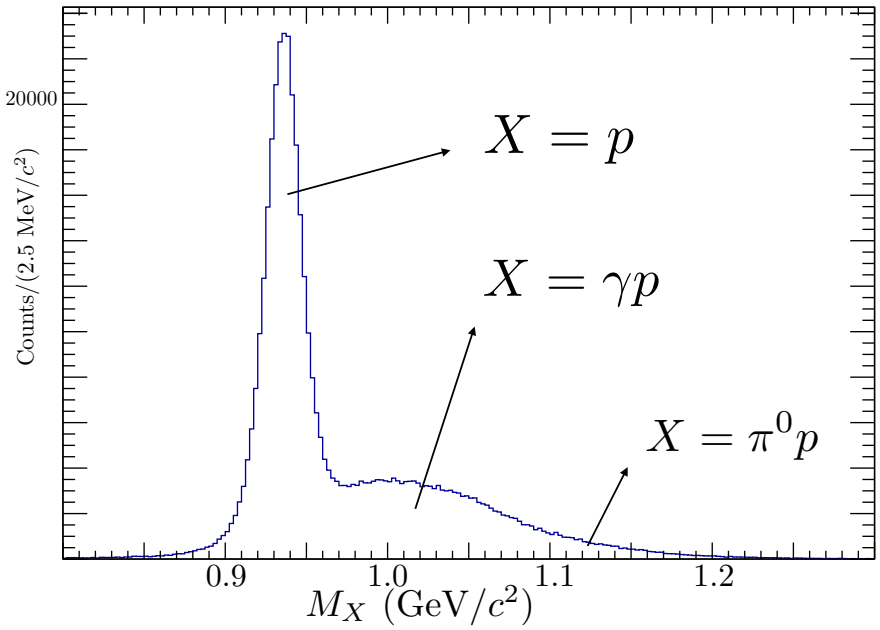

Figure 4.8: The missing–mass, M_X, of $\gamma d \to K^0\Lambda(X)$ with the selection cuts described in Chapter 3 integrated over all kinematics.

dominated region. The main reason why this background subtraction was chosen is that it allows for finer kinematic binning. The $K^0\Lambda$, $K^0\Sigma^0$ and higher–mass channels are polarized, and therefore are dependent on $\cos\theta_x$ and $\cos\theta_z$. If a probabilistic event weighting background subtraction method was used, M_X would need to be binned in $\cos\theta_x$ and $\cos\theta_z$, in addition to E_γ and $\cos\theta^{CM}_{K^0}$. The background subtraction method of correcting the total observables has the advantage of integrating over $\cos\theta_{x,z}$, thus allowing for finer kinematic binning.

The differential cross–section, $\frac{d\sigma}{d\Omega}$, for $K^0\Lambda$ photoproduction using an unpolarized target and circularly polarized photon beam can be written as

$$\frac{d\sigma}{d\Omega} = \frac{d\sigma^0}{d\Omega}[1 - \alpha P_{circ}\cos\theta_x C_x - \alpha P_{circ}\cos\theta_z C_z + \alpha\cos\theta_y P], \tag{4.7}$$

where $\frac{d\sigma^0}{d\Omega}$ is the unpolarized cross–section, α (a constant) is the self–analyzing power of the Λ, and P_{circ} is the degree of circular polarization of the photon beam. For a given E_γ and $\cos\theta^{CM}_{K^0}$, the number of events with helicity + or −, $N_\pm(E_\gamma, \cos\theta^{CM}_{K^0})$,

is proportional to the polarized differential cross–section

$$N_{\pm}(E_{\gamma}, \cos\theta^{CM}_{K^0}) \propto \frac{d\sigma^{\pm}}{d\Omega}(E_{\gamma}, \cos\theta^{CM}_{K^0}). \tag{4.8}$$

For a given kinematic bin of $(E_{\gamma}, \cos\theta^{CM}_{K^0})$, the total number of polarized events, $N^T_{\pm}$, can be expressed as,

$$N^T_{\pm} \approx N^T_0[1 \pm \alpha P_{circ}\cos\theta_x C^T_x \pm \alpha P_{circ}\cos\theta_z C^T_z + \alpha\cos\theta_y P^T], \tag{4.9}$$

where N^T_0 is the number of unpolarized events. N^T_0 can be divided into the number of signal events, N^S, polarized background events, N^B, and unpolarized background events, N^{unpol},

$$N^T_0 = N^S_0 + N^B_0 + N^{unpol}_0. \tag{4.10}$$

The total observables are related to the signal observables ($C^S_x,\ C^S_z,\ P^S$) and a background observables ($C^B_x,\ C^B_z,\ P^B$) as

$$N^T_0 C^T_x = N^S_0 C^S_x + N^B_0 C^B_x, \tag{4.11}$$

$$N^T_0 C^T_z = N^S_0 C^S_z + N^B_0 C^B_z, \tag{4.12}$$

$$N^T_0 P^T = N^S_0 P^S + N^B_0 P^B. \tag{4.13}$$

Equations 4.11–4.13 do not contain terms involving N^{unpol} because the $p\pi^-\pi^+\pi^-$ background events that do not come from a pseudoscalar meson and hyperon decay are unpolarized and the observables are 0. Recall that C_x and C_z measure the polarization transfer from the photon beam to the hyperon, while P is the induced hyperon polarization. These observables require a polarized baryon in the final–state. If no polarized baryon exists, then $C^{unpol}_x = C^{unpol}_z = P^{unpol} = 0$. This was confirmed by extracting the observables in a region far from the Λ and K^0 peaks in the invariant mass distributions. Solving for the signal observable in Eqs. 4.11–4.13 leads to the expressions,

$$C^S_x = \frac{C^T_x - r^B C^B_x}{1 - r^B - r^{unpol}} \tag{4.14}$$

$$C_z^S = \frac{C_z^T - r^B C_z^B}{1 - r^B - r^{unpol}} \tag{4.15}$$

$$P^S = \frac{P^T - r^B P^B}{1 - r^B - r^{unpol}} \tag{4.16}$$

where $r^B = \frac{N_0^B}{N_0^T}$ and $r^{unpol} = \frac{N_0^{unpol}}{N_0^T}$ are the ratios of the polarized and unpolarized background yields to the total unpolarized yield. Figure 4.9 visualizes Eqs. 4.10, 4.11, 4.12, and 4.13 on M_X. In a given region of M_X, shown as the black lines at 0.9

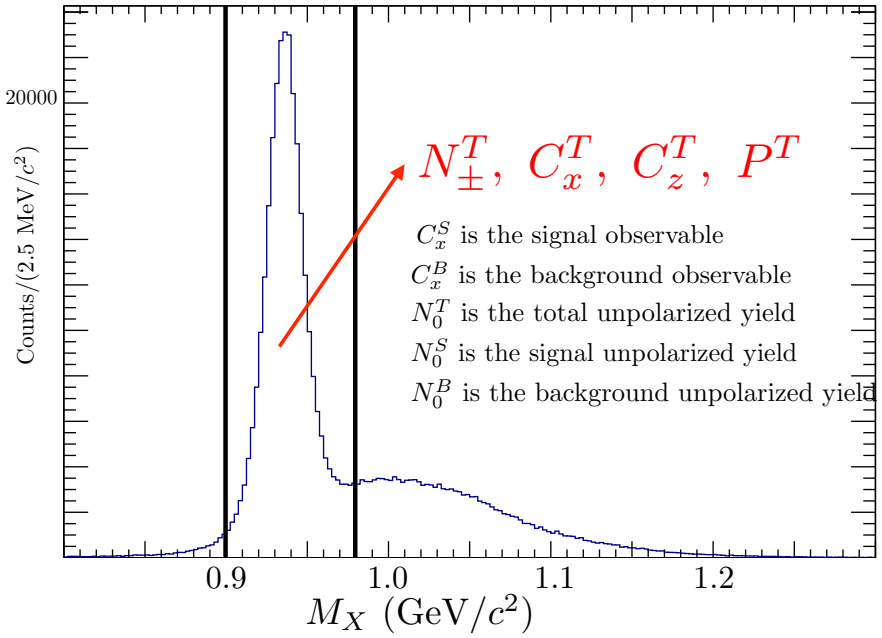

Figure 4.9: A visualization of Eqs. 4.10, 4.11, 4.12, and 4.13 on M_X. In a given region of M_X, shown as the black lines at 0.9 and 0.98 GeV/c^2, the total observable is extracted.

and 0.98 GeV/c^2, the total observable is extracted.

In Eqs. 4.14–4.16, the total observable can be extracted using the maximum likelihood method, and r^B and r^{unpol} can be calculated by fitting the simulated background distributions to the data. The background and signal observables are unknowns. To solve for the signal observable, the missing mass is divided in to two regions. Region 1 corresponds to a "signal dominated" region: $0.90 < M_X < 0.98$ GeV/c^2. Region 2 corresponds to a "background dominated" region: $0.98 < M_X < 1.05$ GeV/c^2. This

separation point of 0.98 GeV/c^2 was chosen because it corresponds to $\approx 3\sigma$ of the width of the missing proton peak. Systematic effects of choosing these regions will be discussed in Chapter 5.5. The signal observable can be written for each region as,

$$C_x^S = \frac{C_{x,1}^T - r_1^B C_x^B}{1 - r_1^B - r_1^{unpol}},\ C_x^S = \frac{C_{x,2}^T - r_2^B C_x^B}{1 - r_2^B - r_2^{unpol}} \tag{4.17}$$

$$C_z^S = \frac{C_{z,1}^T - r_1^B C_z^B}{1 - r_1^B - r_1^{unpol}},\ C_z^S = \frac{C_{z,2}^T - r_2^B C_z^B}{1 - r_2^B - r_2^{unpol}} \tag{4.18}$$

$$P^S = \frac{P_1^T - r_1^B P^B}{1 - r_1^B - r_1^{unpol}},\ P^S = \frac{P_2^T - r_2^B P^B}{1 - r_2^B - r_2^{unpol}}. \tag{4.19}$$

An assumption is made that both the signal observable and background observable do not depend on M_X. Equations 4.17–4.19 each represent a system of two equations with two unknowns. Therefore, solving for the signal observables, one arrives at the expressions,

$$C_x^S = \frac{r_1^B C_{x,2}^T - r_2^B C_{x,1}^T}{r_1^B - r_2^B - r_1^B r_2^{unpol} + r_1^{unpol} r_2^B} \tag{4.20}$$

$$C_z^S = \frac{r_1^B C_{z,2}^T - r_2^B C_{z,1}^T}{r_1^B - r_2^B - r_1^B r_2^{unpol} + r_1^{unpol} r_2^B} \tag{4.21}$$

$$P^S = \frac{r_1^B P_2^T - r_2^B P_1^T}{r_1^B - r_2^B - r_1^B r_2^{unpol} + r_1^{unpol} r_2^B} \tag{4.22}$$

In Eqs. 4.20–4.22, the total observables can be separately extracted in region 1 and 2 using the maximum likelihood method, and r_i^B (r_i^{unpol}) can be calculated using background to total yields from the simulations.

4.4.1 Determination of $p\pi^+\pi^-\pi^-$ Scaling

The non–resonant unpolarized background consists of $p\pi^+\pi^-\pi^-$ events uncorrelated with $K^0\Lambda$ or higher–mass final state production. These events are the background seen in the $M(p\pi^-)$ and $M(\pi^+\pi^-)$ distributions and have a missing–mass peak at $X = M_{proton}$. This means that one cannot distinguish between the signal and background events using M_X. Therefore, the scaling of these events needs to be fixed prior to fitting M_X (discussed in Section 4.4.2). To determine the number of unpolarized

events underneath the M_X peak, the simulated $M(p\pi^-)$ distribution from $p\pi^+\pi^-\pi^-$ events is scaled to the data by fitting the simulated $M(p\pi^-)$ distribution to the data. Before performing the fits, cuts of $0.9 < M_X < 0.98$ GeV/c^2, $p_X < 0.2$ GeV/c^2, and $M(\pi^+\pi^-) \pm 4\sigma$ were applied.

To scale the unpolarized background, $M(p\pi^-)$ was fit with a double Gaussian plus the $p\pi^+\pi^-\pi^-$ simulated $M(p\pi^-)$ distribution:

$$S_{p\pi^+\pi^-\pi^-}(x) = A_1 \exp \frac{(x-\mu)^2}{\sigma_1^2} + A_2 \exp \frac{(x-\mu)^2}{\sigma_2^2} + A_3 H_{unpol} \tag{4.23}$$

where $A_{1,2}$ are the heights of the two Gaussians, μ is the mean, $\sigma_{1,2}$ are the widths of the Gaussians, H_{unpol} is the non–resonant, unpolarized background histogram, and A_3 is the parameter that scales H_{unpol} to the data. Figure 4.10 shows the fit and corresponding scaling of the unpolarized background integrated over all kinematics. The double Gaussian describes the $M(p\pi^-) = M_\Lambda$ events and the scaled unpolarized

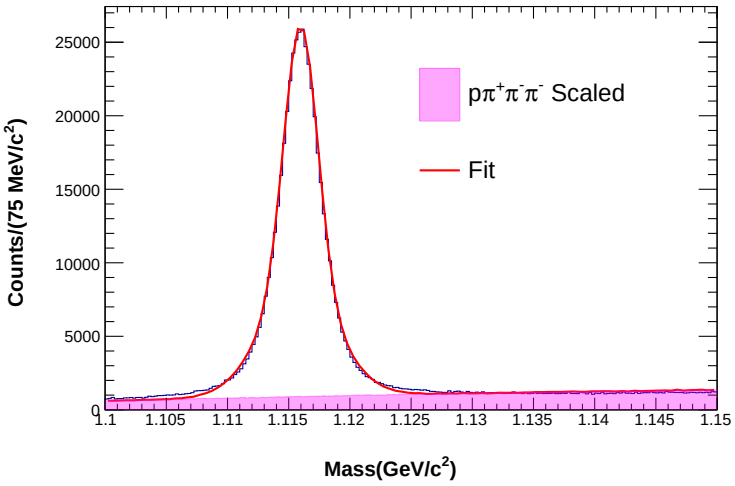

Figure 4.10: An example fit and scaling of the non–resonant, unpolarized $\gamma d \to p\pi^+\pi^-\pi^-(p)$ simulated background to the data using Equation 4.23. A double Gaussian is used to describe the signal and a parameter from the fit, A_3, is used to scale the unpolarized background (magenta) to the data.

simulation accurately represents the background. These fits were performed for every kinematic bin to determine the proper scale factor.

Figure 4.11 shows fits to $M(p\pi^-)$ for 14 different $\cos\theta^{CM}_{K^0}$ bins for $1.2 < E_\gamma < 1.3$ GeV. Visually, the double Gaussian plus background model appears to accurately

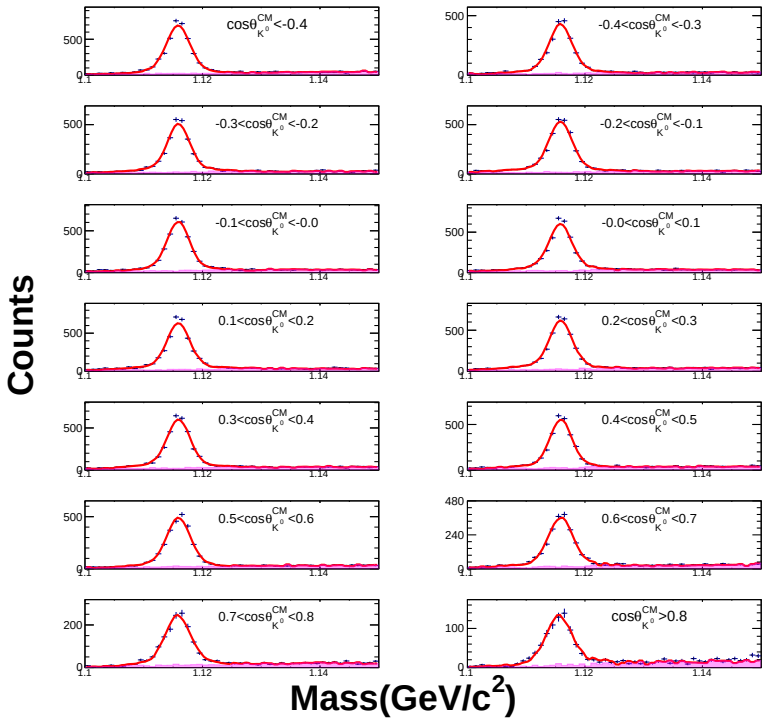

Figure 4.11: Example fits and scaling of the non–resonant, unpolarized simulation to the data for one E_γ bin. The red line is the total fit to the data and the magenta histogram is the $p\pi^+\pi^-\pi^-$ non–resonant background scaled using A_3 from Equation 4.23.

scale the $p\pi^+\pi^-\pi^-$ non–resonant background. Figure 4.12 shows the χ^2/NDF and scale factor (A_3 in Equation 4.23) for all the fits. Using the χ^2/NDF is not the ideal way to determine the "goodness" of the fit, but it still provides valuable information about the performance of the fits. The χ^2/NDF is not ideal because most parameters in the fit are fixed or are allowed to vary within a small range and may default to the maximum or minimum allowed value, potentially causing the χ^2/NDF to be larger than it would be if the fit parameters were allowed to be free. Therefore, a combination of the χ^2/NDF and visual inspection were used to check the fits. With this said, all the χ^2/NDF are less than 5 and it can be concluded that for all the fits,

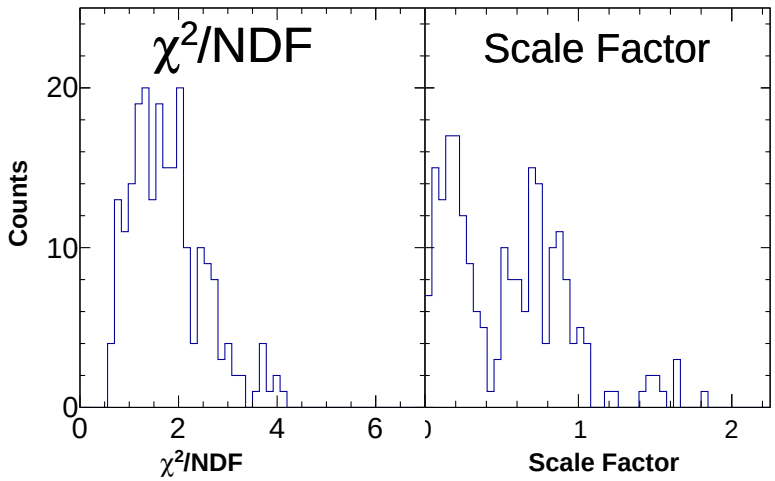

Figure 4.12: The χ^2/NDF and scale factor (A_3 in Eq. 4.23) for all the fits. The χ^2/NDF is used as a check on the goodness of fit, while A_3 provides the scale factor for the $p\pi^+\pi^-\pi^-$ non–resonant background.

after visual inspection, the fitting procedure is working properly.

More specifically, the following procedure was used to fit the $M(p\pi^-)$ distributions:

1. The Λ peak was fit with a Gaussian (G_1) to determine the mean, μ_G, and width σ_G.

2. A double Gaussian (DG_1) was used to fit the Λ peak and tails, with the means of DG_1 fixed to be equal to μ_G.

3. The full distribution was fit with Eq. 4.23. μ is fixed to μ_G, and A_1, A_2, σ_1, and σ_2 are allowed to be within $0.9 \times par < par < 1.1 \times par$, where $par = A_1,\ A_2,\ \sigma_1, \sigma_2$. A_3 was set to 0.5 and allowed to vary between 0 and 5. This range was chosen from studies not discussed in this document.

In step 3, the parameters were chosen to be fixed or allowed to vary in the small range due to having multiple variables in the fit. It was often difficult to visually achieve a "good" fit if the parameters were allowed to be free.

4.4.2 Fitting to M_X and Determining Ratios

The M_X distribution was fit in a similar way to what was done in Section 4.4.1. The full fit function to M_X is given by,

$$S_{M_X}(x) = A_1 \exp \frac{(x-\mu)^2}{\sigma_1^2} + A_2 \exp \frac{(x-\mu)^2}{\sigma_2^2} + A_3 H_{unpol} + A_4 H_{K^0\Sigma^0} + A_5 H_{K^0\Sigma^{\star 0}} + A_6 H_{K^\star(892)\Lambda} \quad (4.24)$$

where $A_{1,2}$ are the heights of the two Gaussians, μ is the mean, $\sigma_{1,2}$ are the widths of the Gaussians, H_{unpol} is the non–resonant, unpolarized background histogram, $H_{K^0\Sigma^0}$ is the $K^0\Sigma^0$ background histogram, $H_{K^0\Sigma^{\star 0}}$ is the $K^0\Sigma^{\star 0}$ background histogram, $H_{K^0(892)\Lambda}$ is the $H_{K^0(892)\Lambda}$ background histogram, and A_3–A_6 are the parameters that scale the background histograms. A_3 is determined from the fits to $M(p\pi^-)$, as previously discussed, and fixed in $S_{M_X}(x)$. The full fitting procedure is as follows:

1. The M_X peak was fit with a Gaussian (G_1) to determine mean, μ_G, and width σ_G.

2. A double Gaussian (DG_1) was used to fit the M_X peak and tails, with the means of DG_1 fixed to be equal to μ_G.

3. The full distribution was fit with Eq. 4.24. μ is fixed to μ_G, and A_1, A_2, σ_1, and σ_2 are allowed to be within $0.8 \times par < par < 1.2 \times par$, where $par = A_1,\ A_2,\ \sigma_1, \sigma_2$. A_3 was fixed using the procedure described in Section 4.4.1. $A_{4,5,6}$ were initially set to a predetermined value based on normalizing each individual background channel to the data in a fixed range of M_X. The initial value for these parameters were then allowed to vary between 0 and 10.

Figure 4.13 shows $S_{M_X}(x)$ fitted to M_X. The colored histograms are scaled using their corresponding fit parameters. This example shows that fitting M_X using this method produces realistic scalings for the background channels. The three black lines

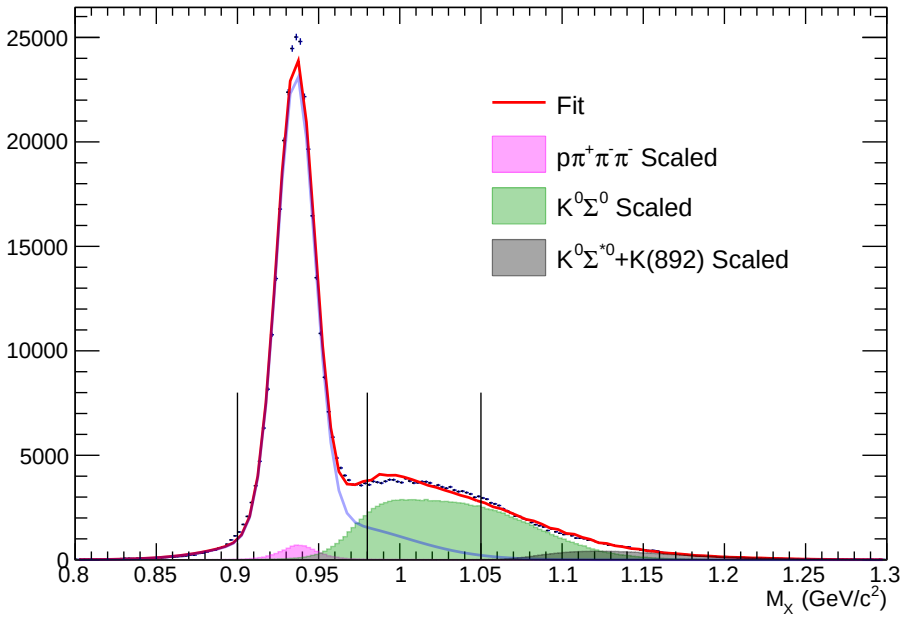

Figure 4.13: Total fit using Equation 4.24 (red line) to the data (blue points) and scaling to M_X integrated over all kinematics. The magenta histogram is the scaled non–resonant background, the green histogram is the scaled $K^0\Sigma^0$ distribution, and the black distribution are the higher mass background channels.

show how Region 1 and 2 are separated. The ratios, r_i^B and r_i^{unpol}, are given by the expressions,

$$r_i^B = \frac{\int_i A_4 H_{K^0\Sigma^0}}{\int_i M_X^{data}} \tag{4.25}$$

$$r_i^{unpol} = \frac{\int_i A_3 H_{unpol}}{\int_i M_X^{data}} \tag{4.26}$$

where i denotes Region 1 or 2.

Figure 4.14 shows fits to M_X for $2.1 < E_\gamma < 2.2$ GeV. The colored histograms are the scaled background distributions and the black lines are drawn to show the separation of the Regions. Overall, the fits in this example look very good in that the background distributions describe what is seen in the data. It should be noted here that the $K^0\Sigma^{\star 0}$ and $K^\star(892)\Lambda$ distributions are included to get a good fit at high M_X. This prevents an over–scaling of $K^0\Sigma^0$. The cut at 1.05 GeV/c^2 removes nearly all

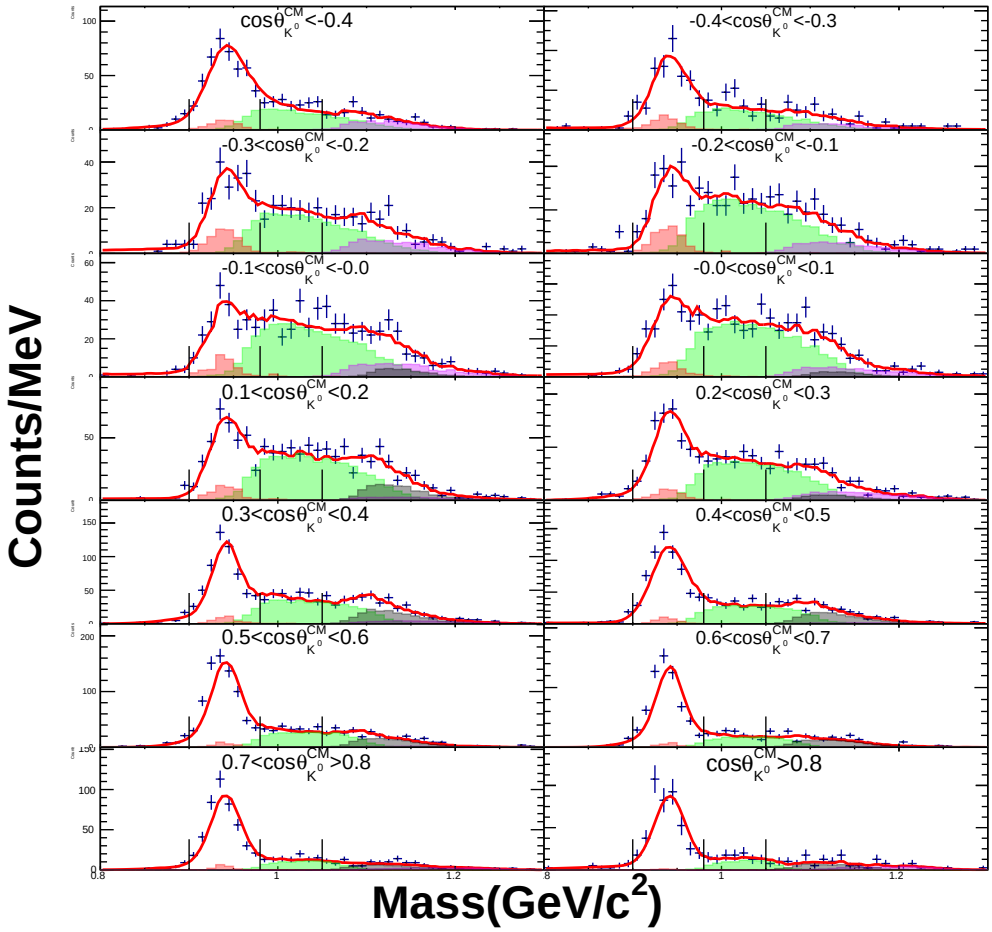

Figure 4.14: Fits and scaling to M_X for $2.1 < E_\gamma < 2.2$ GeV. The red line is the total fit to the data, the red histogram is the scaled $p\pi^-\pi^+\pi^-$ distribution, the green histogram is the scaled $K^0\Sigma^0$ distribution, and the black and violet histograms are the scaled higher mass channels. The black lines are drawn to show the separation of the Regions.

contributions from the higher–mass channels. If any contribution from them remains below the 1.05 GeV/c^2, it is considered negligible as the $K^0\Sigma^0$ channel dominates.

Figure 4.15 shows the χ^2/NDF and scale factor (A_4 in Eq. 4.24) for the Σ^0 background. Similar remarks can be made about these fits based off the discussion in Section 4.4.1 regarding the fits to $p\pi^+\pi^-\pi^-$. The increase in parameters in this fit equation causes the χ^2/NDF, as a whole, to be larger than what was seen in the $M(p\pi^-)$ fits. The scale factor for the $K^0\Sigma^0$ distribution is shown to highlight that

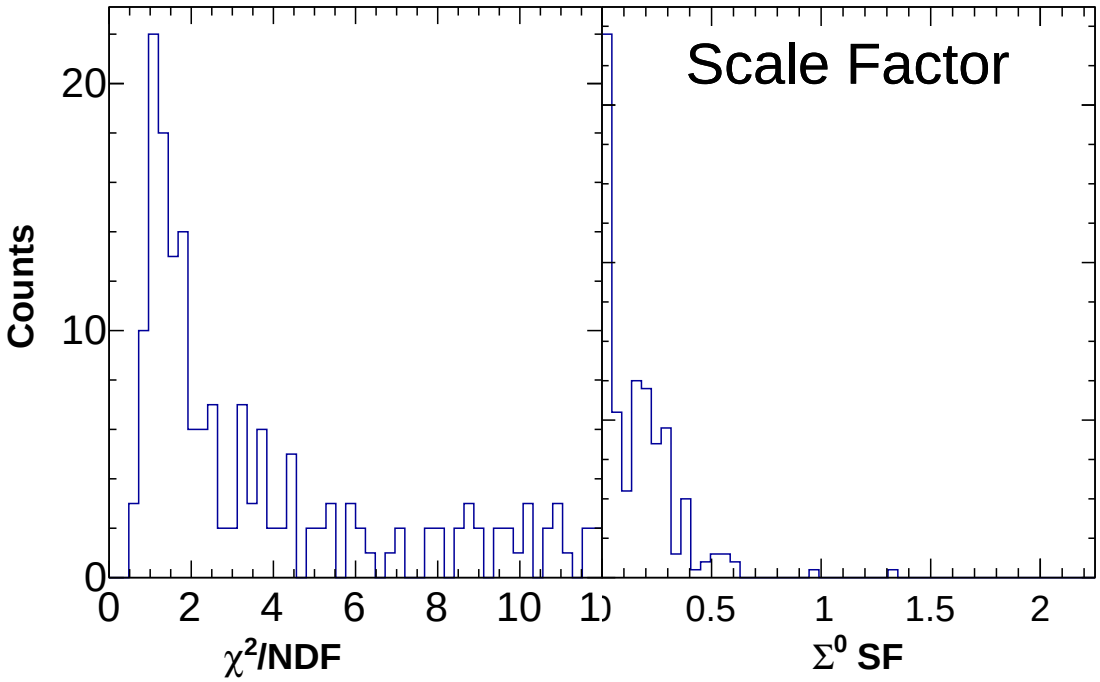

Figure 4.15: The χ^2/NDF and scale factor (A_4 in Eq. 4.24) for all the fits. Generally speaking, the χ^2/NDF from these fits are larger than those seen in the $M(p\pi^-)$ fits. This is likely due to the fact that there are significantly more fit parameters in Equation 4.24 than there are in Equation 4.23. The small value for the scale factor suggests that there is enough statistics in the simulations to accurately scale the background.

almost all values are less than 1. This means that there are sufficient statistics in the simulation to accurately scale the distribution.

Chapter 5

Systematic Studies

There are two types of uncertainties associated with a measurement: statistical uncertainties and systematic uncertainties. Statistical uncertainties originate from the random nature of nuclear reactions that causes the number of particles counted in a given kinematic bin to be a random variable. Since the number of counts has a Poisson distribution, statistical uncertainties are typically determined using the estimator for standard deviation of a Poisson distribution. The value of reported statistical uncertainties, thus, reflects the statistical significance of the experiment. Systematic uncertainties are due to any other sources (than counting statistics) that cause the extracted observable to be a random variable. Typically, such sources are all the quantities, or procedures, used in the extraction of the goal observable(s), that are themselves uncertain. For example, detector acceptance, beam polarization, yield extraction cuts and procedures, or luminosity can be sources of systematic uncertainty. While systematic uncertainties are independent of the number of good events counted in a given kinematic bin, they do depend on the details of the method used to extract an observable. In addition, the reported observable may be a subject of a systematic error, i.e. of an overall bias. Typically, if a bias is discovered, a correction is applied to the value of the observable and the uncertainty of the correction is reported in the systematic uncertainty budget. Here we present the studies we performed to quantify the systematic uncertainties of the polarization transfers and the recoil polarization. We report all systematic uncertainties in a summary table at the end of this chapter.

We classify the systematic uncertainties of the polarization observables into several

types:

- **Instrumental Asymmetries**: Any biases related to the detector itself, known as instrumental asymmetries, are investigated using the reaction $\gamma d \to p\pi^-(n)$. This reaction should not have any helicity asymmetry. Any asymmetry present in the reaction would be due to instrumental effects.

- **Uncertainties of event–selection cuts**: Changing the event selection criteria, such as particle identification or the K^0 and Λ selection, can change the amount of background in the data. For these measurements, two statistically independent samples were created with different selection criteria and the uncertainties were investigated using relative pull distributions.

- **Systematic error of the maximum log-likelihood method**: Systematic uncertainties associated with using the maximum likelihood extraction method were investigated. Potential biases in the observables were studied by creating toy Monte Carlo simulations with generated events.

- **Uncertainty of the background subtraction procedure**: Uncertainties associated with the background subtraction process are calculated.

- **Others**: Here we include the uncertainty of the photon polarization and of the Λ self–analyzing power.

5.1 Instrumental Asymmetry

The helicity asymmetry is defined as the normalized difference between the number of events with positive (N^+) and negative (N^-) helicity:

$$A = \frac{N^+ - N^-}{N^+ + N^-}. \tag{5.1}$$

The helicity asymmetry, when the target is not polarized, of any two–body to two–body reaction, such as $\gamma d \to p\pi^-(p)$ (quasi–free pion production off the neutron),

should be zero. Thus, any observed non–zero helicity asymmetries in this reaction would be due to instrumental effects relating to the photon beam or detector. We refer to such asymmetries as instrumental asymmetries. For example, if the photon beam had significantly more events with + helicity than with − helicity, A would be non–zero. The instrumental asymmetry could also be due to the detector acceptance. Any significant instrumental asymmetry needs to be corrected for and the uncertainty of the instrumental asymmetry needs to be counted for in the systematic–uncertainty budget of the extracted polarization observables.

To estimate the size of the instrumental asymmetry, a pull distribution, which is $\frac{A}{\sigma_A}$, was created and fit with a Gaussian. σ_A is the statistical uncertainty of A and was calculated using standard uncertainty propagation for two uncorrelated random variables, N^+ and N^-:

$$\sigma_A = \frac{2}{(N^+ - N^-)^2} \frac{1}{\sqrt{N^+ N^- (N^+ + N^-)}}. \tag{5.2}$$

The pull distribution is used to test if the fluctuations of A can be accounted for by its statistical uncertainty and if there are biases and/or extra sources of uncertainty in the data sample. If the mean of the Gaussian fit to the pull distribution, μ, is consistent with 0, then A is consistent with zero. When the peak is not centered at zero, then there is some significant instrumental asymmetry. If the standard deviation of the Gaussian fit, σ, is consistent with 1, then any other sources of uncertainty are consistent with zero or are small when compared to σ_A. When the standard deviation of the pull distribution is less than 1, this suggests that the statistical uncertainty, σ_A, of A may be overestimated. When the standard deviation is larger than 1, this suggests that there may be systematic uncertainties associated with A. If either of these three are present in the data set, then the bias and/or systematic uncertainty would need to be quantified and applied to the data. The bias will be used as an estimate of the instrumental asymmetry and applied as a correction to the reported

observables, while the uncertainty of the instrumental asymmetry would be included in the systematic uncertainty budget of the reported polarization observables.

We have analyzed the reaction $\gamma d \rightarrow p\pi^-(p)$ and have extracted the helicity asymmetry as a function of several variables, such as run number, photon energy, scattering angles, etc. in order to probe for temporal or local sources of instrumental asymmetry. The top half of Fig. 5.1 shows A as a function of run number for quasi–free events ($p_X < 0.2$ GeV/c) integrated over all kinematic variables. The bottom

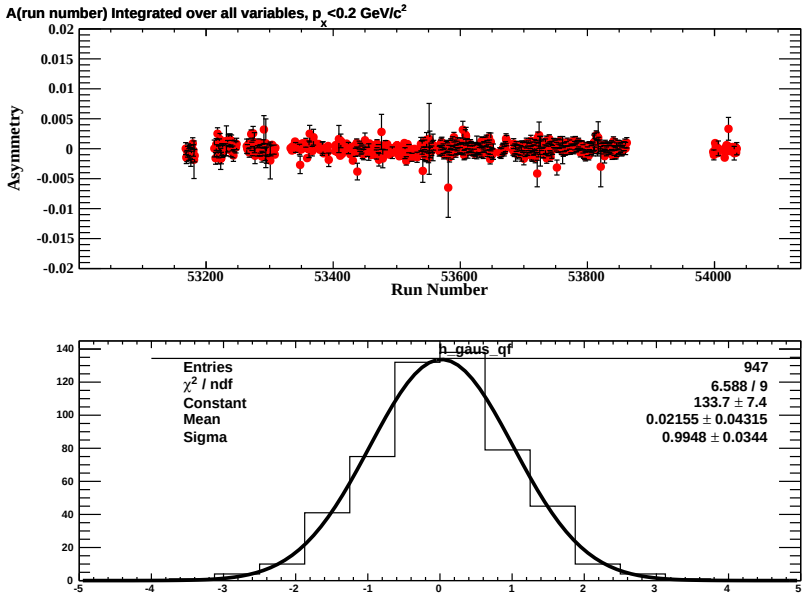

Figure 5.1: (Top) The instrumental asymmetry as a function of run number for $p_X < 0.2$ GeV/c integrated over all kinematic variables. (Bottom) The pull distribution fit with a Gaussian. The results suggest that there is no time–dependent instrumental asymmetry in the g13a data set.

half of Fig. 5.1 shows the corresponding pull distribution. The pull distribution was fit with a Gaussian, which has a μ of 0.022 ± 0.043 and a σ of 0.995 ± 0.034. As μ and σ are consistent with 0 and 1, respectively, we conclude that there is no evidence for a time–dependent instrumental asymmetry. If there is, it is smaller than 4×10^{-2}.

Since the above analysis does not account for kinematics, more in depth studies of the instrumental asymmetry were performed. These studies assessed if there was an instrumental asymmetry as a function of kinematic variables such as the angle of

the π^- in the center–of–mass frame ($\cos\theta^*_{\pi^-}$), the momentum of the spectator proton (p_X), or the azimuthal angle of the proton, ϕ. These studies were carried out in a similar manner as described above. A was calculated for each run number for different kinematic bins. Then the pull distributions were fit with a Gaussian to investigate any potential instrumental asymmetries.

Table 5.25 shows the pull distribution parameters for seven different $\cos\theta^*_{\pi^-}$ bins (integrated over all run numbers). For these seven cosine bins, the means and standard deviations are consistent with 0 and 1, respectively, within 1–2 standard deviations. Thus, it can be concluded that there is no evidence that there is an instrumental asymmetry within specific $\cos\theta^*_{\pi^-}$ ranges.

Table 5.1: Pull distribution parameters (μ, σ) for different $\cos\theta^*_{\pi^-}$ bins. The means and widths do not significantly differ from 0 and 1, respectively. This means no instrumental asymmetry within specific $\cos\theta^*_{\pi^-}$ ranges is present in the data.

Bin	μ	σ
$\cos\theta^*_{\pi^-} < -0.3$	0.101 ± 0.047	1.049 ± 0.034
$-0.3 < \cos\theta^*_{\pi^-} < -0.1$	-0.042 ± 0.048	1.058 ± 0.037
$-0.1 < \cos\theta^*_{\pi^-} < 0.1$	0.022 ± 0.047	1.052 ± 0.039
$0.1 < \cos\theta^*_{\pi^-} < 0.3$	-0.018 ± 0.043	0.969 ± 0.035
$0.3 < \cos\theta^*_{\pi^-} < 0.5$	0.024 ± 0.042	0.9534 ± 0.030
$0.5 < \cos\theta^*_{\pi^-} < 0.7$	-0.017 ± 0.045	1.004 ± 0.034
$\cos\theta^*_{\pi^-} > 0.7$	0.065 ± 0.045	1.023 ± 0.032

Table 5.2 lists the pull distribution parameters for different ϕ bins, where ϕ is the azimuthal angle of the proton in CLAS. The ϕ bins were chosen to match the six sectors of the CLAS detector. Based off the means and widths of the pull distributions, we conclude there is no instrumental asymmetry within specific ϕ regions.

Table 5.3 lists the pull distribution parameters for different p_X bins. At low p_X, there is almost no contribution from events other than $p\pi^-(p)$. As p_X increases, there is some background from multi–pion production. At $p_X > 0.2$ GeV/c, final–state interaction (FSI) events in the reaction $\gamma d \to pp\pi^-$ dominate over the quasi–free

Table 5.2: Pull distribution parameters (μ, σ) for different ϕ bins. The means and widths do not significantly differ from 0 and 1, respectively. This means no instrumental asymmetry within specific ϕ ranges is present in the data.

Bin	μ	σ
$-30^\circ < \phi < 30^\circ$	0.088 ± 0.044	1.003 ± 0.033
$30^\circ < \phi < 90^\circ$	0.054 ± 0.042	0.960 ± 0.030
$90^\circ < \phi < 150^\circ$	-0.054 ± 0.045	1.039 ± 0.032
$150^\circ < \phi > -150^\circ$	-0.017 ± 0.043	0.9818 ± 0.026
$-150\circ < \phi < -90^\circ$	-0.001 ± 0.044	1.002 ± 0.032
$-90\circ < \phi < -30^\circ$	-0.041 ± 0.045	1.034 ± 0.032

Table 5.3: Pull Distribution parameters for p_X bins. The means and widths do not significantly differ from 0 and 1, respectively. This means no significant instrumental asymmetries are present within specific p_X ranges.

Bin	μ	σ
$0.00 < p_X < 0.05$	0.031 ± 0.044	0.995 ± 0.031
$0.05 < p_X < 0.10$	0.034 ± 0.043	0.976 ± 0.034
$0.10 < p_X < 0.15$	-0.059 ± 0.041	0.942 ± 0.032
$0.15 < p_X < 0.20$	0.006 ± 0.046	1.053 ± 0.033
$p_X > 0.20$	-0.006 ± 0.046	1.008 ± 0.039

$\gamma(n) \to p\pi^-$ events. At these p_X the helicity asymmetry is not expected to be zero due to FSI. However, our analysis yields an average value consistent with zero. This is likely due to integration over all kinematic variables. As in previous studies, no significant instrumental asymmetries are present within specific p_X ranges.

Of particular interest is to determine the asymmetry in areas where the acceptance of CLAS is low or is rapidly changing. Therefore, the asymmetry and pull distributions are obtained as a function of ϕ around and between the sectors in CLAS. The top row of Fig. 5.2 shows the helicity asymmetry as a function of ϕ for the π^- (left) and proton (right) integrated over all run numbers and kinematics. Here, one can clearly see the areas near the sector edges where the number of events is small and the asymmetries exhibit large fluctuations and large statistical uncertainties. The

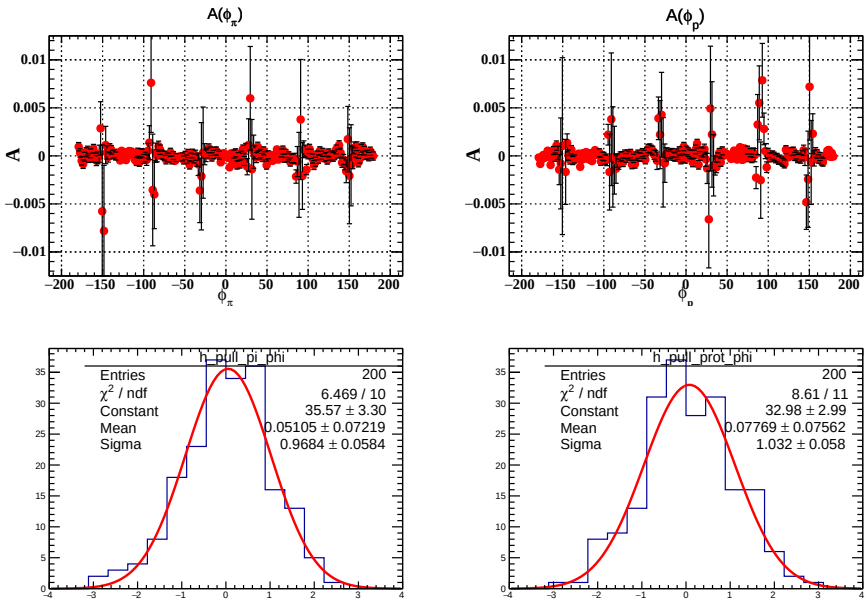

Figure 5.2: A as a function of ϕ (top row) for the pion (left) and proton (right) with their corresponding pull distributions (bottom row). The fits to the pull distributions show no significant biases or unaccounted for uncertainties in the data.

bottom row of Fig. 5.2 shows the corresponding pull distributions and fit parameters. As in the previous studies, no significant deviations from 0 and 1 are observed. Further studies were done by zooming in on the sector edges and calculating the asymmetry and pull distributions in those areas only. Again, no evidence for instrumental uncertainty was found within the statistical uncertainties. Similar studies of A as a function of E_γ were performed and all showed that the mean and width of the pull distributions were consistent with 0 and 1, respectively. Therefore, it can be concluded that there is no evidence for instrumental asymmetries in the data within the statistical uncertainties of the $\gamma d \to p\pi^-(p)$ data. Or, if there are any, they are smaller than the statistical uncertainties in the study.

The statistical uncertainty, 0.043, of the overall instrumental asymmetry (see Fig. 5.1 is added to the systematic-uncertainty budgets of C_x, C_y, and C_z.

5.2 Event–Selection Cuts

5.2.1 Particle Identification Cuts

Particle identification (PID) cuts are determined such that mostly events in the peak of the $\Delta\beta$ distribution are selected. As there is no one strict criterion for the exact width of the cut, the choice of the lower and upper limits of the cut can vary. Wider PID cuts may allow more misidentified particles into the data set. Effectively, changing the PID cuts leads to a different signal to background ratio in the data sample.

The systematic uncertainty due to the PID cuts is studied by creating two statistically independent data sets and evaluating the difference between the observables obtained from each set. The data sets were created by varying the standard 3σ PID cuts discussed in Section 3.1. One data set contains events within -3σ – -0.7σ and 0.7σ – 3σ, called region 1. The second data set contains events within -0.7σ – 0.7σ, called region 2. Each data set has approximately the same number of events. To estimate the systematic uncertainty due to the selection cuts, the relative pull distribution, $RPull$, for each observable was obtained using

$$RPull = \frac{Obs_2 - Obs_1}{\sqrt{\sigma_1^2 + \sigma_2^2}}, \tag{5.3}$$

where $Obs_{1,2}$ is the value of the observable in region 1 or 2 and $\sigma_{1,2}$ is its statistical uncertainty. Like the regular pull distributions, biases or uncertainties are seen if the mean significantly deviates from 0 or the width from 1. If the mean and the width are consistent with 0 and 1, respectively, then any difference seen in the data set is consistent with the statistical uncertainties and no systematic uncertainties and errors are present. In addition to using fit parameters of the Gaussian fits, the mean, μ, standard deviation, σ, and uncertainty of the mean, σ_μ, are calculated for $RPull$

using

$$\mu = \frac{1}{N}\sum_{i=1}^{N} RPull^i,\ \sigma = \sqrt{\frac{1}{N-1}\sum_{i=1}^{N}(RPull^i - \mu)^2},\ \sigma_\mu = \frac{\sigma}{\sqrt{N}}, \tag{5.4}$$

where N is the number of kinematic bins.

Proton Identification

Figure 5.3 shows the relative pull distributions of C_x, C_z, and P for the proton identification with Gaussian fits to the distribution. Table 5.4 lists the means ($\mu \pm \sigma_\mu$),

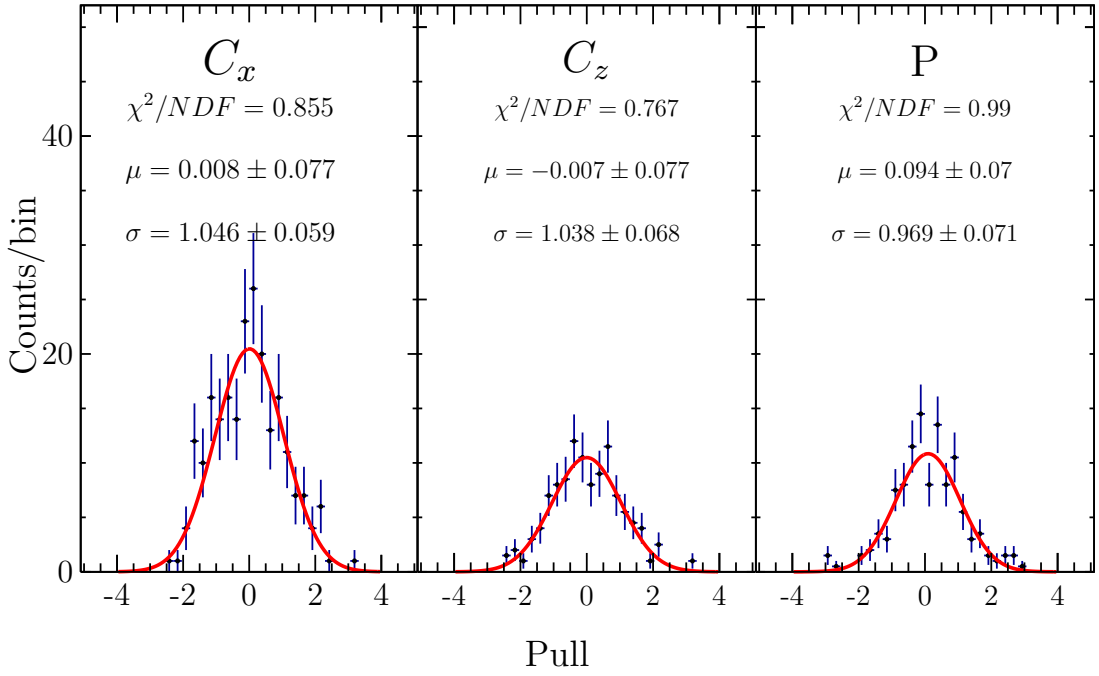

Figure 5.3: Relative pull distributions for C_x (left), C_z (middle), and P (right) from the proton selection. From the parameters, no significant systematic uncertainties are seen in C_x, C_z, or P.

widths (width$\pm\sigma_{width}$), and how much the means ($N\sigma_\mu$) and widths ($N\sigma_{width}$) deviate from 0 and 1, respectively. Table 5.5 lists the calculated means, width, and how far the mean is from 0. From both tables, the means and widths are consistent with 0 and 1, respectively. Therefore, it can be concluded that any difference between the observables is due to their statistical uncertainties.

Table 5.4: Relative pull–distribution fit parameters for the different proton selection cuts. The means and widths of C_x, C_z, and P are consistent with 0 and 1, respectively.

Obs.	$\mu \pm \sigma_\mu$	$N\sigma_\mu$	width$\pm\sigma_{width}$	$N\sigma_{width}$
C_x	0.008±0.077	0.097	1.046±0.059	0.772
C_z	−0.007±0.077	0.098	1.038±0.068	0.559
P	0.094±0.07	1.335	0.969±0.071	0.435

Table 5.5: Relative pull–distribution calculated parameters for the proton selection. The means are all consistent with 0. The widths do not significantly differ from 1.

Obs.	$\mu \pm \sigma_\mu$	$N\sigma_\mu$	width
C_x	−0.006±0.07	0.088	1.047
C_z	0.006±0.071	0.09	1.051
P	0.113±0.069	1.642	1.022

π^+ Identification

Figure 5.4 shows the relative pull distributions for the π^+ identification. Table 5.6

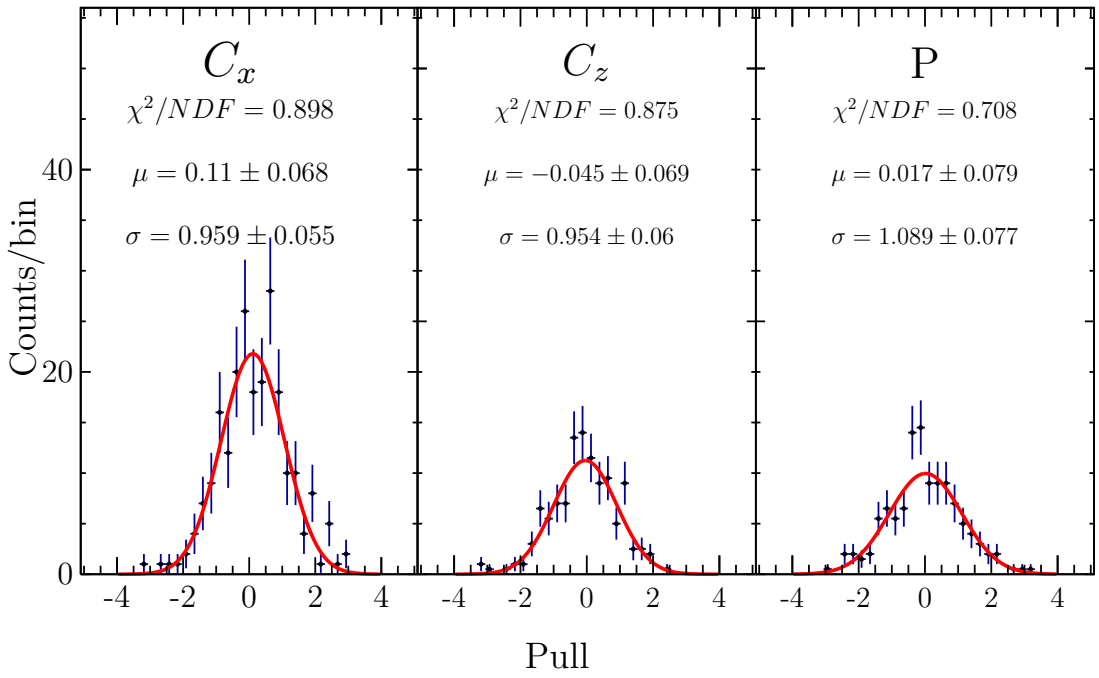

Figure 5.4: Relative pull distributions for C_x (left), C_z (middle), and P (right) from the π^+ selection. From the parameters, no significant systematic uncertainties are seen in C_x, C_z, or P.

lists the means, widths, and how much the means and widths deviate from 0 and 1, respectively. Table 5.7 lists the calculated means, widths, and how much the means

Table 5.6: Relative pull–distribution fit parameters for the π^+ selection. The means and widths of C_x, C_z, and P do not significantly differ from 0 and 1, respectively.

Obs.	$\mu \pm \sigma_\mu$	$N\sigma_\mu$	width$\pm\sigma_{width}$	$N\sigma_{width}$
C_x	0.11±0.068	1.62	0.959±0.055	0.747
C_z	−0.045±0.069	0.649	0.954±0.06	0.769
P	0.017±0.079	0.214	1.089±0.077	1.159

($N\sigma_\mu$) deviate from 0. From both tables, there is no significant systematic uncertainty

Table 5.7: Relative pull–distribution calculated parameters for the π^+ selection. The means of C_x, C_z, and P do not significantly differ from 0 and the widths are close to 1.

Obs.	$\mu \pm \sigma_\mu$	$N\sigma_\mu$	width
C_x	0.178±0.07	2.558	1.042
C_z	−0.085±0.065	1.304	0.976
P	−0.016±0.071	0.221	1.065

observed when varying this selection cut.

π^- Identification

Figure 5.5 shows the relative pull distributions for the π^- identification. Table 5.8 lists the means, widths, and how much the means and the widths deviate from 0 and 1, respectively. Here, the means of the pull distributions are all within 3σ of 0. While

Table 5.8: Relative pull–distribution fit parameters for the π^- selection. The means and the widths of C_x, C_z, and P pulls do not significantly differ from 0 and 1, respectively.

Obs.	$\mu \pm \sigma_\mu$	$N\sigma_\mu$	width$\pm\sigma_{width}$	$N\sigma_{width}$
C_x	−0.096±0.077	1.245	1.048±0.061	0.783
C_z	0.152±0.067	2.282	0.912±0.056	1.566
P	−0.182±0.074	2.461	1.024±0.076	0.319

this is larger than what was seen for the p and π^+ identification cuts, it may not be

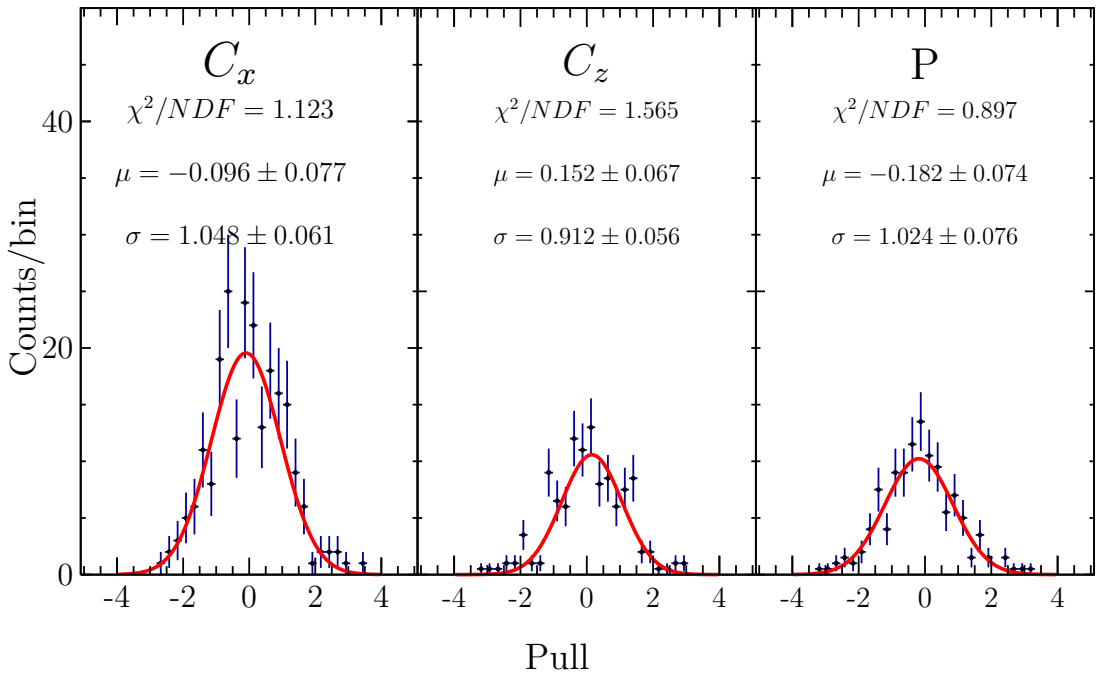

Figure 5.5: Relative pull distributions for C_x (left), C_z (middle), and P (right) from the π^- selection. From the parameters, no significant biases or systematic uncertainties are seen in C_x, C_z, or P.

significant and the difference is attributed to statistics. Table 5.9 lists the calculated means, widths, and how far the mean is from 0. The pull means of C_x and C_z are

Table 5.9: Relative pull distributions for C_x (left), C_z (middle), and P (right) from the π^- selection. The means do not significantly differ from 0 and the widths are close to 1.

Obs.	$\mu \pm \sigma_\mu$	$N\sigma_\mu$	width
C_x	-0.009 ± 0.073	0.129	1.084
C_z	0.058 ± 0.073	0.794	1.086
P	-0.155 ± 0.073	2.115	1.094

within 1σ away from 0, while the pull mean of P is 2.115σ away from 0. We conclude that any difference between the observables when varying the π^- selection is due to statistical uncertainties.

5.2.2 $M(p\pi^-)$ Selection

Changing the selection cut on $M(p\pi^-)$ changes the amount of unpolarized background in the data. Similar studies to those done in Section 5.2.1 were performed to study the systematic uncertainty due to this selection cut. Two (roughly) equal and statistically uncorrelated regions in $M(p\pi^-)$ were defined to investigate the systematic effects of the selection cut described in Chapter 3. Figure 5.6 shows the $M(p\pi^-)$ distribution with four lines that correspond to $\pm 4\sigma$ (black) and $\pm 0.7\sigma$ (red), where σ is determined from the fit in Fig. 3.13. Region 1 is between the two red lines, which corresponds to

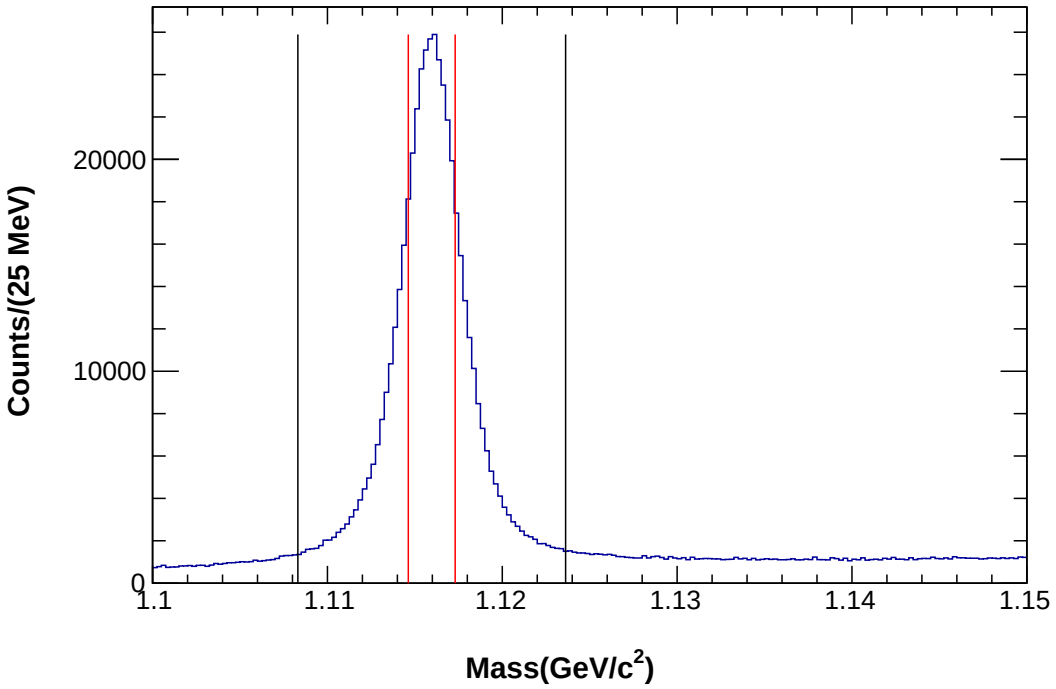

Figure 5.6: $M(p\pi^-)$ distribution with lines representing $\pm 4\sigma$ (black) and $\pm 0.7\sigma$ (red), where σ is determined from the fit in Fig. 3.13. To investigate the systematic uncertainties, a relative pull distribution between each region was fit with a Gaussian.

-0.7σ – 0.7σ. Region 2 is the combination of -4σ – -0.7σ and 0.7σ – 4σ. These two regions contain approximately the same number of events. For the event sample in each region, the background subtraction and observable extraction were performed.

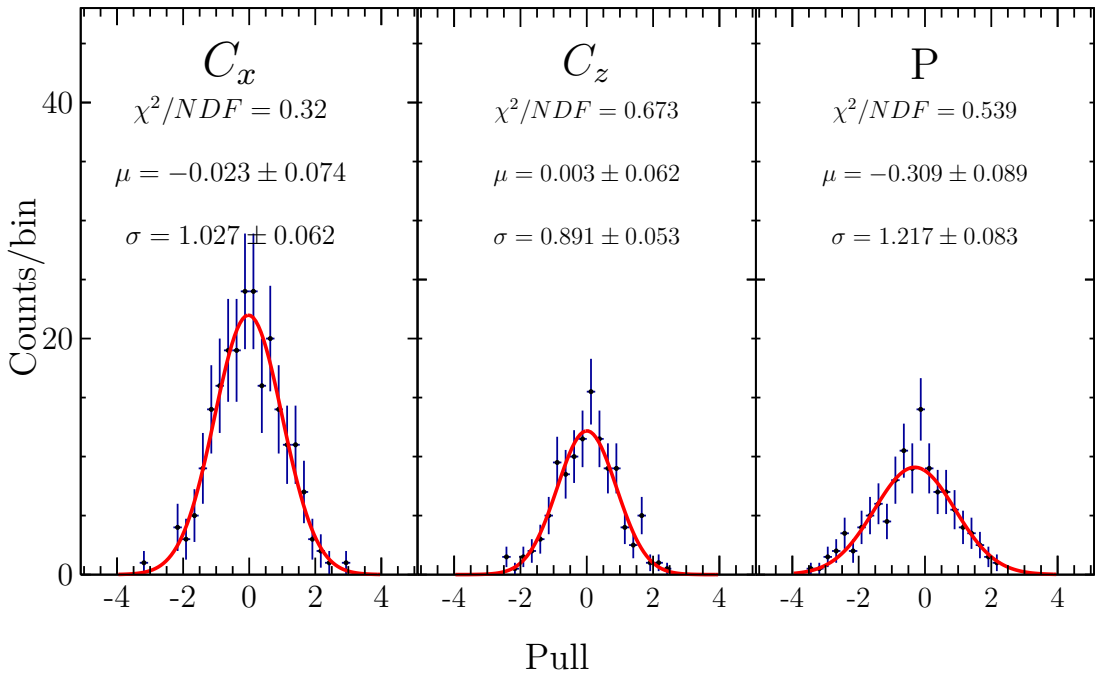

Figure 5.7: Relative pull distributions for the two different regions in $M(p\pi^-)$. From the parameters, no significant biases are seen for C_x or C_z. The mean for P is more than 3σ from 0, which suggests there may be some systematic uncertainty caused by the $M(p\pi^-)$ selection.

Biases in the selection cuts were investigated using the relative pull distributions (Equations 5.3 and 5.4).

Figure 5.7 shows the relative pull distributions of C_x, C_z and P for the $M(p\pi^-)$ selection cut. Table 5.10 lists the mean and width of the Gaussian fits to the relative pull distributions. The columns $N\sigma_\mu$ and $N\sigma_{width}$ list how many standard deviations

Table 5.10: Relative pull-distribution fit parameters for the different $M(p\pi^-)$ regions. The means and widths of C_x and C_z are consistent with 0 and 1. The mean of P is more than 3 standard deviations from 0.

Obs.	$\mu \pm \sigma_\mu$	$N\sigma_\mu$	width$\pm\sigma_{width}$	$N\sigma_{width}$
C_x	-0.023 ± 0.074	0.311	1.027 ± 0.062	0.435
C_z	0.003 ± 0.062	0.048	0.891 ± 0.053	2.057
P	-0.309 ± 0.089	3.472	1.217 ± 0.083	2.614

the mean and the width are from 0 and 1, respectively. From this table, it is clear no

significant differences appear when changing the $M(p\pi^-)$ cut for C_x and C_z. However, the mean of P is more than three standard deviations from 0, which suggests that the $M(p\pi^-)$ cut may introduce a systematic uncertainty for our estimate of P. Table 5.11 lists the calculated means and widths of the relative pull distributions. We see similar results to those from the fits, with the mean of P being further away from 0. The calculated widths of the pull distributions are all close to 1. However, having no estimate of the uncertainty of the width makes it difficult to interpret what the number means. Therefore, using the widths from the fits, it can be concluded that the observed variations of $Obs_1 - Obs_2$ can be accounted for by the statistical uncertainties.

Table 5.11: Relative pull-distribution calculated parameters for the $M(p\pi^-)$ cut. The means of C_x and C_z are consistent with 0. The mean of P is significantly different than 0.

Obs.	$\mu \pm \sigma_\mu$	$N\sigma_\mu$	width
C_x	0.009±0.068	0.132	1.014
C_z	0.017±0.066	0.258	0.981
P	−0.376±0.077	4.884	1.151

To further study the size of the observed bias in P, the difference, $\Delta Obs = Obs_1 - Obs_2$, of the observables was calculated. Figure 5.8 shows the difference of C_x (left), C_z (middle), and P (right) between the two regions. The differences were fit with a Gaussian to show that they have a Gaussian shape. The means of ΔC_x and ΔC_z are consistent with 0, but not the mean of ΔP. Table 5.12 lists the weighted mean, μ_W and its uncertainty, σ_{μ_W}, of ΔObs when calculated with

$$\mu_W = \frac{\sum_{i=1}^{N} w_i \Delta Obs}{\sum_{i=1}^{N} w_i}, \ \sigma_{\mu_W} = \sqrt{\frac{1}{\sum_{i=1}^{N} w_i}}, \tag{5.5}$$

where N is the number of kinematic bins and $w_i = \frac{1}{\sigma_2^2 + \sigma_1^2}$ is the weight as calculated from the statistical uncertainties in region 1 or 2. This method confirms that ΔC_x and ΔC_z are consistent with 0, whereas ΔP may be be inconsistent with zero.

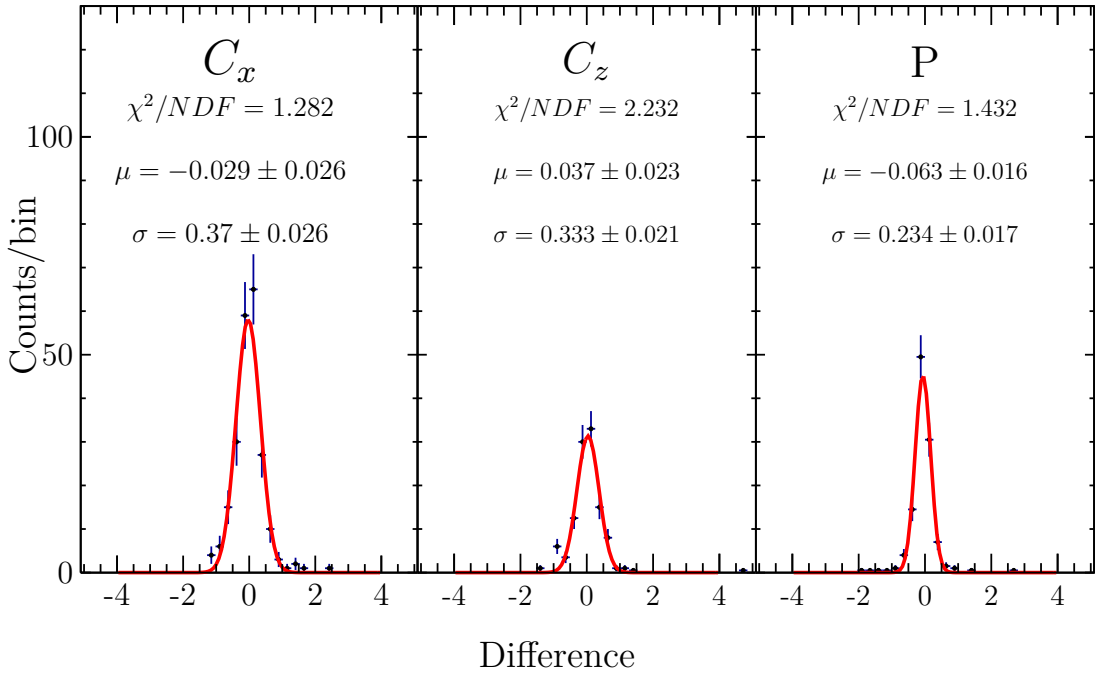

Figure 5.8: Differences between the observables for the two different regions in $M(p\pi^-)$. When fit with a Gaussian, the means of C_x and C_z are consistent with 0. The mean of P is significantly different than 0.

Table 5.12: Calculated weighted mean of the difference ΔObs for the $M(p\pi^-)$ cut.

Obs.	$\mu \pm \sigma_\mu$
C_x	0.009±0.019
C_z	0.005±0.02
P	−0.053±0.015

In an alternative study of the systematic uncertainty due to the $M(p\pi^-)$ selection cut, we use the expression

$$\Delta Obs^2 = (Obs_2 - Obs_1)^2 = \sigma_{stat}^2 + \sigma_{sys}^2, \tag{5.6}$$

where σ_{stat} is the statistical uncertainty and σ_{sys} is the systematic uncertainty of ΔObs. Solving for σ_{sys} in Equation 5.6 yields

$$\sigma_{sys}^2 = \Delta Obs^2 - \sigma_{stat}^2. \tag{5.7}$$

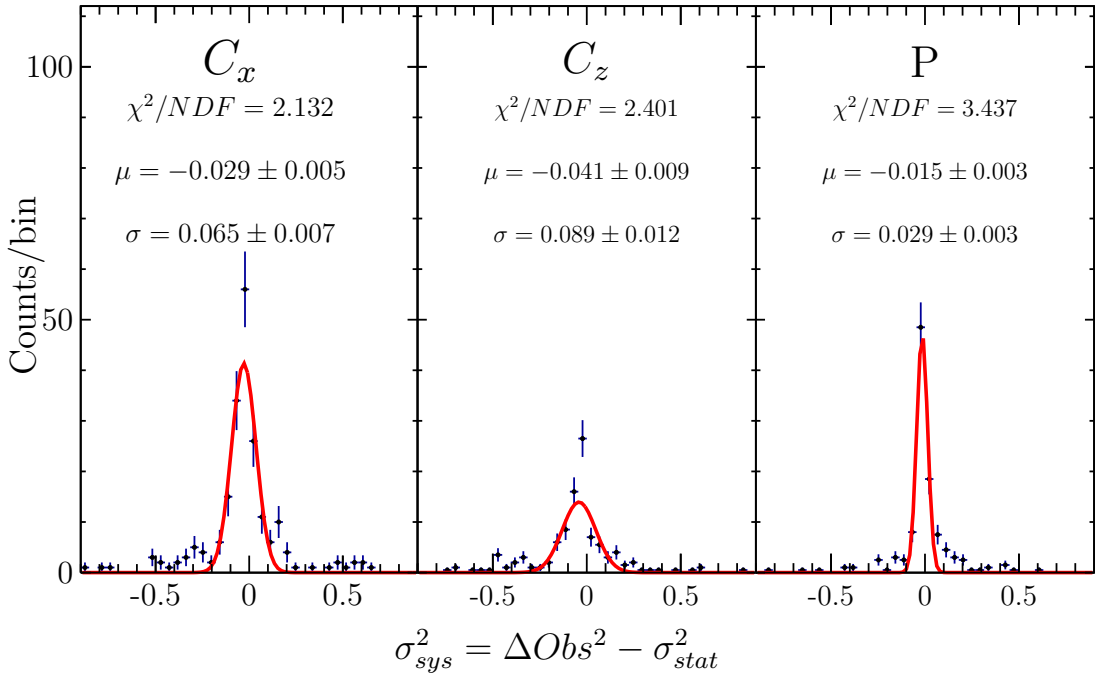

Figure 5.9: Distributions of σ^2_{sys} for the observables. The parameters of the fit suggest there are no significant systematic uncertainties.

A negative σ^2_{sys} means that $\sigma_{stat} > \Delta Obs$, whereas a positive σ^2_{sys} means there may be some systematic uncertainty.

Figure 5.9 shows the distributions of σ^2_{sys} fit with a Gaussian for C_x (left), C_z (middle), and P (right). The parameters of the fit suggest there are no systematic uncertainties associated with the $M(p\pi^-)$ selection as the mean of σ^2_{sys} for each observable is negative. However, these Gaussian fits have large χ^2/NDF and through visual inspection, it is clear these distributions deviate from Gaussians. To account for the long tails, the mean of each distribution is also calculated by hand. Table 5.13 shows the calculated mean of the σ^2_{sys} for the $M(p\pi^-)$ cut. The negative value of σ^2_{sys} for all observables suggests that the statistical uncertainty is larger than the difference in the observable. Any systematic uncertainty associated with the $M(p\pi^-)$ selection is smaller than the statistical uncertainty.

Table 5.13: Calculated mean of the σ^2_{sys} for the $M(p\pi^-)$ cut.

Obs.	$\mu \pm \sigma_\mu$
C_x	-0.071 ± 0.002
C_z	-0.088 ± 0.001
P	-0.003 ± 0.001

In the systematic-uncertainty budgets of the observables, for the contribution due to the $M(p\pi^-)$ selection we include a value of 0.053 for P, as estimated from the weighted mean of the ΔP distribution, and 0 for C_x and C_z.

5.2.3 $M(\pi^+\pi^-)$ Selection

Like the selection cut on $M(p\pi^-)$, the selection cut for $M(\pi^+\pi^-)$ can also create systematic uncertainties of the results. A similar study to what was done for the $M(p\pi^-)$ selection was performed for the $M(\pi^+\pi^-)$ selection. Figure 5.10 shows the $M(\pi^+\pi^-)$ distribution with four lines that correspond to $\pm 4\sigma$ (black) and $\pm 0.7\sigma$ (red), where σ is determined from the fit in Fig. 3.12. Region 1 is between the two red lines, which corresponds to -0.7σ – 0.7σ. Region 2 is the combination of -4σ – -0.7σ and 0.7σ – 4σ. These two regions contain approximately the same number of events.

For each region, the background subtraction and observable extraction were performed. Potential systematic uncertainties were investigated following the procedure in Section 5.2.2. Figure 5.11 shows the relative pull distribution for the $M(\pi^+\pi^-)$ selection cut. Table 5.14 lists the means and the widths of the Gaussian fits to the relative pull distributions. The columns $N\sigma_\mu$ and $N\sigma_{width}$ list how many standard deviations the means and the widths are from 0 and 1, respectively. From this table, it is clear that there are no significant systematic differences in the estimates of the observables when changing the $M(\pi^+\pi^-)$ cut, as the means and the widths are not significantly different from 0 and 1, respectively. Table 5.15 shows the calculated mean and width of the pull distribution. Like in the case of the fit parameters, no

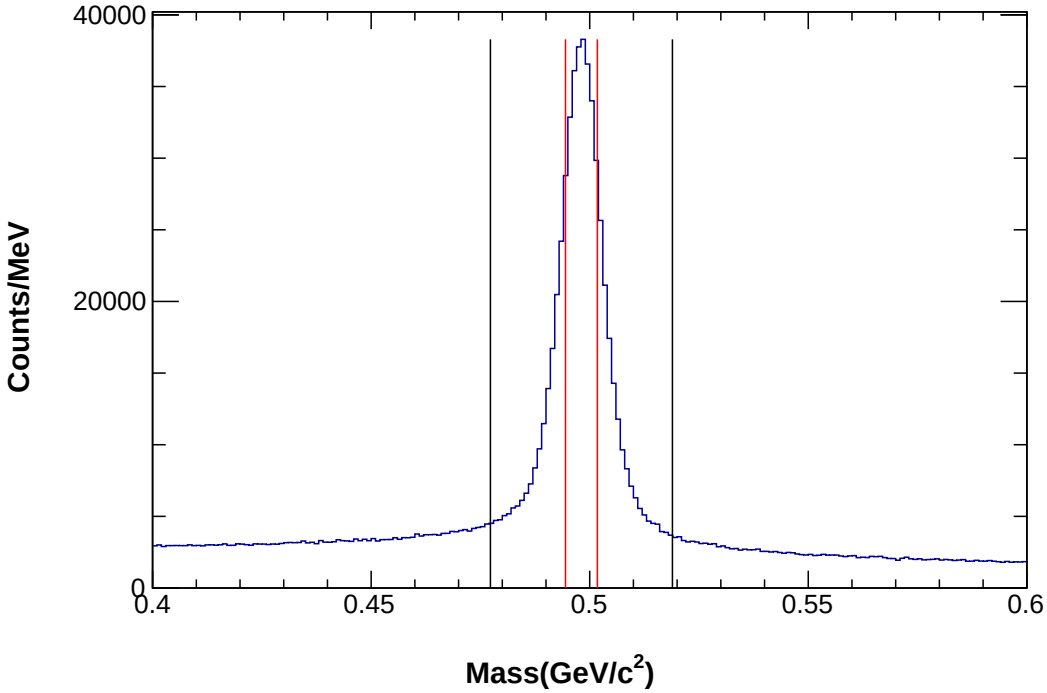

Figure 5.10: $M(\pi^+\pi^-)$ distribution with lines representing $\pm 4\sigma$ (black) and $\pm 0.7\sigma$ (red), where σ is determined from the fit shown in Fig. 3.12. The systematic uncertainty related to the $M(\pi^+\pi^-)$ selection is studied through relative pull distributions and differences in observables between the two regions.

Table 5.14: The mean ($\mu \pm \sigma_\mu$), number of standard deviations of the mean from 0 ($N\sigma_\mu$), width (width$\pm\sigma_{width}$), and number of standard deviations of the width from 1 ($N\sigma_{width}$) of the relative pull distribution fit parameters for the $M(\pi^+\pi^-)$ cut. From the fits, the mean and width do not significantly deviate from 0 and 1, respectively.

Obs.	$\mu \pm \sigma_\mu$	$N\sigma_\mu$	width$\pm\sigma_{width}$	$N\sigma_{width}$
C_x	-0.033 ± 0.075	0.439	0.916 ± 0.062	1.363
C_z	-0.04 ± 0.074	0.542	0.993 ± 0.069	0.108
P	-0.06 ± 0.075	0.801	0.998 ± 0.068	0.035

Table 5.15: Relative pull distribution calculated parameters for the $M(\pi^+\pi^-)$ cut. The means are all consistent with 0. The widths are all close to 1.

Obs.	$\mu \pm \sigma_\mu$	$N\sigma_\mu$	width
C_x	-0.129 ± 0.066	1.948	0.989
C_z	-0.035 ± 0.069	0.506	1.035
P	0.03 ± 0.064	0.464	0.96

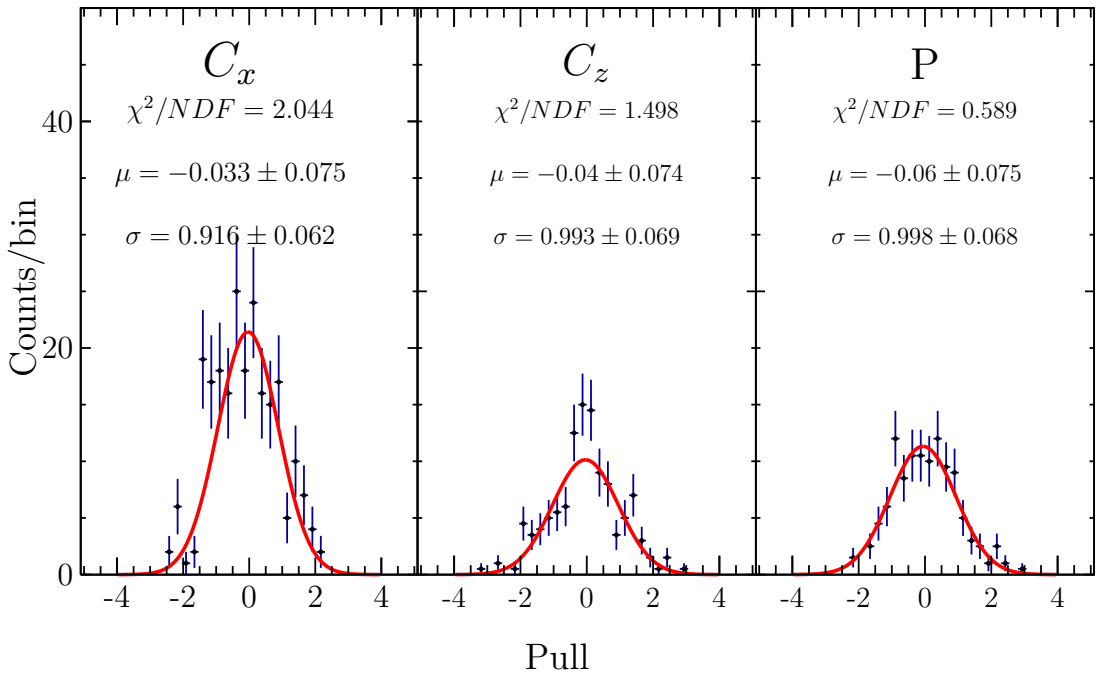

Figure 5.11: Relative pull distributions for C_x (left), C_z (middle), and P (right) from the $M(\pi^+\pi^-)$ selection. From the fit parameters, no significant biases are seen.

significant systematic differences are seen in the calculated means. Therefore, we assign no systematic uncertainties associated with the $M(\pi^+\pi^-)$ selection to C_x, C_z, and P.

5.2.4 Fiducial Cut

This section discusses the studies done to understand the systematic uncertainties and potential biases associated with the fiducial cuts. Fiducial cuts remove events containing particles detected in detector regions with rapidly changing acceptance, such as sector edges. The magnetic field is rapidly changing and the efficiency of the drift chambers decreases in these areas. Although we extract C_x, C_z, and P without the application of fiducial cuts, allowing events from areas with poor or rapidly changing acceptance may affect our estimates. This effect is assessed here.

The fiducial cuts used for each final–state particle of interest are defined in [18]. We form two different event samples: a "good" sample (when all particles pass the fiducial cuts), and a "bad" sample (when at least one particle fails its fiducial cut). The two samples are mutually exclusive, and the combination of both yields the event sample used to extract the nominal estimates of the observables. The events labeled as "bad" total $\approx 40\%$ of events after the selection cuts discussed in Chapter 3. These events may have a systematic effect on the observables if they produce systematically different values of the observables.

Figure 5.12 shows the ϕ vs. θ distribution for a π^- without (left) and with (right) fiducial cuts applied. Figure 5.13 shows the ϕ vs. θ distributions for the events when

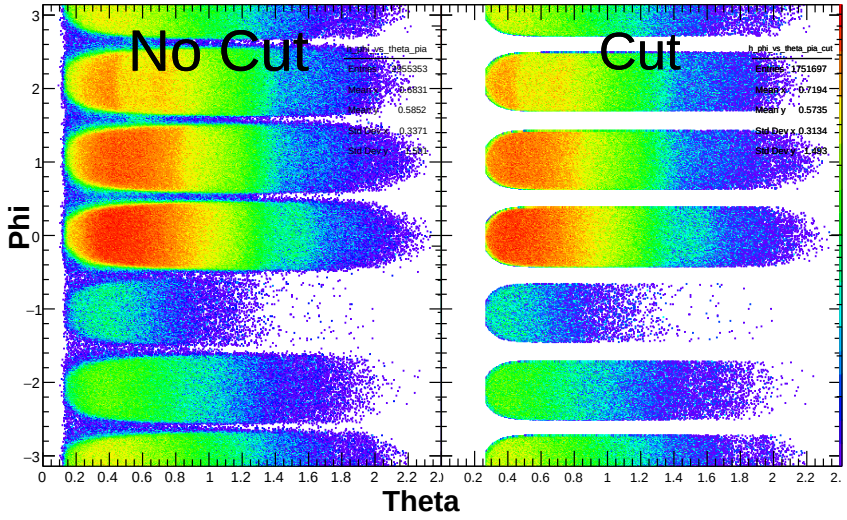

Figure 5.12: Distribution of ϕ as a function of θ for a π^- without (left) and with (right) fiducial cuts applied. The fiducial cuts reject particles that travel close to the sector edges.

at least one particle failed the fiducial cuts (bad events) for the p (top left), π^+ (top right), and π^-s (bottom row). In the "bad" events, p and π^+ are generally uniformly distributed over ϕ. Most of the π^- tracks in the "bad" events are located near the sector edges.

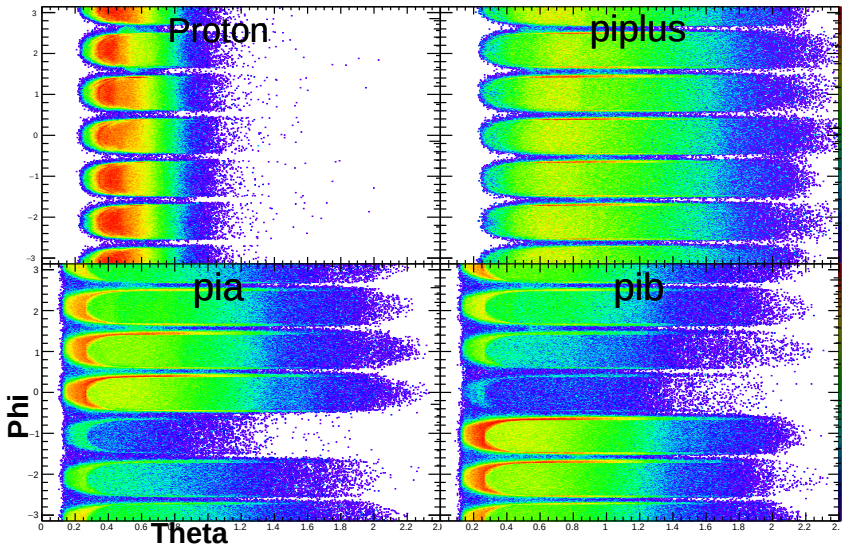

Figure 5.13: Distribution of ϕ as a function of θ for the events removed by the fiducial cuts for the p (top left), π^+ (top right), and π^-s (bottom row).

The background subtraction and observable extraction method were performed on both "good" and "bad" samples. Potential biases were investigated following the procedure outlined in Section 5.2.2. Figure 5.14 shows the relative pull distributions of C_x, C_z, and P for the fiducial cuts. Table 5.16 lists the means and the widths of the Gaussian fits to the relative pull distributions. The columns $N\sigma_\mu$ and $N\sigma_\sigma$ list the

Table 5.16: Relative pull-distribution fit parameters for the fiducial cut. The means and widths for C_x and C_z are consistent with 0 and 1, respectively. The mean for P is $\approx 4\sigma$ from 0.

Obs.	$\mu \pm \sigma_\mu$	$N\sigma_\mu$	width$\pm\sigma_{width}$	$N\sigma_{width}$
C_x	-0.064 ± 0.063	1.024	0.865 ± 0.058	2.311
C_z	0.068 ± 0.07	0.977	0.963 ± 0.069	0.537
P	0.336 ± 0.086	3.922	1.125 ± 0.086	1.457

number of standard deviations the means and widths are from 0 and 1, respectively. From this table, it is clear no significant biases or systematic uncertainties appear when changing the fiducial cut for C_x and C_z. For P, there may be some bias in the mean, with it being $\approx 4\sigma$ away from zero. Table 5.17 lists the calculated relative pull

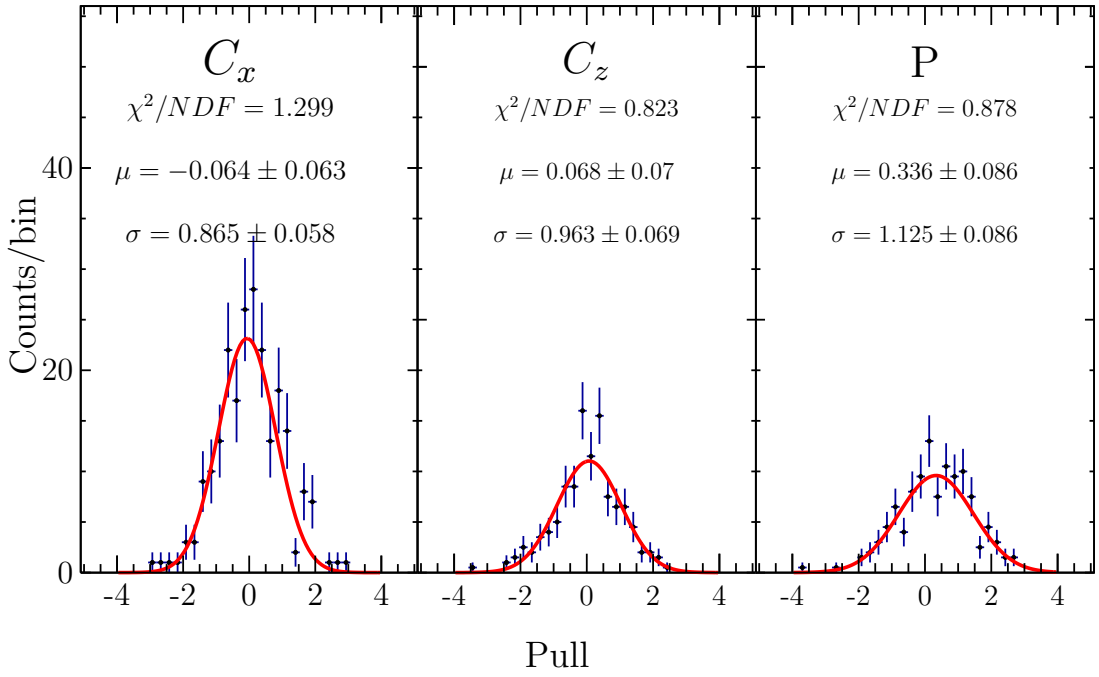

Figure 5.14: Relative pull-distributions for C_x (left), C_z (middle), and P (right) from applying the fiducial cuts. From the parameters, no significant systematic uncertainties are seen in C_x or C_z. The mean of P is significantly different from 0, suggesting there may be some systematic uncertainty.

parameters. As for the fits, the means of C_x and C_z are consistent with 0, while the

Table 5.17: Calculated relative pull-distribution parameters for the fiducial cut.

Obs.	$\mu \pm \sigma_\mu$	$N\sigma_\mu$	width
C_x	0.042±0.066	0.636	0.987
C_z	0.033±0.065	0.515	0.966
P	0.338±0.072	4.68	1.073

mean for P is significantly different.

The differences between the two estimates of the observables can be used to further study and quantify this effect. Figure 5.15 shows the differences between the observables in the two regions fit with Gaussians. Table 5.18 lists the calculated weighted mean of the difference distributions.

Figure 5.16 shows the distributions of σ^2_{sys} for the observables. The means of the

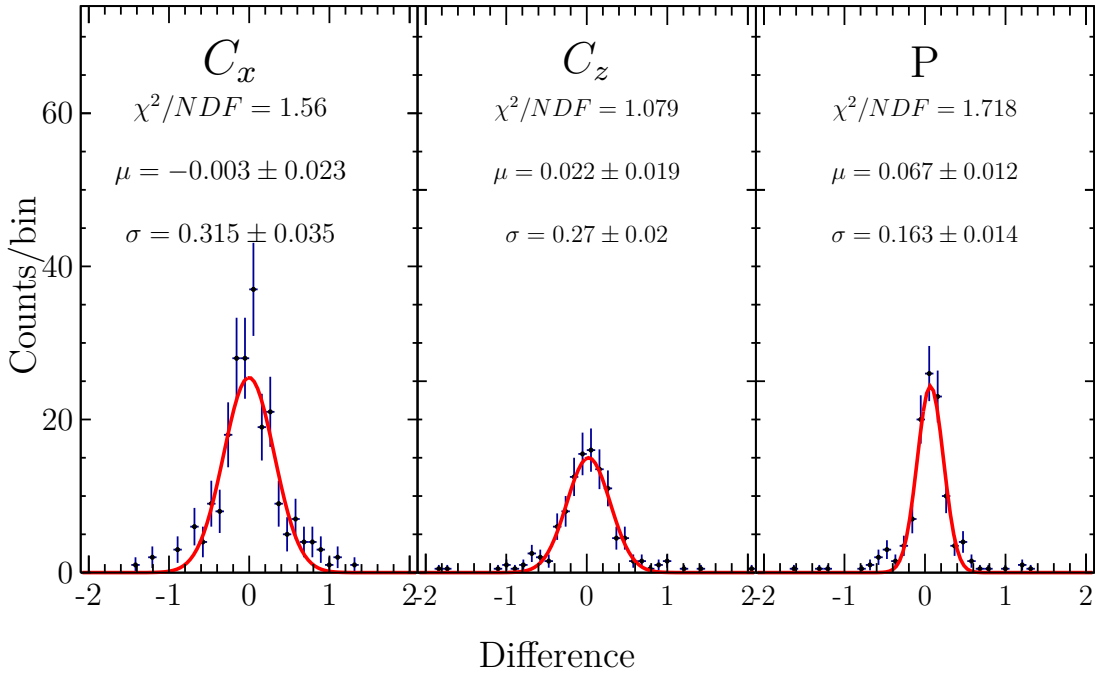

Figure 5.15: Differences between the observables when using "good" and "bad" samples. The means for C_x and C_z are consistent with 0, whereas the mean for P is $\approx 4\sigma_\mu$ from 0.

Table 5.18: Calculated weighted mean of the difference distribution, for the fiducial cut. Only the weighted mean for P is significantly different from 0.

Obs.	$\mu \pm \sigma_\mu$
C_x	0.015±0.018
C_z	0.012±0.018
P	0.055±0.015

fits, since they are all negative, suggest there are no significant systematic uncertainties. Like in previous sections, these distributions are not Gaussian, and the means need to be calculated. Table 5.19 lists the calculated means of σ^2_{sys} for all observables. σ^2_{sys} for C_x, C_z, and P are all negative, meaning the statistical uncertainties are larger than the difference of the observable estimates.

To summarize the above discussion, no evidence for extra uncertainties beyond the statistical uncertainties has been found in any of the assessment methods of C_x,

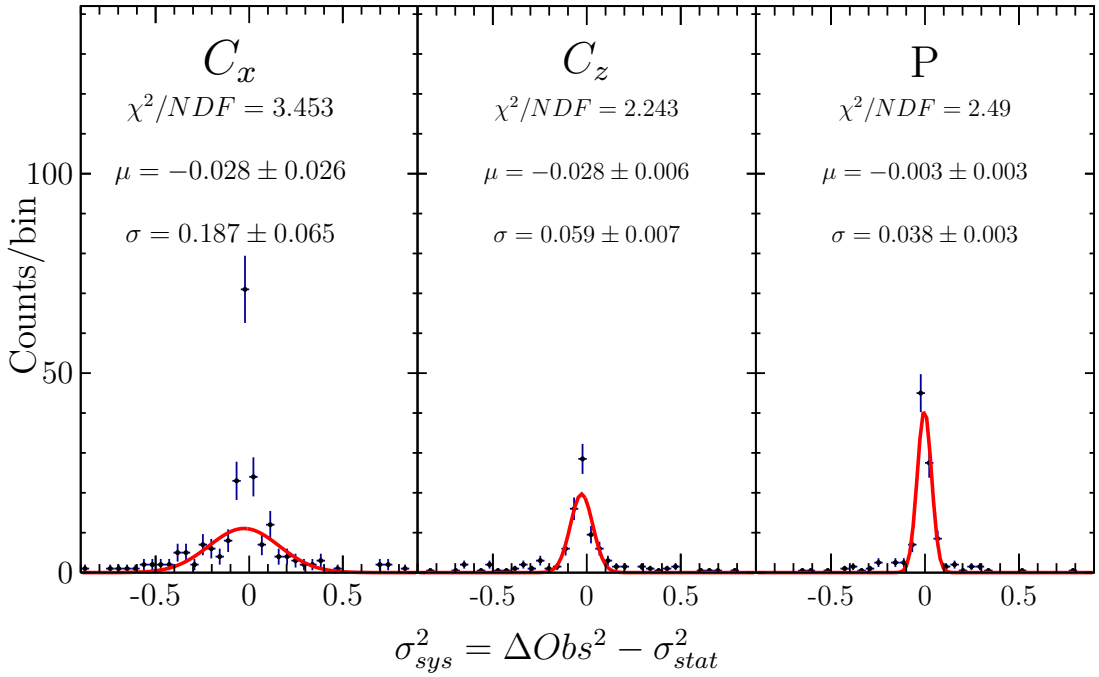

Figure 5.16: Distribution of σ^2_{sys} for C_x (left), C_z (middle), and P (right) . The means of the fits suggest there are no significant systematic uncertainties.

Table 5.19: Calculated mean of the σ^2_{sys} for the fiducial cuts. The negative values for the calculated means of all observables suggest no significant systematic uncertainties can be attributed to the fiducial cuts.

Obs.	$\mu \pm \sigma_\mu$
C_x	-0.062 ± 0.023
C_z	-0.036 ± 0.023
P	-0.018 ± 0.008

C_z, and P; no systematic biases were seen for C_x and C_z; a systematic bias was observed for P.

To further investigate the systematic bias in P, the correlations between "bad" and "good" observable estimates can be evaluated. The correlation plot is able to distinguish whether the bias, δ, has the form of $\mu + \delta$ or δ/μ. If it is the former, then the Y-intercept of a linear fit to the correlation will be inconsistent with 0. If it is the latter, then the slope of the fit will be inconsistent with 1. Figure 5.17 shows the

correlation between fiducial "bad" and "good" observables. Since the Y-intercept for

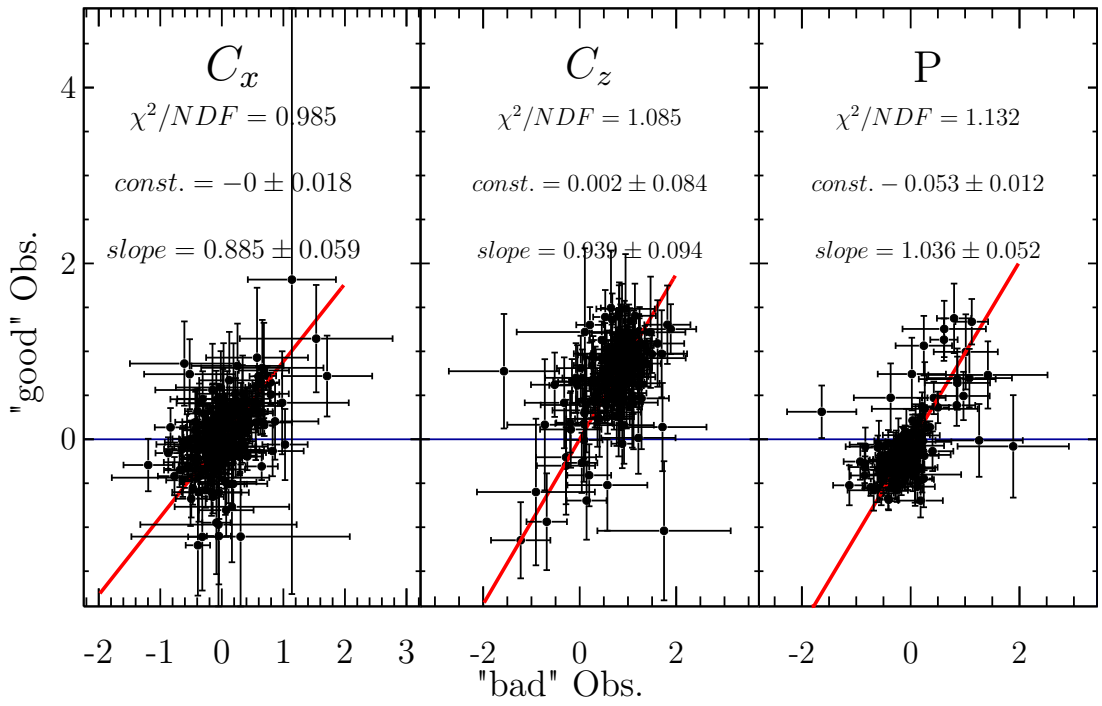

Figure 5.17: The correlation between "good" (estimated from events that pass the fiducial cuts) and "bad" (estimated from events where at least one particle fails the fiducial cut) observables. The parameters of the fits suggest there are no significant systematic biases for C_x and C_z. Since the Y-intercept for P is inconsistent with 0, while the slope is consistent with 1, the systematic bias in P is a bias with the form $\mu + \delta$.

P is inconsistent with 0, while the slope is consistent with 1, the systematic bias in P is a bias with the form $\mu + \delta$.

In the systematic-uncertainty budgets of the observables, for the contribution due to not applying fiducial cuts, we include a value of 0.055 for P, as estimated from the weighted mean of the ΔP distribution, and 0 for C_x and C_z.

5.2.5 Spectator Momentum

The cut on the spectator momentum, p_X, was studied to see if it has an effect on the observables. Recall that the original cut of $p_X < 0.2$ GeV/c was used to create a quasi–

free dominated event sample. The amount of background and final–state interaction events in the sample should change by varying the p_X cut. The systematic effect of the p_X cut was studied by following the procedure outlined in Section 5.2.2. Figure 5.18 shows the quasi–free dominated region of p_X. The red line divides p_X into two

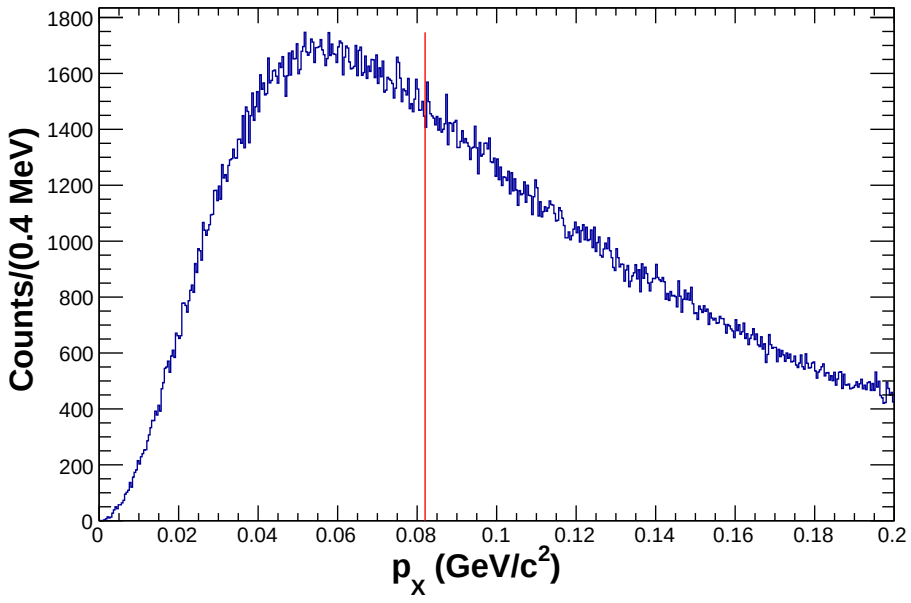

Figure 5.18: Event distribution over the magnitude of spectator momentum, p_X. The red line divides p_X into two regions, Region 1 and Region 2.

regions, Region 1 and Region 2. Both regions have $\approx 50\%$ of events.

The background subtraction and observable extraction were performed on both Region 1 and 2 event samples. Potential biases were investigated following the procedure in Section 5.2.2. Figure 5.19 shows the relative pull distributions of C_x, C_z, and P for the p_X cut. Table 5.20 lists the means and widths of the Gaussian fits to the relative pull distributions. The columns $N\sigma_\mu$ and $N\sigma_\sigma$ list how many standard deviations the means and the widths are from 0 and 1, respectively. From this table, it is clear no significant differences appear when changing the p_X cut for C_x, C_z, and P. Note that the mean for C_z is 2.6σ away from 0. Table 5.21 lists the calculated means and widths of the relative pull distributions. The mean for C_z is now 3.5σ

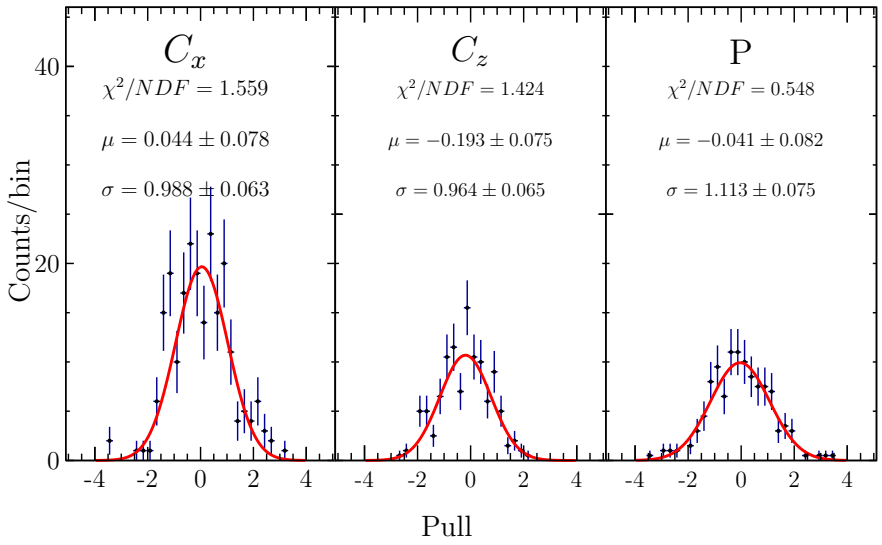

Figure 5.19: Relative pull distributions for C_x (left), C_z (middle), and P (right) from the p_X selection. From the parameters, no significant systematic uncertainties are seen in C_x, C_z, or P.

Table 5.20: Relative pull–distribution fit parameters for the p_X cut. The means and widths do not significantly differ from 0 and 1, respectively.

Obs.	$\mu \pm \sigma_\mu$	$N\sigma_\mu$	width$\pm\sigma_{width}$	$N\sigma_{width}$
C_x	0.044±0.078	0.563	0.988±0.063	0.198
C_z	−0.193±0.075	2.568	0.964±0.065	0.558
P	−0.041±0.082	0.502	1.113±0.075	1.506

Table 5.21: Relative pull–distribution calculated parameters for the p_X cut. The means for C_x and P are consistent with 0, while the mean of C_z is not.

Obs.	$\mu \pm \sigma_\mu$	$N\sigma_\mu$	width
C_x	0.014±0.083	0.164	1.112
C_z	−0.245±0.07	3.515	0.939
P	0.013±0.08	0.157	1.081

away from zero.

Figure 5.20 shows the difference of the two estimates of the observables. The means from the fits show that there are no significant differences between the two p_X regions. To confirm these results, the weighted means of the difference distributions were calculated. Table 5.22 shows the calculated weighted means of the difference

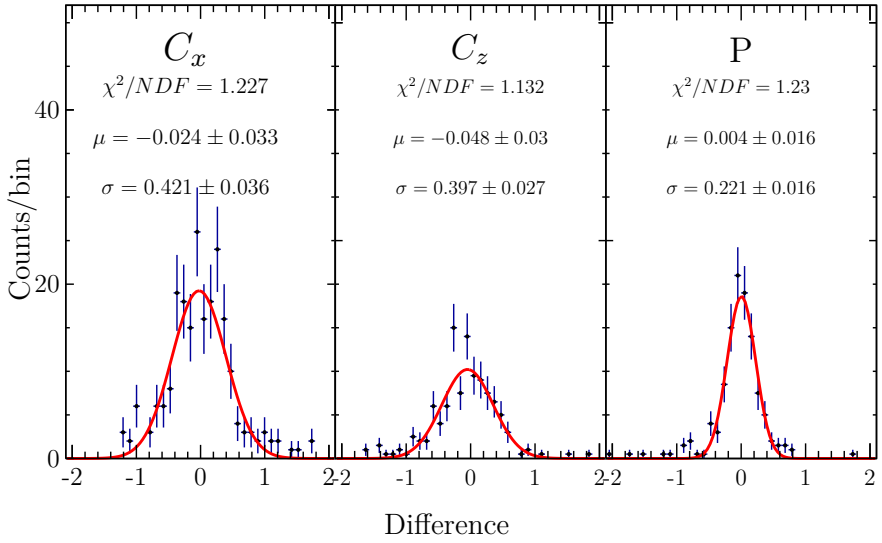

Figure 5.20: Differences between the observables for the two different regions in p_X. When fit with a Gaussian, the means of the differences are consistent with 0.

distributions.

Table 5.22: The calculated weighted mean of the difference distribution, ΔObs for the p_X cut.

Obs.	$\mu \pm \sigma_\mu$
C_x	0.009±0.023
C_z	−0.079±0.024
P	0.009±0.02

Figure 5.21 shows σ^2_{sys} for the observables. As the other σ^2_{sys} distributions, it is not Gaussian and the mean of each distribution was calculated. Table 5.23 lists the calculated μ and σ of these distributions. The negative values of σ^2_{sys} suggest there

Table 5.23: Calculated mean of the σ^2_{sys} for the p_X cut. The negative values for C_x, C_z, and P suggest there is no systematic uncertainty associated with the cut.

Obs.	$\mu \pm \sigma_\mu$
C_x	−0.011±0.024
C_z	−0.045±0.017
P	−0.001±0.012

are no significant systematic uncertainties associated with the p_X cut.

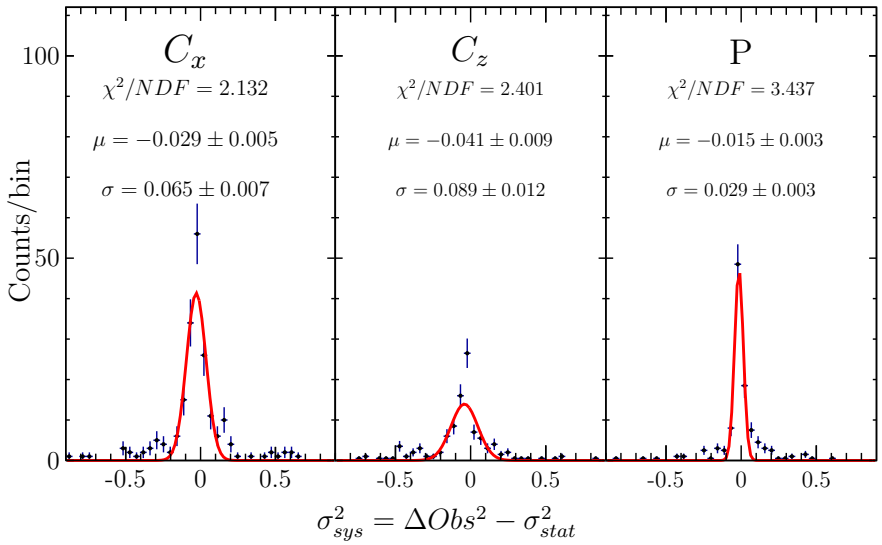

Figure 5.21: Distribution of σ^2_{sys} for C_x (left), C_z (middle), and P (right) . The means of the fits suggest there are no significant systematic uncertainties.

We should note here that some fits to M_X for both p_X samples are very bad due to limited statistics in certain kinematic bins. This is particularly troublesome for events in the largest E_γ bin for the low p_X region. Figure 5.22 shows the fits to M_X for different $\cos\theta^{CM}_{K^0}$ for the highest E_γ bin. Clearly there are multiple bins where the fit is not successful. As a check on the estimated systematic uncertainty, all bins with $E_\gamma > 2.0$ GeV were excluded from calculating the systematic uncertainty using the weighted mean and the resulting value is $\Delta C_z = 0.077$. This value is similar to what was calculated over the full kinematic range.

As for the previous selection cuts, the weighted mean of the ΔObs distribution is reported as the value of the systematic uncertainty. We report a value of 0.077 for C_z and 0 for C_x and P.

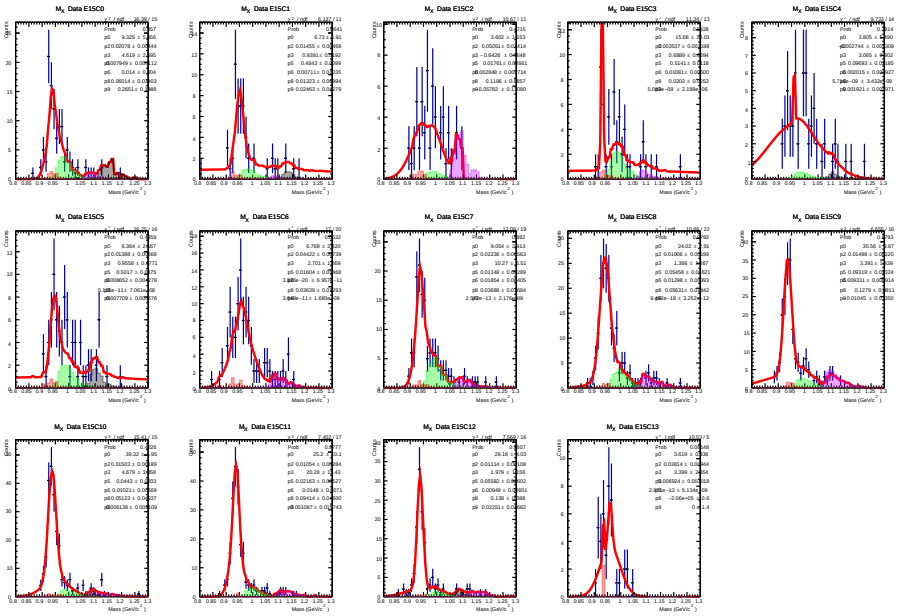

Figure 5.22: Fits to M_X for different $\cos\theta^{CM}_{K^0}$ in the highest E_γ bin. There are multiple $\cos\theta^{CM}_{K^0}$ in this E_γ bin where the fits are not able to describe the data.

5.3 Combinatorial Background

The combinatorial background arises from the pairing of the π^-. There is no way to distinguish which π^- is associated with the Λ or K^0 prior to reconstructing their invariant masses. This leads to there being a chance that both π^-s when paired with the p and π^+ pass both the $M(p\pi^-)$ and $M(\pi^+\pi^-)$ selection cuts. Simply counting the number of events where each π^- simultaneously passes this criteria prior to any selection on p_X or M_X yields 2720 out of a 832585 events (prior to the 0.2 GeV/c cut on p_X). This is $\approx 0.33\%$ of the total number of events. When p_X cuts are applied, 0.31% of events represent the combinatorial background. When $p_X < 0.2$ and $0.9 < M_X < 0.98$ GeV/c^2 (selecting the proton peak) are selected, 0.32% of events are counted in the combinatorial background. Thus, a value of $0.0032\times$Observable is used as a systematic uncertainty.

5.4 Maximum Likelihood Extraction Method

Two potential sources of systematics arise from using an unnormalized maximum likelihood method to extract the observables. Having a normalization constant would take care of (1) normalizing the likelihood function and (2) acceptance effects. Both of these aspects can cause biases and were studied using a custom generator. Figure 5.23 shows the overall procedure used to study the systematic effects of the extraction method using Monte Carlo simulations. The general idea is to generate a large

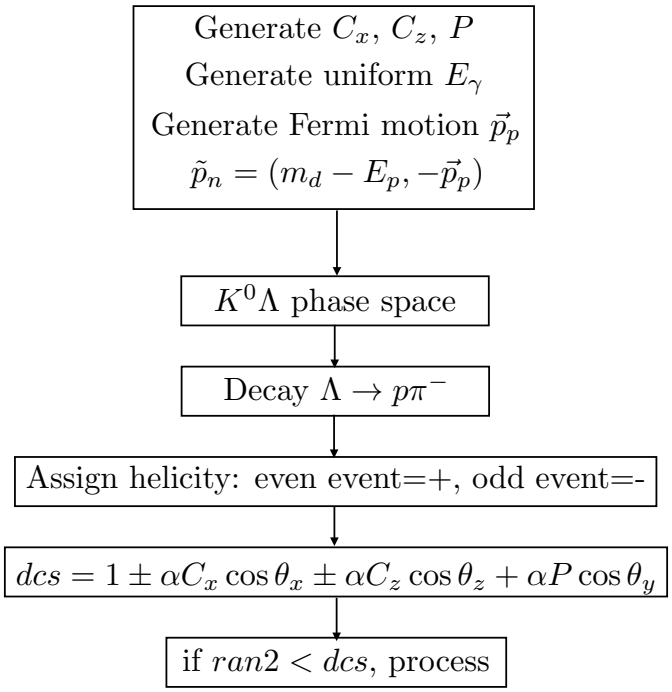

Figure 5.23: Generator flowchart for studying systematic effects originating from the maximum likelihood extraction method.

number of experiments (typically 1,000) each with a unique value for each observable. The extraction method was then applied to the generated events with and without acceptance calculations to check for any biases caused by the acceptance.

The first step in the procedure was to generate a value for each C_x, C_z, and P using fixed or randomly generated values. Secondly, a uniform E_γ distribution was generated between 0.9 – 2.6 GeV that matches the energy range of the experiment.

Thirdly, the Fermi momentum of the spectator proton was generated using the Paris potential, from which the neutron momentum could be calculated. The spectator is assigned the nominal proton mass, whereas the target neutron is off–shell and its mass is calculated using energy conservation, i.e. the total energy of the proton–neutron system must yield the rest mass of deuteron. Next, a $K^0\Lambda$ phase space was generated and then the Λ was forced to decay to $p\pi^-$. From this decay, $\cos\theta_{x,y,z}$, which are the direction cosines of the proton in the Λ rest frame with respect to the unprimed system, were calculated. At this point, a positive helicity was assigned to the event if the event number was even and a negative helicity was assigned to the event if the event number was odd. Using $\cos\theta_{x,y,z}$ and C_x, C_z, and P, the polarized cross section, dcs, was calculated. A random number ($ran2$) was then generated to accept or reject the event.

5.4.1 No Acceptance

Systematic Test $C_x = C_z = P = 0$

To begin, the unnormalized maximum likelihood method was used to extract observables for the case of no acceptance, i.e. acceptance=1 for all kinematics. The purpose of this study was to assess any biases that may arise due to the lack of normalization of the maximum likelihood method. First, the extraction procedure was studied with $C_x = C_z = P = 0$ with 1,000 experiments, each with 10,000 generated events. Setting the observables to 0 removes any potential effect that a polarized cross–section can have on the extraction of the observables. The observables were extracted for each experiment, yielding a sample of 1000 estimates. Figures 5.24 and 5.25 show the pull distribution and the distribution of the difference between the extracted values and the true values of 0. For the pull distributions, all the means and widths are consistent with 0 and 1, respectively, meaning no biases are present in the method, or if there are any, they are smaller than 0.03. The differences also suggest that there

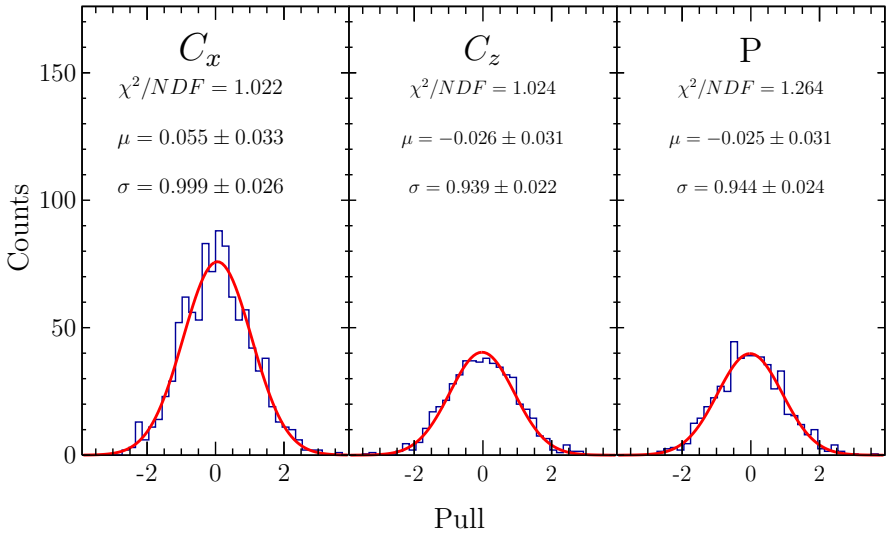

Figure 5.24: Pull distributions for $C_x = C_z = P = 0$ for 1,000 experiments, with 10,000 generated events in each experiment, fit with a Gaussian. The means and the widths of the pull distributions do not significantly differ from 0 and 1, respectively.

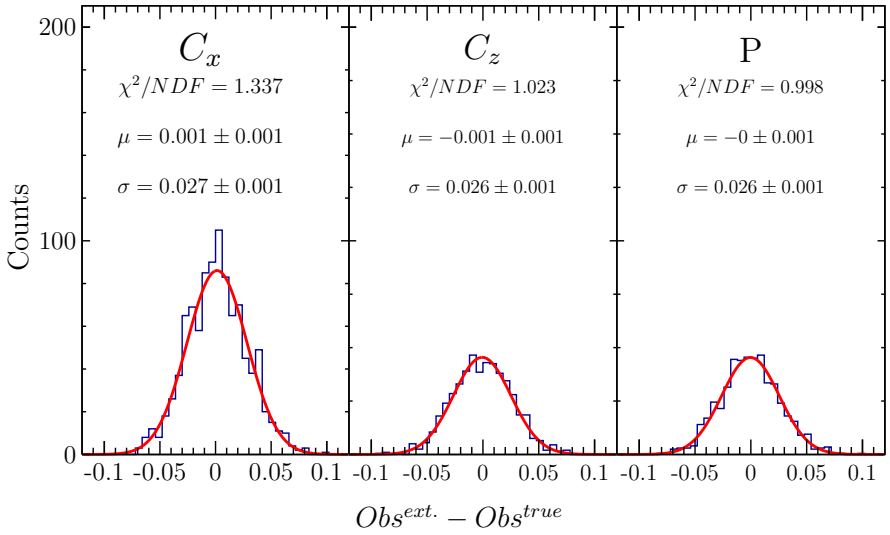

Figure 5.25: Observable differences for $C_x = C_z = P = 0$ for 1,000 experiments with 10,000 generated events fit with a Gaussian.

are no biases as the means are consistent with 0.

These distributions can also be used to test the statistical uncertainty of the fits

obtained from the maximum likelihood method. The widths of these three distributions are ≈ 0.0270 for C_x, ≈ 0.0258 for C_z, and ≈ 0.0258 for P. The standard deviation, when calculated by hand is ≈ 0.0271 for C_x, ≈ 0.0264 for C_z, and ≈ 0.0263 for P. The average of the statistical uncertainties from the maximum likelihood fit is ≈ 0.0270 for C_x, ≈ 0.0270 for C_z, and ≈ 0.0270 for P. Therefore, the statistical uncertainties from the maximum likelihood fit are accurate and are used as the statistical uncertainties of the results.

Systematic Test for $C_x = 0.2,\ C_z = 0.8,\ P = 0.5$

The next test of the the extraction method was done with fixed non–zero values, $C_x = 0.2,\ C_z = 0.8$, and $P = 0.5$. These values were chosen because they reflect the extracted values from the data and correspond to a total polarization transfer of $R = \sqrt{C_x^2 + C_z^2 + P^2} \approx 0.96$. Figure 5.26 shows the pull distributions and difference distributions between the extracted values and the true values. For the pull distri-

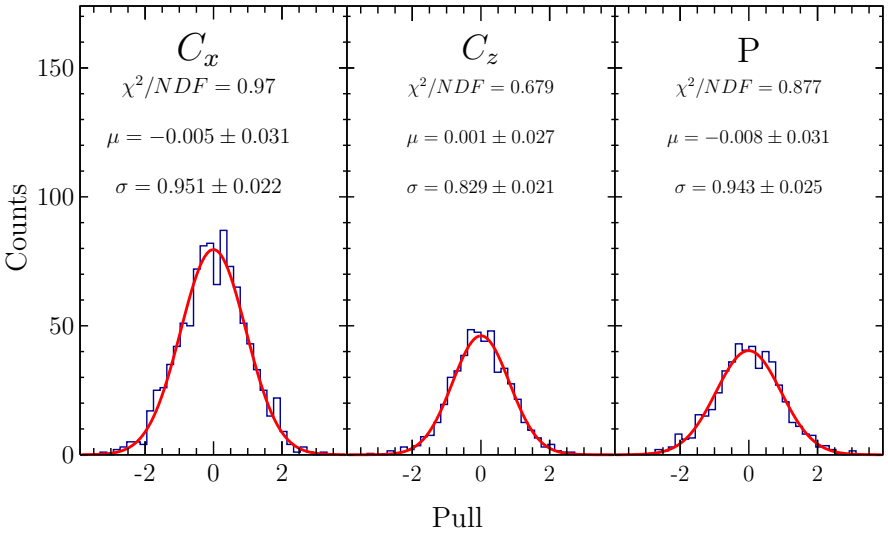

Figure 5.26: Pull distributions for $C_x = 0.2$, $C_z = 0.8$, and $P = 0.5$ for 1,000 experiments with 10,000 generated events fit with a Gaussian. The means and the widths of the distributions do not significantly differ from 0 and 1, respectively.

butions, all the means and widths are consistent with 0 and 1, respectively, meaning no biases are present in the method.

Figure 5.27 shows the differences between the extracted and the true values, which show that the means are consistent with 0. Similar statistical checks can be formed

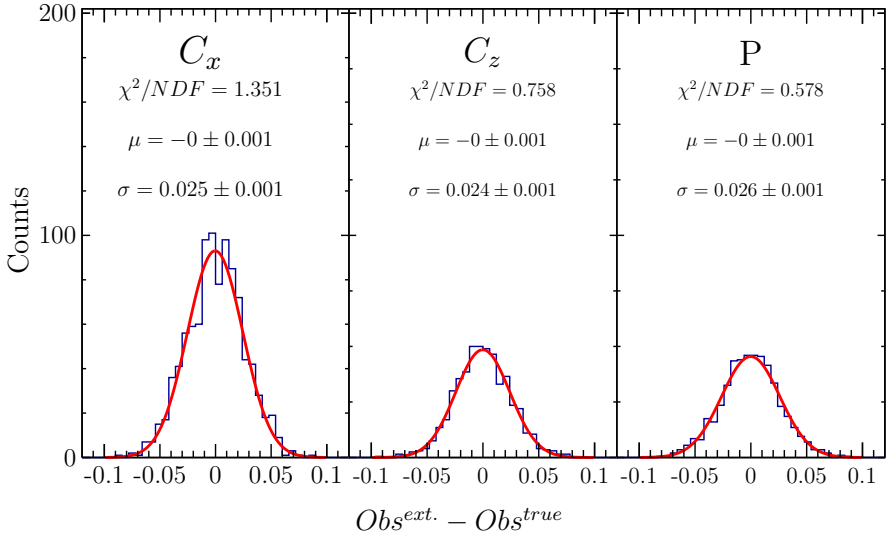

Figure 5.27: Observable differences for $C_x = 0.2$, $C_z = 0.8$, $P = 0.5$ for 1,000 experiments with 10,000 generated events fit with a Gaussian.

as were done in Section 5.4.1. The standard deviation, when calculated by hand is ≈ 0.026 for C_x, ≈ 0.025 for C_z, and ≈ 0.026 for P. The average of the statistical uncertainty from the maximum likelihood fits is ≈ 0.026 for C_x, ≈ 0.029 for C_z, and ≈ 0.027 for P. While these averages are slightly larger than what is seen in the standard deviations, the difference is in the uncertain digit and we conclude that the fit returns accurate statistical uncertainties.

Systematic Test for Random C_x, C_z, P

The observables were then chosen to vary randomly between $[-0.55, 0.55]$. This range was chosen because $R = \sqrt{3(0.55^2)} < 1$, which reflects the physics limitation that R cannot be greater than 1. Figure 5.28 shows the pull distributions for the

random C_x, C_z, and P for 1,000 experiments, with 10,000 generated events in each experiment, fit with a Gaussian. For the pull distributions, all the means and widths

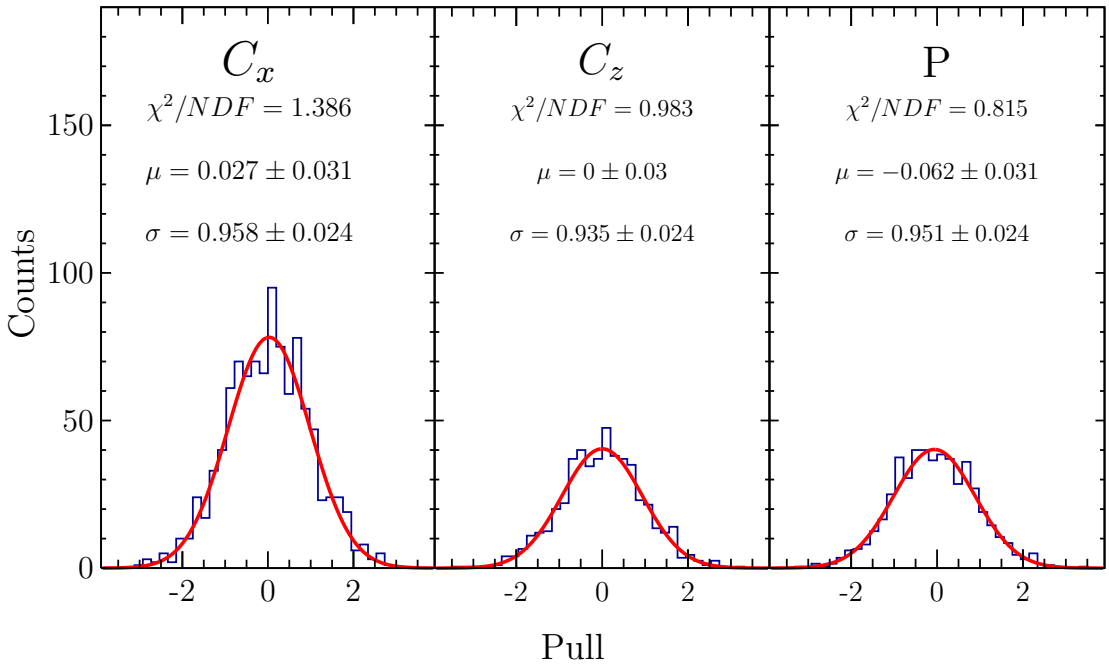

Figure 5.28: Pull distributions for random C_x, C_z, and P for 1,000 experiments with 10,000 generated events fit with a Gaussian.

are consistent with 0 and 1, respectively, meaning no biases are present in the method.

Having values for the observables in a broad range allows for the creation of correlation plots, $Obs^{extracted}$ vs. Obs^{true}. The correlation plots provide an alternative means to identify whether or not there is a bias and/or systematic uncertainties. This is done by fitting the correlation plot with a first order polynomial. The parameters of the fit allow for the determination of a bias, δ, on the order of $Obs^{extracted}$=δObs^{true}, i.e. for the determination of a % uncertainty. The difference, $\Delta Obs = Obs^{extracted} - Obs^{true}$, allows for the determination of a bias in the form of $Obs^{extracted} = \delta + Obs^{true}$, i.e. for the determination of an absolute uncertainty.

Figure 5.29 shows the correlation plot for the current set of extracted observables. Since there is no evidence for biases from the pull distributions, the slope and Y–

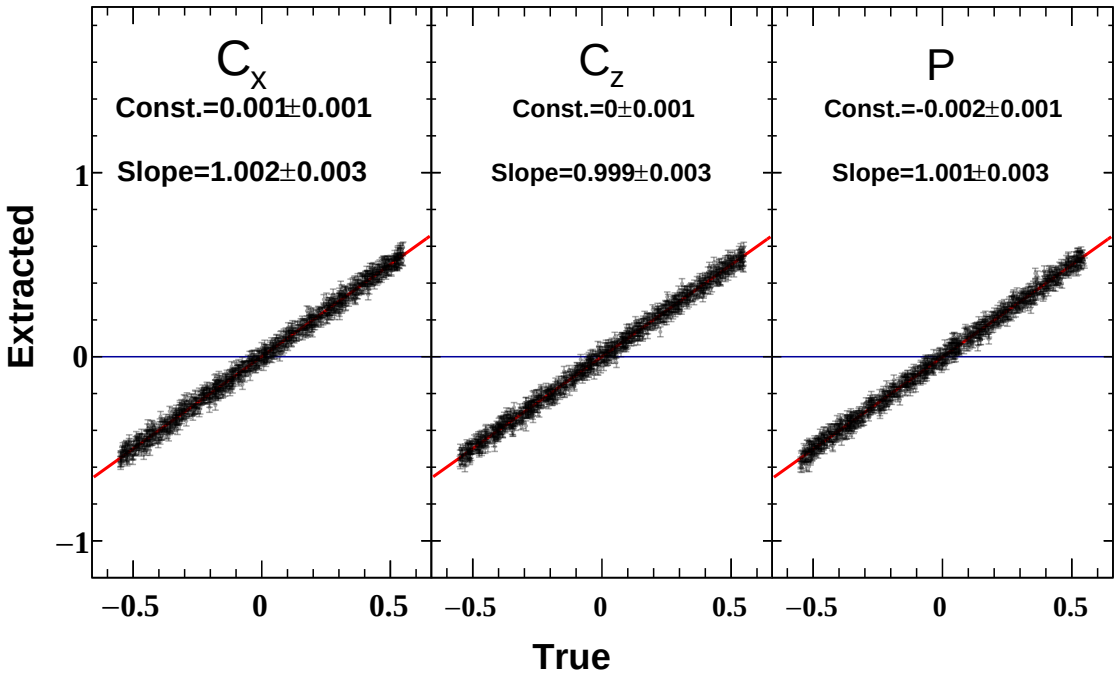

Figure 5.29: Correlation plot for random C_x, C_z, and P for 1,000 experiments, with 10,000 generated events in each experiment, fit with a Gaussian.

intercept (Const.) from the fit are expected to be consistent with 1 and 0, respectively. The parameters from the fits confirm the expectation of no biases in the extracted values of any observable.

5.4.2 Acceptance Effects

Similar systematic checks were done to test the effect of acceptance on the extracted observables. The assessment was done by means of two alternative procedures. In the first instance, the values of the CLAS acceptance were extracted over a binned kinematics $(E_\gamma, \cos\theta^{CM}_{K^0}, \cos\theta_x, \cos\theta_y, \cos\theta_z)$ and used to weight generated phase–space $K^0\Lambda$ events; the observables were then extracted from the acceptance–weighted samples In the second instance, the generated $K^0\Lambda$ events were processed through the detector simulation (GSIM) and the observables were extracted from the events that

passed through GSIM. The results from the second procedure were used to evaluate the accuracy of the results from the first procedure as the GSIM acceptance is more accurate than the binned acceptance. The first procedure, however, is not as CPU demanding as the second procedure, and one can process a very large set of data in a relatively short amount of time.

In the first procedure, we determine the acceptance by generating 5×10^8 $K^0\Lambda$ polarized events, with the values of C_x, C_z, and P randomly generated in the range $[-0.5, 0.5]$, and processing the events through GSIM. The acceptance, A, was then calculated as the ratio of the number of events that survived GSIM and analysis cuts, N_{GSIM}, to the number of events that were generated, N_{Gen}:

$$A = N_{GSIM}/N_{Gen}. \tag{5.8}$$

Figure 5.30 shows $A(\cos\theta^{CM}_{K^0})$ for each E_γ bin and $\cos\theta^{CM}_{K^0}$ bin. The distributions

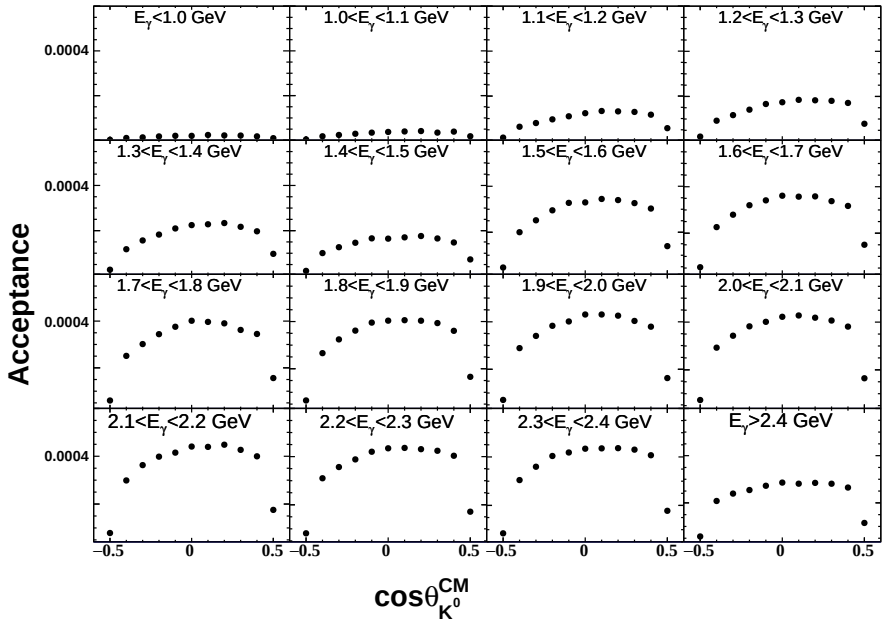

Figure 5.30: Calculated acceptance from Equation 5.8 for each E_γ and $\cos\theta^{CM}_{K^0}$ bin.

have a maximum $A(\cos\theta^{CM}_{K^0})$ of ≈ 0.004 and peak around $\cos\theta^{CM}_{K^0} \approx 0.2$. One limiting factor of using this calculated acceptance is that it is binned, i.e. all the events in one kinematic bin are assigned the same acceptance. For example, all events in the

$\cos\theta_{K^0}^{CM}$ range above 0.5 are assigned a constant non–zero acceptance equal to the acceptance of the closest $\cos\theta_{K^0}^{CM}$ bin (same for all events in the $\cos\theta_{K^0}^{CM}$ range below -0.5. However, this is not the case in the real experiment, and the effect of this will be discussed in Section 5.4.2.

Figure 5.31 shows A for one E_γ and 11 $\cos\theta_{K^0}^{CM}$ bins as a function of $(\cos\theta_y, \cos\theta_z)$. In general, A is a function of $(z, |\vec{p}|, \phi, \theta, \cos\theta_x, \cos\theta_y, \cos\theta_z)$. However, the likelihood

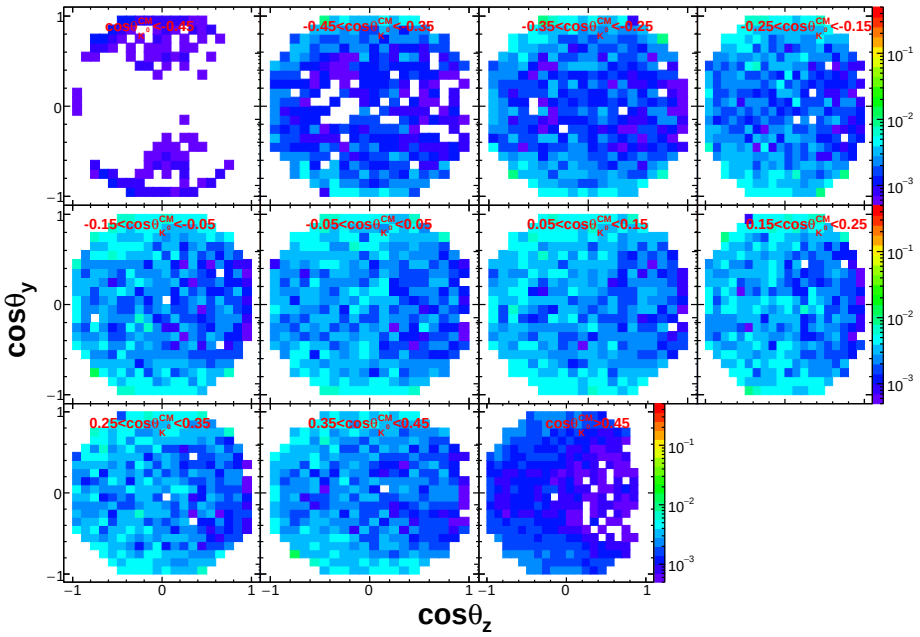

Figure 5.31: Example of $A(\cos\theta_y, \cos\theta_z)$ for $1.5 < E_\gamma < 1.6$ GeV and 11 $\cos\theta_{K^0}^{CM}$ bins. We observe that the CLAS acceptance is non–uniform over the proton direction cosines.

function only depends on $(\cos\theta_x, \cos\theta_y, \cos\theta_z)$. 3d distributions for A are not shown because it is hard to visualize on a 2 dimensional surface. Therefore, $A(\cos\theta_y, \cos\theta_z)$ is used as a visualization example of the calculated acceptance.

Figure 5.32 shows the pull distributions for the random C_x, C_z, and P for 1,000 experiments, with 500,000 generated events in each experiment, fit with a Gaussian. For the pull distributions, the means and widths of C_x and C_z are consistent with 0 and 1, respectively. However, the mean in P is 1.011 ± 0.033, which clearly shows some bias in the extraction of P.

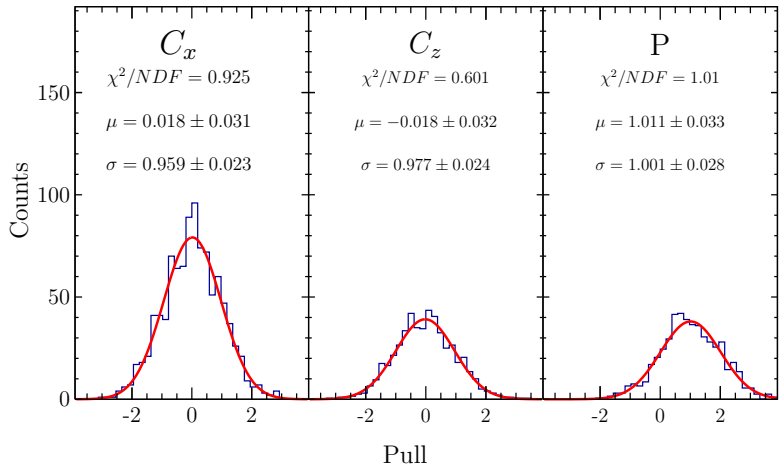

Figure 5.32: Pull distributions for random C_x, C_z, and P for 1,000 experiments, with 500,000 generated events in each experiment, fit with a Gaussian.

The correlation and the difference plots are used to quantify the type and the size of the bias. Figure 5.33 shows the correlation plot for the extracted observables. Since

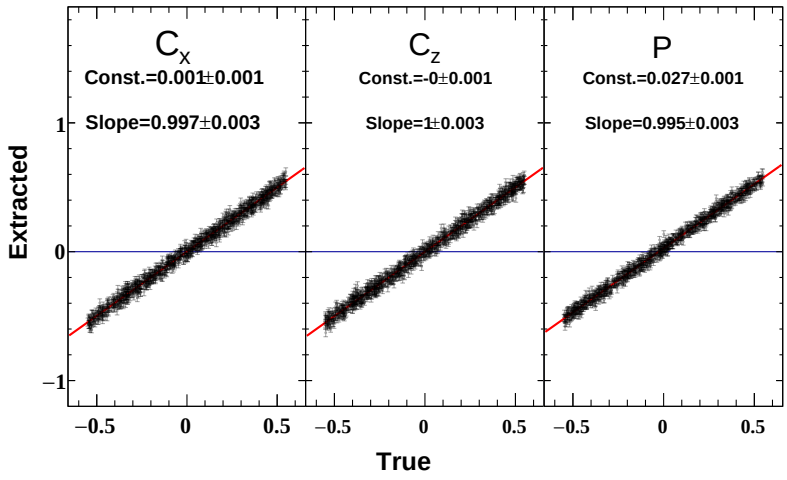

Figure 5.33: Correlation plots for random C_x, C_z, and P for 1,000 experiments, with 500,000 generated events in each experiment, fit with a Gaussian.

there are no biases in the pull distributions for C_x and C_z, we expect to see the slope and Y–intercept of each of the two fits to be consistent with 1 and 0, respectively. The parameters from these two fits confirm the expectation of no biases. The correlation

plot for P (right) has a Y–intercept (Const.) that is 27σ away from 0. Figure 5.34 shows the difference between the extracted and the true values of P, which confirms the bias seen in P.

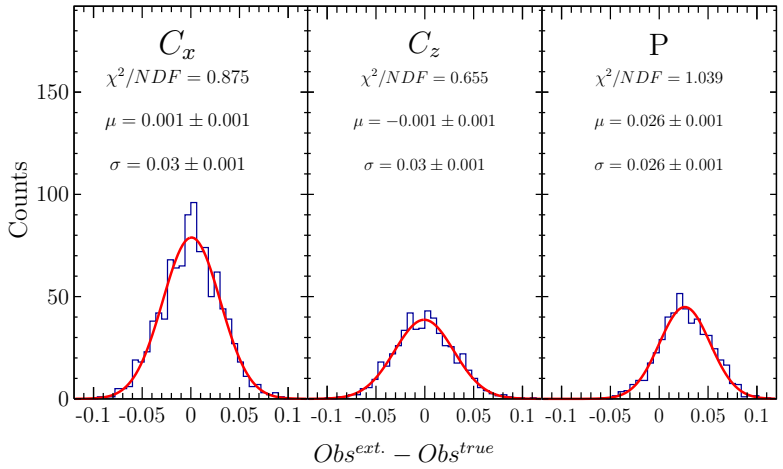

Figure 5.34: Distributions of the difference between the extracted and the true values for random C_x, C_z, and P for 1,000 experiments, with 500,000 generated events in each experiment, fit with a Gaussian. C_x and C_z have means (μ) consistent with 0 and have no bias. P has $\mu = 0.026 \pm 0.001$ which shows that the extracted values of P are biased.

The next step in studying this bias is to look at the difference between the extracted and the true value of the observable, ΔObs, as a function of the true value. If ΔObs has some dependence on the value of the observable, then that observable would need to be corrected on a bin by bin basis. If ΔObs does not depend on the value of the observable, then the slope of the distribution ΔObs over the true value will be consistent with 0 and the mean value can be used as a constant correction to all values of the observable. Figure 5.35 shows ΔObs as a function of the true observable for random C_x, C_z, and P for 1,000 experiments, with 500,000 generated events for each experiment, fit with a Gaussian. The slopes for C_x, C_z, and P are all consistent with 0. This means the shift in observable does not depend on the true value of the observable and that all data for P can be corrected in the same way.

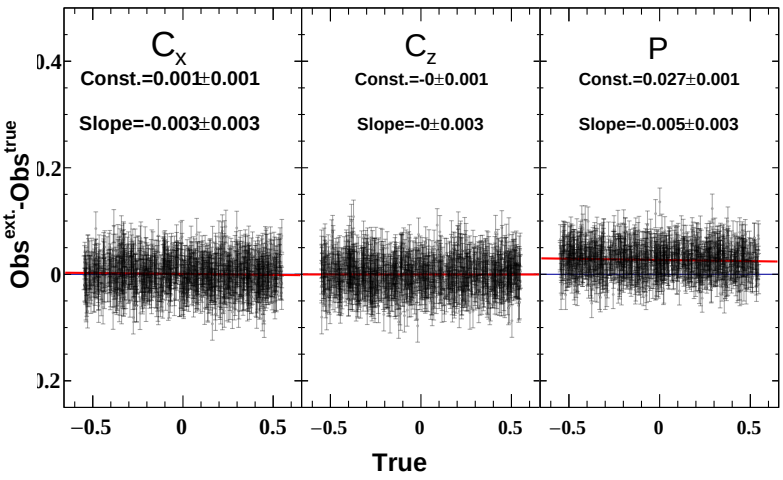

Figure 5.35: ΔObs as a function of the true observable for random C_x, C_z, and P for 1,000 experiments with 500,000 generated events fit with a Gaussian. The slope for each, C_x, C_z, and P is consistent with 0. This means any shift in ΔObs does not depend on the value of the observable.

Testing the Calculated Acceptance

As discussed above, the calculated acceptance was binned in E_γ and $\cos\theta_{K^0}^{CM}$ (in addition to $(\cos\theta_x, \cos\theta_y, \cos\theta_z)$). The main benefit of using the calculated acceptance is speed. One only needs to generate events, apply the acceptance and event selection cuts, then extract the observables. The effect of this binning was tested by generating 1,000 experiments, with 500,000 events per experiment and processing the events through GSIM. As in the previous study, each experiment had random values for C_x, C_z, and P. For the events processed through GSIM, the observables were extracted by applying the same analysis cuts and techniques as done for real data and the pull distributions, correlations, and differences were all calculated. Figure 5.36 shows the correlations for each observable. C_x and C_z have slopes and Y–intercepts consistent with 1 and 0, respectively. The Y–intercept for P is not consistent with 0, but is of the same order of magnitude (0.040±0.002) as obtained with the calculated acceptance (0.027±0.001).

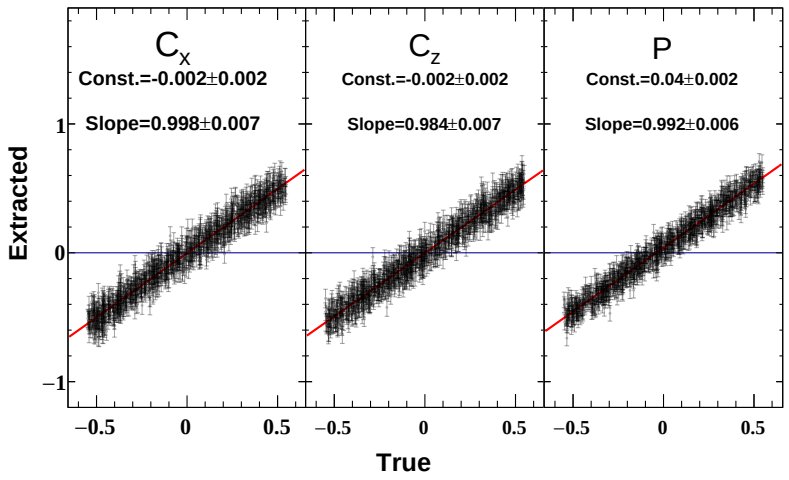

Figure 5.36: Correlation plot for random C_x, C_z, and P for 1,000 experiments with 500,000 generated events in each experiment fit with a Gaussian. C_x and C_z have slopes and Y–intercepts consistent with 1 and 0, respectively. The constant for P is not consistent with 0, but is on the same order of magnitude as the calculated acceptance.

A few remarks about the two different correlation distributions can be made. Firstly, the calculated acceptance is only binned in 11 bins of $\cos\theta_{K^0}^{CM}$. This results in events that would not survive GSIM (ex. $\cos\theta_{K^0}^{CM} = -1$) having a chance of surviving with the calculated acceptance. This leads to larger statistics for the events with observables extracted with calculated acceptance, which one can see in the size of the error bars in Figures 5.33 and 5.36. The biggest disadvantage in obtaining the value of the bias from the GSIM–processed events is the time it takes to analyze 1,000 experiments with 500,000 generated events per experiment. In order to get better statistics, more events would need to be generated as only $\approx 2\%$ of events generated survive GSIM and the selection cuts. Therefore, getting better statistics takes much more time and computing power. This makes using the calculated acceptance a much more attractive option when performing these studies.

Since the likelihood function used to extract the observables is unnormalized, P needs to be corrected for acceptance effects. This corresponds to shifting the extracted

estimates by a constant. This shift, δP, is taken to be

$$\delta P = \frac{0.04 + 0.027}{2} \pm (0.04 - 0.027) = 0.033 \pm 0.013. \tag{5.9}$$

The uncertainty of 0.013 is reported as the value of the systematic uncertainty of P due to the CLAS acceptance.

5.5 Background Subtraction

The systematic uncertainty in the background subtraction method comes from two sources that relate to how well the background channels are modeled in the generator and how well detector resolutions are modeled in GSIM. Recall that for all the background channels, phase–space distributions were generated and processed through GSIM as there were no accurate cross–sections available to weight the distributions. In Section 4, it was shown that phase–space distributed final–state particles processed through GSIM, at least visually, reproduce the shapes observed in the real data. However, there may be some systematic uncertainties related to using phase–space distributions. For example, it is not certain how well the simulated data reproduce the leading edge of the $K^0\Sigma^0$ peak. This can be studied by varying the widths of the two regions in which the observables are calculated. By decreasing the width of region 1, r_1^B decreases, thus changing the value of the observable. To test how accurately GSIM reproduces the detector acceptance and resolutions, an under or over estimation of the shape of the background can be studied by varying the background to signal ratios by 50% and 150%.

5.5.1 Missing Mass Cut

The first source of systematic uncertainty relates to how well the background is understood underneath the neutron peak. The systematic effects of this were tested by varying the cut that separates Region 1 and Region 2. A M_X cut of 0.98 GeV/c^2

was used to separate the two regions when performing the background subtraction. The systematic effects were studied by adjusting the M_X cut to 0.97 GeV/c^2 and 0.99 GeV/c^2, extracting the observables for each cut, and assessing the difference between the two estimates. Figure 5.37 shows the normalized difference, $\frac{N^{0.97}-N^{0.99}}{N^{0.98}}$ for the two different M_X regions. At low energies, there is a small difference between the number

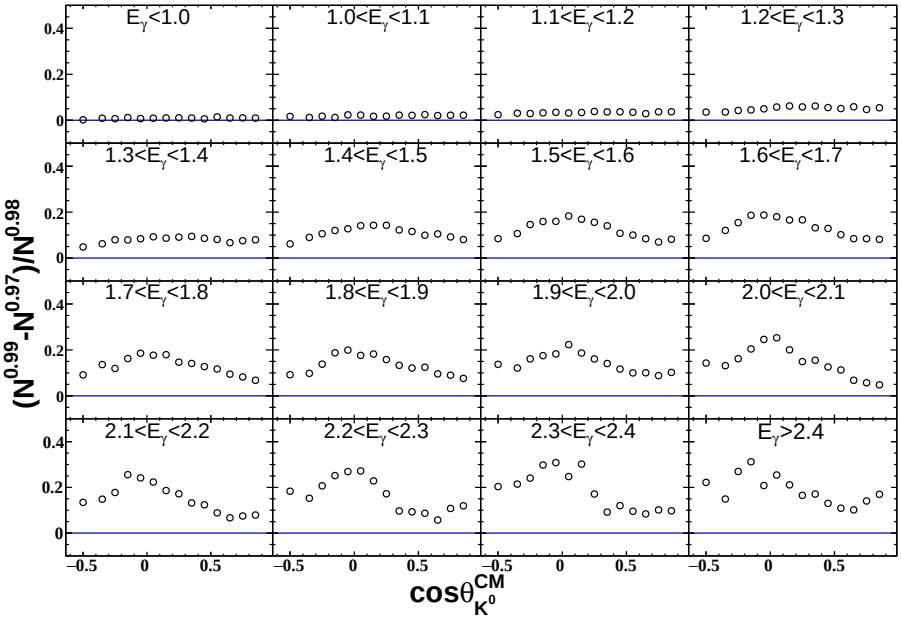

Figure 5.37: Normalized difference between the 0.97 and 0.99 GeV/c^2 selection cut for region 1. At low energies, there is a small difference between the number of events in region 1. At higher energies, there are $\approx 20\%$ more events in region 1 for the M_X separation of 0.99 GeV/c^2.

of events in Region 1. At higher energies, there are $\approx 20\%$ more events in Region 1 for the M_X separation of 0.99 GeV/c^2. This peaks at the kinematic bins where the Σ^0 background is the largest. The difference in statistics means that some of the difference between the two estimates of the observables would originate from the different statistics between the two data samples. We make the assumption that any statistical fluctuations due to difference in statistics are very small and any variations are due to systematics.

Figure 5.38 shows the difference, $Obs^{0.97} - Obs^{0.99}$, in observables when changing the M_X range in the background subtraction method for Region 1. The mean and

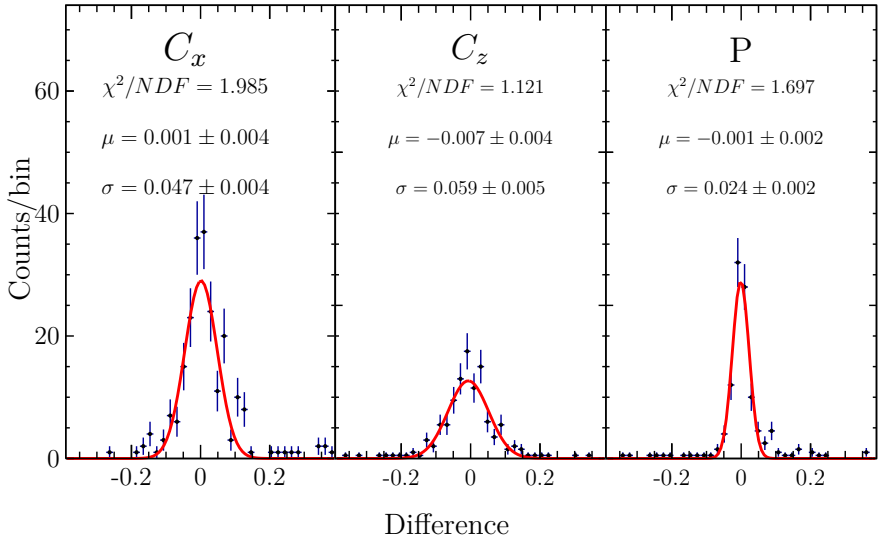

Figure 5.38: Difference in observables when changing the M_X range in the background subtraction method for region 1. The observables are fit with a Gaussian and the mean, μ, plus width, σ, added in quadrature, are reported as systematic uncertainties.

the standard deviation of each distribution is used as an estimate of the systematic uncertainty

$$\Delta C_x = \sqrt{\mu^2 + \sigma^2} = 0.047,$$

$$\Delta C_z = \sqrt{\mu^2 + \sigma^2} = 0.059,$$

$$\Delta P = \sqrt{\mu^2 + \sigma^2} = 0.024.$$

5.5.2 Ratios: r^B and r^{unpol}

The second source of systematic uncertainty, relating to how well the generated data processed through GSIM describes the real data, can be quantified by varying the calculated ratios, r_i^B and r_i^{unpol} in Equations 4.20–4.22. The systematic effect of these ratios was assessed by varying the ratios by 0.5 and 1.5 times their original values, extracting the observables for each ratio, and calculating the difference between the two estimates. The mean and the standard deviation of the observable–difference dis-

tribution are used to estimate the systematic uncertainty due to r^B and r^{unpol}. Figure 5.39 shows the difference in C_z for every kinematic bin. The systematic uncertainty

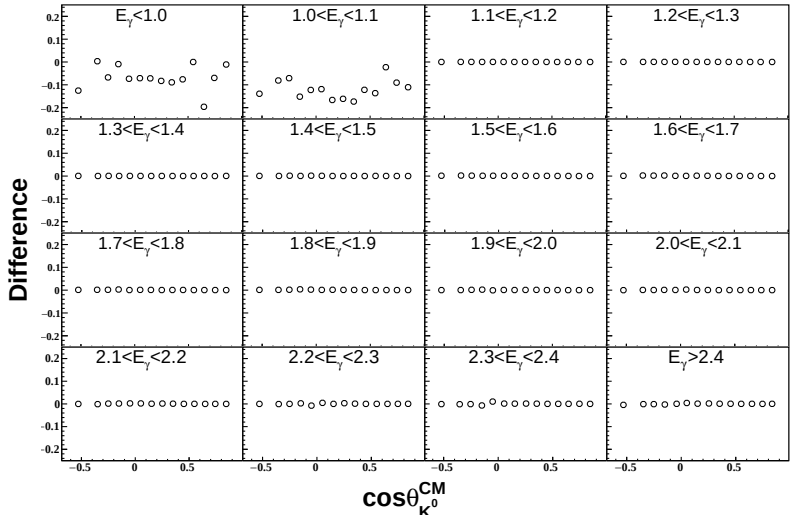

Figure 5.39: ΔC_z when changing the ratios in the background subtraction method for each kinematic bin.

is estimated to be:

$$\Delta C_x = 0.014,$$

$$\Delta C_z = 0.038,$$

$$\Delta P = 0.011.$$

5.5.3 Number of M_X Bins

A third source of systematic uncertainty present in the background subtraction process is the number of bins in the M_X histogram used to calculate the ratios. Changing the number of M_X bins changes the ratios, and systematic uncertainties related to this variaton need to be assessed. This was tested by doing the analysis for 3 different number of bins: 25, 50, and 75, with 50 bins being the nominal value. Since each analysis uses exactly the same number of events, any variations in the extracted observables are due to systematic effects.

Figure 5.40 shows the relative difference, $\frac{Obs^{50}-Obs^{25}}{Obs^{50}}$, for C_x, C_z, and P. The

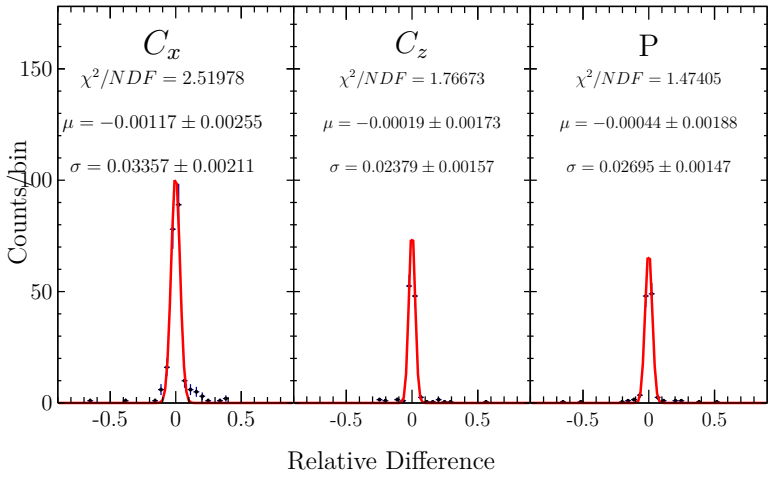

Figure 5.40: Relative difference for C_x, C_z, and P for 25 and 50 M_X bins. All observables have relative differences of 10^{-3} or less and it can be concluded that decreasing the number of M_X bins from 50 to 25 does not cause any systematic error in the observables. The standard deviation of each distribution quantifies the systematic uncertainty of the corresponding observable.

standard deviation of the relative difference distribution provides a measure of the % uncertainty of the observable, while the mean measures the % systematic error. Since all the means are of the order of 10^{-3} or less, it can be concluded that having under 50 M_X bins does not cause any systematic error of the results. Figure 5.41 shows the relative difference, $\frac{Obs^{50}-Obs^{75}}{Obs^{50}}$, for C_x, C_z, and P. As in the case of decreasing the number of M_X bins, increasing the number of M_X bins seems to cause no systematic error of the observables.

Based on the standard deviations of the difference distributions, we assign a 3% systematic uncertainty to each observable due to the M_X-histogram bin number.

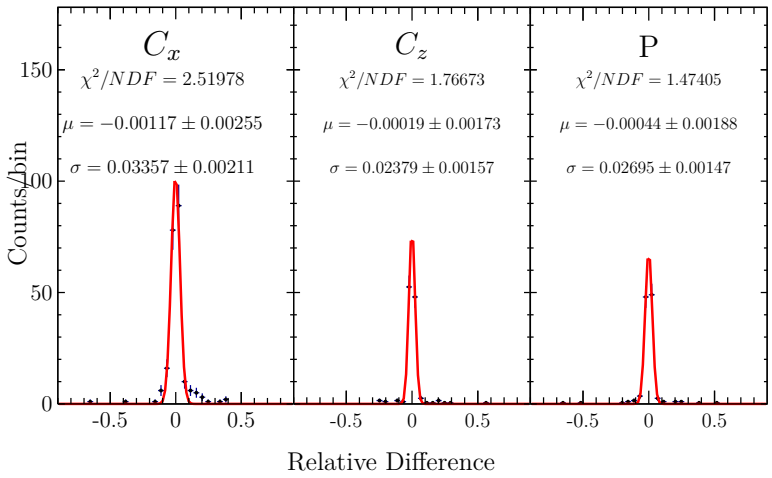

Figure 5.41: Relative difference for C_x, C_z, and P for 75 M_X bins. All observables have relative differences of 10^{-3} or less and it can be concluded that increasing the number of M_X bins from 50 to 75 does not cause any systematic error in the observables. The standard deviation of each distribution quantifies the systematic uncertainty of the corresponding observable.

5.6 Photon Polarization and Self–Analyzing Power of the Λ

The final estimates for C_x and C_z are obtained by dividing the corresponding maximum likelihood fit parameter by $\alpha = 0.642 \pm 0.013$, which is the self–analyzing power of the Λ, and by the photon polarization. The final estimates for P are obtained by dividing its fit parameter from the maximum likelihood method by α. Therefore, C_x, C_z, and P all have a systematic uncertainty due to the uncertainty of α, and C_x and C_z have an additional systematic uncertainty that is due to the uncertainty of the photon polarization.

Uncertainty propagation yields that the relative uncertainty of each observable due to α is equal to the relative uncertainty of α, which is 2%.

The photon poalrization, P_γ was determined using the Maximon Olsen relation [44],

$$P_\gamma = \frac{E_\gamma(E + \frac{1}{3}E')P_e}{E^2 + E'^2 - \frac{2}{3}EE'}, \tag{5.10}$$

where E_γ is the photon energy, E is the electron energy, P_e is the electron polarization,

and $E' = E - E_\gamma$. Table 5.24 lists the electron beam energies, Wien angle, and the electron polarization for the different g13a run groups. For a fixed Wien angle,

Table 5.24: Electron polarizations for each run in the g13a sample. A description of how the polarization was determined is given in [12].

Run	E_e (GeV)	Wien Angle (deg)	Electron Polarization (%)
53164–53532	1.987	92.246	84.97 ± 0.28
53538–53547	2.649	90.844	80.6 ± 0.18
53550–53862	2.649	90.043	78.47 ± 0.18
53998–54035	1.987	93.247	93.246 ± 1.1

the polarization as measured by the Hall–B Møller polarimeter for each g13a run group was found to vary randomly around a mean value [12]. Thus, the electron beam polarization for a given run group was determined by averaging over the set of Møller-polarimeter measurements for that run group [12].

Assuming that both the electron and the photon beam energies are exactly known, i.e. the uncertainty of the photon polarization is only due to the uncertainty of the electron polarization, the maximum relative uncertainty of the photon polarization (based on the values in Table 5.26) is 0.011. Uncertainty propagation yields that the relative uncertainty of each C_x and C_z (due to the uncertainty of P_γ) is equal to the relative uncertainty of P_γ, which is 1.1%. The latter is included in the systematic uncertainty budget of the two polarization transfers, C_x and C_z.

5.7 Summary

Throughout the discussion of this chapter, several methods to study the systematic uncertainties and the systematic errors of the observables were presented. Some methods used generated samples for which the true value of the observable was known and some methods used statistically independent samples of real data. Relative pull distributions formed from two alternative estimates (or from extracted and true values) of an observable in a multitude of kinematic bins were used as initial assessment

– when the means and the widths of the distributions were consistent with 0 and 1, respectively, we concluded that any difference seen in the observables is due to statistics. The systematic effects were quantified by using the mean and the standard deviation of the distribution of the difference between the alternative (or between extracted and true) estimates. In several cases, when the means were not consistent with zero, we performed further studies of the observed bias by making use of the correlation between the extracted and the true value. Some sources of uncertainty were studied by using exactly, or mostly, the same data sample so that any variations between alternative estimates were entirely, or mostly, due to systematic effects.

These systematic–uncertainty studies showed that many event–selection criteria, such as the particle identification, do not cause systematic uncertainties. One of the

Table 5.25: Summary of systematic uncertainties.

Source	C_x	C_z	P
Instrumental Asymmetry	0.043	0.043	0.043
Particle ID	–	–	–
$M(p\pi^-)$ Selection	–	–	0.053
$M(\pi^+\pi^-)$ Selection	–	–	–
Fiducial	–	–	0.055
p_X cut	–	0.079	–
Extraction Method	–	–	–
Acceptance (ML)	–	–	0.013
M_X Cut	0.047	0.059	0.024
M_X Bins	$0.030C_x$	$0.030C_z$	$0.030P$
r^B, r^{unpol}	0.014	0.038	0.011
Combinatorial Background	$0.0032C_x$	$0.0032C_z$	$0.0032P$
Λ Self–analyzing power	$0.02C_x$	$0.02C_z$	$0.02P$
P_γ	$0.011C_x$	$0.011C_z$	–

exceptions to this was the p_X cut, where a large weighted mean of the difference distribution was seen for C_z yet the mean and width of the pull distribution was consistent with 0 and 1, respectively. This large weighted mean of the difference prompted further studies as discussed in Section 5.2.5. The only systematic error we

identified was for the observable P and was due to the effect of the CLAS acceptance in the extraction method. All the values of P need to be reduced by 0.033.

Table 5.25 summarizes all systematic uncertainties of all observables. If $C_x = C_z = P = 1$, then the total systematic uncertainty is ≈ 0.075 for C_x, ≈ 0.120 for C_z, and ≈ 0.099 for P.

Chapter 6

Results

6.1 Kinematic Binning

Figure 6.1 shows the setup of kinematic bins after selection cuts on $M(p\pi^-)$, $M(\pi^+\pi^-)$, and $p_X < 0.2$ GeV/c. Each black box corresponds to a single kinematic bin for a total

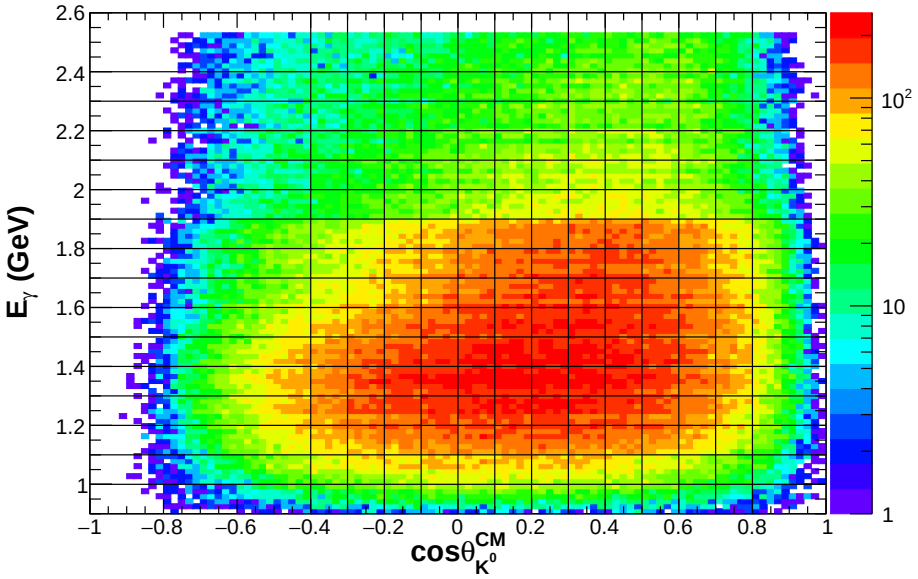

Figure 6.1: E_γ as a function of $\cos\theta^{CM}_{K^0}$ after selection cuts on $M(p\pi^-)$, $M(\pi^+\pi^-)$, and $p_X < 0.2$ GeV/c. The black lines represent the edges of the different kinematic bins. The background subtraction and observable extraction method were done for each kinematic bin.

of 224 kinematic bins. E_γ was divided into 16 kinematic bins of 100 MeV. The one E_γ bin above 2.4 GeV is wider than 100 MeV as it contains events up to 2.6 GeV. $\cos\theta^{CM}_{K^0}$ was divided into 14 bins with a standard bin width of 0.1. The exceptions to this are the bins for $\cos\theta^{CM}_{K^0} < -0.4$ and $\cos\theta^{CM}_{K^0} > 0.8$. These bins contain all

events below -0.4 and above 0.8, respectively.

Table 6.1 lists the average percentage of signal events ($0.9 < M_X < 0.98$ GeV/c^2), polarized background events within $0.9 < M_X < 0.98$ GeV/c^2, and the percentage of unpolarized background events within $0.9 < M_X < 0.98$ GeV/c^2. At low E_γ, ≈90%

Table 6.1: Average percentage of signal, polarized background, and unpolarized background for each E_γ bin.

E_γ (GeV)	% Signal	% Pol. Background	% Unpol. Background
0.95	93.2	0.0	6.8
1.05	89.0	0.0	11.0
1.15	88.9	0.0	10.9
1.25	88.7	1.0	10.1
1.35	86.6	2.6	10.9
1.45	83.9	4.6	11.5
1.55	81.8	6.4	11.9
1.65	80.9	7.3	11.6
1.75	81.3	7.7	10.9
1.85	81.7	7.8	10.6
1.95	83.1	8.5	8.6
2.05	81.9	9.4	8.6
2.15	79.4	10.7	9.9
2.25	77.9	11.9	10.3
2.35	77.9	12.1	10.2
2.5	77.0	12.8	10.0

of events are signal events. As E_γ increases, the number of polarized background events increases causing the amount of signal events to be ≈ 80%. At the highest E_γ bins, there are some $\cos\theta_{K^0}^{CM}$ bins where the percentage of signal events are less than 50%.

6.2 Photon Polarization

The polarization of the photon, P_{circ}, for each event is related to the polarization of the electron, P_e, through the Maximon Olsen relation in Equation 5.10. Shown in Fig. 6.2 is the ratio of photon polarization to electron polarization ($\frac{P_\gamma}{P_e}$) vs. the ratio of photon energy to electron energy ($\frac{E_\gamma}{E_e}$). The electron polarizations used to calculate

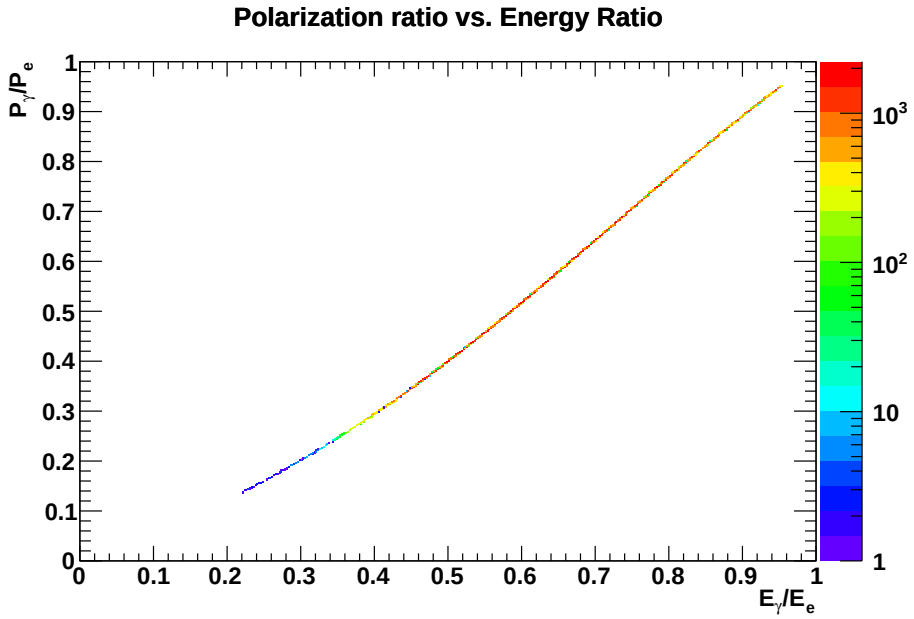

Figure 6.2: The ratio of photon polarization to the electron polarization as a function of the ratio of photon energy to electron energy. The photon polarization was calculated using Eq. 5.10. The electron polarization was measured by the Møller polarimeter in Hall B.

the photon polarizations were measured using the Møller polarimeter located in Hall B. From this figure it is easy to see the range of photon energies and polarizations in the experiment.

6.3 Unprimed Coordinate System

6.3.1 Observables as a function of $\cos\theta^{CM}_{K^0}$

Figures 6.3, 6.4, and 6.5 show C_x, C_z, and P, respectively, for 16 E_γ bins as a function of $\cos\theta^{CM}_{K^0}$. The red and blue curves are the two Bonn–Gatchina solutions from the $K^0\Lambda$ cross–sections projected onto the corresponding observable [18]. Since the observables have not been fit there is no expectation that the observables and solutions should agree.

The maximum likelihood fits were constrained to be nearly within the physically allowed limits of the observables of $[-1,\ 1]$. Specifically, the values were constrained

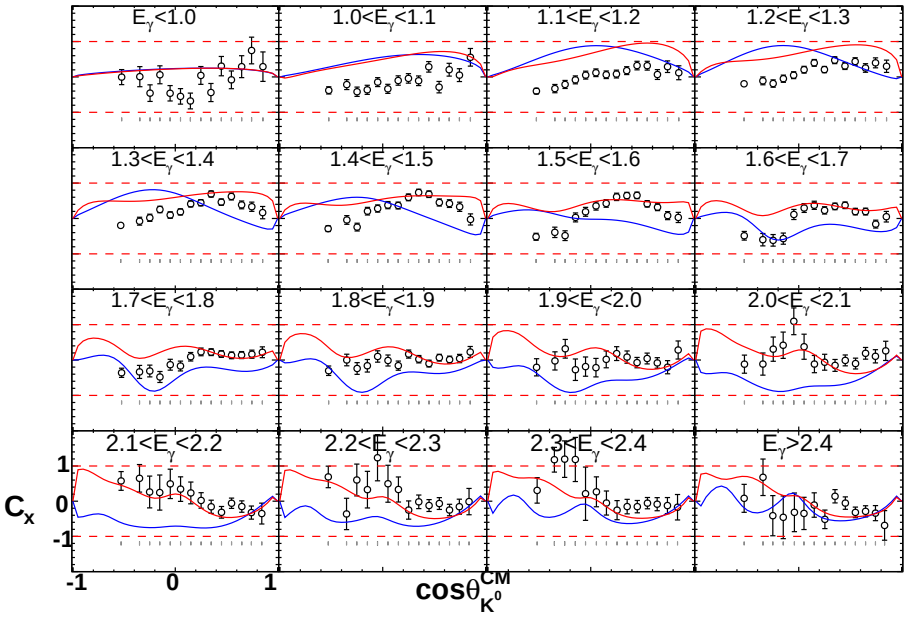

Figure 6.3: C_x as a function of $\cos\theta_{K^0}^{CM}$ for the 16 different E_γ bins. The red and blue curves are the two Bonn–Gatchina soultions from the cross–sections projected (not fit) onto C_x.

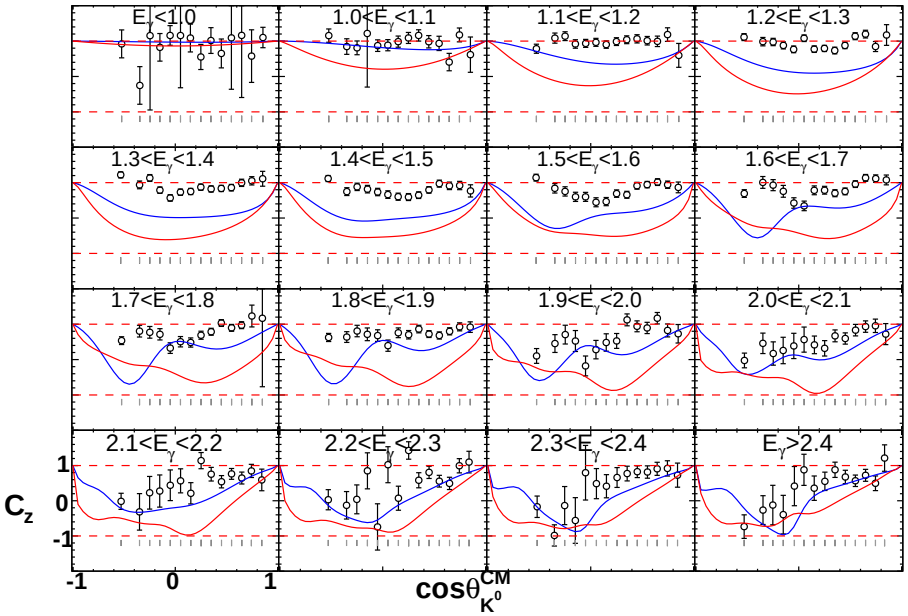

Figure 6.4: C_z as a function of $\cos\theta_{K^0}^{CM}$ for the 16 different E_γ bins. The red and blue curves are the two Bonn–Gatchina soultions from the cross–sections projected (not fit) onto C_z.

between ≈ -1.1 and 1.1. The reason for this is that if the fit returns a value for an observable at the limit, for example $+1$, the statistical uncertainties returned by the

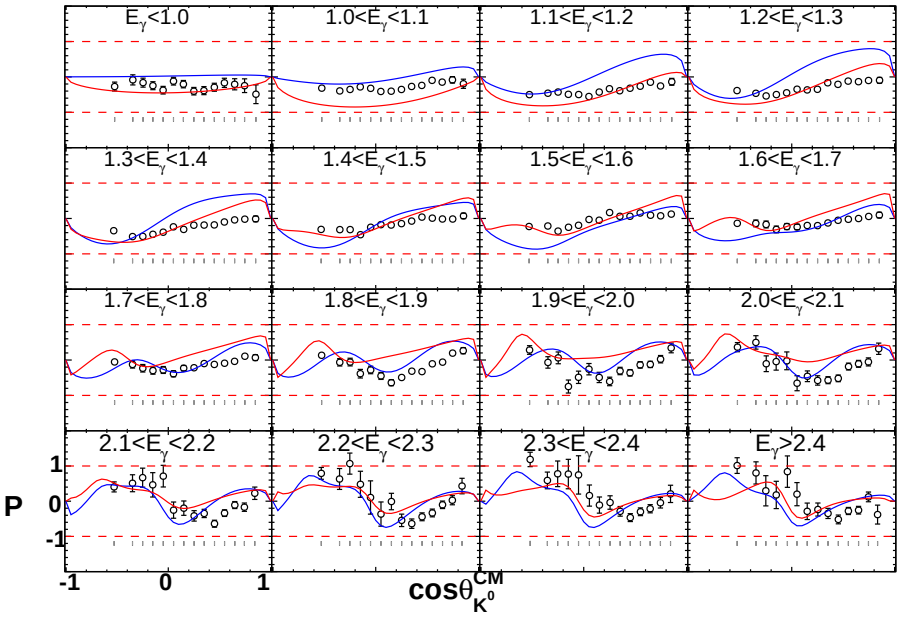

Figure 6.5: P as a function of $\cos\theta^{CM}_{K^0}$ for the 16 different E_γ bins. The red and blue curves are the two Bonn–Gatchina soultions from the cross–sections projected (not fit) onto P.

fit are much larger than the true statistical uncertainty. Some data points, specifically values for C_z of $E_\gamma < 1.0$, still exhibit this trait. Since these data points are at the limit allowed by the fit, they may not be representative of the "true" value. This only appears to be the case for a few points in C_z where the values are large, positive, and in low statistics bins.

At $E_\gamma < 1.3$, C_x shows a general increase when going from backward to forward angles. From $1.3 < E_\gamma < 1.7$ GeV, C_x increases until $\cos\theta^{CM}_{K^0} \approx 0.4$, peaks, then decreases at the most forward angles. From $1.7 < E_\gamma < 2.0$ GeV, C_x is generally constant throughout all the $\cos\theta^{CM}_{K^0}$ bins. Above E_γ of 2.2 GeV, C_x experiences a decrease after $\cos\theta^{CM}_{K^0}$ of ≈ 0. Both Bonn–Gatchina solutions appear to capture some features of C_x at different energy bins. For example, at the highest E_γ bins, the red line captures some on the features seen in the data. It is generally large at backward angles then gradually decreases to the forward angles.

Up to $E_\gamma = 1.9$ GeV, C_z is close to 1 with little shape to it for nearly all $\cos\theta^{CM}_{K^0}$

bins. After $E_\gamma = 1.9$ GeV, C_z is negative at backward angles and close to +1 at forward angles. Like C_x, the Bonn–Gatchina projected solutions seem to describe the general trend of C_z at these higher energy bins.

For $E_\gamma < 1.7$ GeV, P has a slight upward slope when going from backward to forward angles. Throughout most of these bins, P is negative. Above E_γ of 1.8 GeV, P begins to have some shape to it. Below 2.1 GeV, P has a minimum occurring around $\cos\theta^{CM}_{K^0} \approx 0.1$. Above 2.1 GeV, P begins at ≈ 1 at backwards angles, then has a steep slope down to large negative values. Finally, the values appear to plateau at the most forward $\cos\theta^{CM}_{K^0}$ bins. Throughout nearly all the bins, both Bonn-Gatchina projected solutions describe trends that are seen in the data.

Figure 6.6 shows the total polarization transfer, $R = \sqrt{C_x^2 + C_z^2 + P^2}$. Physically, R should be ≤ 1. However, due to the statistical and systematic uncertainties, R may

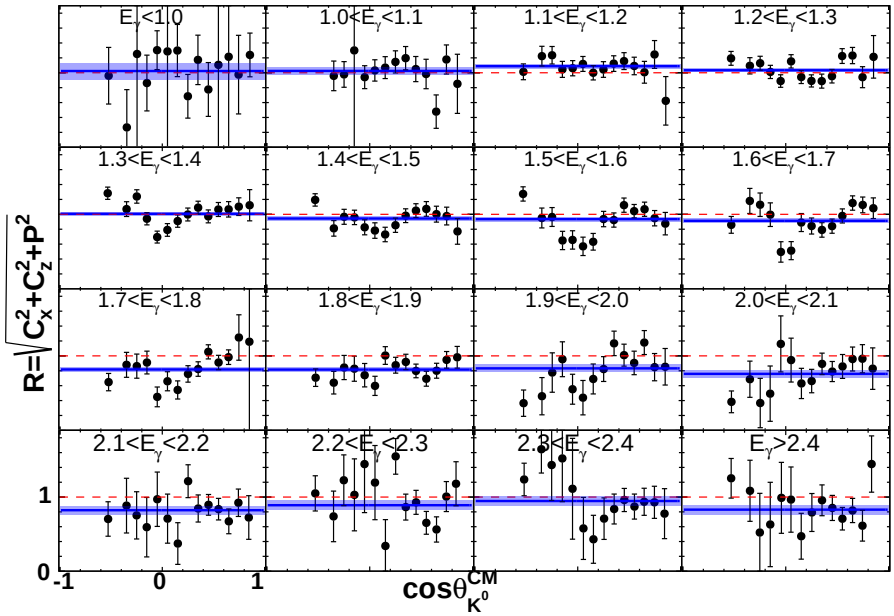

Figure 6.6: $R = \sqrt{C_x^2 + C_z^2 + P^2}$ as a function of $\cos\theta^{CM}_{K^0}$ for the 16 different E_γ bins. The blue line is a constant fit to R for each E_γ bin. The width of the line is the uncertainty of the fit.

be greater than 1. For each $\cos\theta^{CM}_{K^0}$, the values for R were fit with a constant (blue line), with the uncertainty in the fit represented by the blue box. Below E_γ of 1.4

GeV, $R = 1$. At the mid E_γ bins, $0.8 < R < 1$. In general, the largest polarization transfers occur at backward and forward angles in this bin region. There is also a drop in R at $\cos\theta \approx 0$. Above E_γ of 2.2 GeV, $0.9 < R < 1$.

6.3.2 Observables as a function W

Figures 6.7, 6.8, and 6.9 show C_x, C_z, and P as a function of the center–of–mass energy $W = \sqrt{m_n^2 + 2m_n E_\gamma}$ for the 14 $\cos\theta_{K^0}^{CM}$ bins. For $\cos\theta_{K^0}^{CM} < 0.3$, C_z is ≈ 1.0

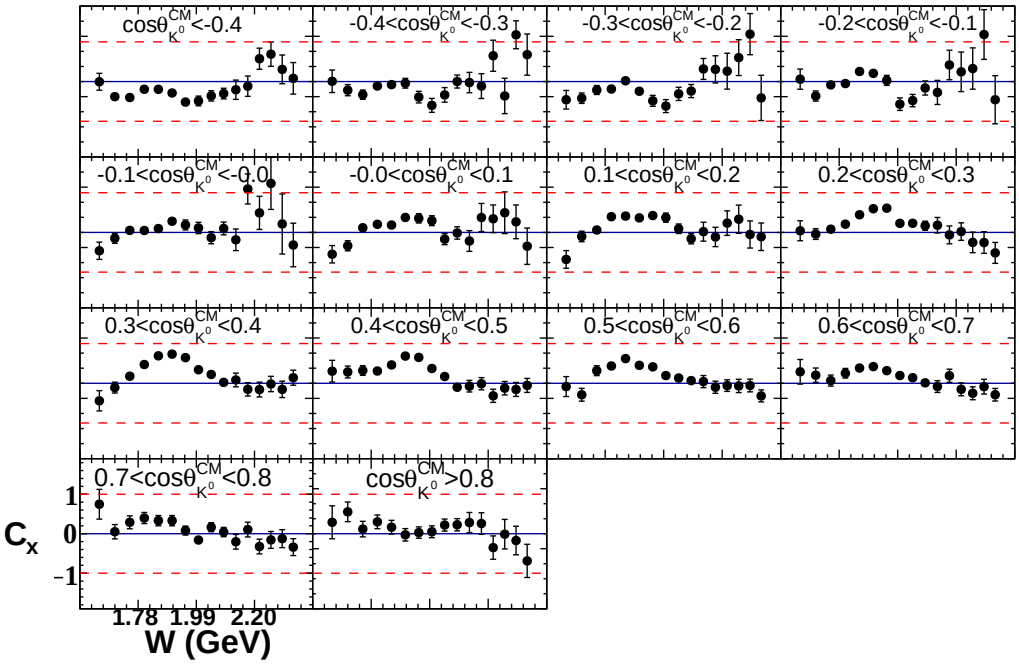

Figure 6.7: C_x as a function of $W = \sqrt{m_n^2 + 2m_n E_\gamma}$ for the 14 different $\cos\theta_{K^0}^{CM}$ bins.

at low energies and gradually decreases in value as W increases. Above these $\cos\theta_{K^0}^{CM}$ of 0.3, C_z is close to 1 and does not drastically change as a function of W. At backward angles, C_x is close to 0 then gradually becomes larger as W increases. For $0.0 < \cos\theta_{K^0}^{CM} < 0.6$, C_x gradually rises at low energies, peaks around $W = 2$ GeV, then gradually deceases at the highest energies. Above $\cos\theta_{K^0}^{CM}$ of 0.6, C_x has some shape to it but is fairly constant throughout all W bins.

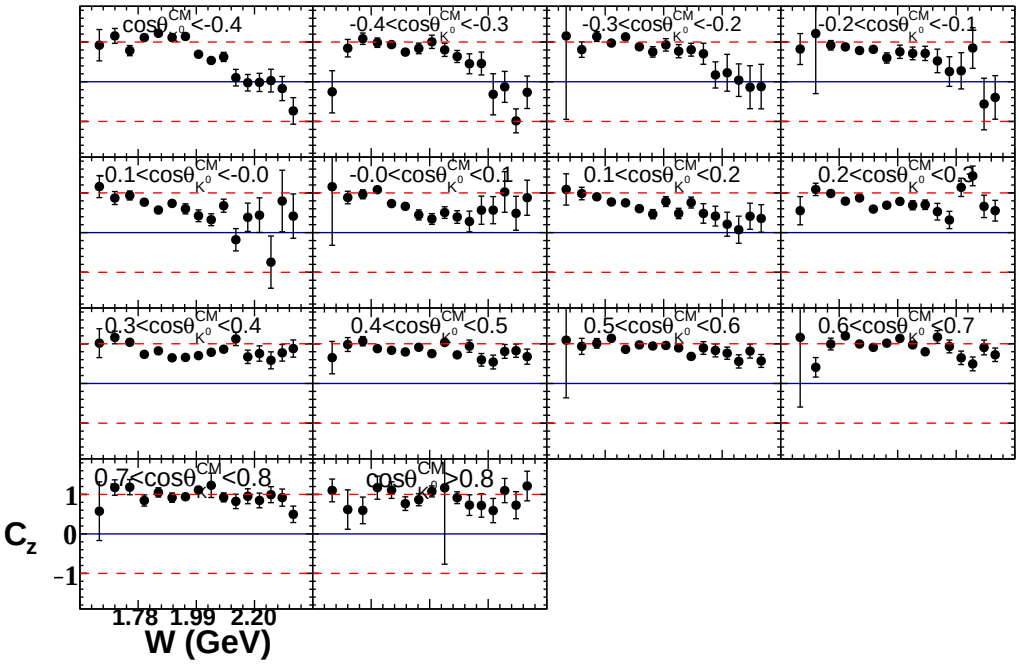

Figure 6.8: C_z as a function of $W = \sqrt{m_n^2 + 2m_n E_\gamma}$ for the 14 different $\cos\theta_{K^0}^{CM}$ bins.

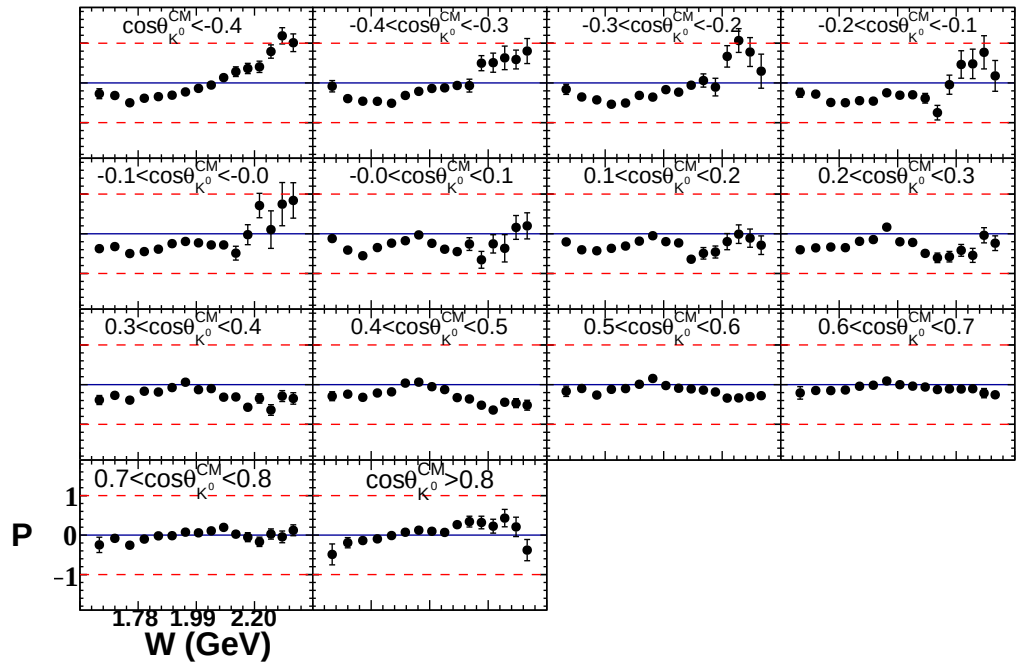

Figure 6.9: P as a function of $W = \sqrt{m_n^2 + 2m_n E_\gamma}$ for the 14 different $\cos\theta_{K^0}^{CM}$ bins.

Throughout all $\cos\theta_{K^0}^{CM}$ bins, P is negative or zero at the lowest W bins. At backward angles, P remains negative until $W \approx 2.0$ GeV. At these bins, P rapidly increases to 1 at large W. Above $\cos\theta_{K^0}^{CM}$ of 0, P remains largely negative throughout all W bins until $\cos\theta_{K^0}^{CM} > 0.7$. These mid and forward $\cos\theta_{K^0}^{CM}$ have a "peak" in P of 0 at $\approx W = 1.9$ GeV. At the the most forward angles, P has a slight slope going from negative to positive values of W over the 16 W bins.

6.4 Primed Coordinate System

6.4.1 Observables as a function of $\cos\theta_{K^0}^{CM}$

For the primed coordinate system, the $\hat{z}'$ axis is aligned along the K^0 momentum in the center–of–mass frame, $\hat{y}' = \hat{z}' \times \vec{p}_{\gamma}^{CM} = \hat{y}$, and $\hat{x}' = \hat{y}' \times \hat{z}'$. Figures 6.10, 6.11, and 6.12 show C_x, C_z, and P, respectively, for 16 E_γ bins as a function of $\cos\theta_{K^0}^{CM}$ for the primed coordinate system. Four different lines are drawn: the dashed lines are

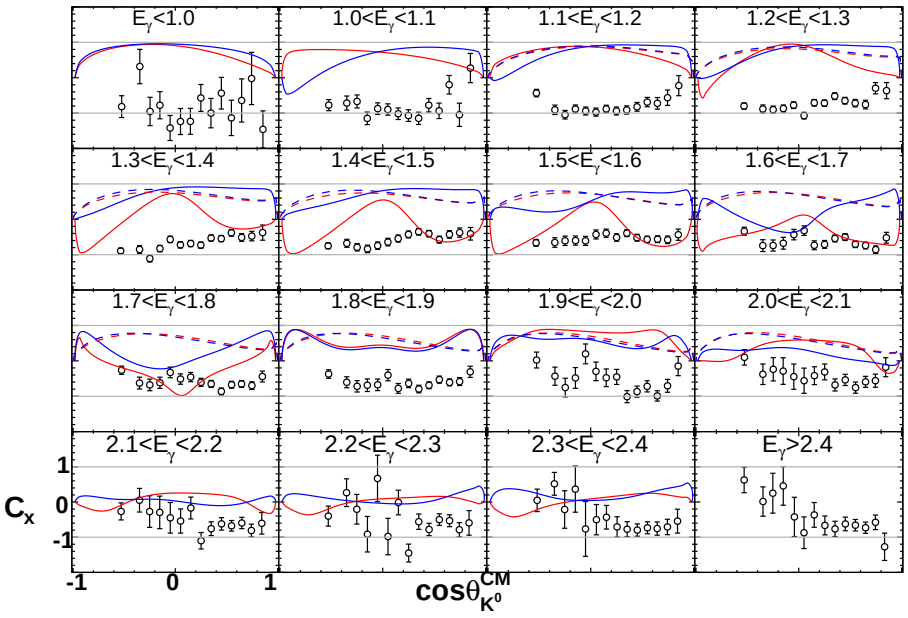

Figure 6.10: C_x as a function of $\cos\theta_{K^0}^{CM}$ for the 16 different E_γ bins for the primed coordinate system. The dashed lines correspond to Kaon–MAID solutions [33] for the observable and the solid line are model predictions from A. Waluyo [55]. The red and blue lines correspond to predictions with and without an extra $N(1900)\frac{3}{2}^-$ state, respectively.

Kaon–MAID solutions [33] for the observable and the solid line are model predictionss from A. Waluyo [55]. The red lines are predictions with an additional $N(1900)\frac{3}{2}^-$

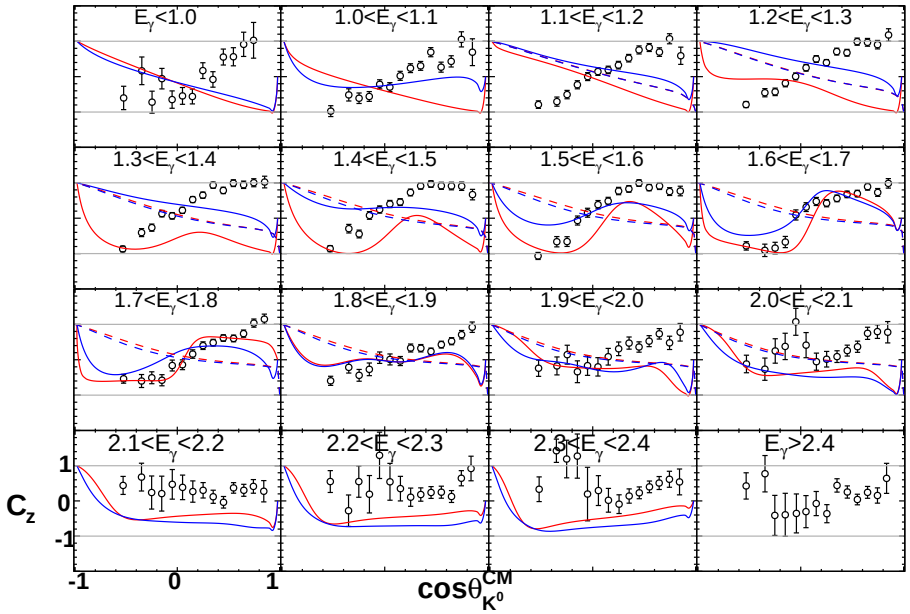

Figure 6.11: C_z as a function of $\cos\theta_{K^0}^{CM}$ for the 16 different E_γ bins for the primed coordinate system. The dashed lines correspond to Kaon–MAID models [33] for the observable and the solid line are model predictions from A. Waluyo [55]. The red and blue lines are predictions with and without an extra $N(1900)\frac{3}{2}^-$ state, respectively.

state and the blue lines are predictions without an additional $N(1900)\frac{3}{2}^-$ state.

In the late 1990's and early 2000's, it was suggested that there may be a yet unseen resonance, a $D_{13}(1900)$ (an $N(1900)\frac{3}{2}^-$ in modern notation) [10]. This state corresponded to a state predicted by a relativistic quark model with a mass of 1960 MeV. Overall, the models do not agree with what is seen in the data, but that is to be expected. Both these predictions were made in the early 2000's, and were not fit to any KY photoproduction data. Since then, there has been significant work done on the extraction of cross–sections and polarization observables in KY photoproduction. The two Kaon–MAID solutions produce similar results to each other. For C_x and C_z, the two predictions from Waluyo produce drastically different results throughout most kinematic bins. This model for P, like Kaon–MAID, produces similar results with and without the additional $D_{13}(1900)$ state.

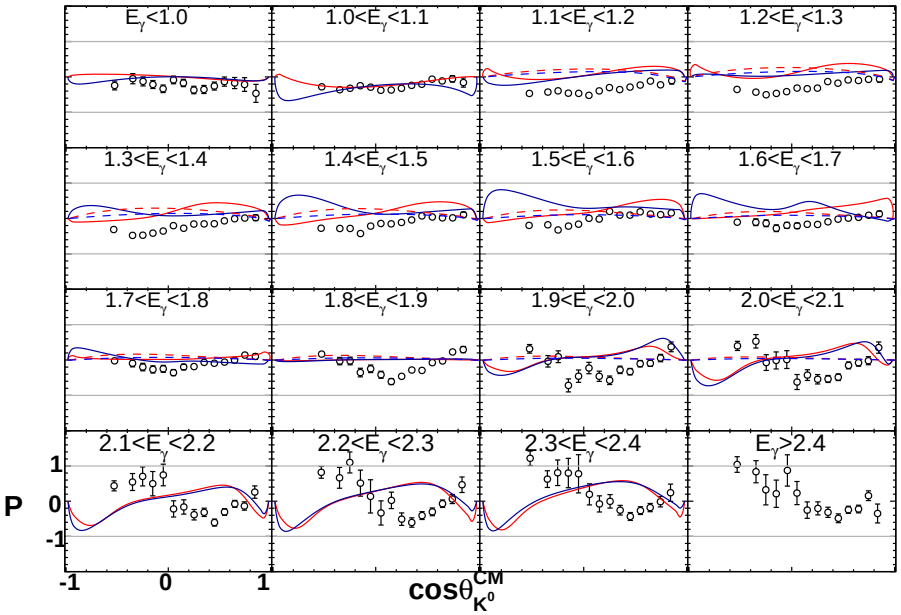

Figure 6.12: P as a function of $\cos\theta^{CM}_{K^0}$ for the 16 different E_γ bins for the primed coordinate system. The dashed lines are Kaon–MAID models [33] for the observable and the solid line are model predictions from A. Waluyo [55]. The red and blue lines are predictions with and without an extra $N(1900)\frac{3}{2}^-$ state, respectively.

6.5 Comparison with $\gamma p \to K^+\Lambda$

To compare the observables to those of the free–proton observables, the data were binned in 16 E_γ bins 100 MeV wide and 9 $\cos\theta^{CM}_{K^0}$ bins. Figures 6.13 and 6.14 show C_x and C_z for $\gamma d \to K^0\Lambda(p)$ (black circles) and $\gamma p \to K^+\Lambda$ (blue circles). When the free proton data was published, there were a couple unexpected results. Firstly and generally speaking, C_z was greater than C_x and close to 1. This means that the Λ is nearly fully polarization along the z–axis, which is the direction of the incoming photon in the center–of–mass frame. Secondly, the total polarization transfer, $R = \sqrt{C_x^2 + C_z + P^2}$, was found to be ≈ 1 throughout most kinematic bins. Not only will it be helpful to see if the quasi–free $K^0\Lambda$ exhibits the same features, but it is useful to see the differences in observables between the two data sets, even though no conclusions about the underlying physics can be made from such a comparison. The two reactions are quite different from each other as they occur off of particles

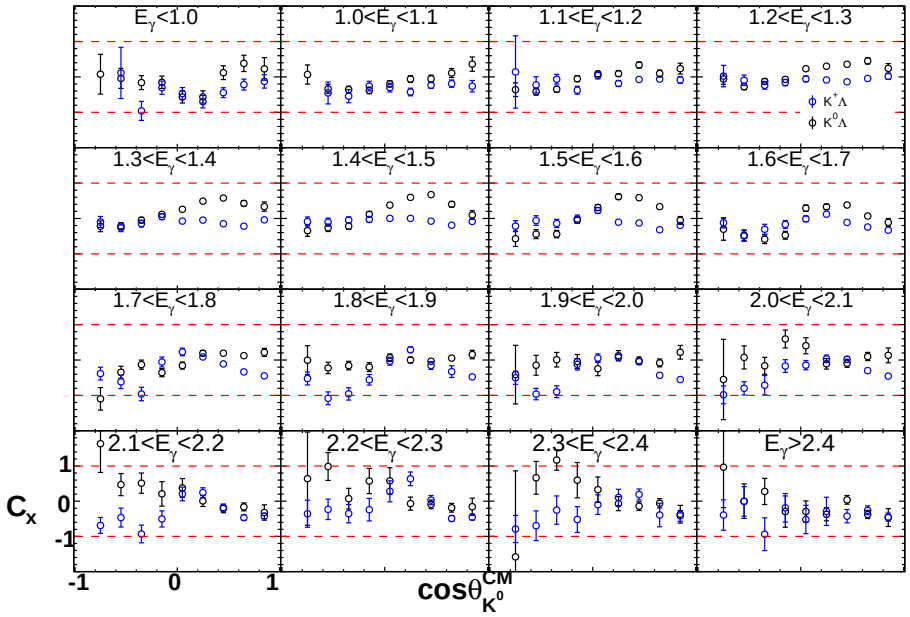

Figure 6.13: A comparison of C_x for $\gamma d \to K^0\Lambda(p)$ (black) and $\gamma p \to K^+\Lambda$ (blue). Each $\cos\theta^{CM}_{K^0}$ bin is drawn at the bin centroid as opposed to the bin average to match the free proton data.

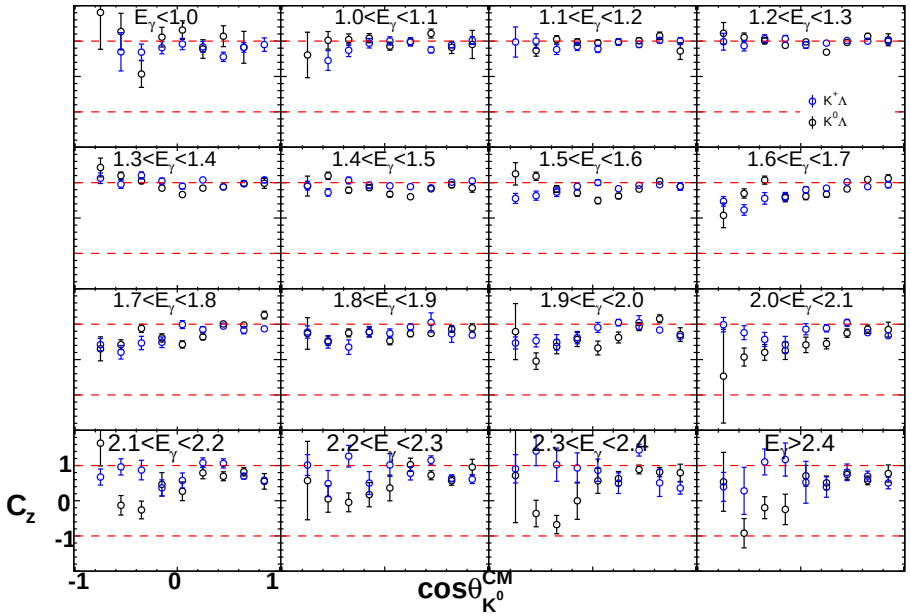

Figure 6.14: A comparison of C_z for $\gamma d \to K^0\Lambda(p)$ (black) and $\gamma p \to K^+\Lambda$ (blue). Each $\cos\theta^{CM}_{K^0}$ bin is drawn at the bin centroid as opposed to the bin average to match the free proton data.

with different isospin, I_3. Furthermore, the reaction dynamics may differ as the $K^0\Lambda$ occurs off a bound neutron while the $K^+\Lambda$ occurs off a free proton.

At low E_γ, C_x for both $K^0\Lambda$ and $K^+\Lambda$ is of the same order of magnitude and follow the same trends. Throughout $1.3 < E_\gamma < 1.6$ GeV, the $K^0\Lambda$ data are larger than the $K^+\Lambda$ at forward angles. Above E_γ of 1.8 GeV, the $K^+\Lambda$ is close to -1 at backward angles, while $K^0\Lambda$ varies between 0 and +1.

At low to mid E_γ bins, C_z is close to +1 for both $K^0\Lambda$ and $K^+\Lambda$. When $E_\gamma \approx 1.6$ GeV, the two observables begin to differ from +1. The observables begin to differ from each other at backward angles when $E_\gamma \approx 2.0$ GeV. Then, at the highest E_γ bins and backward angles, the $K^+\Lambda$ observables remains large and positive while $K^0\Lambda$ observable is close to zero and in some cases, negative.

6.6 Observables as a Function of the Neutron Momentum

The above discussions center around the observables for the quasi–free reaction. This means the neutron is not free but bound with the proton to make deuterium. The fact that it has non–zero momentum and is bound can have some effect on the polarization observables. The quasi–free momentum cut of 0.2 GeV/c can be tested by looking at the observables as a function of the neutron momentum. If the observables are constant over the quasi–free range (or a sub range), then they should accurately represent what would be seen in a free neutron. If the observables are not constant over the quasi–free range, then it may be possible to extrapolate to a "free" neutron ($|p_{neutron}| = 0$) by fitting the observables as a function of neutron momentum.

Figure 6.15 shows C_x (blue), C_z (red), and P (green), integrated over all E_γ and $\cos\theta^{CM}_{K^0}$, as a function of the neutron momentum. Each observable is fit with a first order polynomial. Table 6.2 lists the fit parameters for each observable. P is the only observable having a slope consistent with 0. C_x has a slope consistent within 2σ of 0 and C_z within 3σ of 0.

To view this effect on the kinematics, the observables were extracted into 8 equal width E_γ bins (integrated over all $\cos\theta^{CM}_{K^0}$) and drawn as a function of the neutron

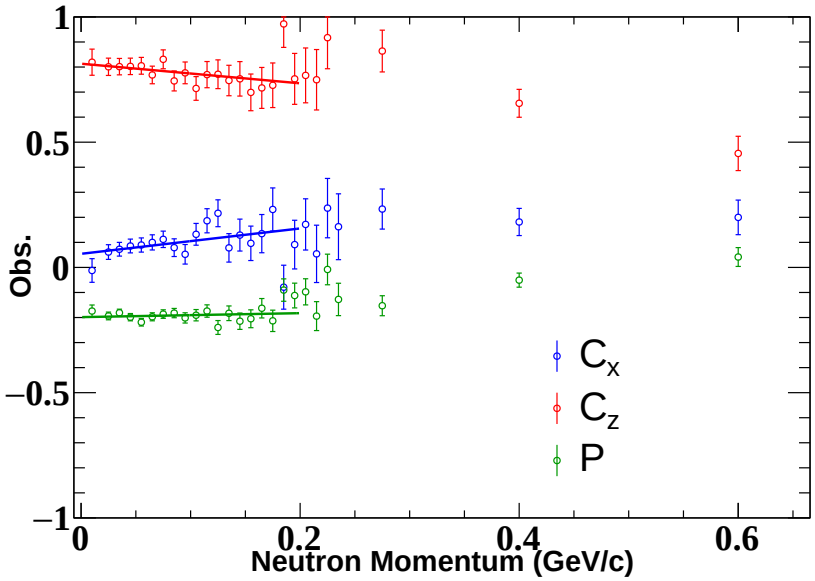

Figure 6.15: C_x (blue), C_z (red), and P (green), integrated over all E_γ and $\cos\theta_{K^0}^{CM}$, as a function of the neutron momentum. Each observable is fit with a first order polynomial.

Table 6.2: Fit parameters for each observable from Fig. 6.15. P is the only observable having a slope consistent with 0. C_x has a slope consistent within 2σ of 0 and C_z within 3σ of 0.

Obs.	Intercept	Slope
C_x	0.054±0.018	0.506±0.221
C_z	0.813±0.021	-0.391±0.243
P	-0.198±0.010	0.079±0.113

momentum. Figures 6.16, 6.17, and 6.18 show C_x, C_z, and P, respectively, for the 8 different E_γ bins as a function of the neutron momentum. Each kinematic bin was fit with a first order polynomial in the quasi–free range (red line). The Y–intercept (red point) and mean of the quasi–free (blue point) were also calculated.

For C_x, the mean and Y–intercept agree for all kinematic bins within the uncertainties. While there is a slope present in most kinematic bins, the value extrapolated to 0 does not greatly differ from the average value. In addition to this, the slopes show no dependence on the E_γ bin.

For C_z, the the mean and Y–intercept agree for all kinematic bins within the

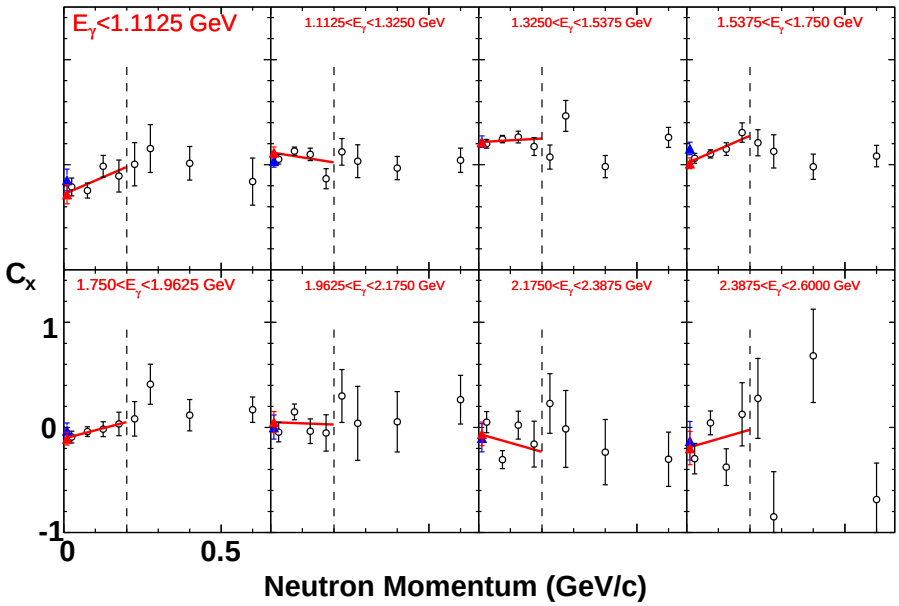

Figure 6.16: C_x for 8 E_γ as a function of the neutron momentum integrated over all $\cos\theta^{CM}_{K^0}$. Each bin is fit with a line in the quasi–free region ($|p_n| < 0.2$ GeV/c).

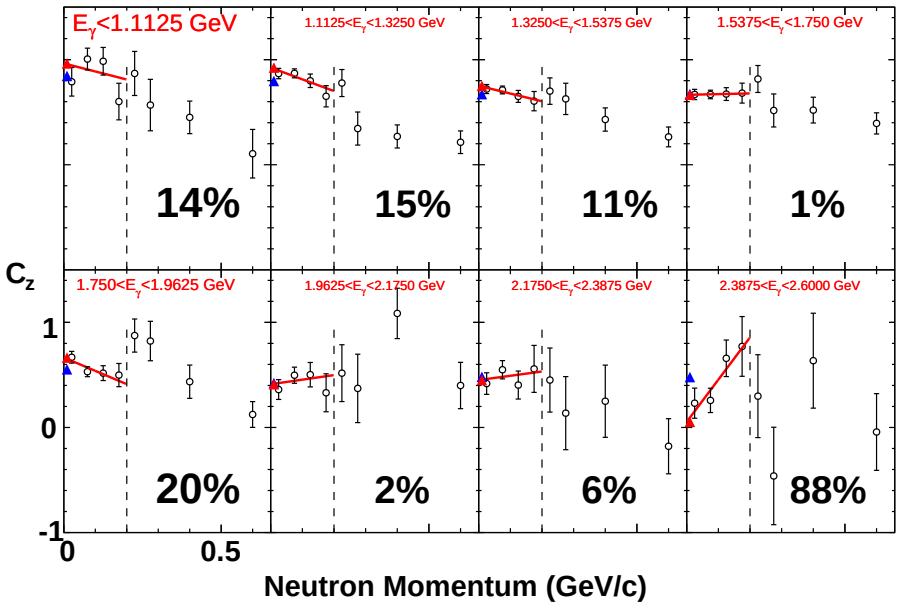

Figure 6.17: C_z for 8 E_γ as a function of the neutron momentum integrated over all $\cos\theta^{CM}_{K^0}$. Each bin is fit with a first order polynomial in the quasi–free region ($|p_n| < 0.2$ GeV/c). The numbers in each panel denote the % difference between the average value of the observable within the quasi–free range of neutron momentum and the extrapolated value to a neutron momentum of zero.

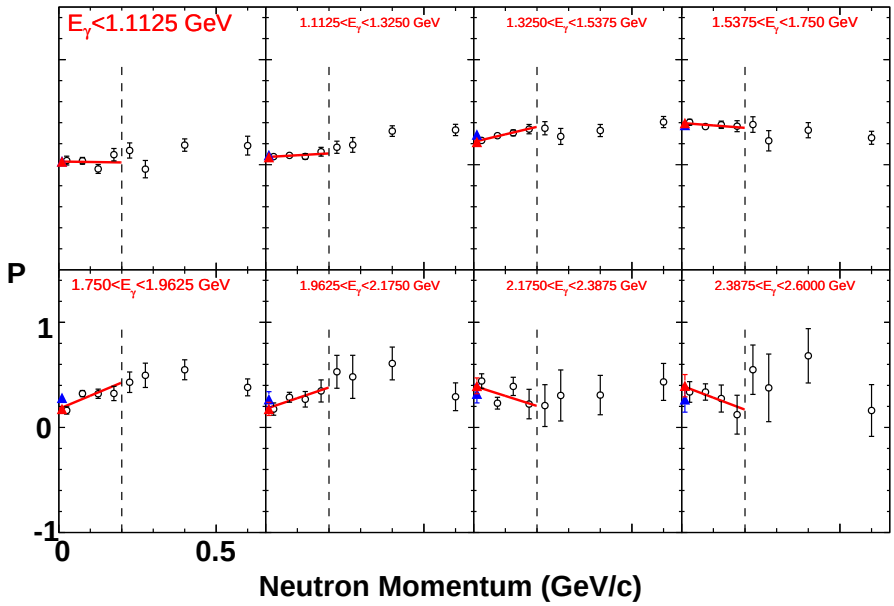

Figure 6.18: P for 8 E_γ as a function of the neutron momentum integrated over all $\cos\theta^{CM}_{K^0}$. Each bin is fit with a first order polynomial in the quasi–free region ($|p_n| < 0.2$ GeV/c).

uncertainties except for the largest E_γ bin. In this bin, the values for the observables change from ≈ 0.2–0.8 over the quasi–free range. There also appears to be some E_γ dependence of the slope of the fit. At the low and mid E_γ bins, the slope is either negative or 0. A positive slope is not seen until the higher E_γ bins.

For P, the mean and Y–intercept overlap for all E_γ bins. At low E_γ, there is little dependence of the quasi–free observables on the neutron momentum. The mid E_γ bins tend to have a positive slope, while the high E_γ bins have a negative slope. These trends are opposite to what is seen in C_x.

6.7 Discussion

Studying the reaction $\gamma n \to K^0\Lambda$ provides new and complimentary information to the reaction $\gamma p \to K^+\Lambda$. Since the production of $K^0\Lambda$ occurs off the neutron, the reaction is able to excite different states than the reaction for the proton. Additionally, $K^0\Lambda$ can also be used to provide further constraints to N^* that couple to all KY channels,

like $K^+\Lambda$. It is also interesting to compare the behaviors of the observables between the free proton and bound neutron.

The most immediate conclusions available (at the moment) relate to the comparison of the observables between the free proton and bound neutron. It is shown that for most kinematic bins the total polarization transfer, the quantity $R = 1$. This is similar to what is seen in the free proton data. While this is similar, there are both similarities and differences in the behavior of C_x and C_z. At low energies, the two values C_z are quite similar to each other. At higher energies, there are significant differences, particularly at backward angles. The two values for C_x behave differently above energies of ≈ 1.3 GeV. While these comparisons are interesting, nothing quantitative about $K^0\Lambda$ can be said.

The most interesting conclusions from this work will be known once C_x, C_z, and P are fit by theoretical groups. When in the primed coordinate system, significant differences appear between the data and theoretical predictions of Kaon–MAID and Waluyo. Clearly, these results will have a large impact on the parameters of these predictions.

The data will be fitted by the Bonn–Gatchina PWA. The functions shown here are not to be interpreted as predictions, but instead show their current solutions projected onto C_x, C_z, and P. Once these observables are fit, they should be able to distinguish between the two solutions. As of now, significant differences are seen between the projections and C_x and C_z. Both solutions follow the trend of P. The fits to the cross–sections did not show any evidence for new N^* states. However, it is too early to discuss whether or not these polarization observables will do so. With that said, the new fits should be able to provide additional constraints to current N^* amplitudes.

The observables were also extracted as a function of the neutron momentum. The goal here is to see how well the quasi–free observables ($p_X < 0.2$ GeV/c) represent the

observables from a free neutron ($p_X = 0$ GeV/c). Overall, the average value of the quasi–free observable agrees within 20% when extrapolated to the free-neutron point of $p_X = 0$ MeV/c. Only one kinematic bin for C_z shows a difference above 50%. These studies are quite promising as they suggest the level of accuracy at which quasi–free observables can represent the free–neutron observables.

One possible extension of this project is to extract the observables for $\gamma d \to K^0\Sigma^0$. In order to extract the observables for this channel, much work would need to be done to understand the high mass (K^{*0}, Σ^*, etc.) channels. Our current background subtraction process only used these events to get the fit to M_X to behave properly at higher masses. These channels were removed from the observable extraction process with a M_X cut. One would have to find a way to accurately represent the contribution of these background channels.

A second extension of this project would be to extract the observables in the region where final–state interactions dominate ($p_X > 0.2$ GeV/c). To do this, the event generator and simulation studies would need to be expanded to include different types of final–state interactions (e.g. Λ rescattering). Once this was done, the background subtraction and observable extraction methods could be employed.

Bibliography

1. *Meson*, Wikimedia Foundation, 2017.

2. *Standard model*, Wikimedia Foundation, 2017.

3. G. Aad et al., *Observation of a new particle in the search for the Standard Model Higgs boson with the ATLAS detector at the LHC*, Phys. Lett. B **716** (2012), 1.

4. R. Adelseck and B. Saghai, *Kaon photoproduction: Data consistency, coupling constants, and polarization observables*, Phys. Rev. C **42** (1990), 108.

5. M. Amarian et al., *The CLAS forward electromagnetic calorimeter*, Nucl. Instrum. Methods Phys. Res. **A 460** (2001), 239.

6. C. Amsler et al., *Rev. Part. Phys.*, Phys. Lett. B **667** (2008), 1.

7. M. Anghinolfi et al., *The CLAS electromagnetic calorimeter at large angles*, Nucl. Instrum. Methods Phys. Res. **A 537** (2005), 562.

8. A. V. Anisovich, V. Kleber, E. Klempt, V. A. Nikonov, A. V. Sarantsev, and U. Thoma, *Baryon resonances and polarization transfer in hyperon photoproduction*, Eur. Phys. J. **A 34** (2007), 243.

9. I. S. Barker, A. Donnachie, and J. K. Storrow, *Complete experiments in pseudoscalar photoproduction*, Nucl. Phys. B **95** (1975), no. 2, 347.

10. C. Bennhold, A. Waluyo, H. Haberzettl, T. Mart, G. Penner, and U. Mosel, *Missing nucleon resonances in kaon production with pions and photons*, Newport News 2000, Excited nucleons and hadronic structure, 2000, pp. 280.

11. R.K. Bradford et al., *First measurement of beam–recoil observables C_x and C_z in hyperon photoproduction*, Phys. Rev. C **75** (2007), 035205.

12. T. Cao, *Determination of the polarization observables C_x, C_z, and P_y for final-state interactions in the reaction $\vec{\gamma}d \to K^+\vec{\Lambda}n$*, Ph.D. Thesis, 2016.

13. S. Capstick, *Quark models of baryon masses and decays*, Prog. Part. Nucl. Phys. **45** (2000), S241.

14. S. Capstick and N. Isgur, *Baryons in a Relativized Quark Model with Chromodynamics*, Phys. Rev. D **34** (1986), 2809.

15. S. Capstick and W. Roberts, *Strange decays of nonstrange baryons*, Phys. Rev. D **58** (1998), 074011.

16. S. Chatrchyan et al., *Observation of a new boson at a mass of 125 GeV with the CMS experiment at the LHC*, Phys. Lett. B **716** (2012), 30.

17. G. F. Chew, M. L. Goldberger, F. E. Low, and Y. Nambu, *Relativistic dispersion relation approach to photomeson production*, Phys. Rev. **106** (1957), 1345.

18. N. Compton et al., *Measurement of the Differential and Total Cross Sections of the $\gamma d \to K^0\Lambda(p)$ Reaction within the Resonance Region*, Submitted to Phys. Rev. C. (2017), available at `1706.04748`.

19. V. Crede and W. Roberts, *Progress towards understanding baryon resonances*, Rept. Prog. Phys. **76** (2013), 076301.

20. B. Dey, C. A. Meyer, M. Bellis, M. E. McCracken, M. Williams, et al., *Differential cross sections and recoil polarizations for the reaction $\gamma p \to K^+\Sigma^0$*, Phys. Rev. C **82** (2010), 025202.

21. R. Edwards, J. Dudek, D. Richards, and S. Wallace, *Excited state baryon spectroscopy from lattice QCD*, Phys. Rev. D **84** (2011), 074508.

22. D. Faiman and A. W. Hendry, *Harmonic–oscillator model for baryons*, Phys. Rev. **180** (1969), 1609.

23. J. Ferretti, A. Vassallo, and E. Santopinto, *Relativistic quark-diquark model of baryons*, Phys. Rev. C **83** (2011), 065204.

24. Z. Fodor and Ch. Hoelbling, *Light hadron masses from lattice QCD*, Rev. Mod. Phys. **84** (2012), 449.

25. M. Gell-Mann and Y. Ne'eman, *The eightfold way*, Frontiers in Physics, Benjamin, New York, 1964.

26. A. V. Glamazdin et al., *Electron beam Moller polarimeter at JLab Hall A*, Fizika B **8** (1999), 91.

27. D. J. Griffiths, *Introduction to elementary particles*, Wiley, New York, 2008.

28. D. J. Gross and F. Wilczek, *Ultraviolet behavior of non-abelian gauge theories*, Phys. Rev. Lett. **30** (1973), 1343.

29. E. Gutz et al., *High statistics study of the reaction $\gamma p \to p\pi^0\eta$*, Eur. Phys. J. A **50** (2014), 74.

30. P. W. Higgs, *Broken symmetries and the masses of gauge bosons*, Phys. Rev. Lett. **13** (1964), 508.

31. H. Kamano, S. X. Nakamura, T.-S. H. Lee, and T. Sato, *Nucleon resonances within a dynamical coupled-channels model of πn and γn reactions*, Phys. Rev. C **88** (2013), 035209.

32. M. Lacombe, B. Loiseau, R. Vinh Mau, J. Côté, P. Pirés, and R. de Tourreil, *Parametrization of the deuteron wave function of the paris nn potential*, Phys. Lett. B **101** (1981), 139.

33. F. X. Lee, T. Mart, C. Bennhold, and L. E. Wright, *Quasifree kaon photoproduction on nuclei*, Nucl. Phys. A **695** (2001), 237.

34. M. Williams, 2004. *Determining Momentum and Energy Corrections for g1c Using Kinematic Fitting*, CLAS-Note 04-017.

35. T. Mart, *MAID 2000*. Accessed: 2017-06-26.

36. Paul Mattione, *Kinematic fitting of detached vertices*, Master's Thesis, 2007.

37. J. W. C. McNabb, *Photoproduction of Lambda and Sigma Hyperons off Protons in the Nucleon Resonance Region using CLAS at Jefferson Lab*, Ph.D. Thesis, 2002.

38. J. W. C. McNabb et al., *Hyperon photoproduction in the nucleon resonance region*, Phys. Rev. C **69** (2004), 042201.

39. B. A. Mecking et al., *The CEBAF Large Acceptance Spectrometer (CLAS)*, Nucl. Instrum. Methods Phys. Res. **A 503** (2003), 513.

40. M. D. Mestayer et al., *The CLAS drift chamber system*, Nucl. Instrum. Methods Phys. Res. **A 449** (2000), 81.

41. N. Zachariou, Y. Ilieva, and T. Cao, 2016. *Determination of polarisation observables for FSI in exclusive hyperon photoproduction off the deuteron*, CLAS-Analysis 2016-003.

42. P. Nadel-Turoński, *Photoproduction and rescattering of polarized hyperons in deuterium*, Few Body Syst. (2008), 227.

43. P. Nadel-Turoński et al., *Kaon production on the deuteron using polarized photons*, Jefferson Lab Experiment E06-103 (2006).

44. H. Olsen, *Photon and electron polarization in high-energy bremsstrahlung and pair production with screening*, Phys. Rev. **114** (1959), 887.

45. E. Pasyuk, *Energy loss corrections for charged particles in CLAS*, CLAS Note 2007–16 (2008).

46. C. A. Paterson et al., *Photoproduction of* Λ *and* Σ^0 *hyperons using linearly polarized photons*, Phys. Rev. C **93** (2016), 065201.

47. C. Patrignani et al., *Review of Particle Physics*, Chin. Phys. **C 40** (2016), 100001.

48. H. D. Politzer, *Reliable perturbative results for strong interactions?*, Phys. Rev. Lett. **30** (1973), 1346.

49. A. M. Sandorfi, S. Hoblit, H. Kamano, and T. S. H. Lee, *Determining pseudoscalar meson photo-production amplitudes from complete experiments*, J. Phys. G **38** (2011), 053001.

50. R. Schumacher, *Polarization of hyperons in elementary photoproduction*, Proceedings, 9th International Conference on Hypernuclear and Strange Particle Physics (HYP 2006):Mainz, Germany, October 10-14, 2006, 2007, pp. 339.

51. Y.G. Sharabian et al., *A new highly segmented start counter for the CLAS detector*, Nucl. Instrum. Methods Phys. Res. **A 556** (2006), 246.

52. E. S. Smith et al., *The time-of-flight system for CLAS*, Nucl. Instrum. Methods Phys. Res. **A 432** (1999), 265.

53. D. I. Sober et al., *The bremsstrahlung tagged photon beam in Hall B at JLab*, Nucl. Instrum. Methods Phys. Res. **A 440** (2000), 263.

54. K. Tsukada, T. Takahashi, T. Watanabe, Y. Fujii, K. Futatsukawa, et al., *Photoproduction of neutral kaons on the liquid deuterium target in the threshold region*, Phys. Rev. C **78** (2008), 014001.

55. A. Waluyo, *Baryon excitation through meson hadro– and photoproduction in a coupled–channels framework*, Ph.D. Thesis, 2006.

56. T. Watanabe, P. Bydzovsky, K. Dobashi, S. Endo, Y. Fujii, et al., *Photoproduction of neutral kaons on C-12 in the threshold region*, Phys. Lett. B **651** (2007), 269.

57. Wikipedia, *Eightfold Way (physics) — Wikipedia, the free encyclopedia*, 2017. [Online; accessed 27-June-2017].

58. Elliot Wolin, *GSIM user's guide version 1.1*, 1996.

59. N. Zachariou, *Determination of the azimuthal asymmetry of deuteron photodisintegration in the energy region E_γ = 1.1 - 2.3 GeV*, Ph.D. Thesis, 2012.